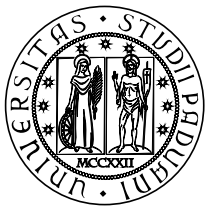

Università
degli Studi
di Padova

DIPARTIMENTO DI METODI E MODELLI MATEMATICI
PER LE SCIENZE APPLICATE

SCUOLA DI DOTTORATO DI RICERCA IN SCIENZE
DELL'INGEGNERIA CIVILE E AMBIENTALE - CICLO XXIII
Sede Amministrativa: Università degli Studi di Padova

Contributions to modeling of Venice coastal peatlands and wetlands

Direttore della Scuola: Ch.mo Prof. Stefano Lanzoni
Supervisore: Ch.mo Prof. Mario Putti
Correlatore: Dott. Ing. Pietro Teatini

Dottoranda: Francesca Zanello

Gennaio 2011

Contents

List of Figures

List of Tables

Contributions to modeling of Venice coastal peatlands and wetlands

Abstract

The Venice Lagoon and its catchment is a unique hydrological resource and ecosystem permanently in quest for equilibrium between the restoration and conservation of environmental system and the anthropic pressure. The intertidal areas are often bound by cultivated peatlands, that are the residues of old wetlands and lagoons that have been drained for agricultural purposes. Peat soils respond to natural cycles of precipitation/imbibition and evapotranspiration as well as to the thaw/freeze cycles with elastic deformations of the soil matrix (swelling/shrinkage). This process induces the reversible displacement of the soil surface that superimposes to the irreversible long term subsidence that occurs naturally in drained peatland because of the bio-oxidation of the organic matter. Land subsidence in drained cultivated peatlands is responsible for a number of serious environmental concerns and economical problems at both the local and the global scale.

The present Thesis reports an articulated research work that covers several aspects connected with the modeling of subsurface hydrology of organic soils in connection to the main hazards induced by land subsidence of peatlands and the conservation and wise use of wetlands in the Venetian area. First a description of the study areas with an accurate overview of the main properties of the organic soils and the interconnection of the different compartments, namely atmosphere, sea, and soil, in these humid zones is provided.

The dynamics of peatland surface deformation both at long and short time scale is studied and a novel two-step modeling approach is proposed to separate the reversible and irreversible components of the land surface displacement.

An empirical relationship is calibrated on the estimated reversible component of the graound displacements recorded in a 4-year long experimental study in a field site located in a Venetian peatland. The expected evolution of the peat thickness in the Venetian peatland over the present century according to the scenarios proposed by IPCC [2007] is then investigated.

The study of the hydrology of organic soils is then focused on the hysteretical behavior of the moisture retention curve measured in the peat soils of the Zennare Basin, Italy. The study of a long term sequence of capillary pressure - saturation measurements shows that the reversible deformation of organic soils enhances the hysteretic behavior of the moisture retention curve.

The results of the application of a modeling approach that couples an hysteresis model with a relationship that links the soil matrix porosity dynamic to water saturation confirm the importance of including the swelling/shrinkage phenomenon in the description and prediction of water flow into organic soils.

In the last part of the Thesis the focus is shifted to the hydrological dynamics of salt marshes as they interact with atmosphere and vegetation. These delicate intertidal zones are characterized by a strong hydrological connection between the atmosphere and the subsurface mainly in terms of air fluxes.

Richards equation, usually adopted for the simulation of water infiltration in soils in variably saturated conditions, assumes that air is readily displaced by water, hence is not able to account for the actual fluxes of air. Therefore in the simulation of flow in salt marshes one needs to take into account the entrapped air on the water infiltration in the soils and its movement. A two-phase flow model is developed in order to investigate the effects of air flow in the wetlands dynamics. A pressure based formulation is chosen to allow for natural treatment of the complex and nonlinear boundary conditions to be imposed at the soil-atmosphere interface to take into account the interplay between evapotranspiration during emersion periods and tidal fluctuations during soil submersion. The results of the application of the model to some test cases aimed at verifying the effect of the inclusion of the air dynamics in the simulation of the water flow in the vadose zone are finally presented.

Contributi alla modellazione delle zone torbose costiere e delle aree umide della Laguna di Venezia

Sommario

La Laguna di Venezia e il relativo bacino imbrifero costituiscono una risorsa idrologica unica, permanentemente alla ricerca di un equilibrio tra il ripristino e la conservazione dell'ecosistema e la pressione antropica. Le aree intertidali sono spesso delimitate da zone torbose coltivate, residui di antiche aree umide e lagune bonificate per fini agricoli. I suoli torbosi rispondono ai cicli di precipitazione/evapotraspirazione e di congelamento/disgelo con spostamenti reversibili della superficie del suolo che si sovrappongono alla subsidenza irreversibile a lungo termine che avviene naturaelmente nelle aree torbose coltivate a causa della bio-ossidazione della sostanza organica. La subsidenza dei terreni nelle aree torbose coltivate è responsabile di gravi conseguenze sull'ambiente e problemi di natura economica sia su scala locale che globale.

La presente Tesi riporta di un lavoro di ricerca articolato che copre numerosi aspetti connessi con la modellazione dell'idrologia sotterranea dei suoli torbosi in relazione alle principali cause di rischio indotte dalla subsidenza e con la conservazione e l'uso consapevole delle aree umide nel comprensorio veneziano. Le zone oggetto di studio sono descritte in dettaglio, dando spazio a una panoramica delle pricipali proprietà dei terreni organici e dell'interconnessione dei diversi comparti che caratterizzano le aree umide, ovvero atmosfera, mare e suolo. Le dinamiche della superficie dei suoli torbosi sia sul breve che sul lungo periodo sono analizzate ed è proposto un nuovo approccio modellistico finalizzato alla separazione delle componenti reversibile ed irreversibile degli spostamenti. Una relazione empirica calibrata sulla componente reversibile stimata mediante il modello degli spostamenti misurati in un campo sperimentale collocato in una zona torbosa veneziana è infine utilizzata allo scopo di determinare l'attesa evoluzione nel secolo corrente delle zone torbose veneziane.

Lo studio dei processi idrologici che interessano i suoli organici è ulteriormente approfondito attraverso l'analisi del fenomeno di isteresi che caratterizza le curve di risalita capillare. In particolare, l'analisi di un lungo set di dati di pressione capillare - contenuto d'acqua raccolti nel Bacino Zennare, Italia, ha mostrato come le deformazioni reversibili della matrice solida enfatizzino il fenomeno di isteresi.

I risultati dell'applicazione di un modello che accoppia una relazione empirica che descrive l'isteresi delle curve di risalita capillare ad una che lega le dinamiche della porosità

alla saturazione in acqua confermano l'importanza di includere il fenomeno di rigonfiamento/restringimento nella descrizione e nella predizione del flusso idrico nei suoli organici.

L'ultima parte della Tesi è incentrata sulle dinamiche idrologiche delle aree umide costiere. Queste delicate zone intertidali sono caratterizzate da una forte connessione idrologica con l'atmosfera e il sottosuolo, principalmente in termini di flussi d'aria. L'equazione di Richards, usualmente adottata per la simulazione della filtrazione di acqua nei suoli in condizioni di saturazione variabile, assume che l'aria sia spostata istantaneamente dall'acqua, quindi non è in grado di valutare correttamente gli effettivi flussi d'aria. Perciò tale approccio non è adeguato alla descrizione dei processi idrologici nei suoli barenali in quanto non consente di valutare le conseguenze dell'intrappolamento dell'aria. È stato sviluppato un modello bifase al fine di investigare gli effetti del flusso dell'aria nelle dinamiche delle aree umide. Si è scelto di adottare una formulazione che assume come variabili principali le pressioni delle fasi aria e acqua che consente di trattare in modo naturale le complesse condizioni al contorno nonlineari che devono essere imposte all'interfaccia suolo-atmosfera. Ciò consente di includere l'interazione tra l'evapotraspirazione durante i periodi di emersione e la fluttuazione mareale in quelli di sommersione della superficie della barena. Il modello è stato applicato ad alcuni casi test finalizzati al verificare l'effetto dell'iclusione della dinamica dell'aria nella simulazione del flusso idrico nella zona insatura.

Chapter 1

Introduction

The Venice Lagoon and its catchment is a unique hydrological resource and ecosystem permanently in quest for equilibrium between the restoration and conservation of environmental system and the anthropic pressure. The importance of the humid areas has been recognised by several international treaties, as the Ramsar convention. The humid areas that are present in the Venice Lagoon are characterized by diverse structures, such as tidal channels, tidal flats and salt marshes, that stand out because of their high biodiversity and primary productivity [Ramsar Convention Secretariat, 2006]. The complexity of the eco-morphodynamics as well as the role of buffer between land and sea of the intertidal areas and the strong connection between the sea, the atmosphere, and the soil has rised and renewed the interest in echo-hydrological studies in the last few years [e.g., Rinaldo *et al.*, 1999a,b]. An example of the strong feedbacks between the different components in the wetlands is the positive influence of vegetation on the salt marsh surface increase, through the trapping of mineral sediments, the production of organic soil from the biomass decomposition, and the active action against the erosive action of wind-induced waves, that would not occur in case of non-vegetated areas [Marani *et al.*, 2006a]. Also groundwater interaction cannot be neglected. For example, Ursino *et al.* [2004] and Marani *et al.* [2006b] emphasize that development of potentially unsaturated conditions in soil may influence the vegetation growth, which in turn acts on evapotranspiration fluxes through soil and so on. Nevertheless, the mechamisms that create the propitious circumstances for the halophitic vegetation colonization in soils in conditions close to saturation are still obscure. In those conditions, the role of evapotranspiration might be potentially relevant in the whole balance of moisture content in the soil also during the periods in which the marsh surface is flooded by the tide. An accurate description of the eco-hydrological dynamics of these systems requires for example the modeling of the oxygen flux exchange

between atmosphere and soil, as a result of tidal influence, as well as oxygen consumption due to vegetative exchanges. Vegetation growth, on the other hand, has a strong influence on the hydrodynamics and morphodynamics of marshlands [Marani *et al.*, 2006a], and a strong nonlinear feedback exists between all these different components of these natural systems. The strong connection in terms of air fluxes from the soil to the atmosphere through the salt marshes surface requires the quantification of the hydrological processes using modeling approaches that consider the actual air dynamic. The intertidal areas are often bound by cultivated peatlands, that are the residues of old wetlands and lagoons that have been drained for agricultural purposes. The soils of the salt marshes and along the southern part of the Venice lagoon margin are often characterised by the presence of peat. Peat soils respond to natural cycles of precipitation/imbibition and evapotranspiration as well to the thaw/freeze cycles with elastic deformations of the soil matrix (swelling/shrinkage). This process induces the reversible displacement of the soil surface that superimposes to the irreversible long term subsidence that occurs naturally in drained peatland because of the bio-oxidation of the organic matter. Land subsidence in drained cultivated peatlands is responsible for a number of serious environmental concerns and economical problems at both the local and the global scale. In low lying coastal areas it enhances the risk of flooding, the saltwater contamination of shallow aquifers, and the maintenance costs of the systems that help keep the farmland drained. Since the occurrence is a major consequence of the bio-oxidation of the soil organic fraction in the upper aerated zone, cropped peatlands in temperate and tropic regions are important sources of CO_2 into the atmosphere. At the end of 2001 a 4-year long experimental study started in the Zennare Basin, a drained peatland located in the southern part of the Venice Lagoon margin that in the last 70 years experienced 1.5–2 m of land subsidence [Gambolati *et al.*, 2005]. Continuous monitoring of the hydrological regime and land displacements by an ad-hoc accurate instrumentation shows that the vertical movement of the peat surface consists of the superimposition of daily/seasonal time-scale reversible deformations related to soil moisture, depth to the water table, and temperature fluctuations, and long-term irreversible subsidence due to peat oxidation.

The sequence of swelling and shrinkage events (*mire breathing*) induced by the wetting/drying cycles introduces short term changes of the structure of the porous matrix, hence of the density and hydraulic properties of the soil from time to time [Price and Schlotzhauer, 1999]. Therefore, not only the porosity but also the saturated conductivity and the moisture retention, i.e. the relation between the moisture content and the capillary pressure, should vary according to the current water content, which in turn affects

the density of the bulk [Schlotzhauer and Price, 1999].

The present thesis reports an articulated research work that covers several aspects connected with the modeling of subsurface hydrology of organic soils in connection to the main hazards induced by land subsidence of peatlands and the conservation and wise use of wetlands in the Venetian area. Because of the variety of themes studied, the work is organized in three different self-containing chapters each containing literature overview of the subject, the description of the methodology, results, and conclusions. Hence, after the introduction, the second chapter reports the description of the study areas, i.e. the Venice peatland and wetlands, with an accurate overview of the main properties of the organic soils and the interconnection of the different compartments, namely atmosphere, sea, and soil, in these humid zones.

The third chapter studies the dynamics of peatland surface deformation both at long and short time scale. Both the subsidence due to bio-oxidation and soil deformation caused by the variation in water content and groundwater depth are studied. A novel two-step modeling approach is proposed to separate the reversible and irreversible components of the land surface displacement. First, the elastic part is computed by integrating the peat vertical deformations evaluated by a constitutive relationship describing the porosity variation with the moisture content proposed by [Camporese *et al.*, 2006a]. The measured surface movement trend is then filtered from the computed reversible displacement thus obtaining a subsidence record that is free of short term elastic deformation. This can then be optimally used to calibrate the empirical relationship proposed by Stephens *et al.* [1984], relating long term land subsidence to drainage depth and soil temperature. The model is then used to investigate the expected evolution of the peat thickness in the Venetian peatland over the present century according to the scenarios proposed by IPCC [2007].

The fourth chapter deals with the accurate study of the hysteretical phenomena of the moisture retention curve measured in the peat soils of the Zennare Basin. The study of a long term (7 months) sequence of capillary pressure - saturation measurements shows that the reversible deformation of organic soils enhances the hysteretic behavior of the moisture retention curve. In fact, application of a simple hysteresis model such as the one proposed by Haverkamp *et al.* [2002] does not allow a good fitting of the observed cycles. Not even a more complete model, such as the one proposed by Parker and Lenhard [1987], that allows for the distinction of the wetting and drying processes, is capable of describing the data satisfactorily. Only when the hysteresis model chosen is coupled with a relation that links the soil porosity variation with the water saturation [Camporese *et al.*, 2006a],

in order to include the variation of the soil matrix porosity in the description of the moisture content/capillary pressure relationship, then observed trend is captured. The results confirm the importance of including the porosity variation with water content in the description and prediction of water flow into organic soils.

In the last chapter the focus is shifted to the hydrological dynamics of salt marshes as they interact with atmosphere and vegetation. These delicate intertidal zones are characterized by a strong hydrological connection between the atmosphere and the subsurface mainly in terms of air fluxes: a complete description of the hydrological dynamics requires the quantification of the air budget (oxygen) as determined by the inflow from the atmosphere through the soil surface, the seepage through the soil in the root zone, and the consumption by plant roots. After the first works of Ursino *et al.* [2004] and Marani *et al.* [2006b], who showed the importance of groundwater exchanges between the tidal forcings and atmosphere/vegetation extraction (evapotranspiration), several authors have shown the importance of describing the motion of air and water phases [Li and Lockington, 2005; Tosatto *et al.*, 2009]. In fact, the presence of air can significantly affect the mobility of water in the soil, thereby impacting soil aeration, hence plant selection and the morphodynamics of the wetlands. Richards equation is not able to account for the actual fluxes of air, therefore the simulation of flow in salt marshes, where the effect of the entrapped air on the water infiltration in the soils may not be neglected, requires a different approach. All the previous modeling attempts considered a two-phase numerical formulation based on a water - saturation and pressure as dependent variables. This approach has the advantage of being conservative and numerically efficient. However, its use in the current context requires the development of artificial boundary conditions at the surface to account for the exchange between soil and atmosphere. Thus Li and Lockington [2005] propose the inclusion of an artificial soil layer at the surface where an arbitrary constant water saturation is imposed during low tidal cycles. This approach limits the applicability of two-phase simulation to the current modeling problem.

Hence, we present a two-phase flow model based on a pressure-pressure formulation to simplify the treatment of the complex and nonlinear boundary conditions at the soil-atmosphere interface. The formulation is developed to ensure accurate elemental expansion of saturation time derivatives through a proper definition of the capacity coefficient. The new model is tested on some examples taken from the literature and the main numerical difficulties are described.

Chapter 2

Peatlands and wetlands of the Venice Lagoon

The section provides a comprehensive description of the ecosystems considered in this thesis. More precisely, in section 2.1 the features of the Zennare Basin are discussed. This is the area where the numerical study of the peat subsidence and of the zone dynamics has been carried out. First, a background of the nature and classification od the organic soils to better understand the processes that take place in the study area is provided, conforming to the description of the main characteristics of this type of soils proposed by Stephens *et al.* [1984]. Afterwards, the classification of the outcropping peat deposit and a description of the problems related to land subsidence due to peat oxidation are given. The geomorphological and hydrological characterization is then provided, followed by a brief description of the materials and methods used to monitor the oxidation process and the related hydrological parameters. In section 2.2 the main characteristics of the Venice Lagoon as intertidal zone are portrayed with particular emphasis on the wetland features. The importance of tidal marshes as buffer zone between the land and the sea is enlighted, and the light is brougth on the necessity of understanding the complex mechanisms that link vegetation, subsurface, hydrology, and atmosphere.

2.1 Peatlands in the Venice catchment

2.1.1 Nature and classification of organic soils

Peat is basically a fossil coal formed by plant remains at the first stage of the carboniferous process. In general, peat forms in depressed areas where soil is flooded by fresh, brack-

ish or even salty backwater. Areas with potential presence of peat include marginal and depressed zones of alluvial plains, deltaic plains, glacial valleys, zones in which morainic deposits form natural dams, fluvial valleys with stagnating areas, and subsiding territories. In these areas, marshes and swamps therefore form, rich of aquatic plants like sphagnum, heather, sedge, and reeds. In such anoxic environments the action of anaerobic micro-organisms breaks down the parent plant structure and creates peat that accumulates because biomass production is greater than biomass decomposition. After land reclamation by drainage of the marshlands, the peat soil becomes aerated, and aerobic micro-organisms are responsible for the decomposition of the organic fraction.

Peat soils are characterized by a dark color, low bulk density, and an absorbent sponge-like texture. They have low albedo (defined as the ratio between reflected and incident solar radiation) and high emissivity for thermal radiation. Compared with mineral soils, organic soils have a high heat capacity (they burn at a relatively low temperature) and at the same time a low heat conductivity. Peat soils tend to be acid, but the range of variability of pH can vary between 3.5 and 8.

According to the FAO soil classification system [Andriesse, 1988], organic soil deposits are classified as "Histosols" or "Gleysols". Histosols must contain at least 12 to 18% of organic carbon by weight and exceeds 30 to 40 cm in depth, while Gleysol are mineral soils with gleyed horizons that may have a moderately high organic carbon content, but contain less than the minimum required for Histosols.

According to the U.S. soil taxonomy system, histosols are defined by the presence of a large organic matter fraction (>50%) and they are usually termed "peat" when fibrous plant remains are still visible [Galloway *et al.*, 1999].

The present thesis deals only with Histosols, since this classification fits the organic soil located in the Zennare Basin. Histosols may further be classified as peat and muck. Several taxonomies have been developed in different parts of the world, based on either soil profile properties or botanical composition. One classification defines peat as a soil containing less than 50% of mineral matter by weight, while muck has a percentage of mineral matter ranging between 50 and 80%. Other classifications separate peat and muck based on the state of decomposition without regard to organic matter content. Peat soils are then identified with soils that are only partially decomposed and retain a fibrous or granular nature, while mucks are deeply decomposed, finely textured, uniform, amorphous, and black.

Based on the botanical origin, sedimentary, fibrous, woody, and moss peat can be recognized:

- sedimentary peats derive from submerged succulent open water plants that contain a relatively small proportion of cellulose material. They can be mixed with fecal matter from aquatic animals, algae, dead micro-organisms, pollen, leaves coming from plants surrounding the area, and sedimentary materials brought by wind and water. Drainage of sedimentary peats seldom yields good agricultural soils;

- fibrous peats are composed of the remains of sedges, reeds, and related marsh plants that grow in shallow water of marshes. They contain a relatively high fraction of cellulose material. The water retention capacity is high and so is the hydraulic conductivity for drainage and agricultural management. Fibrous peats are less acid than moss peats and have a better texture for tillage than sedimentary peats. Most of the fibrous peats, once drained, yield good agricultural soils;

- woody peats are formed by residues of trees and shrubs that grow in the forest floor of the swamp. They have a smaller water retention capacity than fibrous peats and, during drainage, they allow water to readily flow through their loose granular and blocky structure. This soil is usually rated as intermediate between fibrous and sedimentary peat from an agricultural point of view;

- moss peats form in northern latitudes where the cool wet climate favors their development. Extensive areas occur in Canada and northern Europe. This kind of peat forms mainly from Sphagnum mosses and associated vegetation, the latter depending on rainfall, dew, and fog for moisture and nutrients. The sphagnum peats can hold up to 15–16 times their weight of water. They are extremely acid and not easily decomposable. It is a poor type of soil for the growth of micro-organisms causing decomposition and the nitrogen content is low. Even when drained they represent poor soil for the growth of high plants, unless the low pH is increased by means of lime, and a complete fertilization is carried out to include micro-nutrient elements. Sphagnum peat deposits are used in Europe and Canada for forest production and as pastures. Other uses are for fuel (e.g., in Russia and northern Europe), for the improvement of other soils, such as soil mixes for horticultural use, for packing plants and flowers, and for related uses where its high water retention capacity is of value.

Worldwide estimates of peatlands extension have been attempted by many scientists, but the results vary widely and are likely incomplete because of the difficulties of monitoring the less accessible zones of the Earth. Recent developments of satellite based

observation may change the perspective in the near future [Nicoletti *et al.*, 2003].

2.1.2 Peat groundwater hydrology

Hydrological and geotechnical parametrization

A complete understanding of the hydrological properties of organic soils is important for the effective management of the subsidence phenomenon and its effects. Several studies on the hydraulic properties of peat have been carried out in different fields of research (hydrology, climatology, ecology, etc). Among the first work in this field [Dasberg and Neuman, 1977] show the results of laboratory and field investigations on the mechanical and hydraulic properties of peat soil from the Hula Basin, Israel, an ancient marshland drained in the middle of the last century to free land for agriculture, to conserve water, and to eliminate malaria. The purpose of the research was the characterization of the flow conditions in the basin, a prerequisite to control the two major problems caused by the drainage of the area: i) the eutrophication of the Lake Kinneret due to the generation and release of nitrates and ii) land subsidence at a continuous rate of 2–10 cm per year. Laboratory tests were conducted on several samples collected at various depths, to determine bulk density, hydraulic conductivity, porosity, void ratio, retention curves, organic matter content, and compressibility parameters. Field tests were performed in order to estimate the in situ saturated horizontal hydraulic conductivity. The results of the laboratory tests show that, going from the deepest saturated layer to the shallow unsaturated zone, bulk density varies between 0.20 g/cm^3 and 0.69 g/cm^3, porosity ranges from 90 to 67% with void ratio between 14 and 2.4, while organic matter content decreases from 65 to 33%. Storage coefficient was found to be higher in the saturated layer. If one accepts that "field capacity" is included in the range 0.1–0.3 bar of suction, then the effective porosity varies from 20 to 30%, versus a total porosity up to 90%. From the in situ tests a horizontal hydraulic conductivity range of 3×10^{-7}–4×10^{-6} m/s was determined. Hula peat is also characterized by a high compressibility and a specific storage coefficient up to 10^5 times greater than typical values for confined sandy aquifers.

A similar behavior of the vertical profile has been found also for the peat deposits of the Zennare Basin, Italy [Gatti *et al.*, 2002], that are characterized by an upper, amorphous, well-decomposed layer with bulk density 0.25 g/cm^3, overlying a fibrous layer having bulk density 0.30 g/cm^3. These characteristics may be hypothesized as typical for drained peat soils, while in pristine conditions the vertical profile is reversed. In this case the deepest layers are more decomposed and dense than the shallowest and the hydraulic conductivity

decreases with depth [Letts *et al.*, 2000].

According to Letts *et al.* [2000] the range of variability of the saturated hydraulic conductivity spans three orders of magnitude, going from 10^{-7} m/s for sapric amorphous peat to 10^{-4} m/s for fibric peat, depending on density, composition, stage of decomposition, etc. Analogous results were found by Waddington and Roulet [1997] in a Swedish peatland where a range between 2.0×10^{-7}–8.0×10^{-3} m/s of Dissolved Organic Carbon (DOC) has been estimated. The values determined by Dasberg and Neuman [1977] in the Hula basin fall in the lower part of both the above indicated intervals, corresponding to sapric amorphous peat.

In Canada, the properties of a cutover peatland were investigated in order to verify the capability of artificial rewetting as a restoration strategy [Schlotzhauer and Price, 1999; Price and Schlotzhauer, 1999]. An average bulk density of 0.106 g/cm^3 was determined, with a specific yield of 0.48 and a mean hydraulic conductivity of 1.7×10^{-6} m/s. Vertical elastic surface displacements in phase with the fluctuations of the water table were observed, with magnitude that was 5 times greater during water loss as compared with the case of rewetting. The specific storage showed a considerable hysteresis, changing drastically from drying (9.4×10^{-4} cm^{-1}) to rewetting (2.6×10^{-4} cm^{-1}). The compressibility of peat was found to be high and the specific storage (S_s) was more important than the specific yield (S_y) in the overall aquifer storativity, in agreement with Dasberg and Neuman [1977].

According to Weiss *et al.* [1998], the properties of the unsaturated zone (relative hydraulic conductivity, soil moisture, and water saturation) can be reliably described by means of the widely accepted van Genuchten retention curves [van Genuchten, 1980]. However, peat is highly compressible and responds to drying/wetting cycles with important deformations due to changes in gravimetric water content. These deformations result in relatively large vertical movements of the soil surface [Hobbs, 1986]. The sequence of swelling and shrinkage events, known also as "mire breathing", is an important feature of the hydrologic behavior of peatlands as it produces short-term changes in the pore structure, and thus on the density and hydraulic properties of peat soils [Price and Schlotzhauer, 1999]. For these reasons, not only the porosity but also the entire set of retention and conductivity curves, together with saturated hydraulic conductivity and water storativity, should be considered to vary dynamically with changes of water content [Schlotzhauer and Price, 1999; Kennedy and Price, 2004]. Neglecting these phenomena may yield inaccurate predictions in the modeling of the peatland hydrologic response [Kennedy and Price, 2004]. Many other studies concerning peat hydrology and hydraulic properties exist in

the literature in different disciplines such as ecology, agronomy, climatology, etc. [see for example Baird, 1997; Quinton *et al.*, 2000; Evans *et al.*, 1999; Holden and Burt, 2003], where the reader is referred for further information is needed.

Irreversible subsidence due to bio-oxidation

Drainage of waterlogged locations for agricultural purposes brings the peat soils to aerobic (oxygen-rich) conditions. When atmospheric oxygen enters into the peat, this oxidant reacts with the organic matter and generates carbon dioxide and water. Representing the readily degradable part of the peat with the simplified formula CH_2O and assuming complete degradation, the reaction responsible for aerobic decay can be written as [Bozkurt *et al.*, 2001]:

$$CH_2O + O_2 \rightarrow CO_2 + H_2O \tag{2.1}$$

Several laboratory tests and in-situ experiments have been performed in the area of soil science, hydrology, and bio-ecology to study the process of peat oxidation and quantify the CO_2 emissions from the soil surface into the atmosphere [e.g. Rojstaczer and Deverel, 1993; Silvola *et al.*, 1996; Melling *et al.*, 2005]. Most of these studies provide evidence that decomposition of organic matter mainly depends upon soil temperature and moisture content. Soil microbial activity becomes significant when soil temperature is larger than 5°C and generally doubles for each 10°C increase in temperature [Davidson and Janssens, 2006]. Oxygen availability is directly connected to the degree of water saturation and hence with the depth of drainage, the higher the water table the lower the CO_2 efflux from the soil [Stephens *et al.*, 1984].

Swelling/shrinking behavior of peat soils

In peatlands, drier periods cause peaks of the bulk density in the unsaturated zone, yielding a stronger matrix suction and a decrease of pore volume (shrinkage). On the other hand, lowering of the water table induces a saturated peat compression as the effective stresses increase [Price, 2003]. Depending on the ratio between the thickness of the unsaturated and saturated zones, shrinkage and compression may have different relative importance, even though it is recognized that the rate of volume change in the unsaturated zone is greatest [Price, 2003; Kennedy and Price, 2005]. Experimental evidence shows that the high compressibility of peat may yield volumetric changes up to 10 times larger than in swelling clay soils [Hobbs, 1986]. Fibrous and poorly decomposed peatlands may experience displacements induced by water content changes of the order of

0.1 m [Price and Schlotzhauer, 1999], whereas seasonal movements are relatively small ($\approx$ 0.01 m) in highly mineralized amorphous organic soils [Deverel and Rojstaczer, 1996; Camporese *et al.*, 2005]. The latter case is typical of histosols subject to intensive agriculture. In this situation, the amorphous partially mineralized shallow layer, whose thickness depends on agricultural practices, often coincides with the unsaturated zone, and may be subject to swelling/shrinking deformations with magnitudes comparable with the rates of irreversible subsidence due to the long-term organic matter oxidation. Over short time periods (1–2 years) the superposition of the two phenomena may interfere with measurements of irreversible subsidence, so that the understanding of the long-term behavior needs to take into consideration possible deviations from the general trend due to the reversible deformations. Hydrological models of swelling/shrinking peat soils can thus be employed to separate the two deformation components.

Several swelling/shrinkage models have been proposed in the literature in the last few years. An overview of the more interesting results are proposed in section 3.1.

2.1.3 The Zennare Basin

In Italy, histosols have an areal extent of about 1200 km^2 [Andriesse, 1988], with a significant fraction located in the eastern Po River valley, along the coast of Veneto, Emilia-Romagna, and Friuli-Venezia Giulia Regions.

The Zennare Basin (45°10' east and 12°9' north) is located in the southern catchment of the Venice Lagoon, approximately 10 km from the Adriatic Sea and 1 km south of the lagoon margin (Figure 2.1a). It is one of the 32 hydraulic basins composing the district managed by the Consorzio di Bonifica Adige-Bacchiglione (Adige-Bacchiglione Reclamation Authority) and it is located at the eastern tip of the district, just south to the Venice Lagoon margin and close to the confluence of the Bacchiglione and Brenta Rivers. The basin was occupied until the XIX century by swamps and marshes and was completely reclaimed in the late 1920's.

A detailed reconstruction of the basin evolution and peatland formation over the Holocene can be found in Rizzetto *et al.* [2003]. The position of the inner coastline during the Flandrian transgression, 5000-6000 years BP, has been identified in the north-western part of the basin. Intensive fluvial sediment supplies caused a rapid eastward progradation of the coastline. Evidences of beach ridges dated 4500 years BP are recognizable about 1-2 km east of the Zennare Basin. Coastal tidal flats characterized the area, with the marine sediments buried by alluvial (sands and silts) soils along the fluvial ridges and

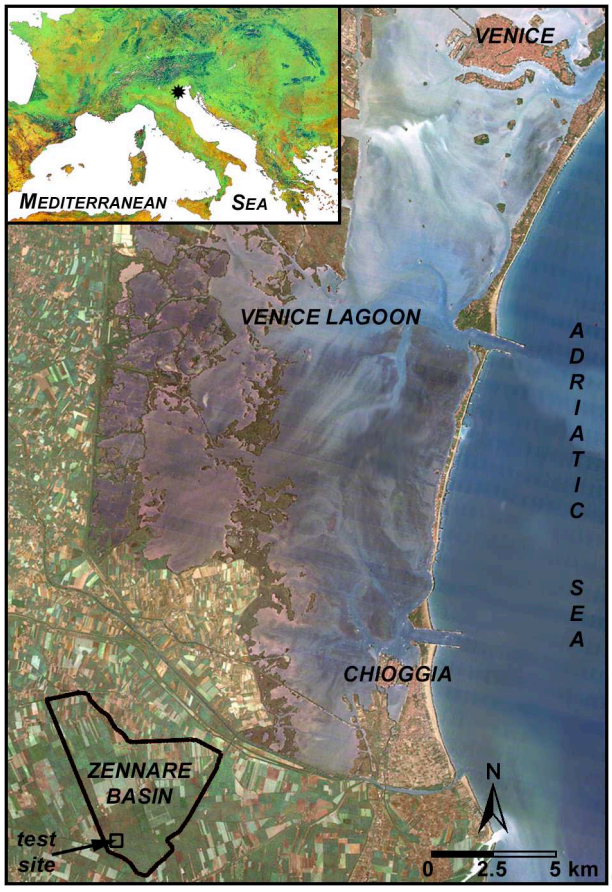

(a)

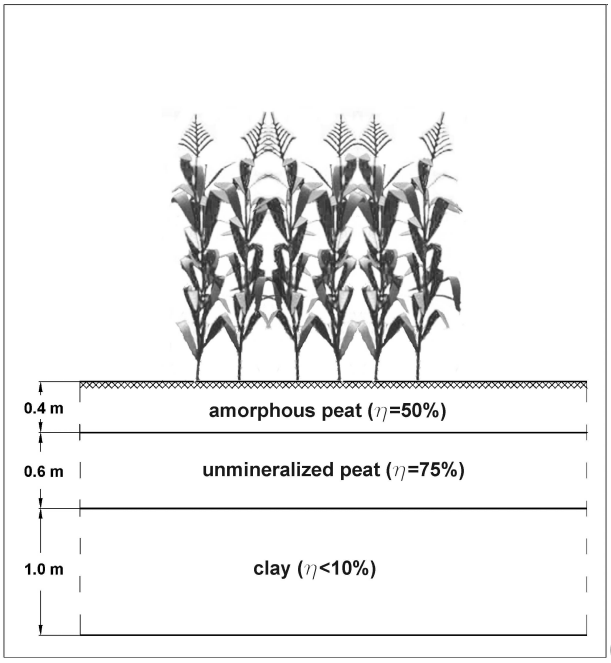

(b)

Figure 2.1: (a) Location of the Zennare Basin south of the Venice Lagoon. The position of the experimental site is also shown. (b) Schematic section of the shallow subsoil in the Zennare Basin. For each layer the corresponding organic matter content η is provided.

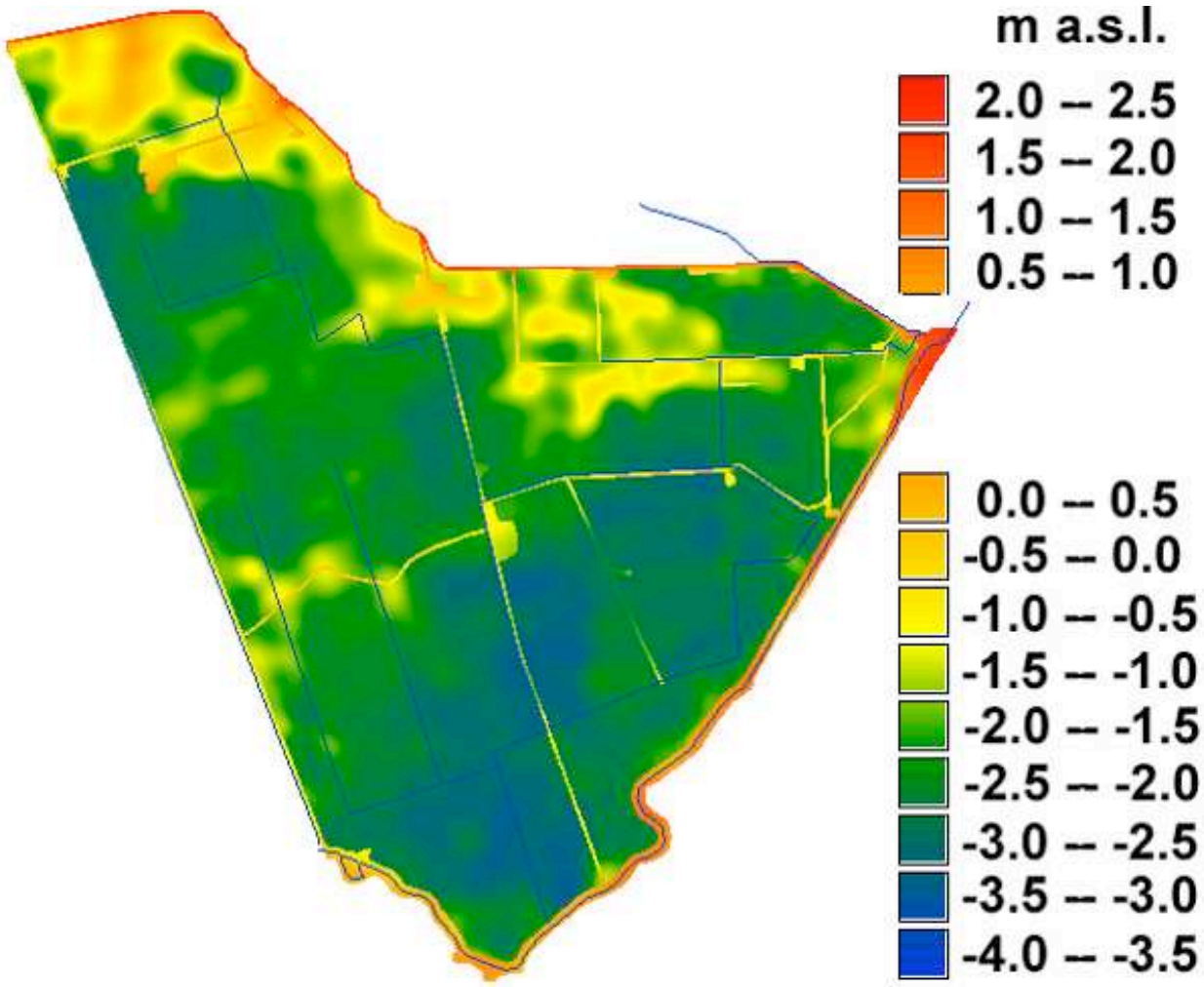

Figure 2.2: DEM (Digital Elevation Model) of the Zennare Basin, constructed on a regular grid of 15 m resolution from the CTR (Technical Regional Map) on a 1:5000 scale [after Rizzetto *et al.*, 2003].

organic matter produced by reed (*Phragmites Australis*) decomposition in the interdistributary lowlands occupied by marshes and swamps. A 1833 map by government officials of the Lombardo-Veneto kingdom indicates the predominance of marshlands all over the basin with the exception of the relatively higher north-eastern part already cropped and urbanized. The first pumping station and a few canals are reported in a map drawn by the Padua Province dated 1862, and a first structured network of drainage channels appears in the 1896 map by the Italian Geographic Military Institute. The reclamation of the area for agricultural activities started in the second half of the 19-th century and was completed around 1927.

At present the basin lies almost entirely below the mean sea level, down to as much

as -4 m a.m.s.l (above mean sea level) in the southernmost zone, near the Cuori Channel (Figure 2.2).

The basin is hydrologically well defined, being completely bounded by road or channel embankments that are at least 2 m higher than the surrounding cultivated plain. The depth to the water table, h, is controlled by a dense drainage network that conveys the surplus water to the "Zennare" pumping station that discharges the water into the Cuori Channel [Gambolati *et al.*, 2006]. The pumps operate automatically based upon the shaft water level so that the values of h are maintained between 0.40 and 0.50 m as is required by the local agricultural practices. Finally, the water from the Cuori Channel is lifted again by the "Cà Bianca" pumping station and the uplifted water flows into the Venice Lagoon through the "Botte delle Trezze" outlet, which passes below the Bacchiglione and Brenta Rivers.

Geomorphological and hydrological characterization

Field surveys, geophysical investigations, and remote sensing analyses have been used to map the areal extent and the thickness of the outcropping peat deposits [Francese *et al.*, 2002; Rizzetto *et al.*, 2003; Nicoletti *et al.*, 2003; Gambolati *et al.*, 2005]. The peatland, located mainly in the southern part of the basin, is characterized by 1 m thick surface layer originating from the decomposition of reed (mainly *Phragmites Australis*). The upper 0.40 m of the organic soil is composed of black oxidized amorphous granular peat with an organic matter content (η) ranging between 40 and 60%. The remaining 0.60 m are formed by brown slightly decomposed peat, more than 80% rich in organic content, with high coarse-fiber content. A thick plastic clay unit confines from below the surface peat layer (Figure 2.1b) [Gatti *et al.*, 2002].

Hystorical subsidence records can be assessed from the protrusion of a number of old hydraulic structures founded on the mineral soil underlying the outcropping peat (Figure 2.3). Figure 2.4 shows a bridge, whose foundations totally prevent the water flow. The lowering of the water level at the pumping station entry provides further documentary evidence of an average subsidence rate of approximately 20–30 mm/a over the last 70 years. Similar values were found by comparing a DEM (Digital Elevation Model) based on an aerial photogrammetric survey performed in 1983 with the results of a kinematic DGPS (Differential Global Positioning System) survey carried out in March 2002 [Gambolati *et al.*, 2006].

The data recorded by a nearby weather station managed by the Adige-Bacchiglione

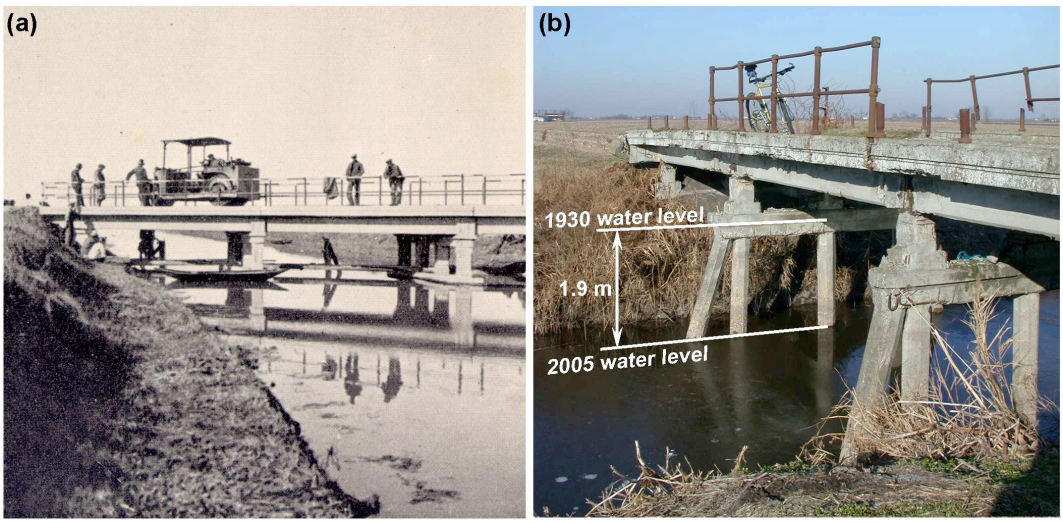

Figure 2.3: Evidence of the peatland subsidence in the Zennare Basin: (a) a photo of a bridge made in the 1930s soon after the basin reclamation and (b) the same bridge in the present condition hanging over the canal bank which settled by approximately 1.9 m.

Figure 2.4: Bridge with culvert, whose foundations currently above the channel level prevent the water flow.

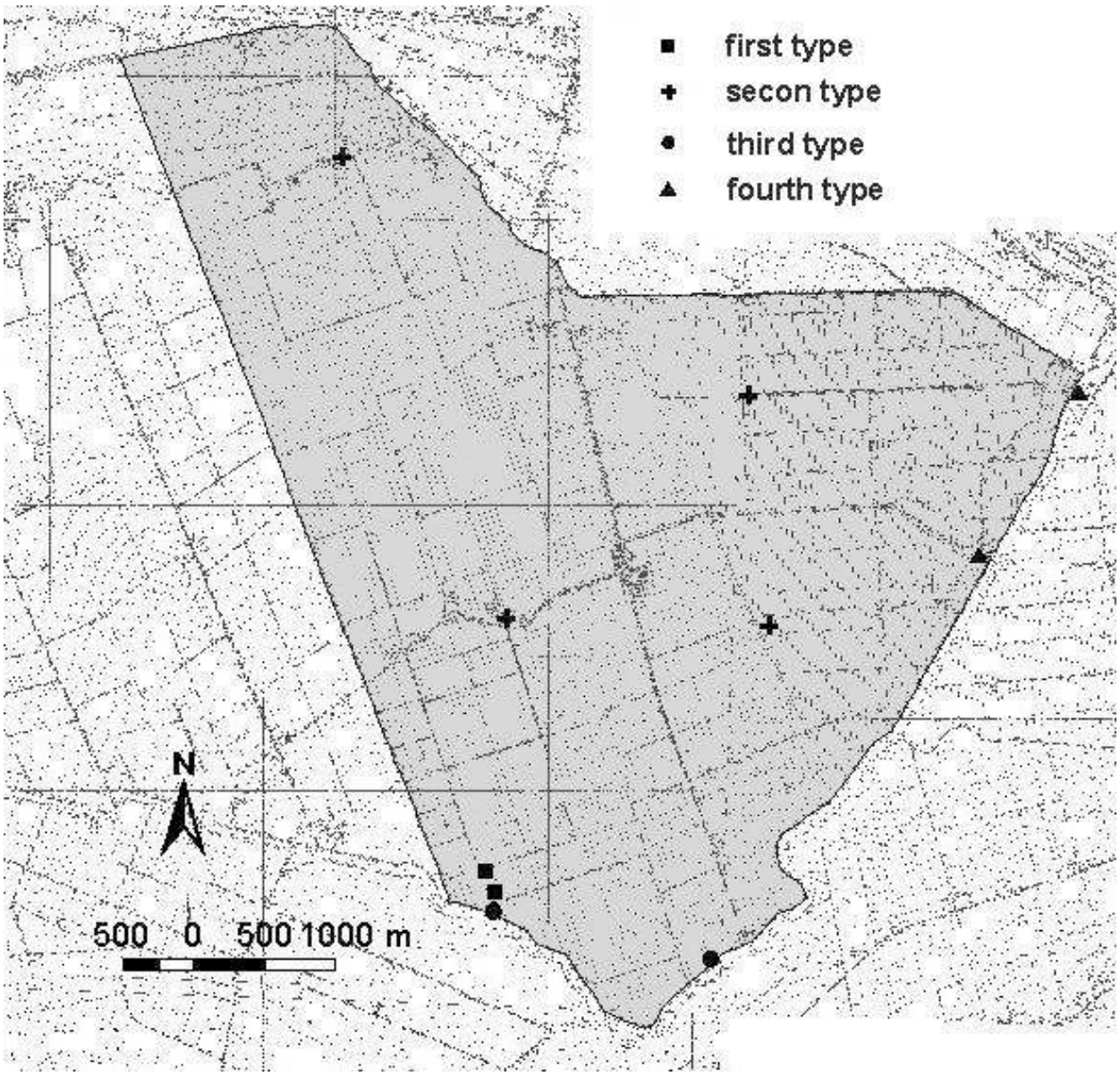

Figure 2.5: Location of the experimental sites inside the Zennare Basin after [after Fornasiero *et al.*, 2002].

Reclamation Authority provide a 10 year long record of climate regime in the area, yielding an annual average precipitation of 700 mm. The annual average air temperature is 15°C, with monthly averages ranging from 3°C in January and 28°C in July, and an average relative air humidity equal to 83%.

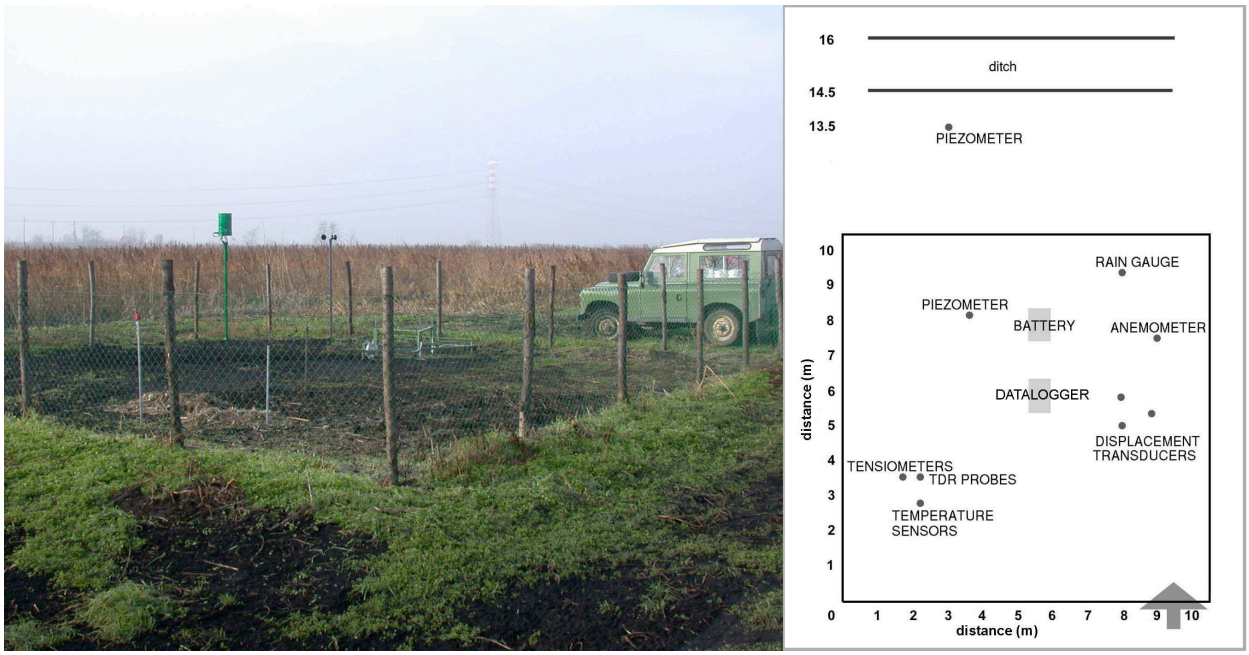

Figure 2.6: Picture of the "Campo 1" experimental site and schematization of the instrument position in the site.

Experimental fields

A number of field site has been established at the end of 2001 and operated for more than 4 years in the Zennare Basin (Figure 2.5) to quantify the present land subsidence due to peat oxidation and to address the expected relation between the hydrological regime, the soil loss in the form of CO_2 fluxes to the atmosphere, and the settlement rate. The comprehensive dataset collected at the experimental sites range from soil elevation changes and soil CO_2 efflux to hydrological parameters such as soil moisture content, capillary suction, temperature, etc. Four types of monitoring sites can be distinguished, depending on the instrumentation (Figure 2.5). The two main sites (first type), named "Campo 1" and "Campo 2", have been instrumented to measure all the main hydrologic variables that affect the peat oxidation process. For this reason the test sites have been placed in the southern tip of the basin, where the outcropping peat layer is most continuous. Moreover, they have been installed relatively close to each other in order to get redundant measurement sets and a relatively reliable control on the collected records. Both sites are equipped (as shown in Figure 2.6) in order to measure the main hydrologic variables, i.e. precipitation, wind velocity, capillary pressure, soil moisture content and temperature, as well as the ground surface displacement. More details about the instuments installed can be found in chapters 3 and 4.

Four peripheral sites (second type) have also been installed, named "Baretta", "Galimberti", "Guzzo", and "Viale", to measure the spatial variability of rainfall and water table depth. Each site is equipped with one tilting bucket rain gauge and one piezometer. Both instruments are connected to a data logger and sampled hourly, as well as in the main sites.

Two other sites ("Brazzo" and "Argine", third type), have been equipped with a piezometer placed at the foot of the Cuori Channel levee, in order to obtain data allowing for the estimate of the infiltration flow through the bank.

Finally, in the Zennare and Cà Bianca pumping stations (fourth type) the upstream and downstream water levels are recorded every 15 minutes, together with the functioning timetables of the pumps.

The data are pubblished in several works [Gatti *et al.*, 2002; Fornasiero *et al.*, 2002, 2003; Teatini *et al.*, 2004; Gambolati *et al.*, 2005; Camporese *et al.*, 2006a,b; Gambolati *et al.*, 2006; Camporese *et al.*, 2008] and are available from the following website: http://voss.dmsa.unipd.it. In chapter 3 the displacement of the peat surface, water table, soil temperature, and precipitation data collected in the 4 - year long field experiment are presented and analysed in relation to the Zennare Basin peatland subsidence. In chapter 4 shows and discusses in detail moisture content and capillary pressure data collected over the last two years.

2.2 The intertidal wetlands in the Venice Lagoon

Wetlands act as buffer zone between the land and the sea, and are characterized by extremely high biodiversity and primary productivity, providing critical habitats for rare and endangered vegetation and animal species and mediating the effects of floods and the action of the sea on the coast. The Venetian lagoon is the largest wetland in the Mediterrean Basin [Ramsar Convention Secretariat, 2006], the widest lagoon in Italy (Figure 2.7), and the most important survivor of the system of lagoons which in Roman times characterized the upper Adriatic coast from Ravenna to Trieste. Its name in the Venetian language, *Laguna Veneta*, cognate of Latin *lacus*, "lake", has provided the international name for enclosed, shallow embayment of saltwater, a lagoon. Sited at the end of a largely enclosed sea, the lagoon is subject to high variations in water level, the most extreme being the winter tides known as the *acqua alta* (Italian for "high waters"), which regularly flood much of Venice. The lagoon was formed nearly 6–7 kyr BP during the Flandrian transgression, when the marine transgression [Gatto and Carbognin, 1981] following the

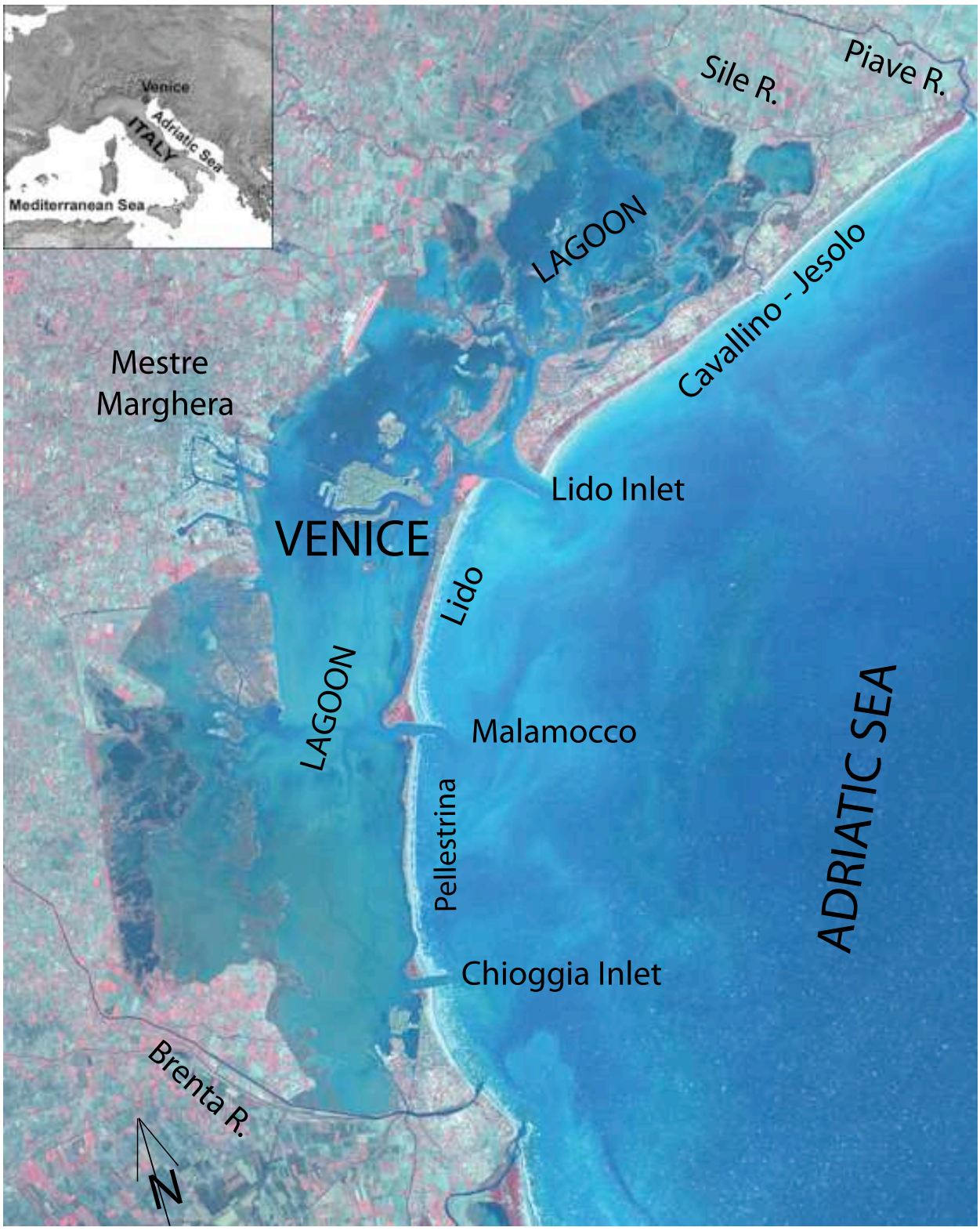

Figure 2.7: ASTER image of the Venice Lagoon and its surrounding mainland. Main localities are indicated.

Ice Age flooded the upper Adriatic coastal plain. Deposition of river sediments compensated for the sinking coastal plain, and coastwise drift from the mouth of the Po tended to close tidal inlets with sand bars. Human activities have hystorically had a strong impact on the lagoon morphology. In the fifteenth and sixteenth centuries, Venetian hydraulic projects to prevent the lagoon from turning into a marsh reversed the natural evolution of the lagoon. Pumping of aquifers since the nineteenth century has increased subsidence. Originally many of the lagoons islands were marshy, but a gradual program of drainage turned them habitable. Many of the smaller islands are entirely artificial, while some areas around the industrial harbour of Mestre (Figure 2.7) are also reclaimed islands. The remaining islands are essentially dunes, including those of the coastal strip (Lido, Pelestrina, and Cavallino) [Brambati *et al.*, 2003].

Bounded by the Sile River to the North and the Brenta River to the South, the Venice Lagoon is oblong and arched in shape. Presently it covers an area of roughly 550 km^2, with a mean water table depth of 1.5 m. The tidal regime is semidiurnal with a range of about $\pm$ 0.7 m around mean sea level. The mean water volume of the lagoon is about 700×10^6 m^3, the semi-diurnal volume exchange with the sea is about 350×10^6 m^3 during spring tides and 175×10^6 m^3 during neap tides [Silvestri *et al.*, 2000] The total freshwater input into the lagoon is 900×10^6 m^3 per year, discharged by 27 channels, while the rainfall volume directly falling on the lagoon is 440×10^6 m^3 per year [Silvestri *et al.*, 2000]. Two barrier islands about 0.5-1.0 km wide separate the tidal basin from the sea, while communication and active exchange is granted by three inlets (mouths), namely Lido, Malamocco, and Chioggia, whose width approximately ranges from 400 to 900 m. Like all intertidal areas, i.e. environments connected to the sea and subject to flooding by tidal fluctuations, the lagoon of Venice may be divided into three main elements: the channel network, the tidal flats and the salt marshes [Marani *et al.*, 2004].

The tidal channel network is constituted by a connected and branched structure in which water flows due to tidal oscillations. Tidal flows are concentrated during floods and ebbs and through the network of channels most water, sediment and nutrient fluxes exchange between the sea and the intertidal area. The links forming the channel network have different elevations with respect to mean sea level. The larger links have lower elevations and are usually flooded throughout the tidal cycle, while smaller (and farther from the inlets) channel reaches have higher elevations and thus effectively participate to tidal flows only when the water level is relatively high. The development of drainage patterns on tidal marshes and tidal flats controls the hydrodynamics and sediment exchanges between the various compartments of the entire intertidal area [e.g., Pestrong, 1965; Boon,

1975; Boon and Byrne, 1981; Pethick, 1984; Steel and Pye, 1997; Rinaldo *et al.*, 1999a,b].

Tidal flats are areas generaly about or below the mean sea level, usually located on the margins of the main channels, which are flooded during most tidal fluctuations. Tidal flats lie at elevations which do not allow their colonization by halophytic plants, i.e. of plants adapted to live in very salty soils [Armstrong, 1982; Adam, 1990; Ungar, 1991; Silvestri and Marani, 2004].

Salt marshes are areas, generally located just above mean sea level, which are frequently inundated by the tide (on average twice a day in the lagoon of Venice), but where flooding periods and root oxygen availability are such as to allow the development of halophytic vegetation. The topography of salt marshes is not extremely variable but the small elevation gradients induce an important variability in halophytic vegetation species whose description constitutes a key step in the comprehension of tidal system dynamics [Marani *et al.*, 2004].

The mutual interaction of the wetland vegetation and the phyical processes occuring in tidal areas affects the morphological evolution of this peculiar environment, involving several aspects of the complex ecosystem [e.g. Leonard and Luther, 1995; Friedrichs and Perry, 2001; Ursino *et al.*, 2004]:

- the hydrodinamic circulation and the associated sediment transport are influenced by the presence of plants;
- halophytic vegetation stabilize marsh surface sediments, increasing friction to hydrodynamic flow and reducing water sediment transport capacity;
- plants increase deposition rates by means of the organic sediment flux associated to biomass production;
- vegetation roots increase sediment stability;
- plants standing biomass reduces erosion by attenuating wind-induced waves;
- plant transpiration influences wetland hydrological processes by alterating groundwater table levels;
- transpiring plants can induce the presence of a persistent aerated layer even below the flooded surface soil;
- vegetation development is strongly linked to the topographic characteristics of the marsh.

Quantitative maps of intertidal vegetation obtained by recent advances in remote sensoring technology provide unprecedented descriptions of vegetation *zonation* [Fuller and Eastwood, 1998; Silvestri *et al.*, 2003; Marani *et al.*, 2006a], that is of the characteristic patchy distribution of marsh vegetation with sharp transitions from one species to another [Adam, 1990]. Marani *et al.* [2006b] showed that the zonation lacks of preferred spatial scales and emphasized how the vegetation patterns are the result of interspecific competition within a habitat whose geomorphic dynamics is strongly coupled to ecological processes. Species distribution has often been found to be strongly correlated to topographic elevation and its typically clustered organization is usually ascribed to differences in the duration of submersion periods corresponding to different soil elevations. These differences are often characterized by introducing the concept of *hydroperiod*, i.e. the ratio between the length of time during which a given marsh area is submerged to the total duration of the reference period (usually 1 year or the growing season). Silvestri *et al.* [2005] showed that the same vegetation species can experience very different hydroperiods in different sites, concluding that the hydroperiod cannot justify the differences in characteristic elevations.

Therefore, qualitative and quantitative efforts are needed to improve the knowledge of the water-soil-vegetation interactions, hence of the processes that connect geomorphology and ecology evolution in humid areas.

2.3 Conclusions

The drainage basin and the lagoon of Venice are dynamic and delicate ecosystems exposed to the effects of climate change and often subject to the increasing human pressure. The southern part of the Veneto coastland as well as the salt marshes of the intertidal areas are characterised by the presence of hystosols. In the end of 2002 a field site has been instrumented in the Zennare Basin, a cropped area located in the southern part of the Venice Lagoon margin, in order to study the subsidence of a drained peatland 1.5 m thick. Because of the consequences of subsidence, i.e., the continuous raising of the drainage costs and a greater seawater intrusion threat, the study of the overall process is of paramount importance for the local authorities. The choice of this specific site for studing the faith of the peatlands in relation to climate change and human activities follows naturally, since a large amount of measurements are available for comparison with model predictions.

The Venetian lagoon is a wide, shallow tidal basin in the northeast of Italy, recognised as the largest wetland in the Meditterean area by the Ramsar Convention Ramsar Con-

vention Secretariat [2006]. A complete understanding of the complex dynamics that relate hydrology, geomorpholgy, and ecology of these unique environment requires an explicit consideration of all the biotic and abiotic compartments. A more detailed understanding of the feedbacks between soil, water, and vegetation is needed in order to clarify the mechanisms controlling geomorphological and ecological coevolution in wetland environments. In particular, the detailed study of subsurface saturated/unsaturated water flow, forced by tidal fluctuations and surface evapotranspiration, can provide a better understanding of the interplay between salt-marsh flooding, soil elevation, and soil oxygen availability.

Chapter 3

Long Term Peatland Subsidence

Peatlands respond to hydrologic precipitation-evapotranspiration cycles with reversible soil surface displacements induced by moisture content and pore pressure changes in the vadose and saturated zone, respectively. Elastic surface movements superimpose to irreversible long term subsidence induced by organic matter bioxidation. A two-step modeling approach aimed at quantifing the two components of peatland surface movement is presented. First the elastic component is computed by integrating the peat vertical deformations evaluated by a constitutive relationship proposed by Camporese *et al.* [2006a] and relating the porosity variation with the moisture content and pore pressure changes. The two-parameters expression has been implemented into a variably saturated flow equation-based numerical code through a suitable modication of the general storage term that allows consideration of porosity changes with water saturation. The observations of the peat surface displacement at the Zennare Basin, Italy, is filtered from the reversible component computed by this model and is used to calibrate an empirical relationship relating irreversible land subsidence to drainage depth and soil temperature. The calibrated relation is finally used to investigate the expected evolution of the peat thickness in the study area over the present century.

3.1 Literature review on peatland subsidence

Peatlands are characteristic waterlogged locations where, because of the anaerobic conditions, organic residues have accumulated and still accumulate, usually on relatively flat landscapes, to a depth greater than 0.3-0.4 m and often up to several meters. In the past centuries wetlands were generally considered to be of low economic value. Depending on local conditions and local policy, large portions of temperate, subtropical, and tropi-

cal lowland peatlands were reclaimed worldwide over the last millennium for agricultural purposes and forestry. The low-moor peat soils in the old polders in western Netherlands were reclaimed in a period between the 9-th and the 13-th centuries [Nieuwenhuis and Schokking, 1997] and those of the English Fens began to be drained in the 1650s [Darby, 1956]. The Sacramento-San Joaquin Delta was reclaimed in the late 1800s when levees were built to convert tidal marshlands into agricultural tracts and islands [Deverel and Rojstaczer, 1996]. Since the early 1900s a large portion of the peat bogs covering the Waikato Region, New Zealand, have been drained and converted into pasture [Nieveen *et al.*, 2005]. Due to pressure for land reclamation, substantial areas of peat swamp forests have been recently reclaimed in South-East Asia. About 1000 km^2 of peat swamps in Western Johore, Malaysia, were drained in the early 1970's within the Integrated Agricultural Development Project funded by the Malaysian Minister of Agriculture [Wösten *et al.*, 1997]. In the late 1990's the Indonesian Government realised the Mega Rice Project with the development, by drainage, burning, and deforestation, of about 10000 km^2 of peatswamp forest in Borneo for rice cultivation [Vries, 2003].

Aerobic conditions establish in drained peat soils, inducing the bio-oxidation of the organic content of the peat soils. A major environmental hazard related to peat oxidation is anthropogenic land subsidence. Systematic drainage of farmed organic soils is responsible for lowering the peatland surface elevation by an amount that can reach several meters [Wösten *et al.*, 1997; Stephens *et al.*, 1984] thus increasing the risk of flooding [Mount and Twiss, 2005] and the cost of land drainage [Gambolati *et al.*, 2006] or mantainace of the levees integrity [Suddeth *et al.*, 2010]. In drained peatlands the subsidence rate strongly depends on a number of factors, including type of peat, density of the organic material, drainage depth, climate, and cultivation practices. The overall settlement of the peatland surface is the sum of three components [Wösten *et al.*, 1997]: (i) the consolidation of the saturated porous medium due to the effective stress increase following the lowering of the water table; (ii) the volume reduction of peat due to organic matter oxidation; and (iii) the swelling/shrinking of the shallow unsaturated peat layer due to seasonal wetting/drying cycles. Irreversible long term subsidence of drained peatlands is commonly characterized by an initial, very rapid consolidation followed by a slow biochemical oxidation, the latter generally being recognized as the main contributor to the overall land settlement [Stephens *et al.*, 1984; Armentano and Menges, 1986; Deverel and Rojstaczer, 1996; Price and Schlotzhauer, 1999]. This is supported by the worldwide subsidence rates that are recorded in drained peat areas and that range from few millimeters per year in boreal climates to several centimeters per year in tropical conditions.

Among the several studies that have been carried out in many countries we list:

- in The Netherlands subsidence of 1–2 m in 8–10 centuries was recorded before the installation of steam pumping stations, after which the ground lowered further for about 0.5 m in less than a century [Schothorst, 1977; Nieuwenhuis and Schokking, 1997];

- in England well documented records of peat subsidence show a rate of 3.14 m in 84 years [Hutchinson, 1980];

- in Russia [Skoropanov, 1962] and Norway [Løddesøl, 1949] sinking rates of 1 m in 47 years and 1.5 m in 65 years were recorded, respectively, with different percentages attributable to soil bio-oxidation;

- in the USA several records of subsidence exist: in California [Rojstaczer and Deverel, 1995], Florida [Stephens, 1969], Michigan [Davis and Engeberg, 1955], Minnesota [Roe, 1936] and Indiana [Jongedyk *et al.*, 1950], with different rates of sinking.

Summarizing, worldwide subsidence rates were found to vary between 0.2 cm/a and 8 cm/a, as reported in Table 3.1, with the exception of Malaysia,where the subsidence rate is higher. This occurrence is probably due to the higher mean temperature characteristic of the tropical belt and it represents a confirmation of the importance of soil temperature as the main controlling factor of the process. The more extreme results come from the Province of Friesland (The Netherlands), where organic soil subsidence has been occurring since 1000 years ago. Nieuwenhuis and Schokking [1997] carried out a study to predict the effects of different scenarios of water managements on the future development of the process in the next 50 years. The evaluation of historical subsidence rates from field data showed that for freeboards greater than 0.8–1.0 m (measured in the drains or ditches), subsidence rates appear independent on the freeboard values. This may be related in part to a decrease in permeability with depth, that causes a higher convexity of the water table between the ditches or drains, resulting in a relatively higher water tables compared to the water level in the ditches. Also the rate of oxygen entry decreases at greater depth beneath the surface.

Large agricultural areas south of the Venice Lagoon, Italy, are characterized by soils with high-organic content. They were reclaimed starting from the middle of the 19–th century to the late 1930's, and at present lie almost entirely below mean sea level (down to as much as 4 m). In normal conditions the area is protected from the sea

Table 3.1: Selected areas of anthropogenic land subsidence due to peatland reclamation worldwide.

Location	Latitude	Area of occurrence (km^2)	s_T (cm/year)	Time of occurrence	Principal reference
Western Johor	1°40' N	950	12.5	1960-1974	Wösten *et al.* [1997]
(Malaysia)			6.4	1974-1988	
			2.0	1988-2000	
Everglades	25°40' N	2800	5.0	1914-1950	Stephens *et al.* [1984]
(Florida)			1.6	1950-1980	
San Joaquin Delta	38°03' N	800	1.3-7.5	1925-1980	Deverel and Rojstaczer [1996]
(California)			1.0	1990-1992	
Waikato	37°55' S	85	3.4	1960-2000	Schipper and McLeod [2002]
(New Zealand)					
Central Quebec	48°47' N	40	0.7	1998	Waddington *et al.* [2002]
(Canada)					
Friesland	53°00' N	20	0.2	10th-20th cent.	Nieuwenhuis and Schokking [1997]
(The Netherlands)			0.8	1960-1995	
West Norway	58-63° N	630	1.8	1950-2004	Gronlund *et al.* [2008]
			0.7	1983-2004	

by coastal embankments. Drainage of the outcropping peat soil, together with yearly ploughing for agricultural purposes, systematically brought poorly-decomposed peat to ground surface, resulting in an overall cumulative land subsidence of 1.50-2.00 m in the last 70 years [Gambolati *et al.*, 2006]. The continuous maintenance of a given water table depth, as dictated by agricultural requirements, has caused the lowering of the inlet shaft of the drainage pumping stations and the simultaneous increase of the pumping head. As a major consequence, pump efficiency has decreased and drainage costs raised. Moreover, the risk of flooding during exceptionally severe storms has increased together with the occurrence of adverse events, such as saltwater contamination from nearby rivers, the lagoon, and the sea [Carbognin *et al.*, 2006]. Since the continuous loss of land elevation relative to the mean sea level is threatening more and more the hydrogeological safety of the area, and its sustainable development as a farmland is becoming increasingly expensive and questionable, an experimental and modeling study has been performed to evaluate possible mitigation strategies.

As already remarked, peats respond to natural hydrologic cycles of precipitation/evapotranspiration and freeze/thaw with reversible ground surface displacement that superimpose to the irreversible long term subsidence, with short term deformation rates usually comparable with the yearly sinking rates due to the peat oxidation.

A number of swelling/shrinking models of peat soils have been proposed in the last few years. Some of these models are empirical [Oleszczuk *et al.*, 2003; Hendriks, 2004] and require both fitting and/or site specic measured parameters. On the other hand, physically based models [Pyatt and John, 1989; Price, 2003; Kennedy and Price, 2004] often require a large number of measurable parameters, but adequate calibration data from laboratory experiments and in situ tests are not always available. Starting from the approach proposed by Pyatt and John [1989], valid for saturated conditions, only. Camporese *et al.* [2006a] apply a two-parameter constitutive model that relates the short term reversible dynamics of the peat surface to the hydrologic characteristics of the unsaturated zone. Pyatt and John [1989] propose a two stage model expressing the shrinkage of well-decomposed saturated peats in terms of specific volume and gravimetric water content changes. A threshold value of the gravimetric water content separates the stage of one-dimensional vertical deformation from the stage where the peat experiences an isotropic three-dimensional deformation with the development of cracks in the porous medium. An attempt to apply this model to reproduce the data set collected from a bog in Québec, Canada, did not provide satisfactory results, probably because of the effect of methane bubbles, not taken into account by the model [Price, 2003; Kellner *et al.*, 2005].

Generally, shrinkage characteristic curves are commonly described using empirical expressions relating void ratio versus moisture ratio. Several laboratory experiments on European peats show that the shrinkage behavior is significantly different from that of clay soils [Van den Akker and Hendriks, 1997; Oleszczuk *et al.*, 2003; Hendriks, 2004]. According to Hendriks [2004], three phases can be distinguished during peat drainage. A near-normal shrinkage phase occurs when the soil volume decreases at approximately the same rate of moisture content and the peat matrix remains close to saturation. Sub-normal shrinkage takes place when moisture loss exceeds volume change and the soil becomes definitely unsaturated, with air entering the larger pores, while the smaller pores in the organic fibers remain water-filled. Finally, super-normal shrinkage develops when the volume reduction is greater than moisture loss. During this phase, also the small pores dry and the matrix collapses to its minimum volume as moisture content approaches zero. A simple three line constitutive model has been proposed by Oleszczuk *et al.* [2003] as a first attempt to reproduce this characteristic behavior. In this model six constitutive constants must be determined by fitting laboratory data. A more complex expression has been developed by Hendriks [2004] by employing a moisture–void ratio relationship that depends again on six parameters: moisture ratio at saturation and at the transition from the near- to the sub-normal phase, residual void ratio, i.e. void ratio at zero moisture content, and three fitting parameters. Such a large number of degrees of freedom entails an accurate description of the overall deformation process, but requires the availability of specific laboratory data and the estimation of their representativity at the field scale.

A different approach is followed by Kennedy and Price [2004, 2005], who developed a conceptual model that considers several hydrological parameters as functions of peat density and, consequently, of effective stresses. This model, which allows the simulation of reversible deformations in both the saturated and unsaturated zone, is based on Terzaghi's theory of consolidation [Terzaghi, 1943], extending the validity of the effective stress principle to the unsaturated zone. Several processes are simultaneously taken into account in both zones: shrinkage and temporally variable retention curves are considered in the partially saturated soil portion, while below the water table primary consolidation, secondary compression, and variable hydraulic conductivity are addressed. Again, the value of a large number of physically based and empirical parameters needs to be obtained from laboratory experiments and in situ tests. Application of this model and results from field observations at the Lac Saint-Jean cutover bog, Québec, show that shrinkage in the unsaturated zone and compression below the water table represent 55-59% and 38-41% of the total soil surface elevation change, respectively. The shrinkage rates were larger

than compression rates, even if the relative importance was similar. These results are explained by the fact that the unsaturated layers represent a small proportion ($\leq 30\%$) of the overall aquifer thickness [Kennedy and Price, 2005].

In the present thesis the model proposed by [Camporese *et al.*, 2006a] is considered. The authors proposed a constitutive two-parameter expression, derived from simple but rigorous physical considerations that takes into account both anisotropic and isotropic behavior of peat deformation and expresses the void ratio as a function of moisture ratio. The model and its application to simulate the swelling/shrinkage behavior of the Zennare Basin organic soils are discussed in section 3.4.

3.2 Experimental methods and measurements

At the beginning of 2002 the Department of Mathematical Methods and Models for Scientific Applications (DMMMSA) of the University of Padova designed and installed a number of sites in the Zennare Basin. The main objectives of the experimental activity were (i) to record the land subsidence rate due to peat oxidation and (ii) to measure the hydrological parameters controlling the biochemical process [Fornasiero *et al.*, 2002, 2003; Teatini *et al.*, 2004; Camporese *et al.*, 2006b]. The peat surface elevation at the monitoring site is -3.1 m a.m.s.l. Ground surface displacements were measured by means of a specific structure modeled after Deverel and Rojstaczer [1996] and shown in Figure 3.1. A steel tripod with 2 m length sides is anchored on three piles set into the ground to a depth of 11–12 m below m.s.l. where an over-consolidated clay layer is located. Each pile was pushed 3 m deep through a pre-drilled borehole completed with PVC pipe through the organic layer to minimize friction between the anchoring and the subsiding peat layer. Three LVDT (linear-voltage displacement transducers, LZW Series, WayCon GmbH, Germany, sensitivity ± 0.125 mm, range 0-25mm) are connected at one end to the triangular structure in the middle of each side and to the other end to the land surface through a 0.005 m thick, 0.10×0.10 m aluminum plate that rests on the soil surface. The bodies of the LVDTs are attached to the steel triangle through a threaded rod that can be adjusted to follow the soil movements at larger excursions. The steel structure has been designed to be as light as possible but subject to a negligible deformation, with respect to the magnitude of the forecasted land subsidence, when loaded with the force exerted by the spring of the LVDTs (2.5 kg each) and by a thermal excursion of about 40° C.

The site was equipped with a tilting bucket pluviometer with a 0.2 mm sensitivity and five soil temperature sensors at 0.01, 0.05, 0.2, 0.3, and 1 m depth (PT100 with a

Figure 3.1: Steel tripod constructed to continuously monitor the elevation changes of the peat surface. A zoom of the displacement transducer is shown on the right. The anchoring piles and the displacement transducers are highlighted.

measurement range between -15°C and 50°C and sensitivity of ±0.1°C). The depth to the water table has been determined by two atmosphere-compensated pressure transducers (ATM/N/T Series, STS AG, Switzerland, with a measurement range of 0-300 mbar, sensitivity of ±1.5 mbar), submerged in 3 m deep PVC wells, one located within the field site and the other close to the adjacent drainage ditch. Power supply was provided by a 12 V, 260 Ah battery and all sensors were connected to a 8-bit datalogger (Geolog, TER Srl, Italy) and sampled hourly.

3.3 Data analysis

The data collected from January 2002 to February 2006 at the field site are summarized in Figure 3.2. In spite of two major periods of instrument malfunction from May to September 2004 and from February to June 2005, the measurements recorded over four seasonal cycles allow for a significant characterization of the peatland hydrologic dynamics. Figure 3.2a shows the time series of hourly precipitation together with the cumulative precipitation for the years 2002, 2003, 2004, and 2005 as measured by the weather station of the reclamation authority located at the basin outlet. A severe drought occurred in

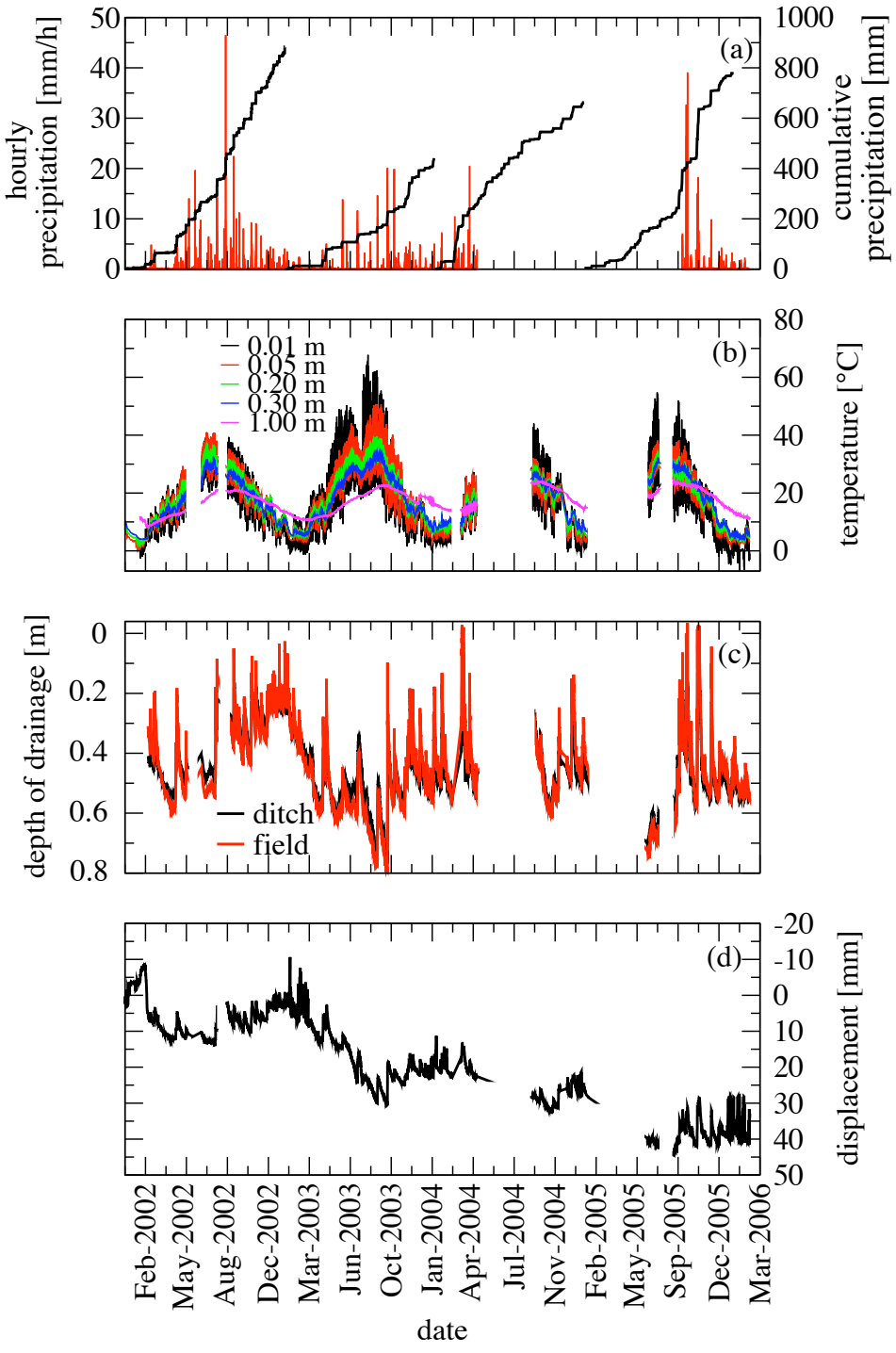

Figure 3.2: (a) Hourly precipitation, (b) soil temperature at various depths, (c) depth to the water table, and (d) land displacement as measured between January 2002 and February 2006 at the Zennare Basin field site. Yearly cumulative precipitation shown in (a) is measured at a nearby weather station managed by the reclamation authority. Two major periods of instrument malfunction are from May to September 2004 and from February to June 2005.

2003 when the summer precipitation amounted to only 120 mm and the yearly total to 440 mm. Summer 2002 and 2005 were wetter, with a cumulative precipitation of about 300 mm in three months and a total yearly precipitation of 800-850 mm. Due to the intense rainfall events and some troubles at the drainage system the entire area around the test site was flooded by 0.10 m of water during August 2002. Average pluviometric conditions characterized the year 2004.

Figure 3.2b provides the soil temperature measurements. Large daily variations were recorded for the near-surface probes. It is interesting to observe that the deeper probe shows a seasonal fluctuation of about 10°C. Summer 2003 was characterized by very high temperatures that caused the upper 5 cm of peat to be almost permanently above 40°C for three months, with peaks well above the sensor FS (Full Scale) (50°C).

The water table depth ranged from ground level, soon after heavy rainfall events, to a maximum 0.80 m depth in summer 2003 as can be seen from Figure 3.2c, which plots the water table depth h measured in the ditch and in the field piezometer. Since the water level in the ditches is strictly controlled by the pumping station, the average depth of the water table is generally maintained between 0.40 and 0.50 m. However, the behavior of h is characterized by significant time-fluctuations in connection with atmospheric events. As can be seen from the zoom of Figure 3.3, during a precipitation event the water infiltrates through the surface causing a rapid decrease of the water table depth. Soon after the event, because of pumping, a groundwater mound forms and seepage from inside the field toward the ditch occurs. Conversely, water level from the ditch recharges the peat layer during dry periods, generally during the summer season, when water levels in the drainage network are maintained high for irrigation purposes.

The peat surface elevation was measured by three independent LVDTs. The redundance of the measurements was used to correct the data for local inconsistencies. A careful inspection of the three series shows a general coherent behaviour with few anomalies concentrated in one single trasducer. These anomalies were verified for consistency with pluviometric events and corrected for by using the records of the other LVDTs. The cause of this behaviour must be attributed to the sinking of the plate sustining the LVDT because of the presence of mud (fluidized peat). The resulting displacement is shown in Figure 3.2d as a function of time. The sizable uplift of the soil surface during January 2002 is due to freezing of the surface soil, followed by a large downward movement occurred during and just after the ice melting period. The 40–45 mm cumulative land subsidence recorded as of February 2006 develops through a very complex surface peat dynamics due to the superposition of reversible and irreversible processes. The former

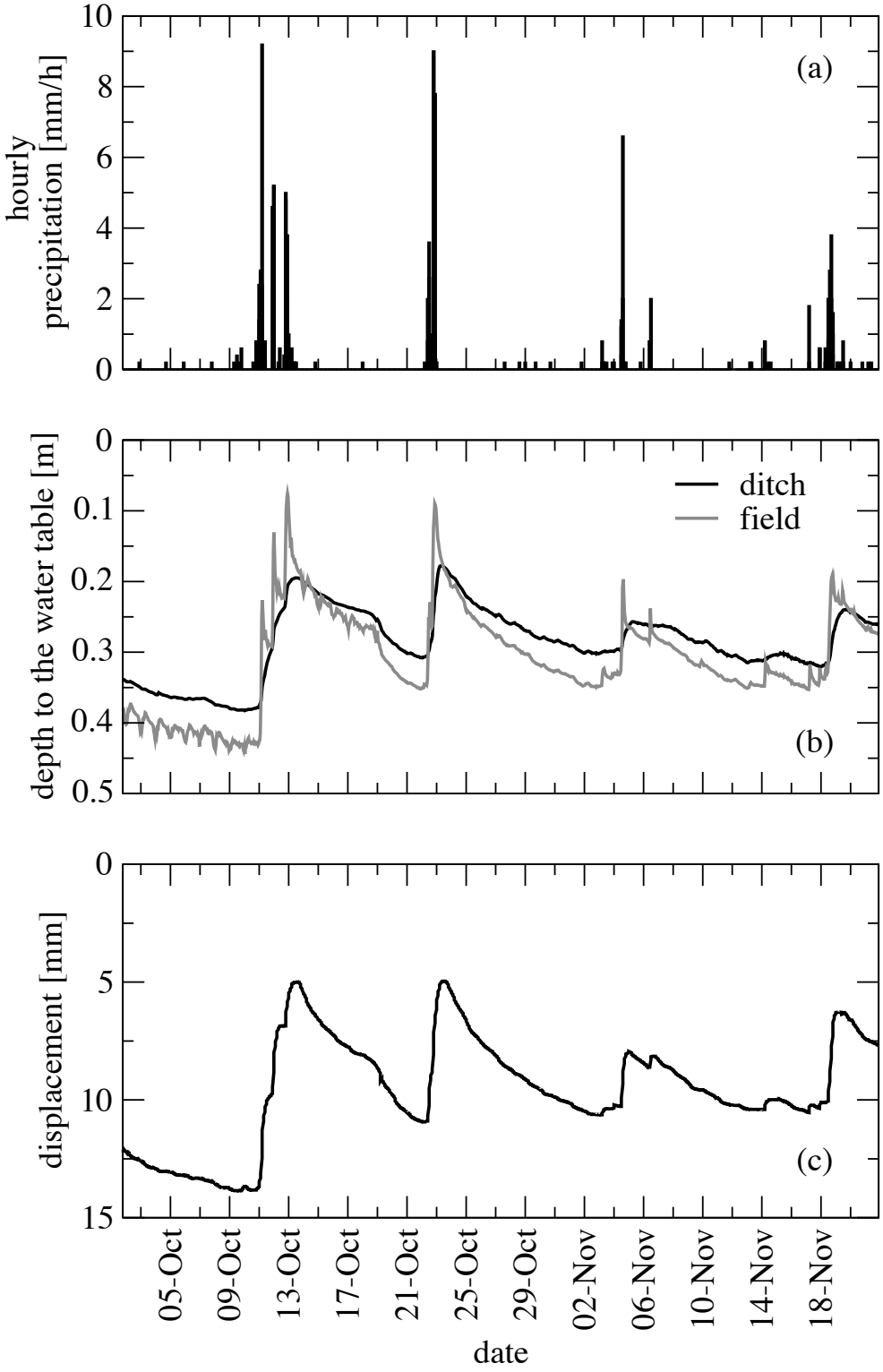

Figure 3.3: (a) Hourly precipitation, (b) depth of the water table at the ditch and field piezomenter, (c) and land subsidence measured between October 3, 2002 and November 17, 2002, at the Zennare Basin field site.

phenomenon can be related to the peat swelling/shrinking process in response to drying/wetting or freeze/thaw cycles and the latter phenomenon is related to the oxidation of the organic matter. Therefore, an accurate quantification of the present subsidence rate characterizing the Venice peatland requires the separation of the two contributions from the available records.

3.4 Reversible peat displacement

Effect of soil temperature

Visual inspection of the 4-years long soil vertical displacement record (Figure 3.2d) reveals significant oscillations occuring at very short time scales (of the order of less than 1 day) connected to soil daily temperature fluctuations in winter. Figure 3.4 compares the soil temperature at a depth of 0.01 m with the recorded displacements during January 2006: when water freezing temperatures are reached at night, large upward soil displacements, up to 10 mm, are clearly visible. This is an entirely reversible phenomenon, which quickly dissipates over 2-3 hours when the temperature increases in the morning. Since our analysis does not consider temperature driven deformations, these phenomena have been removed from the signal (black line in Figure 3.4b).

Effects of soil moisture and water pressure changes

As described in Camporese *et al.* [2006a], and as can be seen from Figures 3.2 and 3.3, the continuous recording of the ground vertical displacement unfolds significant reversible movements of the land surface. The elastic component of the deformation can be detected at short time-scales, when land settlement due to histosol oxidation can be considered negligibly small. Figure 3.3 shows hourly rainfall, depth to the water table, and land subsidence measured at the field site from October 3, 2002 to November 17, 2002. Synchronism between rainfall events, groundwater table depth, and the movement of the soil surface can be observed. Peat expands at each rainfall event, showing that swelling progresses quickly soon after precipitation initiates and decreases at a slower rate following the water table decline.

Looking at the precipitation event of October 21, 2002 we note that the sharp increase in soil elevation, corresponding exactly to the precipitation event, completely dissipates by November 2. Thus we can estimate the time scale of the swelling/shrinking behavior at approximately two weeks. At these time scales, deformations can be considered as

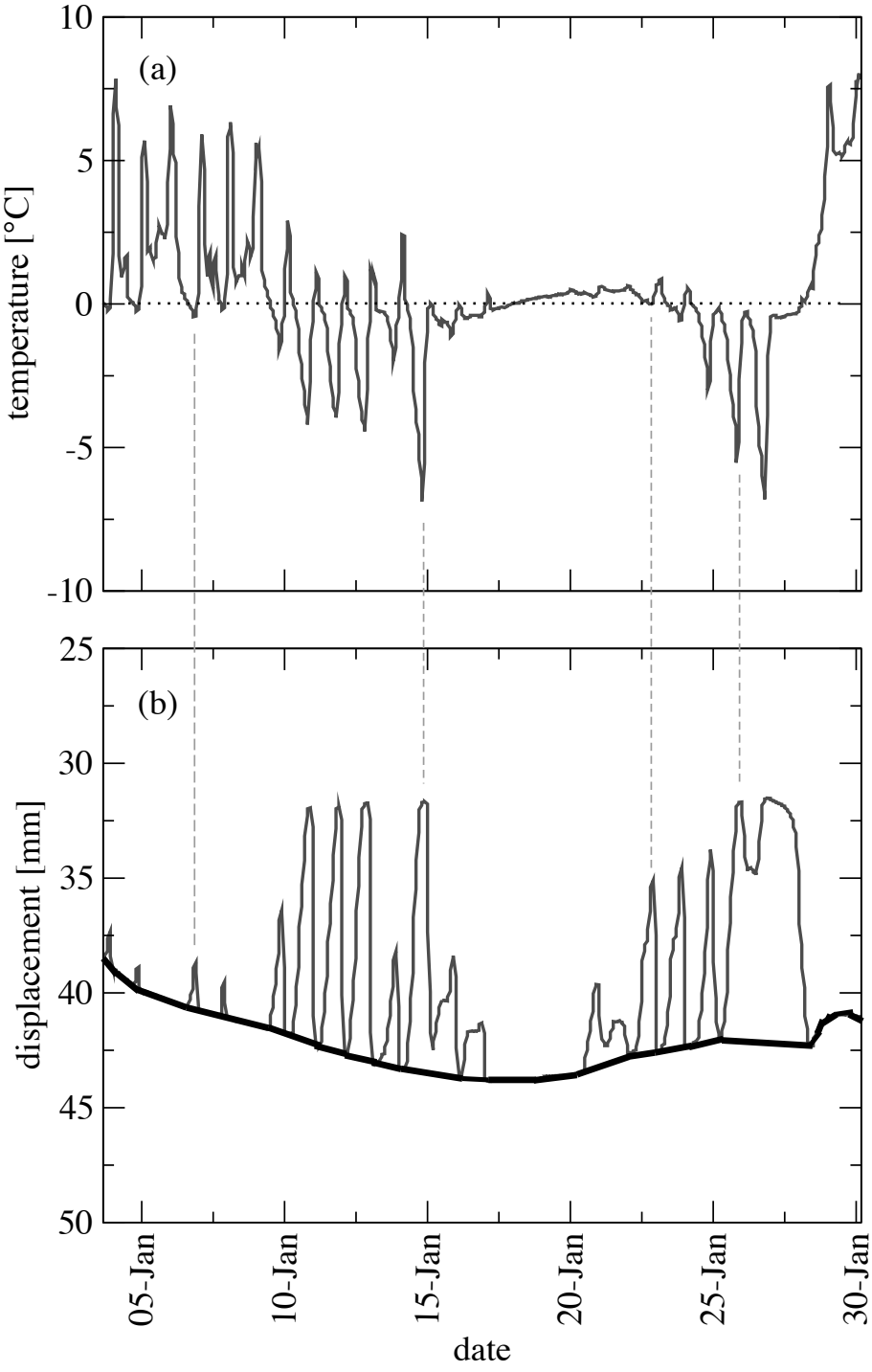

Figure 3.4: (a) Soil temperature at 1 cm depth and (b) soil surface displacement measured during January 2006 at the Zennare basin field site. The black line in (b) represents the movement once the temperature effect is filtered out.

completely reversible, and thus elastic. We note here that elastic deformations at the scale of a single precipitation event are mainly related to changes in water content in the unsaturated zone [Camporese *et al.*, 2006a]. Comparison of Figures 3.2c and 3.2d suggests that the elastic displacement follows the dynamics of h also beyond the single precipitation event, as witnessed by the recordings of the second half of 2002, during which the average h was 0.3 m, smaller than normal by about 0.2 m, as consequence of heavy rainfalls and drainage system malfunction. This relationship cannot be ascribed to changes in water content in the unsaturated zone alone, and the elastic compressibility of the saturated zone (i.e. deformations due to pore pressure variations) must be considered as well [Price and Schlotzhauer, 1999; Price, 2003; Camporese *et al.*, 2006a]. A simple linear regression between the peat expansion and the water table rise provides an estimate of 0.3–0.4 mm soil displacement per 0.01 m variation of the water table level [Teatini *et al.*, 2004; Camporese *et al.*, 2006b]. This is a cumulative estimate, taking into account the processes occurring both in the unsaturated and saturated zones. In the present work, we try to evaluate the two contributions by modeling them separately.

Several swelling/shrinking models have been proposed in order to reproduce real dynamics of peat response to soil water content variations [Pyatt and John, 1989; Schlotzhauer and Price, 1999; Price, 2003]. Here, we adopt the modeling approach proposed by Camporese *et al.* [2006a], in which the swelling/shrinking dynamics is described by a power-law type constitutive relationship that relates the void index $e = \phi/(1-\phi)$, ϕ being the medium porosity, with the volumetric moisture ratio ϑ, defined as the ratio between the volume of water and the volume of solids:

$$e(\vartheta) = \begin{cases} (\vartheta_0 + 1)^{1-\delta}(\vartheta + 1)^{\delta} - 1 & \text{if } \vartheta \leq \vartheta_0 \\ \vartheta & \text{if } \vartheta > \vartheta_0 \end{cases}, \tag{3.1}$$

where ϑ_0 is the threshold moisture ratio above which the soil is fully saturated and the exponent δ characterizes the deformation dynamics. Isotropic deformations occur for $\delta = 1/3$ and with $\delta = 1$ the volume deforms along the vertical direction only. Values of δ ranging between 1/3 and 1 identify a process of three-dimensional anisotropic soil deformation [Oleszczuk *et al.*, 2003; Camporese *et al.*, 2006a]. Equation (3.1) is implemented in a three dimensional finite element code called FLOW3D, one of the modules of CATHY, a coupled model for the numerical simulation of surface and subsurface flow [Bixio *et al.*, 2000; Camporese *et al.*, 2010]. The code solves the flow equation for variably saturated porous media, also known as Richards equation, that in terms of pressure head ψ is written

as:

$$\sigma \frac{\partial \psi}{\partial t} = \nabla \cdot [K_s K_r \cdot \nabla (\psi + z)] + q \tag{3.2}$$

where $\sigma(S_w)$ is the general storage term, with $S_w = \vartheta \cdot [(1-\phi)/\phi]$ being water saturation, t is time, ∇ the spatial gradient operator, K_s and K_r the saturated and relative hydraulic conductivity, respectively, z is the vertical coordinate (positive if directed upward), and q represents the source or sink term. Equation (3.2) is completed by proper initial conditions, water table and evapotranspiration boundary conditions, and by retention curves $S_w(\psi)$ and $K_r(S_w)$. For mineral soils, the general storage term can be written as: $\sigma = S_w S_s + \phi \cdot (\partial S_w / \partial \psi)$, where S_s is the elastic storage coefficient. When dealing with organic soils in unsaturated conditions, the storage term has to be suitably modified in order to include porosity variation as a function of water saturation [Camporese *et al.*, 2006a] yielding:

$$\sigma = \phi \frac{\partial S_w}{\partial \psi} \left[\frac{\delta (S_w \cdot \phi/(1-\phi) + 1)^{-1}}{1/S_w - (\vartheta_0 + 1)^{1-\delta} \delta (S_w \cdot \phi/(1-\phi) + 1)^{\delta - 1}} + 1 \right] \tag{3.3}$$

For fully saturated soil $\sigma = S_s$.

After solving (3.2)-(3.3), the vertical deformation Δ_u at time t of an unsaturated peat layer whose initial thickness is $\ell(0)$, is calculated as [Camporese *et al.*, 2006a]:

$$\Delta_u(t) = \frac{\ell(t)}{\ell(0)} = \left[\frac{1 - e(t)}{1 - e(0)} \right]^{\delta} \tag{3.4}$$

where $t = 0$ refers to the initial stage and the time evolution of void index is evaluated by means of equation (3.1). The vertical deformation in saturated conditions, $\Delta_s(t)$, is modeled following the classical theory of vertical soil consolidation as described in Gambolati [1973]. Neglecting water compressibility, the following relationship is used:

$$\Delta_s(t) = \frac{\ell(t)}{\ell(0)} = 1 + S_s [\psi(t) - \psi(0)] \tag{3.5}$$

where $\psi(t)$ is the solution of equation (3.2). The soil surface displacement is calculated by adding together the integrals of Δ_u and Δ_s evaluated over the actual unsaturated and saturated thickness of the peat soil, respectively.

We apply the modeling approach described above on the 1 m thick peat column representative of the Zennare peatland starting from the set-up, capillary relationships, and parameter values calibrated by Camporese *et al.* [2006a]. A more refined model calibration was performed on the parameter δ (equation 3.4) and S_s (equation 3.5) to achieve a more accurate separation of the effects of the unsaturated and saturated elastic

deformations. The Willmott index of agreement [Willmott, 1948] was used to evaluate the best fit between measured and simulated surface displacements. Since amorphous peat experiences larger deformations with respect to coarse fibrous peat, we use two different values of the elastic storage coefficient in equation (3.5). The results of the calibration yields $\delta = 0.30$ and $S_s = 0.1$ m^{-1} for the upper layer and $S_s = 0.06$ m^{-1} for the deeper layer. These values of S_s fall within the variability range $0.001 \div 0.1$ m^{-1} estimated for peat soils by Dasberg and Neuman [1977] and Price and Schlotzhauer [1999].

The comparison between the measured and the computed elastic movements is shown in Figure 3.5 over the three periods from November, 12, 2002 to January, 11, 2003, from March 24, 2004 to April 5, 2004, and from August 19, 2005 to September 3, 2005. The three time intervals are representative of the entire behavior. The last two intervals are characterized by a short enough duration so that the irreversible component of the displacement is negligible, and by the occurrence of more than one pluviometric event with intensity higher than 10 mm/h. The first interval is a three months period during which the average water table depth was less than 0.25 m (Figure 3.2c) resulting in a soil water content close to 100%, thus preventing the progressing of bio-oxidation.

Figure 3.6a shows the vertical displacements caused by the elastic swelling/shrinkage behavior as computed by the proposed model over the whole time interval covered by the experimental study. The distinct contributions of saturated and unsaturated layers to soil surface displacement are also shown in Figure 3.6b and 3.6c. The vadose zone deformations play a leading role during the dry periods, particularly during summer 2003 when about 70% of the total elastic movement was produced by unsaturated zone deformation. During wet seasons the major contribution to the total elastic movement occurs in the saturated zone. During winter 2003-2004, for example, when the depth to the water table reduced to less than 0.4 m the swelling component attributed to the saturated zone was dominant. Finally, note that the model is capable of reproducing the dynamics of the vertical displacements measured also in very wet conditions, where large swelling records occur (Figure 3.5a). Subtracting the elastic deformations (Figure 3.6a) from the recorded land displacement, the time series of the soil surface movement is filtered from both the short-time scale fluctuations connected to soil temperature and the "mire breathing" component (Figure 3.7, grey line). The resulting signal reveals the persistence of some fluctuations occurring at a very short time scale due to residual model inaccuracies in the estimation of the major swelling peaks. These oscillations have been filtered out by using a moving average technique with a calibrated window of 90-days. The result is reported in Figure 3.7 (black line).

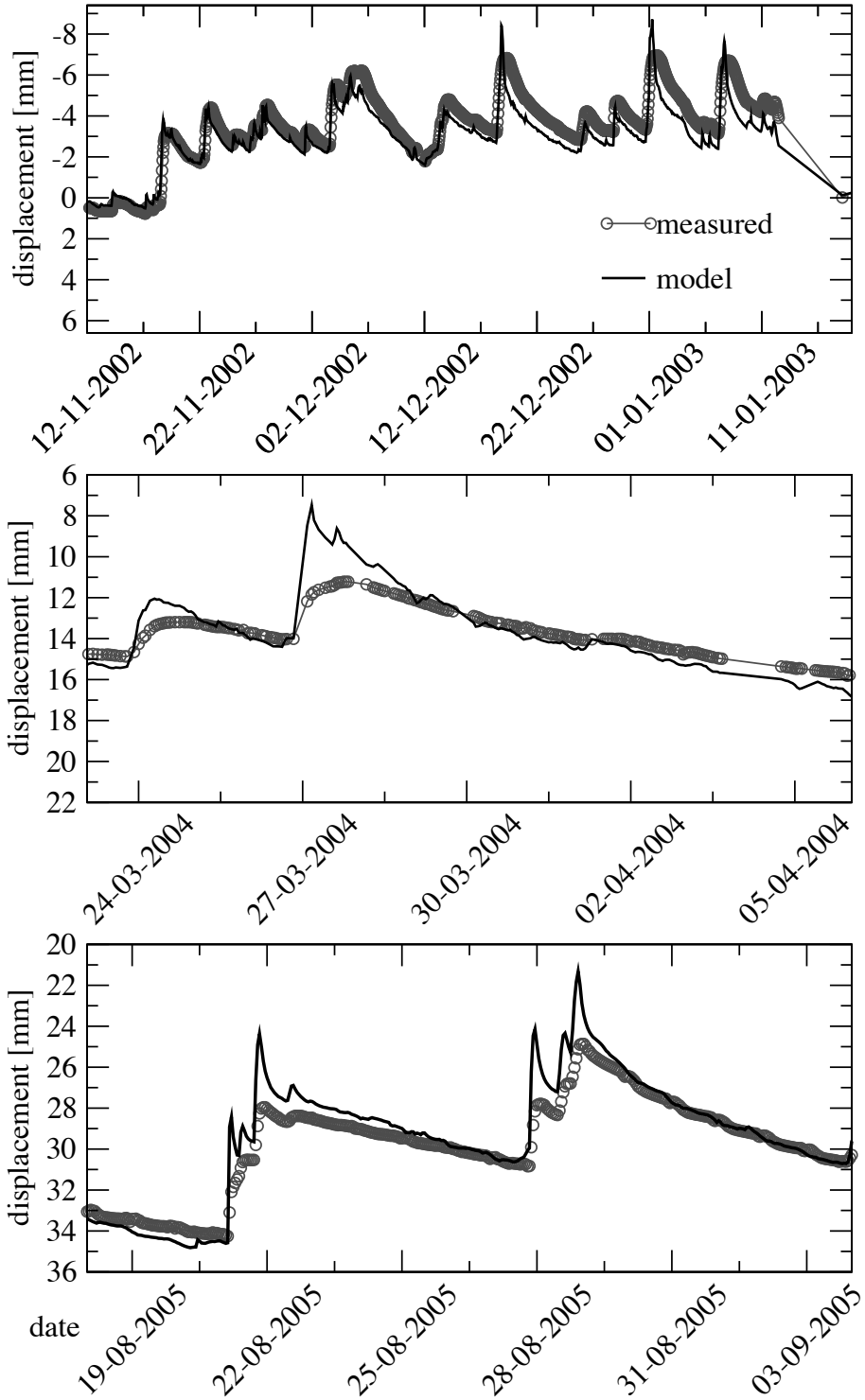

Figure 3.5: Comparison between the measured land displacements and the computed elastic movements for three time intervals. The model results represent the sum of the reversible contributions occurring in the unsaturated and saturated zones.

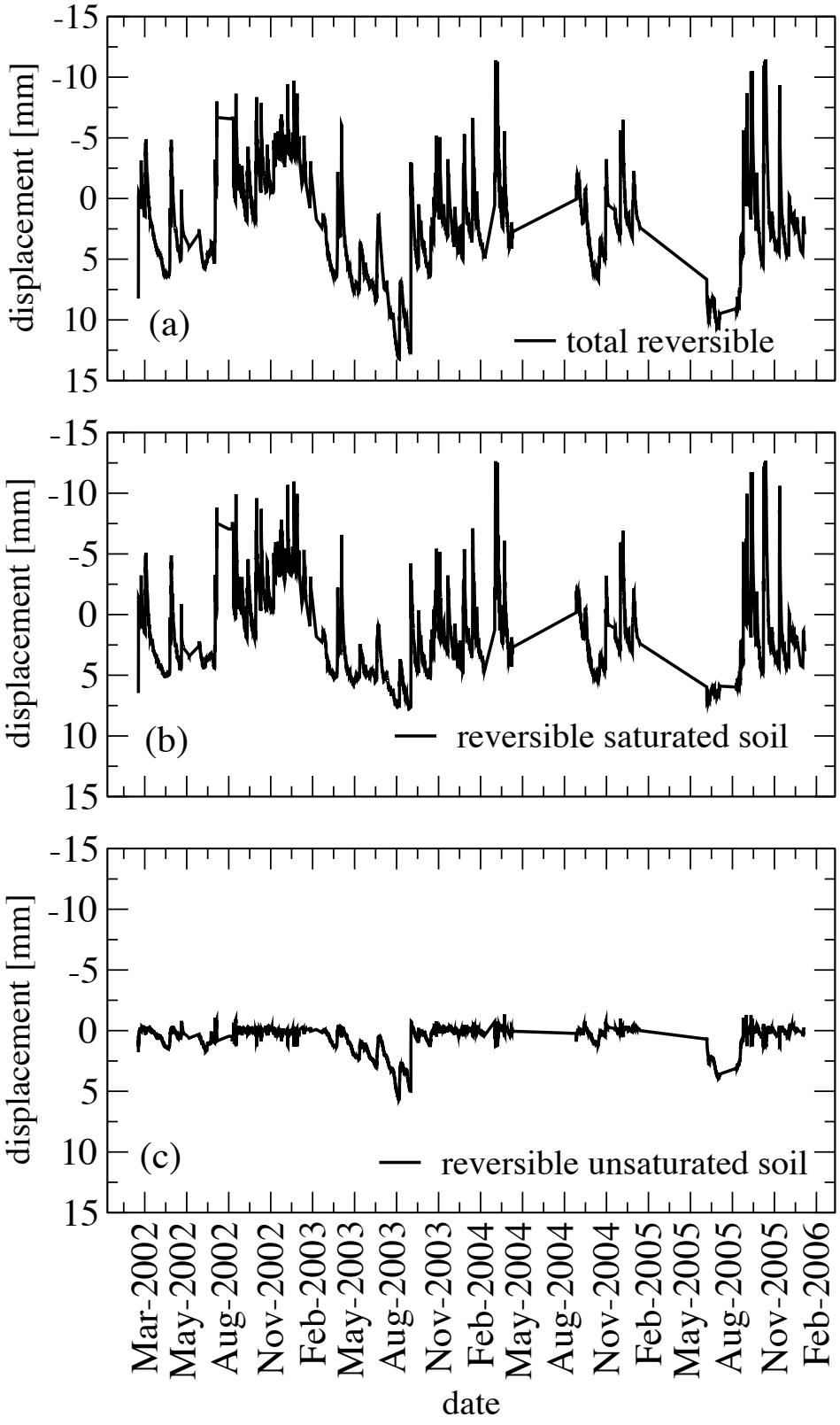

Figure 3.6: (a) Reversible land displacement computed over the entire monitoring interval of the Zennare experiment (a). The contributions due to the saturated (b) and vadose (c) portions to the overall elastic soil surface displacement are also shown.

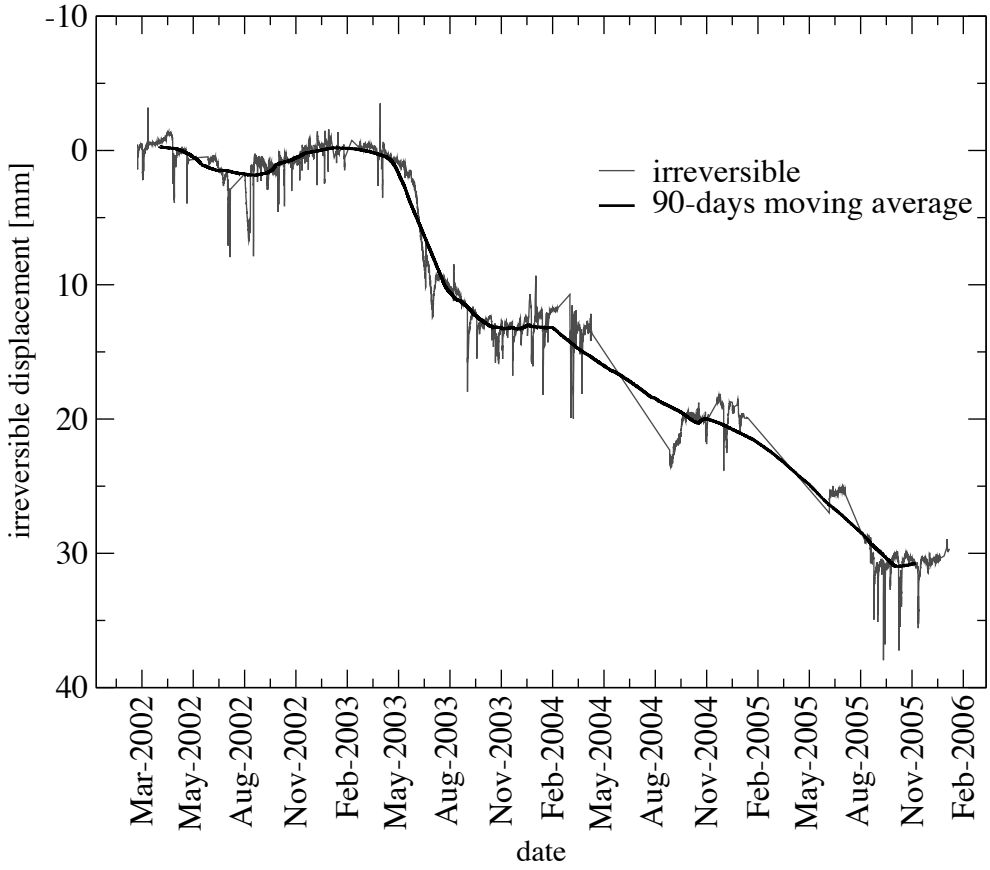

Figure 3.7: Irreversible land subsidence computed by subtracting the elastic component of the peatland displacement from the recorded land settlement (grey line) and the relative 90 days-moving average (black line).

3.5 Irreversible peat displacement

Figure 3.8 shows that the cumulative land subsidence measured during the period January 2002 - February 2006 (panel c) compared to the recorded temperature (panel a) and water table (panel b). The total subsidence at the end of the measurement period amounts to almost 30 mm. The largest settlement rates are recorded in the year 2003 (about 13 mm/a), with larger values ($\sim$ 30 mm/a) in the summer, when extreme dry and hot weather conditions occurred. The available time series in 2004 and 2005, even though incomplete, allow for the evaluation of an average subsidence rate of 6 mm/a and 8 mm/a, respectively. Year 2002 is characterized by the high precipitation, and, consequently, small average depth to the water table (between 0.2 and 0.3 m) in both summer and fall. The measured subsidence rates over the entire period varied in the range of 3.0-15.0 mm/a, in agreement with indirect assessments from CO_2 efflux measurements, which varied in the interval $25\pm15 \times 10^{-4}$ t C/m^{2}a [Camporese *et al.*, 2008]. Looking at the simple relationship between annual subsidence rate and depth to the water table, the values recorded at the Venice site are comparable with those recorded in Indiana. Here, on a peatland with characteristics similar to the site of Zennare, rates ranges between 3 mm/a and 20 mm/a with a water table depth varying between 0.2 and 0.7 m [Stephens *et al.*, 1984].

Irreversible subsidence can be modeled with the approach proposed by Stephens *et al.* [1984]. The model relates land subsidence due to peat oxidation to depth of drainage and soil temperature. By the use of Arrhenius's law [Arrhenius, 1889], which states that the logarithm of a chemical reaction rate is linearly related to the reciprocal of the absolute temperature, these authors propose the following equation:

$$s\left(T,h\right) = \left(a + bh\right) \cdot e^{k(T-T_0)} \tag{3.6}$$

where $s\left(T,h\right)$ is the biochemical subsidence rate at temperature T and depth of water table h, k is the reaction rate constant, T_0 is the threshold soil temperature above which the biochemical reaction is active, and a and b are fitting parameters. From laboratory investigations on the peat soils of the Florida Everglades, Stephens *et al.* [1984] estimated the values of $k = 0.06931$ and $T_0 = 5^{\circ}$C, while parameters a [mm/a] and b [1/a], were obtained so as to reproduce the recorded yearly subsidence rate $s\left(T,h\right)$ [mm/a]. Here h [mm] and T [$^{\circ}$C] denote the annual average depth to the water table and soil temperature at 0.10 m depth, respectively.

We have calibrated the above model by assuming that (i) k and T_0 are the same

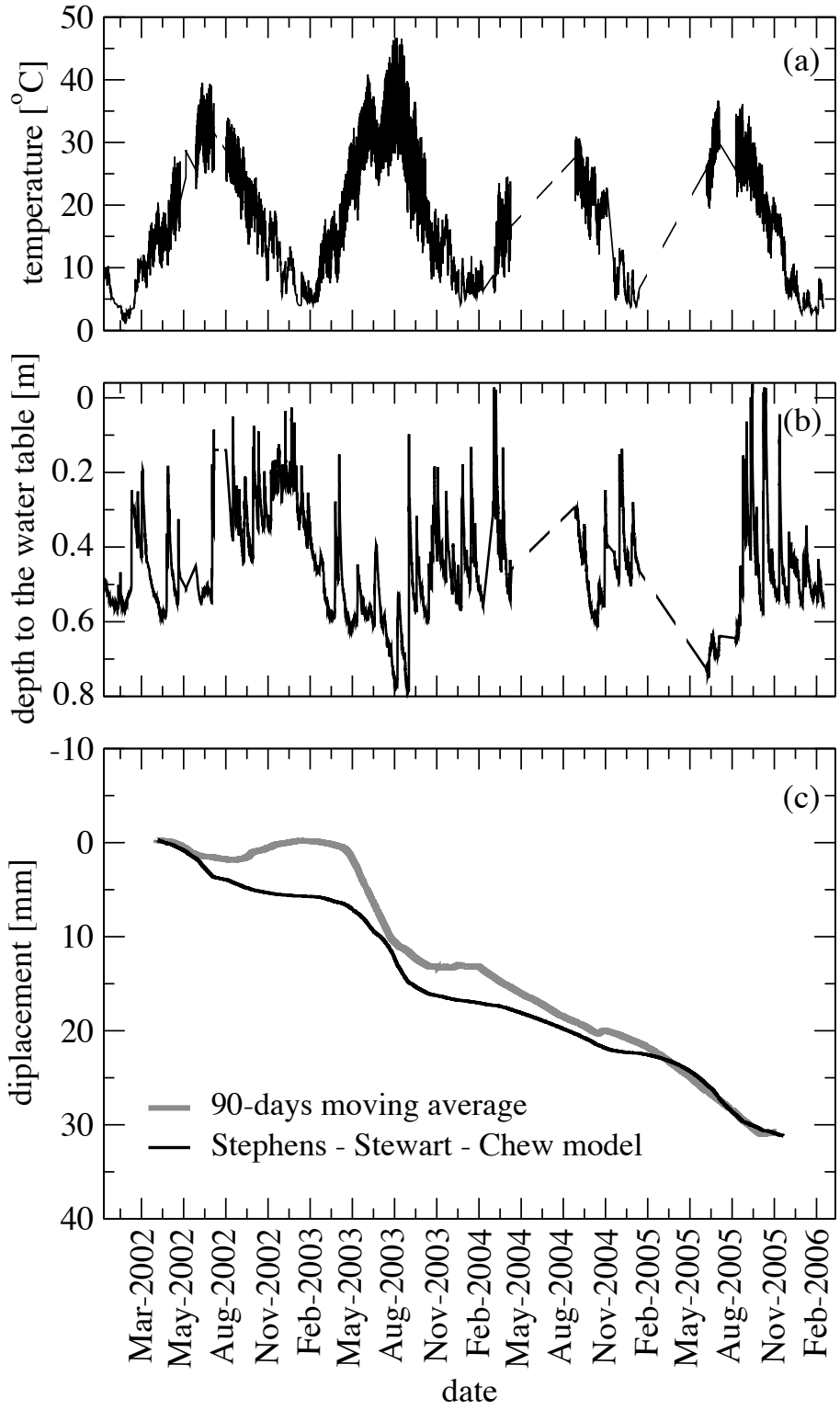

Figure 3.8: (a) Soil temperature at 10 cm depth and (b) depth of drainage used in the model by Stephens *et al.* [1984]. (c) Comparison between the measured irreversible land subsidence (grey line) and the prediction from the calibrated Stephens *et al.* [1984] model (black line).

as the ones calculated for the Everglade peats, (ii) the organic matter content remains constant over the monitored time interval. The first assumption is reasonable in that both soils come from the decomposition of *Phragmite Australis*, whereas the second hypothesis is a consequence of the local agricultural practices at the Zennare Basin. Infact, annual ploughing takes place usually in early spring and involves the upper 0.40 m thick peat layer. Ploughing brings a certain amount of poorly decomposed peat (with organic content η up to 85%) to the ground surface and subsequent tillage mixes it with the shallower amorphous peat. We assume that the increase in organic matter of the top layer due to the unmineralized peat contribution is annually balanced by the organic matter loss in term of CO_2 efflux from the soil into the atmosphere [Camporese *et al.*, 2008]. Larger yearly subsidence values bring larger portions of unmineralized peat to the ground surface. Consequently, this seasonal natural/antrophogenic cycle yields an upper peat layer characterized on the average by a constant organic matter content η_0 of 0.5 (50%). Moreover, we assume that no external input of biomass occurs since crop residues are completely removed for cattle feeding, and the root contribution is negligible compared to the surfacing of unoxidized peat due to ploughing.

The parameters a and b are evaluated so as to reproduce the irreversible land subsidence starting from February, 2002 after ice melting. Instead of computing a mean annual value, the model has been applied over a hourly time-scale, consistently with the sampling rate of the available hydrological information and peatland surface displacement. The soil temperature at 0.10 m depth is obtained from linear interpolation of the data collected at 0.05 m and 0.20 m depths. The gaps in the h and T time series due to instrument malfunction (Figures 3.8a and 3.8b) are filled by simple linear interpolation. We have imposed the constraint that all the hourly calculated $s(T,h)$ are always non-negative (to guarantee the physical meaning of equation (3.6)), and $s(T,h)$=0 has been assumed for the periods when soil temperature is less than 5°C. The Nash-Sutcliffe fitting criterion [Nash and Sutcliffe, 1970] has been used providing the values a=-0.15 mm/a and b=0.006 1/a.

Figure 3.8c compares the irreversible land subsidence as obtained by subtracting the elastic components from the observed measurements with the land subsidence as predicted by Stephens *et al.* [1984] model. The global long term settlement is satisfactorily reproduced by the model. The results show that almost 50% of the irreversible land subsidence occurred over spring-summer 2003, while the hydrological conditions have practically precluded the hystosols oxidation from July 2002 to April 2003, as evidenced by the almost flat displacement behavior evaluated during this period.

3.6 Modeling the expected land subsidence

The strong relationship between the peatland settlement rate, the soil temperature and the depth to the water table, suggests that, if no remedial strategies are implemented and the soil oxidation continues at the present rate, the remaining peat layer is bound to disappear in a few tens of years. To obtain a quantitative estimate of the time to complete peat disappearance, our calibrated model is applied to forecast the long term evolution of the peatland thickness in the Zennare Basin over the next 100 years. This application, however, requires some additional comments and appropriate model modification to take into account the localized characteristics of the Zennare Basin. More specifically, we need to take into consideration local agricultural practices and adapt our model accordingly. As described in paragraph (3.5) the annual ploughing with the histosol oxidation yields an upper peat layer characterized on the average by a constant organic matter content $\eta_0 = 0.5$ (50%). The current subsidence rates will necessarily decrease as soon as ploughing intercepts the clay layer underlying the peat. When the actual thickness τ of the outcropping peat layer, at present equal about to 1 m at the experimental site, is reduced to less than $\tau^* = 0.40$ m, i.e the ploughing depth, the soil organic content η will decrease due to the mixing of the new mineral soil fraction supplied by ploughing and the ongoing oxidation. These effects are taken into account by introducing a corrective factor to equation (3.6) as follows:

$$s^*(T,h) = \begin{cases} s(T,h) \cdot \frac{\tau}{\tau^*} \cdot \left[1 - e^{-\eta/(\eta_0 - \eta)}\right] & \tau < \tau^* \\ s(T,h) & \tau \geq \tau^* \end{cases} \tag{3.7}$$

where η_0 is the initial organic matter content and η is the actual value of the organic content computed reducing η_0 according with the the peat layer thickness oxidation as:

$$\eta = \eta_0 \cdot \left[1 - \left(\frac{\tau^* - \tau}{\tau^*}\right) \cdot \frac{1}{\eta_0}\right] = \eta_0 - \frac{\tau^* - \tau}{\tau^*} \tag{3.8}$$

with $(1 - \eta_0)\,\tau^* < \tau < \tau^*$. Hence, when $\tau = (1 - \eta_0)\,\tau^*$ then $\eta = 0$. The complete disappearence of the peat organic fraction yields $s^* = 0$ in equation (3.7).

Equations (3.7) and (3.8) are used to investigate the reduction rate of the peat thickness at the Zennare Basin over the present century for different scenarios of climate conditions and hydraulic management (Table 3.2). For this task, we use the calibrated model with a yearly averaged water table depth h and a seasonally variable soil temperature according with the records collected in the field site as follows. We define as "reference year"(RY) the scenario that yields a 10 mm/a subsidence rate, corresponding

Table 3.2: Summary of the depth to the water table h and soil temperature T used in the simulated scenarios.

Scenario	Parameter	
	h (m)	T °C
reference year (RY)	0.5	20±15
H1	0.6	RY
H2	0.4	RY
H3	0.2	RY
T1	RY	RY+B1$_{\text{IPCC}}$
T2	RY	RY+A2$_{\text{IPCC}}$
T3	RY	29
HT	0.6	29+A2$_{\text{IPCC}}$

to the yearly average measured at the experimental site. This rate is obtained from the calibrated Stephens *et al.* [1984] model setting h=0.50 m and a seasonally variable temperature 20 ± 15°C, i.e. the average $\pm$ the maximum variation calculated for the 4 year measurements at the Zennare Basin. These values are considered as the base case for the subsequent investigation. We then construct three different scenarios (H1, H2 and H3) to address the influence of varying hydraulic management. Thus the scenarios are designed by changing the average h, a condition that can be enforced by properly adjusting the pumping schedules and using the RY temperature series. The three scenarios are: H1: dry conditions, $h = 0.6$ m; H2: wet conditions, $h = 0.4$ m; H3: extremely wet conditions, $h = 0.2$ m.

A second set of simulations is aimed at undestanding how the expected temperature rise due to climate change affects the bio-oxidation rate. In the last Synthesis Report written by the Intergovernmental Panel on Climate Change [IPCC, 2007], a number of projections of future climate conditions are provided on the basis on global forecasted GHG emission during the 21st century. Among the different scenarios considered by IPCC, we choose to use the two extreme scenarios of GHG emissions, namely B1 and A2 of the 2007 Synthesis Report. In scenario B1 a reduction of the GHG emissions starting from 2040 is expected. On the contrary, scenario A2 is characterized by an almost constant rate of increase of emissions during the entire century. The expected temperature rise at the end of the century in Europe will amount to 1.5°C and 3.5°C in cases B1 and A2, respectively. We translate these hypothesis by using our model with h=0.50 m together with a yearly temperature rise of 0.015°C/a (Scenario T1) and 0.035°C/a (Scenario T2) with respect to the RY base case.

Finally we address two worst-case scenarios. The first (Scenario T3) is characterized by

a 15 mm/a subsidence rate, i.e. the value measured at the experimental site during 2003. This settlement is obtained from the calibrated model with h=0.50 m and a constant average year temperature T=29°C. This value is consistent with the average temperature recorded in summer 2003 when a severe heat wave affected continental Europe from June to August causing summer temperatures from 20 to 30% higher than the seasonal average [Schär *et al.*, 2004]. In the last Scenario (HT), we combine the worst cases of the investigated h and T variability (see Table 3.2 for a summary of the different scenarios).

The predicted peatland subsidence evaluated for the different scenarios is shown in Figure 3.9 in comparison with the *RY* case. The curves show an almost linear trend in time, as long as the ploughing layer does not reach the underlying clay soil, above which a relatively small oscillation due to temperature fluctuations is superimposed.

The curves for all the scenarios except for the last two cases show an oscillatory decreasing trend in time, due to the inter-annual variability of the soil temperature. We remark the importance of considering seasonal temperature variations as its use results in a faster subsidence with respect to the constant temperature case. For example, in scenario *RY* the slope of the linear part of the curve is 9.4 mm/a whereas the same at constant temperature is 7.8 mm/a.

The exponentially decreasing soil organic content considered in Equation (3.8) is responsible for the decrease in subsidence rate at later times. The results show that in the reference scenario about 90% of the peat layer is expected to disappear in approximately 80 years from now.

The effects of changing management practices can be seen in the top panel (a) of Figure 3.9. Scenarios H1 and H2 can be viewed as a "confidence interval" of about ±20 years for the most probable scenario. On the other hand, scenario H3 shows that about 200 years would be needed to completely oxidize the peat when an average water depth of 0.20 m is enforced in the Basin. Thus, preservation of the agricultural land in the area would require careful management to keep water table as close as possible to the soil surface for most of the year, compatibly with agricultural practices.

The results from the scenarios T1 and T2 are compared to the base case in Figure 3.9b. As expected faster peat oxidation occurs with scenario T2, where a higher temperature increase is considered. However, the impact of temperature is not as important as the consequences of management of appropriate drainage depths. The reason for this can be attributed to the fact that bio-oxidizing bacteria are able to respire (even though may be not at maximum efficiency) in a wide range of temperature. This is confirmed in the experimental study reported in Camporese *et al.* [2008], who show only a slight

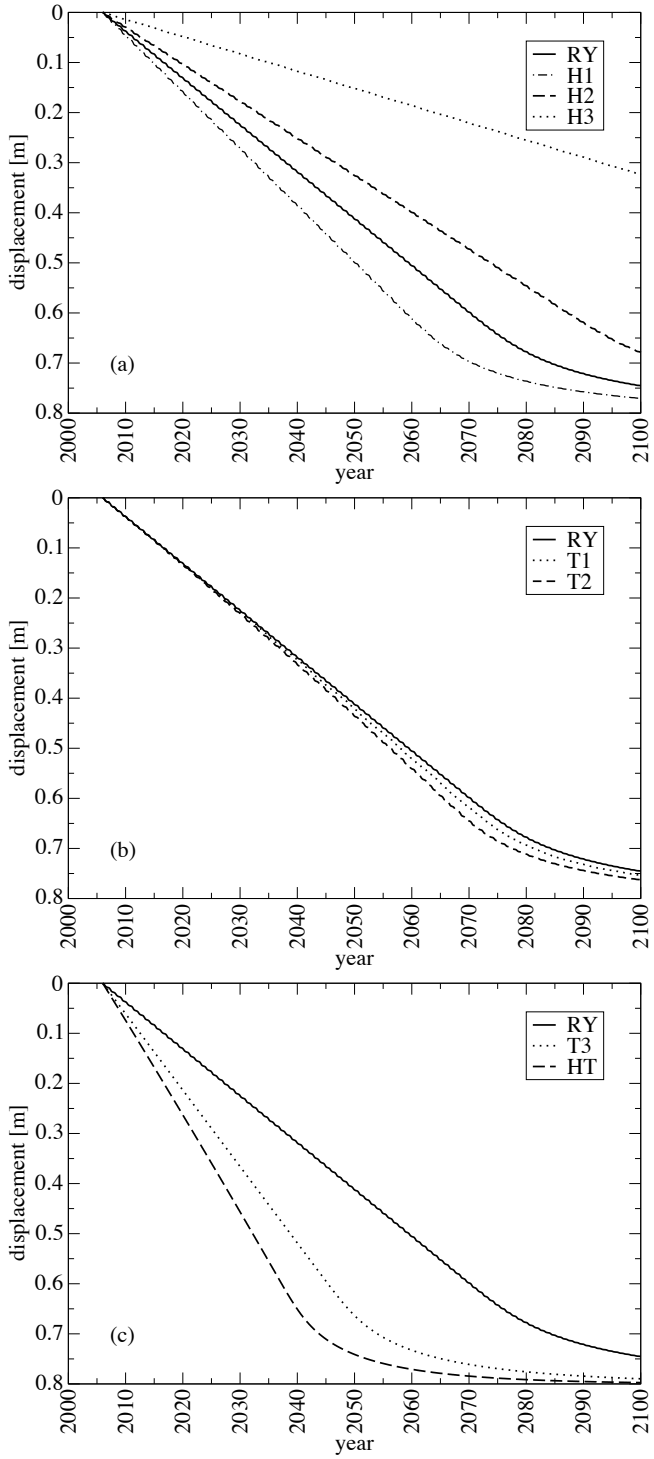

Figure 3.9: Expected land subsidence versus time (a) for the "reference year" RY and the H1, H2, and H3 scenarios, (b) for the "reference year" and the T1 and T2 scenarios, and (c) for the "reference year" and the T3 and HT scenarios.

increase in the values of the CO_2 fluxes, measured in the Zennare basin, at increasing soil temperatures.

Finally, Figure 3.9c shows that the peat thickness is reduced to 10% of the present value in only 50 and 40 years with the T3 and HT scenarios, respectively. In these cases the peatland would completely disappear much before the end of the century, showing the importance of changing current agricultural practices and hydraulic regimes, if the basin is to be considered as a valuable asset to the community.

3.7 Conclusions

We have analyzed soil surface displacement data coming from a field experiment carried out in a drained cultivated peatland in the southernmost part of the Venice Lagoon catchment, Italy. The experiment carried out from January 2002 to February 2006 has produced hourly measurements of the surface peat displacement and the main hydrological variables of interest. The land displacement has been found to be influenced by bio-chemical oxidation of the organic fraction causing irreversible subsidence, and reversible deformations in response to variations of soil water content in the unsaturated zone, and pore pressure changes in the saturated one. Hence, long term measurements are required to quantify the permanent land settlement when the latter is of the same order of magnitude as reversible displacements.

A novel two-step modeling approach is developed to separate the elastic and the irreversible components of the movement time series. We used first a peat swelling/shrinking model to simulate the deformations induced by the moisture content and pore pressure variations. The result of the simulation is then subtracted from the observed record of land displacement to estimate the long term settlement. Land subsidence rates range between 3 and 15 mm/a over the monitoring period.

The processed data are used to calibrate an empirical model of land subsidence due to bio-chemical oxidation of the peat oganic matter. In agreement with the observation that the biochemical activity is controlled by temperature and is limited by the absence of oxygen, the model estimates the subsidence rate using the depth of drainage and the soil temperature at 0.10 m depth. During the monitored period, drastically different climate conditions have been experienced in the area, thus providing the opportunity to calibrate the subsidence model in extreme hydrological regimes, with an extremely wet winter in 2002 and an exceptionally hot and dry summer in 2003.

The calibrated model is used to investigate some possible scenarios of expected peat-

land subsidence over the 21st century. The main results can be summarized as follows:

- the land subsidence rate is mainly controlled by the depth of drainage. An effort must be made to keep the water table depth as small as possible, consistently with agricultural crop requirements. Accurate planning and timely control of the drainage system and the pumping stations activity can be used to obtain this control;

- the influence of temperature on the subsidence process is less pronounced than the groundwater depth. Global warming due to the expected climatic changes is likely to impact only negligibly on the subsidence due to peat oxidation, at least in reclamation areas where the depth to the water table is kept under strict control independent of the precipitation regime. Larger consequences could be expected under extreme climatic events, such as heat waves, whose frequency and duration have been observed to increase during the second half of the 20th century [Frich *et al.*, 2002];

- the oxidation of the organic matter can be mitigated, at least partially, by appropriate agricultural practices. For example, conservative tilling as a substitute to ploughing may help decrease the exposure of unmineralized peat to atmosphere. Freibauer *et al.* [2004] estimate in 1.4×10^{-4} t C/m^{2}a the equivalent carbon sequestration that can be obtained by avoiding deep ploughing. Crop residue incorporation in place of removal might yield a carbon sequestration ranging from 0.1×10^{-4} t C/m^{2}a [Morari *et al.*, 2006] to 0.7×10^{-4} t C/m^{2}a [Freibauer *et al.*, 2004].

These observations must also be considered in the light of the buffer property that peatlands can exert worldwide in the global gas emission rates as they have been widely recognized as being important CO_2 sinks. Peatlands contain one third of the sequestered terrestrial carbon [Holden, 2005], and this fraction is in extreme danger of being released into the atmosphere by the consequences of agricultural practices and climate changes [Jungkunst and Fiedler, 2007; Wösten *et al.*, 2008].

Chapter 4

Hysteretical retention curves and peat elastic deformations

4.1 Introduction

An effective exploitation for horticultural practices and a conscious environmental management of peat soils require a deep understanding of the processes that control the water flow mainly in the unsaturated zone. In contrast with mineral soils, much less is known about hydraulic properties of organic soils in the vadose zone. Further uncertainty is introduced by the swelling/shrinkage behavior of organic soils in response to natural cycles of precipitation and evapotranspiration, that induce reversible displacement of the soil surface (mire-breathing). In 2002 a field experimental study has been carried out in the Zennare Basin, a drained peatland located at the southern margin of the Venice Lagoon, Italy [Gatti *et al.*, 2002; Fornasiero *et al.*, 2003; Teatini *et al.*, 2004; Gambolati *et al.*, 2005; Camporese *et al.*, 2006a,b; Gambolati *et al.*, 2006; Camporese *et al.*, 2008] to study the hydrology of these peculiar soils, the land subsidence due to the oxidation of the soil organic fraction [Camporese *et al.*, 2006a], and the daily/seasonal time-scale reversible deformation (swelling/shrinkage) related to soil moisture. To quantitatively predict the water movement through variably saturated soils, detailed knowledge of the hydraulic properties is needed. The relation between volumetric water content θ and the water pressure head h, as well as the dependency of unsaturated hydraulic conductivity K on θ must be specified before analytical or numerical models can accurately predict water flow during infiltration/evaporation, or drainage/imbibition. Unfortunately, because of hydraulic hysteresis, these relationships are not simple linear functions and show a great

deal of variation between wetting and drying cycles. In highly deformable soils, such as peats, variation of void ratio according to moisture content changes enhances the hydraulic hysteresis. Taking the shrinkage into consideration, peat soils show a substantial higher volumetric water content at ranges of high water tension [Schwärzel *et al.*, 2002]. The present chapter reports first the analyses of the main hydrological data, collected at the Zennare Basin field site in the last 7 months of activity. Afterwards, a study of the effect of including hysteresis in the description of the moisture retention curve in peat soils is presented. Two different approaches, one proposed by Haverkamp *et al.* [2002] and the other by Parker and Lenhard [1987] are discussed and used to reproduce the volumetric water content versus pressure head measurements collected in the field site. Finally, the coupling of the approach proposed by Parker and Lenhard [1987] with a model that describes the void index variation with saturation in peat soils [Camporese *et al.*, 2006a], allows us to effectively investigate the effect of considering the consequences of porous matrix reversible deformation on the moisture retention curve behavior.

4.2 Literature Review

After a brief review of basic concepts, taken mostly from Bear [1972], that underline the theory of simulataneous flow of two immiscible fluids in a porous medium, the phenomenon of capillary hysteresis is discussed and the main modeling approaches appeared in the literature are proposed. In particular, the models by Haverkamp *et al.* [2002] and Parker and Lenhard [1987] are described in detail. Finally, the modeling approach proposed by Camporese *et al.* [2006a] for the description of the porosity variation due to moisture content change in peat soils is presented.

4.2.1 Flow of immiscible fluids in porous media

Most natural soils and rocks contain a certain percentage of their volume of empty spaces, which may be occupied by water or other fluids, e.g. air. For a given representative elementary volume (*R.E.V.*), the *porosity* is an adimensional, scalar quantity $\phi(x, y, z)$ defined as the ratio:

$$\phi = \frac{\text{volume of voids within a REV}}{\text{bulk volume of REV}} \tag{4.1}$$

The value of porosity theoretically can range from 0 to 1, but generally it is never bigger than 0.45. In sedimentary basins the porosity generally decreases with depth, because of the higher degree of compaction. From the standpoint of flow through the porous

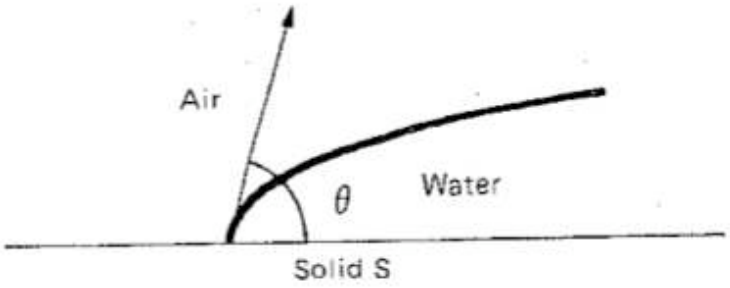

Figure 4.1: Interface between air, water and a solid.

medium, only *interconnected pores* are of interest, hence the concept of *effective porosity* is introduced as the ratio of the interconnected pores to the total volume of the medium. When the void space of the porous medium is filled by two or more immiscible fluids (liquids or gasses), the *saturation* (or *degree of saturation*) at a point, with respect to a particular fluid, is defined as the fraction of the void volume of the porous medium occupied by that particular fluid within a *REV* around the considered point. Here "point" is the microscopic point inside the void space.

$$S_\alpha = \frac{\text{volume of fluid } \alpha \text{ within a REV}}{\text{volume of voids within a REV}}; \quad \sum_{(\alpha)} S_\alpha = 1 \tag{4.2}$$

In the theory of unsaturated flow, the volumetric *water content* (or *moisture content*) is defined as:

$$\vartheta = \phi S_w = \frac{\text{volume of water within a REV}}{\text{bulk volume of REV}} \tag{4.3}$$

When a liquid is in contact with another substance (another liquid immiscible with the first, a gas or a solid), a free *interfacial energy* present between them develops. The interfacial energy arises from the difference between the inward direction of the molecules of each phase and those at the surface of contact. Since a surface possesing free energy contracts if it can do so, the free interfacial energy manifests itself as interfacial tension σ_{ik}, defined by the quantity of work needed to separate a surface of unit area of the substances i and k. The tension σ_{ik} is constant for two given substances, and varies only with the temperature. For two fluids in contact with each other, Young's equation gives the connecting angle of the interface, as in Figure 4.1:

$$\cos\theta = \frac{\sigma_{sa} - \sigma_{sw}}{\sigma_{aw}} \tag{4.4}$$

where the subscript sa stands for solid-air, sw for solid-water, and aw for air-water. There is no equilibrium possible if the ratio is larger than 1; in that case, one of the fluids (here,

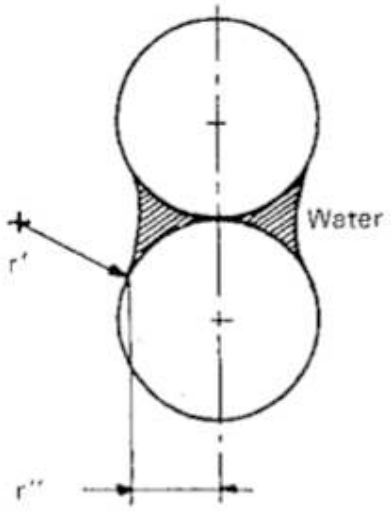

Figure 4.2: Air-water interface curvature

water) spreads indefinitely over the solid. If $\theta < 90°$, the fluid is said to be wetting. This is the case of the water here. If $\theta > 90°$, the fluid is said to be nonwetting. This is the case of air here. Interfacial tension and wettability may be different when a fluid-fluid interface (e.g., an air-water interface) is advancing or receding on a solid surface. This phenomenon is called hysteresis, and will be discussed in section 4.2.2. Within the fluids, on either side of the nonwetting - wetting fluids (e.g., air-water) interface the pressure is not the same. The pressure difference is called the *capillary pressure*:

$$p_c = p_{nw} - p_w \tag{4.5}$$

In the water-air system, water is the wetting phase and air is the non-wetting one. The unsaturated (air-water) flow is a special case of simultaneous flow of two immiscible fluids, where the nonwetting fluid (air) is assumed to be *stagnant*. If the air pressure is taken as a datum for measuring the pressure in the wetting fluid, i.e. $p_{nw} = 0$, we have from equation (4.5):

$$p_c = p_{nw} - pw = -p_w \tag{4.6}$$

where p_w denotes the pressure in the water immediately adjacent to the interface. If r is the mean radius of the interface curvature,

$$\frac{2}{r} = \frac{1}{r'} + \frac{1}{r''} \tag{4.7}$$

where r' and r'' are the principal curvature radii (Figure 4.2). Then the Laplace equation

gives the capillary pressure

$$p_c = \frac{2\sigma_{aw}}{r} \tag{4.8}$$

This pressure may be very high if the curvatures are small. In a capillary tube, interfacial tension causes the water to rise and to form a meniscus above the level of the tank. The height of this rise is a function of the radius and measures the capillary pressure accross the water-air interface in the tube.

In porous media the shape of the interface is very complex, and equations (4.5) through (4.7) have the meaning of a statistical average taken over the void space in the vicinity of a considered point in the porous medium. Because of the dependency of p_c locally (i.e., within each pore) on σ_{aw} and r, capillary pressure depends on the geometry of the void space, on the nature of solids and liquids in terms of the contact angle θ and on the degree of saturation S_w. In natural porous media, the geometry of the void space is extremely irregular and complex and cannot be described analytically. Several empirical and semi-empirical expressions have been derived in the literature to describe the relationship $p_c(S_w)$, two of the most widely used being the Brooks and Corey [1964] and the van Genuchten [1980]. The Brooks and Corey [1964] defined the moisture retention curve as:

$$S_e(\psi_c) = \begin{cases} (\psi_d/\psi_c)^{\zeta}, & \psi_c < \psi_d \\ 1 \quad \text{if } \psi_c \geq \psi_d \end{cases} \tag{4.9}$$

where:

ψ_d is the *threshold presure head*, i.e., the minimum pressure necessary in order to move the wetting phase (water) from the non-wetting one (air) in a completely saturated medium;

ζ is the *sorting factor*, also called the *pore distribution factor* that depends (as n) on the grain distrubution and generaly varies between 0.2 (very well sorted soil) to 7 (poorly sorted soil).

Similarly, the van Genuchten [1980] approach defines the effective saturation as:

$$S_e = \frac{S_w - S_{wr}}{1 - S_w} = (\psi) = \begin{cases} (1 + \alpha\psi)^{-m} & \text{if } 0\psi < 0 \\ 1 \quad \text{if } \psi \geq 0 \end{cases} \tag{4.10}$$

where:

S_{wr} is the residual water saturation;

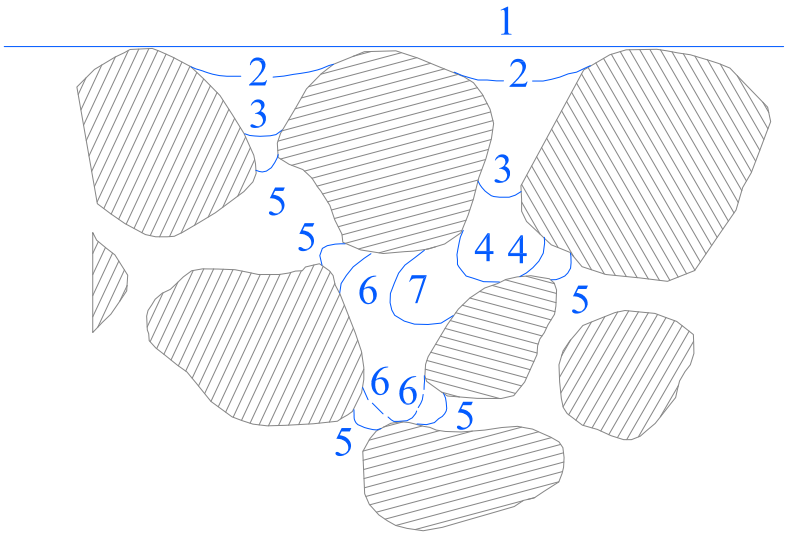

Figure 4.3: Drainage (1–5) and imbibition stages (6–7) [after Childs and Collis-George, 1950].

n is the *pore ditribution index* that depends on the pore distribution in the medium and genaraly is such that $1.25 < n < 6$;

$\psi_s = \alpha^{-1}$ is the *entry pressure head*;

$m = 1 - 1/n$.

The parameters of the moisture retention curve n and ψ_s for van Genuchten [1980], and ζ and ψ_d for Brooks and Corey [1964] depend on the type of soil and fluids that flow into it.

4.2.2 Moisture retention curve hysteresis

Hystersis in the moisture retention curve (MRC) has been detected for the first time by Haines [1930]. He observed that it is possible to have different values of moisture content corresponding to the same pressure head depending on the imbibition hystory experienced by the studied porous medium. He emphasized that also in an ideal porous medium the advancing/retreating of water can be strongly nonlinear, and can develope in a series of "jumps" as the wetting fluid proceeds from one pore to the other. Moreover, Haines [1930] stressed how the mechanism of generation of the hysteretic phenomenon is related to the imbibition/drainage processes that occur in the soil. A schematic representation at microscopic level of the soil porous matrix is shown in Figure 4.3. Several

different drainage stages are shown: the initial one is denoted by 1. As water is drained, interfaces (*meniscii*) are formed, stage 2. The radius of curvature of the interfaces depend on the suction. As water is drained and the interfaces are drawing further down, the curvature starts to increase as well as the suction (the negative value of the water pressure in the soil). At every stage, the greatest suction that can be maintained by the interface corresponds to the sharpest curvature that can take place in the channel through which the interface is being withdrawn. This happens in the narrowest part of the channel (e.g., meniscus 3). As drainage progresses, the interface retreats into channels which support a curvature of greater radius (equilibrium condition, e.g., interface 4). In general the pores have different size, hence they are not withdrawn by the same suction: the biggest (or with larger entry channels) are emptied before by lower suction values , whereas higher suction is necessary for those characterised by a smaller diameter. This implies that usually most of the water is retained inside the soil as a thin water veil and some isolated pores remain filled by water also for extremely high capillary pressure, generating an irreducible water content θ_r. If the process is reversed, i.e. the imbibition of the soil begins, the suction decreases. The process that occurs at microscopic scale is described in Figure 4.3 by the interfaces 6 and 7 that show curvature radii progressively smaller.

Macroscopically, the imbition moisture retention curve does not follow the same path that described the drainage process, as the hysteresis marks the process. The hysteresis effect can be attributed to the following main cause [e.g. Hillel, 1980; O'Kane *et al.*, 2004]:

the *ink-bottle effect*: results form the fact that as water reenters narrow channels, a local increase of suction is required. In the soil at this stage we have instability and the interface cannot advance until a neighboring pore is filled;

different spatial connectivity of pores during wettin and drying processes;

the *raindrop effect*: the contact angle at an advancing interface difffers from that at the receding one;

the entrapped air can be another source of hysteresis.

The hysteretical behaviour of the moisture retention curve is enhanced by strong flow reversals. For fine grained soils, such as peats, an additional factor causing and enhancing hysteresis is the swelling/shrinkage behavior following imbibtion/drainage [Bear, 1972]. Taking the shrinkage into consideration, peat soils show a substantial higher volumetric water content at ranges of high water pressure [Schwärzel *et al.*, 2002]. Figure 4.4 shows

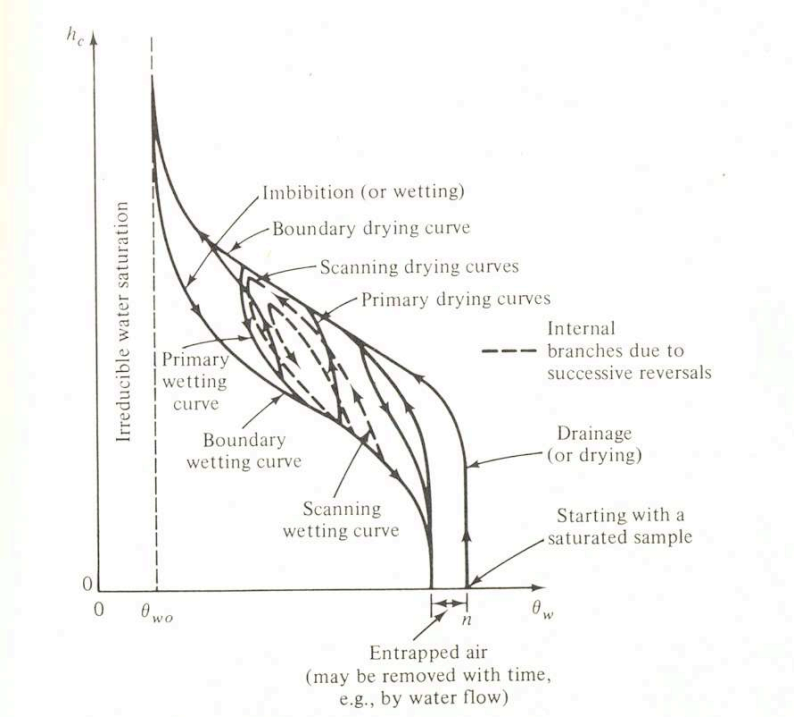

Figure 4.4: Hysteresis in moisture retention curve for a coarse material [after Bear, 1972]

hysteresis in the relationship moisture content versus capillary pressure $h_c = h_c(\theta_w)$. The drainage and imbibition curves form a closed loop. It is possible to start an imbibition process from any point on the drainage curve, leading to the dashed line, called *drying* and *wetting* scanning curves. In this way, the relationship between capillary pressure and saturation (expressed by the retention curve) depends also in the wetting-drying hystory of the particular sample under consideration. This phenomenon has been measured by several authors, [e.g. Morrow, 1965; Topp, 1969; Colonna *et al.*, 1972]. For a given capillary pressure, a higher saturation is obtained when a sample is drained than during imbibition. As long as there is no change of the porous medium, i.e., no consolidation occurs, the hysteresis loop can be repeatedly traced [Bear, 1972].

4.2.3 Capillary hysteresis models

Capillary hysteresis is often neglected in the description of flow and transport in the unsaturated zone partly because its effects are assumed to be negligible, especially under field conditions where it is often masked by heterogeneities and spatial variability, partly because of the lack of well-validated hysteretic models easy to be calibrated.

Nevertheless, many authors [e.g. van Genuchten and Biggar, 1986; Parker and Lenhard,

1987; Russo *et al.*, 1989; Heinen and Raats, 1997; Otten *et al.*, 1997; Si and Kachanoski, 2000] have shown that hysteresis is important in simulations of water transfer, solute transport, and multiphase flow, and that its disregard it leads to significant errors in predicted fluid distributions with concomitant effects on solute transport and contaminant concentrations [e.g. Gilham *et al.*, 1976; Hoa *et al.*, 1977; Kool and Parker, 1987; Kaluarachchi and Parker, 1987]. Theoretically, it should be possible to predict hysteresis from the first principles of thermodynamics [e.g. Hassanizadeh and Gray, 1990; Gray and Hassanizadeh, 1991]. Recently Wei and Dewoolkar [2006] proposed a thermodynamically consistent framework for modeling the hysteresis of capillarity in partially saturated porous media in which capillary hysteresis is viewed as an intrinsic dissipation mechanism, which can be characterized by a set of internal state variables. However, this problem remains largely unsolved, and our sketchy knowledge and understanding of the soil structure suggests that only a few soil models are related to this approach [Haverkamp *et al.*, 2002].

The different approaches that have been proposed in the literature to describe hysteresis in moisture retention curve can be divided into two main groups: conceptual and empirical models. The first group is based on the domain theory and the second group mainly relies on an analysis of MRC shape and properties.

The first group (*conceptual models*) is based on the independent domain theory developed by Néel [1942, 1943] and used by several authors [e.g. Everett and Whitton, 1952; Everett and Smith, 1954; Enderby, 1955]. This theory assigns soil water to domains and each domain wets at a characteristic water pressure h_w and dries at a water pressure h_d, regardless of the neighbouring domains. The first application of this theory into hysteresis models was done by Poulovassilis [1962] and by Topp and Miller [1966]. These two models need 4 branches for model calibration. Mualem [1973, 1974] models I and II, which are 2-branch models, and Mualem Universal Model [Mualem, 1977], which presents a universal relation between the main and drying curves using only one branch, also use the independent domain theory. Parlange [1976] has proposed a one branch model based on the same theory. Other authors have proposed modifications to the independent domain theory to take into account interactions between domains. Many models requiring more than two branches for calibration were developed [e.g. Poulovassilis and Childs, 1971; Topp, 1971; Mualem and Dagan, 1975]. The latest model developed by Mualem [1984] needs only two branches for calibration; this model uses a correction factor for water content variations calculated on the basis of the independent domain theory.

Empirical models are based on an analysis of the shape and properties of moisture

retention curve. These models use closed-formed empirical expressions to represent hysteresis curves [e.g. van Genuchten, 1980]. They are often developed for a specific soil type and can not be used for different types since their derivation is not based on a physical representation of hysteresis. Among these approaches can be recalled the scaling-down model proposed by Scott *et al.* [1983], the linear model conceived by Hanks *et al.* [1969], the interpolation approach developed by Dane and Wierenga [1975] Hoa *et al.* [1977], and Pickens and Gilham [1980], and the slope model developed by Jaynes [1984] and derived from Dane and Wierenga [1975] work. Recently other authors developed new approaches based on different concepts and assumptions. Bagagiolo and A.Visintin [2000] developed a mathematical framework of the flow in unsaturated porous media, demonstrating the existence and uniqueness of the solution, using the hysteresis operator as defined by Visintin [1993]. O'Kane *et al.* [2004] inserted the capillary hysteresis in the nonlinear systems theory, using the Preisach [1935] operator to describe the memory and delay effects induced by hysteresis and basing the model on the concept of a continuous analog of a finite parallel connection of relays. Haverkamp *et al.* [2002] applied a theoretical approach to derive parameters for a model based on the concept of ration extrapolation [Parlange, 1976] and on geometric scaling. This approach is discussed in detail afterwards. Another hysteresis empirical model was developed for sandy soil using the basic concept of shape similarity between the MRC and the cumulative particle-size distribution function (Haverkamp and Parlange 1986). In this case, the hysteresis is predicted from the basic properties of the soil, not from a moisture retention curve. A series of papers [Parker and Lenhard, 1987; Lenhard and Parker, 1987b; Lenhard *et al.*, 1989, 1991] presented a model for saturation - pressure relationships in rigid porous media systems containing up to three immiscible fluid phases. The model, which accounts for hysteresis and fluid entrapment effects, was formulated by proposing a single hysteretic scaled saturation-capillary head functional which describes water saturation versus air-water capillary head in two-phase systems and water saturation versus oil-water capillary head or total liquid saturation versus air-oil water capillary head in three-phase systems. Scaling of heads is obtained by a linear transformation and saturations are scaled by introducing the concept of apparent fluid saturations which include entrapped nonwetting fluid contents within those of the fluids under consideration. This approach is going to be discussed in detail.

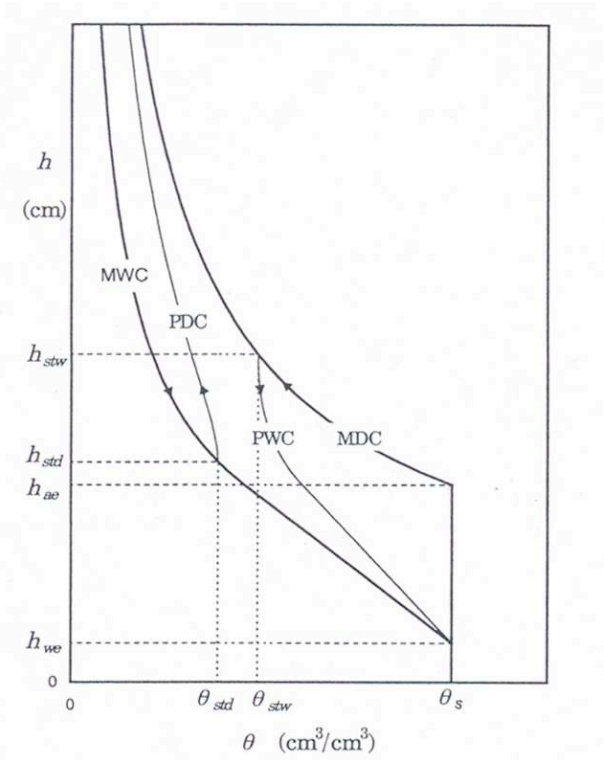

Figure 4.5: Schematic representation of moisture retention curve with hysteresis proposed by Haverkamp *et al.* [2002]. The Main Wetting Curve (MWC), the Main Driying one (MDC), a Primary Drying Curve (PDC), and a Primary Wetting Curve (PWC) with starting pointi (θ_{std}, h_{std}), and (θ_{stw}, h_{stw}), respectively, are represented.

Haverkamp hysteresis model

Parlange [1976] proposed a model based on the concept of *rational extrapolation*. This theory requires the knowledge of only one of the two curves that define the main hysteresis envelope to predict the other boundary and all the inner scanning curves in between. The basic equation proposed by Parlange [1976] to estimate the main drainage curve starting at a given soil water pressure condition h_{std} on the wetting curve, can be generalized to the differential equation:

$$\theta_d\left(h, h_{std}\right) = \theta_w\left(h\right) - \left[h - h_{std}\right] \frac{d\theta_w}{dh} \tag{4.11}$$

where the subscripts d and w refer to the drainage and imbibition phases, respectively. The subscript *std* indicates the pressure head h_{std} on the wetting branch from which the drying curve departs. Equation (4.11) is valid only if $\theta_d \leq \theta_{std}$ dove $\theta_{std} = \theta\left(h_{std}\right)$ (see Figure 4.5). The main drawback of the model proposed by Parlange [1976] is the requirement that the MDC does not have any inflection point, as shown in Figure 4.5

where the MDC is described by a modified Brooks and Corey [1964] relationship. The same inconvenience remains if the equation proposed by van Genuchten [1980] is used.

Haverkamp *et al.* [2002] developed a simple analytical hysteresis model that adopts the same functional form for all wetting and drying curves, e.g. the one proposed by van Genuchten [1980]. The theoretical basis is provided by the Parlange [1976] model, but instead of the differential equation (4.11) they use some simple geometricaly scaling conditions.

In order to obtain a simpler description of the Haverkamp *et al.* [2002] model, it is useful to rewrite relation (4.10) in term of moisture content:

$$\theta^* = \frac{\theta - \theta_r}{\theta_s - \theta_r} = \left[1 + \left(\frac{h}{h_g}\right)^n\right]^{-m} \tag{4.12}$$

where h_g, corresponding to the parameter ψ defined in equation (4.10), is the *scaling paramenter* for pressure, θ_r is the volumetric residual moisture content, whereas m and n are the two adimensional *shape parameters* of the relation $h - \theta$.

It is worth to focus on the meaning of θ_r: in general, this parameter is evaluated by fitting equation (4.12) on the measured $h(\theta)$ values. This procedure reduces the θ_r within the range of the available data and hence it gives questionable results when applied outside of that range. Under field conditions a soil rarely approaches a θ_r close to zero because small quantities of water are always retained by adsorptive forces an trapped in dead-end pores. This results in non-zero values of residual moisture content that depends not only upon soil structure, but also upon the initial conditions prior to wetting. In Haverkamp *et al.* [2002] approach, the value of θ_r evaluated from the wetting-drying hystory available besides to $h(\theta)$ measurements. data points. Haverkamp *et al.* [2002] assume that the main branches are characterized by $\theta_r = 0$, hence the scanning curves have non-null values. The approach is also valid when non-zero θ_r are used to mark the main drying and the main wetting curves. The model proposed by Haverkamp *et al.* [2002] is schematically represented in Figure 4.6. The main hysteresis envelope is delimited by the main drying (MDC) and wetting curve (MWC). If the wetting process is interrupted and reversed to drying at a pressure head h_{stpd} on the MWC, a primary drying curve (PDC) is followed. Analogously, a primary wetting curve (PWC) departs from the MDC at a pressure head h_{stpw} and finishes at moisture content θ_S. This implies that the variation of the air volume in the pore space during rewetting is neglected [Hopmans and Dane, 1986]. Any imbibition (or drainage) curve, e.g. a secondary wetting curve SWC, departs from a curve of a lower order, e.g. a primary drying curve PDC, at some pressure head (e.g., h_{stsw}) and rejoyns

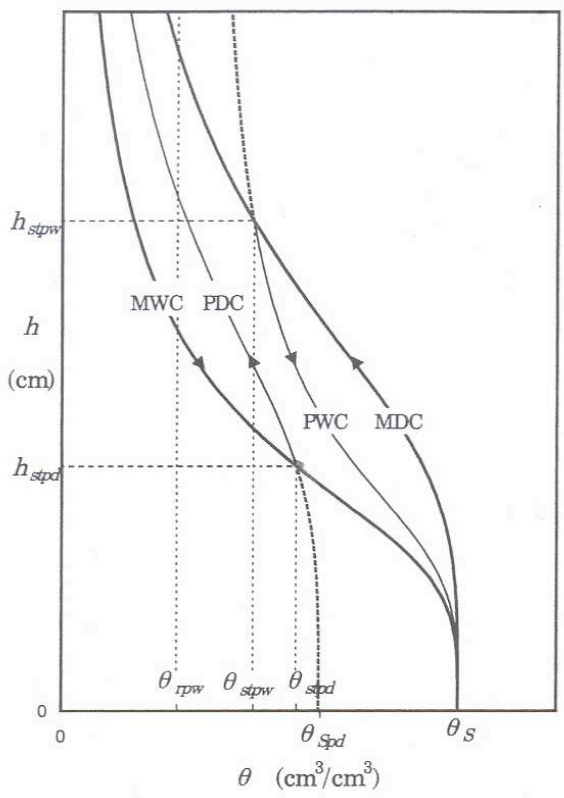

Figure 4.6: Schematic diagram of the hysteresis model with the main wetting curve (MWC), the main drying curve (MDC), a primary wetting curve (PWC) with starting point $(\theta_{stpd}, h_{stpd})$ and a primary wetting curve $(\theta_{stpw}, h_{stpw})$ [after Haverkamp *et al.*, 2002].

	SHAPE and SCALE Parameters	
Scanning order	Wetting	Drying
Main curves ($k=0$)	$m_{mw}, n_{mw}, \theta_S, h_{gmw}$	$m_{md}, n_{md}, \theta_S, h_{gmd}$
Primary curves ($k=1$)	$m_{pw}, n_{pw}, \theta_S, \theta_{rpw}, h_{gpw}$	$m_{pd}, n_{pd}, \theta_{Spd}, h_{gpd}$
Secondary curves ($k=2$)	$m_{sw}, n_{sw}, \theta_{Ssw}, \theta_{rsw}, h_{gsw}$	$m_{sd}, n_{sd}, \theta_{Ssd}, \theta_{rsd}, h_{gsd}$
Tertiary curves ($k=3$)	$m_{tw}, n_{tw}, \theta_{Stw}, \theta_{rtw}, h_{gtw}$	$m_{td}, n_{td}, \theta_{Std}, \theta_{rtd}, h_{gtd}$
Quarternary curves ($k=4$)	$m_{qw}, n_{qw}, \theta_{Sqw}, \theta_{rqw}, h_{gqw}$	$m_{qd}, n_{qd}, \theta_{Sqd}, \theta_{rqd}, h_{gqd}$

Table 4.1: Specific notation of the parameters used to describe the main curves and the scanning paths for both wetting and drying processes. Parameter k designates the scanning order [after Haverkamp *et al.*, 2002].

it at the point where the previuos wetting (or drying) process was truncated, e.g. at the point $(\theta_{stpd}, h_{stpd})$ where the PDC departed from its wetting parent MWC.

The main hypothesis Haverkamp *et al.* [2002] model is based on is that all the scanning paths, independently on their order, have the form of the normalized van Genuchten [1980] retention function (4.12), i.e. they have *shape similarity*. Each path is characterized by its specific shape parameters n and m, pressure head scale parameter h_g, and water content scale parameters θ_r and/or θ_S depending upon the starting and end points of the curves. For instance, the PDC that departs from the MWC at $(\theta_{stpd}, h_{stpd})$ ends in $\theta_{rpd} = 0$. It might be extended over the MWC towards the θ axis (Figure 4.6, dashed line). If $h = 0$, then $\theta = \theta_{Spd}$, that is completely determined by the starting point θ_{stpd} from which the PDC departed. Although the physical meaning of θ_{Spd} is quite vague, the mathematical one is well defined. Similarly, is is possible to define the residual moisture content of the inner scannig curves, i.e. for $h \to \infty$ and for $\theta \to \theta_r$. In particular for the PWC $\theta_r = \theta_{rpw}$ although it is out of the main hysteresis loop. The whole set of shape parameters used to describe the scanning curves are reported in table 4.1. To simplify the description of the formulation, a reduction of the number of the parameters is introduced. As the arrows in table 4.1 show, two types of relations exist: one relates the parameters of the scanning curves of the same order that belong to different "families" (e.g., a main draying

and wetting curve), the other connects the parameters of the paths that belong to the same family but have different order (e.g., the main drying curve and the primary drying one). Haverkamp *et al.* [2002] verified that in order to keep the validity of Parlange [1976] theory (i.e. the rational extrapolation), the fact that the MWC and the MDC have the same shape, i.e. the same value of the product mn, is required. Therefore the relations that describe the paths of any order collapse to a unique adimensional expression, that is:

$$\theta^*_{kw} = \frac{\theta_{kw} - \theta_{rkw}}{\theta_{Skw} - \theta_{rkw}} = \left[1 + \left(\frac{h}{h_{gkw}}\right)^n\right]^{-m} \tag{4.13}$$

for wetting paths, and:

$$\theta^*_{kd} = \frac{\theta_{kd} - \theta_{rkd}}{\theta_{Skd} - \theta_{rkd}} = \left[1 + \left(\frac{h}{h_{gkd}}\right)^n\right]^{-m} \tag{4.14}$$

for drying ones. The pressure scale parameters are specific for each curve and are defined as a function of the shape parameter mn and according with the family (imbibition or drainage) the path belongs to. For the wetting curves the relation adopted is:

$$h_{gkw} = h_{gmw}\left[\frac{\theta_S}{\theta_{Skw} - \theta_{rkw}}\right]^{1/mn} \tag{4.15}$$

and for the drying paths:

$$h_{gkd} = h_{gmd}\left[\frac{\theta_S}{\theta_{Skd} - \theta_{rkd}}\right]^{1/mn} \tag{4.16}$$

The connection between equation (4.15) and (4.16) is given by:

$$h_{gmd} = \xi h_{gmw} \tag{4.17}$$

where ξ is the pressure head scale ratio which depends upon the value of mn:

$$\xi = \begin{cases} (1+mn)^{1/mn} & \text{if } 0 < mn \leq 1 \\ 2 & \text{if } mn > 1 \end{cases} \tag{4.18}$$

The moisture content scale parameters for scanning curves of order higher than one are determined using the scaling relations given the corresponding main branch and the starting (h_1, θ_1) and ending (h_2, θ_2) points specific for each curve. The general expressions are

$$[\theta_{Skw} - \theta_{rkw}] = \frac{\left[\theta_{(k-1)d}(h_1) - \theta_{(k-1)d}(h_2)\right]}{\left[\theta^*_{kw}(h_1) - \theta^*_{kw}(h_2)\right]} \tag{4.19}$$

$$\theta_{rkw} = \frac{\left[\theta_{(k-1)d}(h_2)\,\theta^*_{kw}(h_1) - \theta_{(k-1)d}(h_1)\,\theta^*_{kw}(h_2)\right]}{\left[\theta^*_{kw}(h_1) - \theta^*_{kw}(h_2)\right]} \tag{4.20}$$

valid for the wetting and drying paths, respectively, where:

$$\theta^*_{kw}(h_1) = \left[1 + \xi^n \left(\frac{\theta_{Skw} - \theta_{rkw}}{\theta_{S(k-1)d} - \theta_{r(k-1)d}}\right)^{1/mn} \left(\frac{h_1}{h_{g(k-1)d}}\right)^n\right]^{-m} \tag{4.21}$$

and

$$\theta^*_{kw}(h_2) = \left[1 + \xi^n \left(\frac{\theta_{Skw} - \theta_{rkw}}{\theta_{S(k-1)d} - \theta_{r(k-1)d}}\right)^{1/mn} \left(\frac{h_2}{h_{g(k-1)d}}\right)^n\right]^{-m} \tag{4.22}$$

The procedure used to define the residual moisture content θ_{rkw} associated to the current scanning curve of order k consists in calculating the difference $[\theta_{Skw} - \theta_{rkw}]$ after the determination of the value $\theta^*_{kw}(h_1)$ and $\theta^*_{kw}(h_1)$ through equations (4.21) and (4.22) in which the parameters of the scanning curves of order $k-1$ are known. The so-calculated moisture content in saturated conditions is used to evaluate θ_{rkw} through the relation (4.20).

For the drying curves the following relations exist:

$$[\theta_{Skd} - \theta_{rkd}] = \frac{\left[\theta_{(k-1)w}(h_1) - \theta_{(k-1)w}(h_2)\right]}{\left[\theta^*_{kd}(h_1) - \theta^*_{kd}(h_2)\right]} \tag{4.23}$$

and

$$\theta_{rkd} = \frac{\left[\theta_{(k-1)w}(h_2)\,\theta^*_{kd}(h_1) - \theta_{(k-1)w}(h_1)\,\theta^*_{kd}(h_2)\right]}{\left[\theta^*_{kd}(h_1) - \theta^*_{kd}(h_2)\right]} \tag{4.24}$$

where:

$$\theta^*_{kd}(h_1) = \left[1 + \xi^{-n} \left(\frac{\theta_{Skd} - \theta_{rkd}}{\theta_{S(k-1)w} - \theta_{r(k-1)w}}\right)^{1/mn} \left(\frac{h_1}{h_{g(k-1)w}}\right)^n\right]^{-m} \tag{4.25}$$

$$\theta^*_{kd}(h_2) = \left[1 + \xi^{-n} \left(\frac{\theta_{Skd} - \theta_{rkd}}{\theta_{S(k-1)w} - \theta_{r(k-1)w}}\right)^{1/mn} \left(\frac{h_2}{h_{g(k-1)w}}\right)^n\right]^{-m} \tag{4.26}$$

from which it is possible to determine the moisture content scaling parameters value with a procedure similar to the one followed for the wetting paths.

Lenhard hysteresis model

Parker and Lenhard [1987] conceived a theoretical modeling approach for two or three-phase porous media systems subjected to arbitrary saturation paths. Non-wetting phase entrapment, hysteretic behaviour induced by different contact angles associated with imbibition and drainage processes and by irregular pore geometry are all taken into account by the model. The approach is based on the hypothesis that entrapped non-wetting fluid is discontinuous and immobile while the wetting fluid phase is always continuous and discrete pendula rings are interconnected by thin fluid films. Parker and Lenhard [1987]

introduce the concept of *apparent saturation* instead of actual or effective saturations to account for fluid entrapment effects. An apparent saturation S_w^* is defined as the sum of *effective saturation* of a continuous fluid phase (water) $\bar{S}_w$ and the effective saturations of entrapped air phase $\bar{S}_{at}$:

$$S_w^* = \bar{S}_w + \bar{S}_{at} \tag{4.27}$$

Water effective saturation is defined as:

$$\bar{S}_w = \frac{S_w - S_{wm}}{S_{ws} - S_{wm}} \tag{4.28}$$

where S_w is the *actual water saturation*, S_{ws} is the water saturation in condition of completely saturated soil, and S_{wm} is called *irreducible water saturation* that is defined in the model as the volume of wetting fluid when the water relative permeability approaches zero during drainage processes. This irreducible saturation is different from the *residual saturation* that is the volume of air when the non-wetting fluid relative permeability approaches zero during imbibition processes.

Fluids with lower wettability for solid surface can become entrapped by those with greater wettability. For example, in a two-phase fluid system air can be trapped by advancing air-water intefaces in flow channels larger than $\theta = \theta_r$ Such a small saturation value, called *historic minimum apparent water saturation*, is associated to the main drying saturation pressure path. It is supposed that, during the process described by that path, no fluid entrappement occurs, i.e. $\bar{S}_{at} = 0$, hence $S_w^* = \bar{S}_w$. All the other scanning curves show some entrapped non-wetting fluid, hence the apparent water saturation is greater than the effective saturation for the same capillary pressure. Therefore, the amount of entrapped air in a two-phase system is supposed to be zero at the historic minimum apparent water saturation and at the maximum when the porous medium is at a zero capillary pressure on an imbibition path. Every time the Main Drainage Curve is followed, ${}^{\Delta_{MDC}}\bar{S}_w$ has to be updated. The main assumption on which equation (4.30) is based, is that the more space is occupied by the non-wetting fluid during water drainage, the larger the amount of entrapped non-wetting fluid will be after the first reversal. This hypothesis implies that the maximum value of $\bar{S}_{at}$ corresponds to the main wetting curve. The amount of entrapped air is supposed to vary linearly between zero, at the reversal, to $\bar{S}_{ar}$ since Land [1968] assumes that the non-wetting fluid will be entrapped in proportion to pore volume:

$$\bar{S}_{ar} = \frac{1 - {}^{\Delta}\bar{S}_w}{1 + R \cdot \left(1 - {}^{\Delta}\bar{S}_w\right)} \tag{4.29}$$

The *maximum entrapped air saturation*, which corresponds to an imbibition path starting with a reversal point at an apparent saturation ${}^{\Delta_{MDC}}\bar{S}_w$ from the main drying branch is estimated by the algorithm proposed by Land [1968]:

$$\bar{S}_{at} = \bar{S}_{ar} \cdot \frac{S_w^* - {}^{\Delta_{MDC}}\bar{S}_w}{1 - {}^{\Delta}\bar{S}_w} \tag{4.30}$$

where:

$$R = \frac{1}{{}^{MWC}\bar{S}_{ar}} - 1 \tag{4.31}$$

To take into account raindrop and ink bottle effects, Lenhard and Parker [1987a] proposed to describe the main drainage saturation–pressure relations by the van Genuchten [1980] retention functions, according with [Parker and Lenhard, 1987]. The main imbibition relations are also described by the van Genuchten [1980] function, but the shape parameter ${}^{I}\alpha$ used is halved with respect to the one used for the main drainage path ${}^{D}\alpha$. The remaining parameters, i.e. n and $m = 1 - 1/n$ are the same for both branches and are assumed to be constant. Therefore, the main drainage and imbibition apparent saturation - capillary pressure relations are described by:

$${}^{p}S^*(h^*) = \begin{cases} \left[1 + ({}^{p}\alpha \cdot h^*)^n\right]^{-m} & \psi < 0 \\ 1 & \psi \geq 0 \end{cases} \tag{4.32}$$

where $p = D, I$ identifies the type of process occuring, i.e. drainage or imbibition. $h^* = \beta_{aw} h_{aw}$ is a scaled capillary head defined on a water-height equivalent basis where and $h_{aw} = (P_a - P_w) / (g\rho_w)$ with P_a and P_w the air and water pressure, respectively, ρ_w is the aqueous phase mass density, and g the gravitational acceleration. The fluid-pair dependent scaling paramenter β_{aw} may be estimated from fluid interfacial tensions, and for the pair air–water is assumed equal to 1 [Parker *et al.*, 1987]. To describe the relation between apparent saturation and capillary head for internal scanning curves, Lenhard and Parker [1987a] assume that the scanning paths have the same general shape of the corresponign main curves. More precisely, for the prediction of the internal scanning curves in the $S^*(h^*)$ relation the drying and wetting internal paths are scaled from the main drying and the main wetting curve, respectively, [Scott *et al.*, 1983], enforcing the passage through the most recent reversal point $\left[{}^{\Delta}h_j^*, {}^{\Delta}S_j^*\right]$ and the previous one $\left[{}^{\Delta}h_{j-1}^*, {}^{\Delta}S_{j-1}^*\right]$ (i.e. not including the pumping effect [Jaynes, 1984]):

$$S^*(h^*) = \frac{\left[{}^{p}S^*(h^*) - {}^{p}S^*\left({}^{\Delta}h_{j-1}^*\right)\right] \cdot \left[{}^{\Delta}S_j^* - {}^{\Delta}S_{j-1}^*\right]}{{}^{p}S^*\left({}^{\Delta}h_j^*\right) - {}^{p}S^*\left({}^{\Delta}h_{j-1}^*\right)} + {}^{\Delta}S_{j-1}^* \tag{4.33}$$

where j indicates the order of the current scanning curve, $p = D$ for odd j values, i.e. for drying scannig curves, and $p = I$ for even j values, i.e. for wetting curves. ${}^{p}S^*(h^*)$,

${}^{p}S^{*}\left({}^{\Delta}h^{*}_{j-1}\right)$ and ${}^{p}S^{*}\left({}^{\Delta}h^{*}_{j}\right)$ are apparent saturations of the main branch that correspond to current scaled capillary head, last and previous reversal points, respectively. Therefore, only the main curves has to be parametrize in order to describe the whole evolution of the $S^{*} - P$ relation. In Figure 4.7(a) wetting fluid apparent saturation - capillary head relation is shown in terms of apparent saturation. The main drying and wetting curves, a primary drying curve and a secondary wetting one are displayed together with the relevant terminology and corresponding curves indices. The corresponding effective saturation-capillary head and actual saturation-capillary head relations are shown in Figure 4.7(b) and (c), respectively. It is worth to note that the main branches close at capillary pressure equal to zero if the apparent saturation is considered, whereas when the effective and actual $S - P$ relations are modeled the paths do not close. The three paths are shown together in Figure 4.7(d).

4.2.4 Peat Swelling/Shrinkage

Peatlands respond to natural hydrologic cycles of precipitation and evapotranspiration with reversible deformations due to variations of water content in both the unsaturated and saturated zone. This phenomenon results in short-term vertical displacements of the soil surface that superimpose to the irreversible long-term subsidence typically occurring in drained cropped peatlands because of bio-oxidation of the organic matter. The yearly sinking rates due to the irreversible process are usually comparable with the short-term deformation (swelling/shrinkage) and the latter must be evaluated to achieve a thorough understanding of the whole phenomenon.

Several different approaches has been described in the last decade in order to describe the peat swelling/shrinkage [Pyatt and John, 1989; Price, 2003; Oleszczuk *et al.*, 2003; Hendriks, 2004; Kennedy and Price, 2004, 2005]. As already reported in section 2.1, some of them are empirically based, whereas others start from well-defined physical processes and need several physically based and empirical parameters to be defined through in situ and laboratory tests. Starting from the approach of Pyatt and John [1989], valid only for saturated conditions, Camporese *et al.* [2006a] developed a two-parameter constitutive model that relates the short-term reversible dynamics of the peat surface to the hydrologic characteristics of the unsaturated zone by means of a constitutive relationship relating volume variations, expressed in terms of void index, to moisture content changes.

The peat soil moisture is linked to the void ratio, which in turn affects the thickness of the peat layer. Porosity evolution calculated from the flow equation solution allows for the

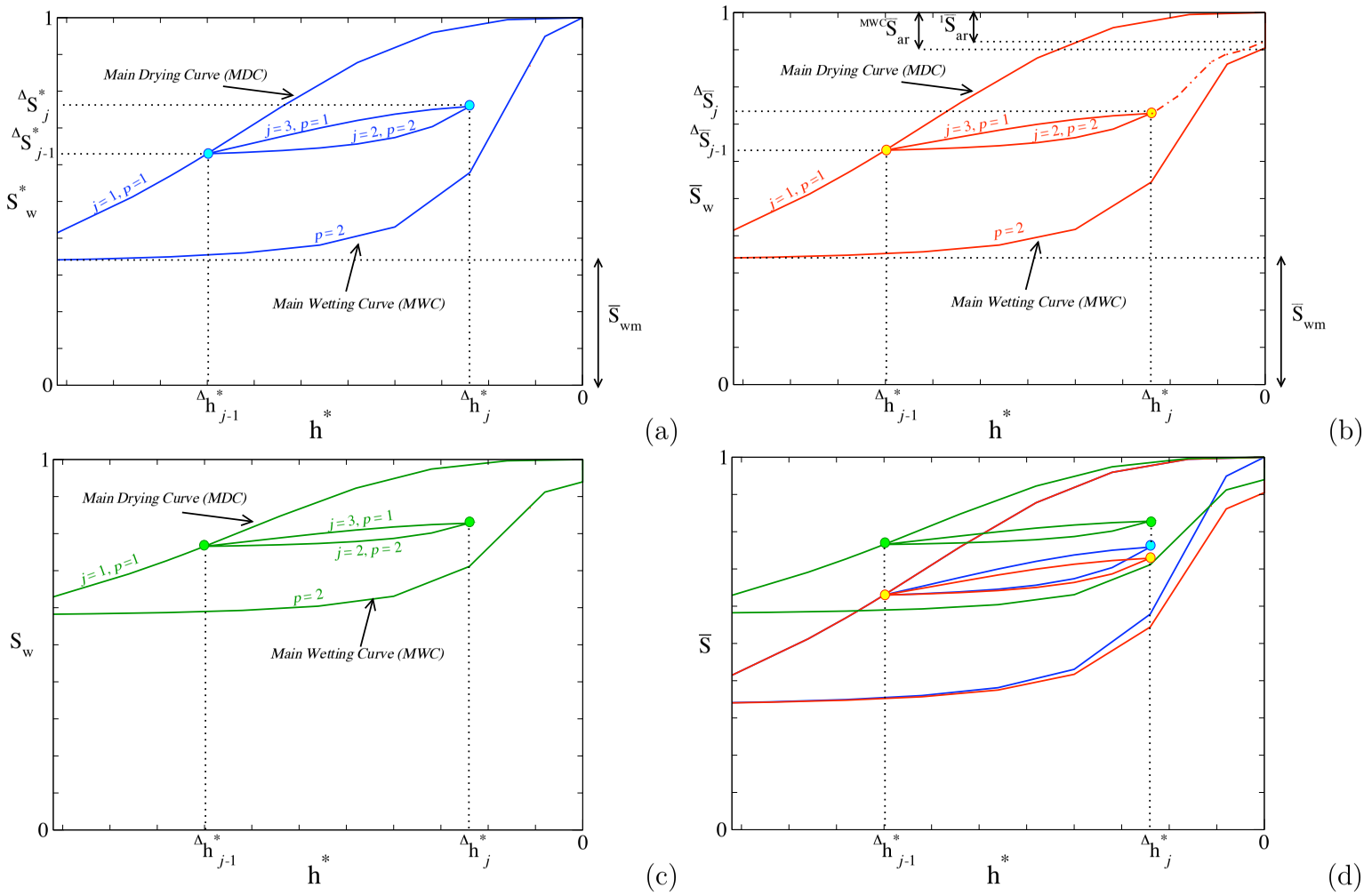

Figure 4.7: Apparent saturation S_w^* - capillary pressure relation showing main drainage and imbibition branches and a scanning path scenario. (b) Corresponding $\bar{S}_w$ effective water saturation - capillary pressure and (c) actual saturation S_w scanning path scenario. (d) Superimposition of the paths expressed in terms of apparent saturation (blue line), effective saturation (red line), and actual saturation (green line).

determination of the soil surface displacements, these being the integral of deformations over the total thickness of the aquifer.

Swelling/shrinkage of peat is described by constitutive relationships relating volume variations to moisture content changes. A volume V of peat is considered, expressed as $V = V_s + V_v$, where V_s is the volume of the solid fraction and V_v the volume of the voids. The voids can be partially or totally filled by water, and hence the water volume fraction V_w can be smaller or at most equal to V_v. Let e be the void ratio, defined as V_v/V_s, and ϑ the moisture ratio, equal to V_w/V_s and linked to the volumetric water content $\theta = V_w/V$ by the function $\vartheta = \theta(1 + e)$.

The voids can be partially or totally filled by water, and hence the water volume fraction V_w can be smaller or at most equal to V_v. The mass of the solid and water fractions are denoted by M_s and M_w, respectively. Experimental results reported by Pyatt and John [1989] show that, during drainage, the volume of a saturated cube of peat ($V_w = V_v$) decreases linearly with water content. The specific volume ($v = V/M_s$) can be expressed as $v(\Theta) = \Theta v_w + v_s$, where $\Theta = M_w/M_s$ is the gravimetric water content, $v_w = V_w/M_w$ is the specific volume of water, and $v_s = V_s/M_s$ is the specific volume of solids. The relationship $v(\Theta)$ is known as the *saturation line*. According to Pyatt and John [1989], in these conditions shrinkage occurs in two stages. One-dimensional vertical displacements take place for a gravimetric water content above a threshold value Θ_0 (stage 1). Below this value, cracks appear in the soil and a fully three-dimensional isotropic deformation pattern is considered (stage 2). Note that, also in the second stage, peat is saturated and air is present in the soil only inside the cracks, but not in the pores. To exemplify this situation, assume that a peat volume of initial height ℓ_i is characterized by a gravimetric water content Θ_i, and is subject to drainage. During stage 1, the peat shrinks vertically in the same proportion as the specific volume decreases along the saturation line. Thus, denoting by Θ the current water content, we can write:

$$\frac{\ell}{\ell_i} = \frac{v}{v_i} = \frac{\Theta v_w + v_s}{\Theta_i v_w + v_s} \quad \text{for } \Theta_0 \leq \Theta \leq \Theta_i, \tag{4.34}$$

where ℓ is the vertical height of the current volume. At the inception of cracks, deformations become isotropic, i.e., identical in the three directions of the reference system, and a cube of initial volume ℓ_0^3 will shrink to ℓ^3 following the relationship:

$$\left(\frac{\ell}{\ell_0}\right)^3 = \frac{v}{v_0} = \frac{\Theta v_w + v_s}{\Theta_0 v_w + v_s} \quad \text{for } 0 \leq \Theta \leq \Theta_0. \tag{4.35}$$

Up to here just the model by Pyatt and John [1989] has been described. In more general conditions peat may be partially saturated, anisotropic three-dimensional de-

formations may occur, and the above equations cannot be used. Following the development proposed by Bronswijk [1990] for clay soils, we may postulate that the peat volume shrinks following a general behavior between the particular cases given by equations (4.34) and (4.35). These general conditions are characterized by a gravimetric water content smaller than the threshold value, i.e., $\Theta < \Theta_0$. In this situation, three-dimensional anisotropic deformations need to be taken into account. To this aim, let ℓ' be the horizontal dimension of a peat volume after shrinkage, equal to the vertical dimension ℓ only in the isotropic case. Horizontal and vertical relative displacements of this volume may be imagined as related by a power law function, $(\ell'/\ell_0) = (\ell/\ell_0)^\gamma$, which can describe the whole physically admittable space of deformation behavior. Consequently, the following expression arises:

$$\left(\frac{\ell'}{\ell_0}\right)^2 \frac{\ell}{\ell_0} = \left(\frac{\ell}{\ell_0}\right)^{2\gamma+1} = \frac{v}{v_0} = \frac{\Theta v_w + v_s}{\Theta_0 v_w + v_s}, \tag{4.36}$$

with γ a non-negative dimensionless parameter. The shrinkage geometry factor r_s of Bronswijk [1990] and Oleszczuk *et al.* [2003] is recovered as $r_s = 2\gamma + 1$. For $\gamma = 1$ the isotropic case is considered and $r_s = 3$. For $\gamma = 0$, $r_s = 1$ and $\ell' = \ell_0 = const$, taking into account only one-dimensional vertical displacements. A value of $\gamma > 1$ ($r_s > 3$) corresponds to an event in which significant cracks form [Pyatt and John, 1989; Oleszczuk *et al.*, 2003]. Values of r_s ranging between 1 and 3 identify a process of three-dimensional anisotropic soil deformation not included in the model of Pyatt and John [1989], in which subsidence is predominant.

Since an aquifer system within a peatland can be idealized as a sequence of layers, a volume contained in one of these layers is then considered. As already mentioned, in their original model Pyatt and John [1989] take into account peat cubes that remain always saturated, and air can enter the soil only through the cracks. In order to extend the approach of equation (4.36) to unsaturated conditions, the idealization of a continuous porous medium must be used, so that a relationship between the specific volume and the gravimetric water content of the peat layers can be defined for each point of the considered aquifer. The continuum hypothesis is verified only if no cracks develop. Here we assume that vertical deformations prevail over the horizontal ones and that no or negligible small cracks occur, i.e., $0 \leq \gamma \leq 1$ or equivalently $1 \leq r_s \leq 3$, a situation which has already been verified in cropped peatlands [Camporese *et al.*, 2004]. In other words, it is assumed that the air partially fills the soil pores, so that the relevant quantities, such as void ratio, moisture ratio, specific volume, and water content, can be defined as continuous variables by appropriate spatial averages, according to a consolidated procedure of subsur-

face hydrology [De Marsily, 1986; Dagan, 1989]. In fact, when a peat volume undergoing three-dimensional anisotropic stresses is considered to be inserted in a soil layer, symmetry considerations suggest that horizontal displacements are prevented, provided that other effects, such as for example dynamics of biogenic gas bubbles [Glaser *et al.*, 2004; Kellner *et al.*, 2005], do not occur. As a matter of fact, it is generally agreed that field volume change, macroscopically, is constrained to the vertical. This approach, however, accepts three-dimensional volume change of soil structural units, whose behavior may be described by a representative average vertical displacement, as discussed by Smiles [2000]. The horizontal component of the deformation must then translate into a pore structure rearrangement, causing a variation of the void ratio. The value of Θ_0 can now be considered as the threshold value below which relationship (4.34) ceases to be valid, and not as the limiting value for which manifest cracks occur. Thus, the void ratio becomes a function of water content. Indicating with v^* the volume in the peat layer, expressed as:

$$v^* = \frac{\ell \ell_0^2}{M_s}, \tag{4.37}$$

and using equation (4.36), we obtain:

$$v^* = (\Theta_0 v_w + v_s)^{1-\delta} (\Theta v_w + v_s)^{\delta}, \tag{4.38}$$

where $\delta = 1/(2\gamma + 1) = 1/r_s$. Note that similar concepts have been first formulated by Philip [1969], whose theoretical analysis on swelling soils applies on an appropriate scale also to cracking soils, so long as pressure head, hydraulic conductivity and void ratio can be defined as functions of water content, crack volume counting as void space in the definition of void ratio.

The final version of the proposed model is obtained by reformulating equation (4.38) in terms of volumetric quantities. To this aim, the specific volume inside a layer can be expressed as a function of the void ratio:

$$v^* = v_s(1 + e), \tag{4.39}$$

and the gravimetric moisture content can be defined as a function of the moisture ratio $\vartheta = V_w/V_s$:

$$\Theta = \frac{\vartheta v_s}{v_w}. \tag{4.40}$$

Substituting v^* and Θ in equation (4.38) the shrinkage characteristic curve of the peat can be written as:

$$e = (\vartheta_0 + 1)^{1-\delta} (\vartheta + 1)^{\delta} - 1, \tag{4.41}$$

where ϑ_0 is the moisture ratio corresponding to the threshold gravimetric water content Θ_0. For $\delta = 1$, the proposed model collapses onto the saturation line $e = \vartheta$, written in terms of volumetric quantities. For values $\delta \neq 1$ the intersection between equation (4.41) and the saturation line occurs at $\vartheta = \vartheta_0$. When the moisture ratio is greater than the threshold value ϑ_0 and $\delta \neq 1$ the shrinkage curve lies below the saturation line. This situation has no physical meaning as it would yield $V_v < V_w$. Thus, equation (4.41) must be considered valid only for $\vartheta \leq \vartheta_0$. Note that laboratory evidence [Pyatt and John, 1989] show that, for large moisture ratios and saturated soil, the swelling/shrinkage line follows the saturation line, corresponding to a stage 1 behavior ($\delta = 1$), as described by equation (4.34). According to the previous interpretation of Θ_0, the threshold moisture ratio ϑ_0 can then be defined as the value above which peat is totally saturated. The final model can then be written as:

$$e = \begin{cases} (\vartheta_0 + 1)^{1-\delta}(\vartheta + 1)^{\delta} - 1 & \vartheta \leq \vartheta_0 \\ \vartheta & \vartheta > \vartheta_0 \end{cases} . \tag{4.42}$$

4.3 Experimental methods

The study of the relationship between the hysteretical retention curves and peat deformations, is conducted on a dataset aquired by a field experimental project operating since the end of 2001 in the Zennare Basin, a cropped area located along the southern part of the Venice Lagoon margin. The field site was located within a rectangular bog of size 30×200 m^2 with a 1.5 m thick peat layer and drained laterally by ditches [Fornasiero *et al.*, 2003]. Several measurement instruments have been installed. The site was equipped with a tilting bucket pluviometer with a 0.2 mm sensitivity and five soil temperature sensors at 0.01, 0.05, 0.2, 0.3, and 1 m depth (PT100 with a measurement range between -15°C and 50°C and sensitivity of ±0.1°C). The capillary pressure has been measured by five tensiometers, inserted at a 45° slope so that the ceramic cups are all located along the same vertical line at depths of 0.15, 0.30, 0.45, 0.60 and 0.75 m. The measurement range of the electronic pressure sensor is from -100000 to 85000 Pa with an accuracy of ±20 Pa. Six three-wire time domain reflectometry (TDR) probes for soil moisture content measurement (accuracy ±0.02 m^3/m^3), 0.15 m long, one inserted horizontally along the same vertical of the tensiometers, at depths of 0.10, 0.20, 0.30, 0.45, 0.60, and 0.75 m, and connected to a multiplexer (Tektronix 1502C TDR). The probe inserted at 0.30 m depth stop working because of a malfunction so the data collected by that instrument are not shown. Ground displacements are measured by an ad hoc extensometer. All sensors are

connected to a datalogger and sampled hourly, so that a large data set is available to study the hydrological and swelling/shrinking peat dynamics. It is worth recalling that TDR provides measurements of the bulk dielectric constant K_b, that can subsequently be related to the volumetric water content θ [Topp *et al.*, 1980]. The conversion from K_b to θ depends on the soil characteristics. For peats, several calibration functions have been proposed in the literature. A review of calibration functions for TDR applications on peat soils and their evaluating on the basis of laboratory measurements on undisturbed peat samples can be found in Kellner and Lundin [2001]. Since an ad hoc TDR calibration curve is not currently available for the Zennare peat, we have elected to use the function proposed by Myllys and Simojoki [1996], developed for cultivated peat soils, and thus similar to the conditions of our basin.

4.4 Data Analysis

The study refers to the period from August 5, 2005 to February 08, 2006. Following a very dry June and July, the first two months (August – September) have been very wet also with respect to remaining period from October to February. In fact, a cumulative precipitation of about 560 mm and 240 mm fell in August and September and in the remaining period, respectively (Figure 4.8a). The summer period has been also characterized by very high temperatures, hence strong evaporation (Figure 4.8b). During August 2005 the temperature probe inserted in the very first 0.05 m of peat soil recorded values equal or higher than 40°C, reaching the instrument FS (Full Scale, equal to 50°C). The winter period was cold, generally marked by negative temperatures below 0°C, at least over night, as the 0.01 m probe has revealed (Figure 4.8b). It was also a very dry winter, with only 56 mm of cumulative rainfall. Observing the temperature trend recorded at various depths strong oscillations of the values recorded by the topmost probes are evident, whereas the instrument inserted at - 1 m depth recorded only a gentle variation of ± 2 °C.

Figure 4.8(c) shows the water table level in the field and at the near ditch with respect to to the mean sea level: the average water table depth varies between -3.25 m and -3.66 m and between -3.32 m and -3.80 m, respectively. During the main precipitation events water infiltrates in the soil, rapidly the water table level rises (Figure 4.8c), the pressure head and water content increase (Figure 4.9a and b, respectively), and the porous matrix swells inducing a reversible soil surface upward displacement (Figure 4.9c). The imbibition phase is followed by a much slower drainage phase, that induces a lowering of the water table

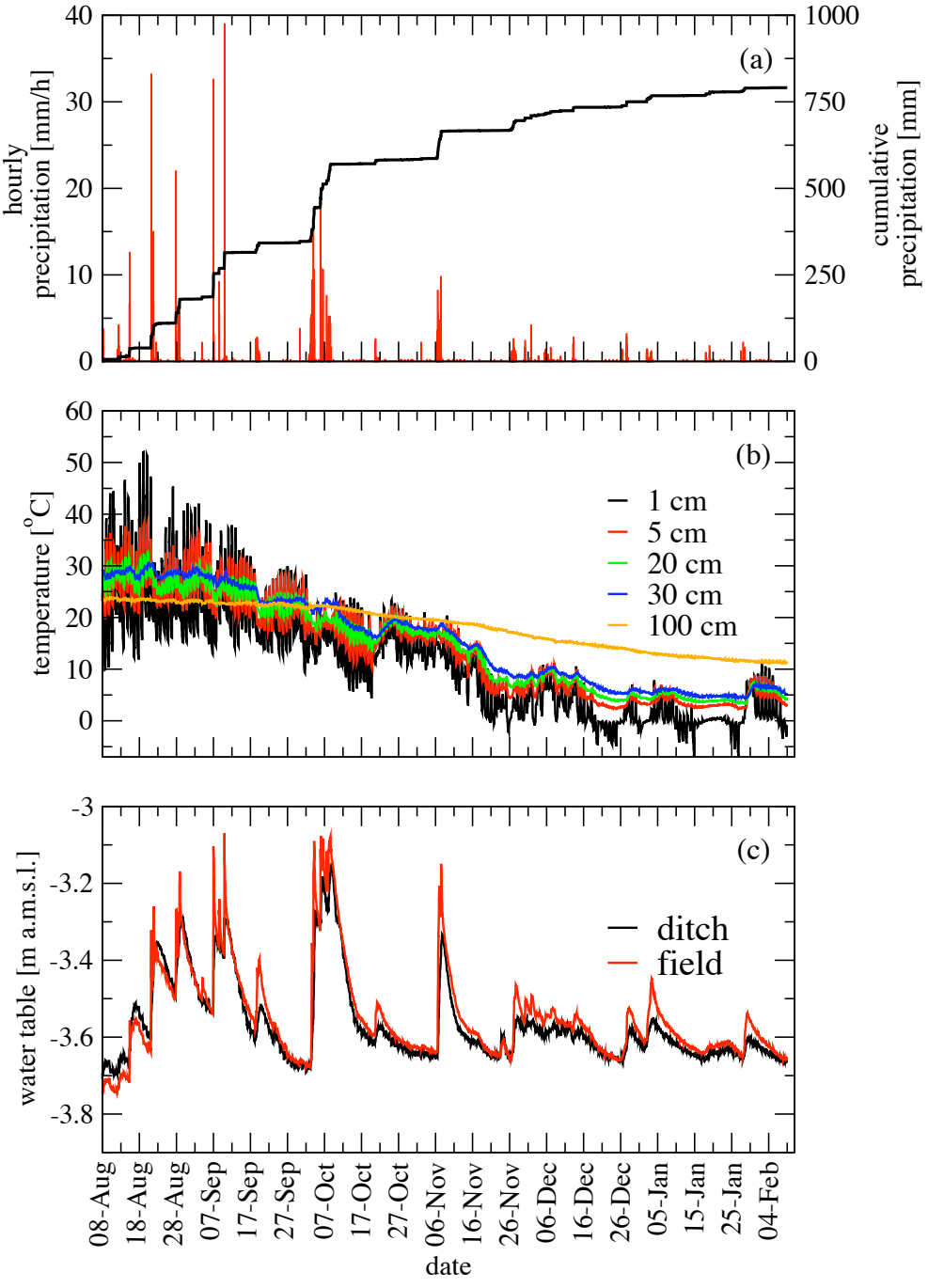

Figure 4.8: (a) Hourly and cumulative precipitation, (b) soil temperature at various depths and (c) depth of the water table as measured between August 2005 and February 2006 at the Zennare Basin field site.

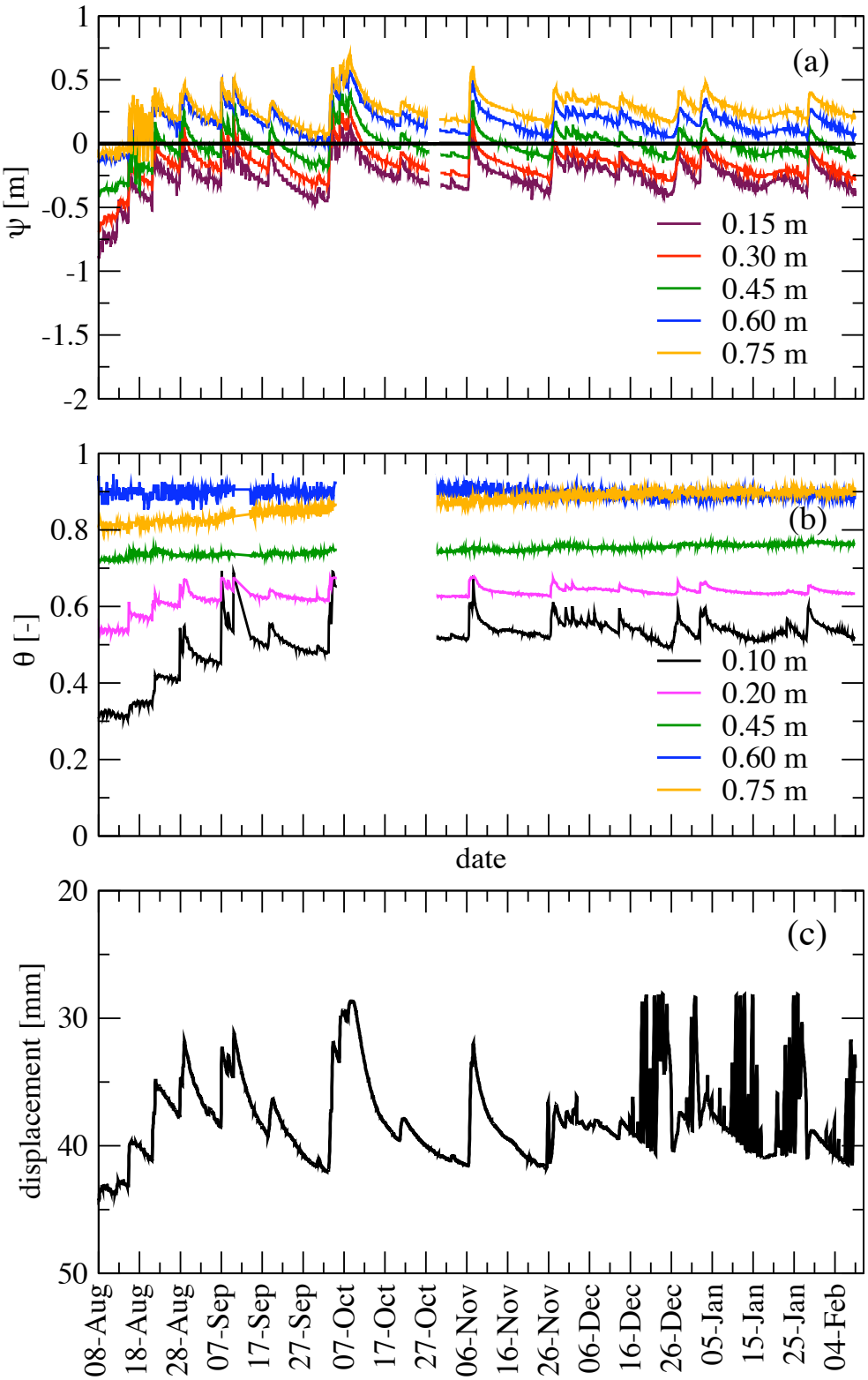

Figure 4.9: (a) Pressure head at various depths, (b) water content, and (c) soil surface displacement as measured between August 2005 and February 2006 at the Zennare Basin field site. The effect of the soil expansion due to nightime freezing is clearly visible in (c) from December, 16.

depth, a reduction of the moisture content in the shallower layers, hence a shrinking of the peat with a reduction of the soil surface elevation. Section 3 of this thesis shows that significant elastic peat volume changes are caused by variation of soil moisture. Peat swelling has been measured after every rainfall event. The swelling dynamics is very rapid after a precipitation event, while shrinkage progresses at a slower rate, closely following the water table decrease and exhibiting a time scale from few hours to few weeks [Teatini *et al.*, 2004] (cfr. chapter 3)

Figure 4.9(b) shows the recorded dynamics of the water content: unfortunately no data are available between October 5 and October 27 for TDR out of order, but the available long period allows for a physically meanigful characterization of peat hydrology and surface displacement dynamic. The monitored time interval is characterized by a very dry initial period due to the former metereological conditions. The soil in the upper 0.30 m depth is in unsaturated condition for most of the monitored time interval and becomes completely saturated only in October due to a sequence of shortly separated pluviometric events (Figure 4.9a). The soil is usually saturated at larger depths. In particular, the water content recorded at 0.10 m depth was lower than 40 % and increase gradually to 50 % and peaks 70 % in agreement with the main pluviometric events. A similar trend is followed by the data collected at 0.20 m of depth, although the obscillations induced by the precipitation events are smaller and the range of variability of moisture content values are narrower (0.55 % – 0.65 %).

Figure 4.10 shows the volumetric water content θ versus pressure head ψ as collected at different depths from September, 17^{th} to October, 2^{nd}, 2005. Because the TDR probes and the tensiometers were not inserted at the same depths, the θ values at 0.15 m are obtained by linear interpolation of the measurements collected at 0.1 and 0.2 m depth. The data set points out that the retention curves vary with depth and a flattering of the function may be observed passing from 0.15 to 0.45 m depth.

We elect to analyse in more detail the pressure head data and the corresponding volumetric water content measured at 0.15 m depth, where unsaturated conditions prevail, in order to investigate the hysteretical properties of retention curves for the peat soils. Figure 4.11 shows the volumetric water content data plotted versus the pressure head measurements collected at the Zennare Basin from August, 5, 2005 to February, 8, 2006. The time series is splitted into 21 subsets according with the main meteoric events, i.e. each set spans the interval from the beginning of a pluviometric event and the following one. A very strong hysteresis clearly appears from the plot: the main loop can be qualitatively identified by the brown dashed lines and the 21 subsets can be viewed as internal

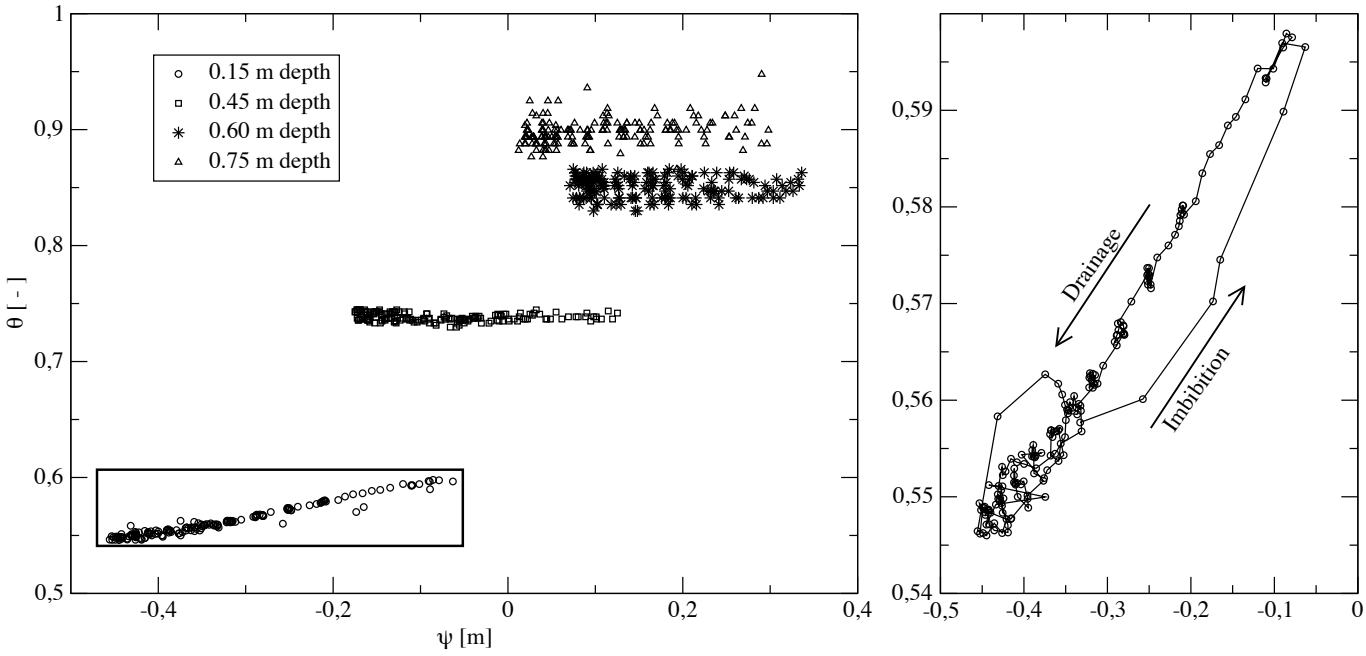

Figure 4.10: Volumetric water content and pressure head at various depths, as measured by TDR probes and tensiometers from September, 17 – October, 2, 2005. On the right an enlargement of the data points collected at 0.15 m depth is provided. The two branches of the behavior, i.e., the imbibition and drainage phases, can be clearly distinguished due to hysteresis.

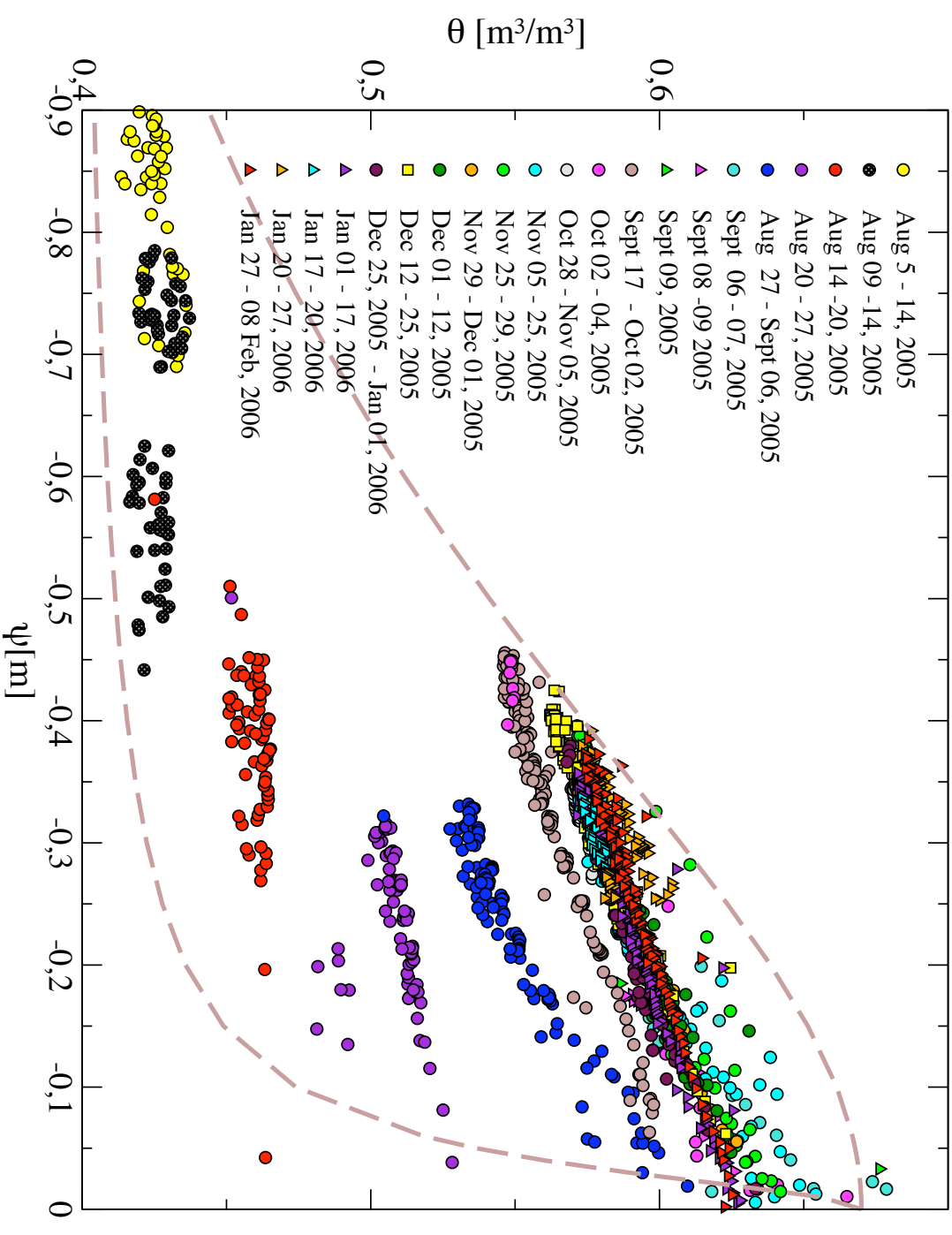

Figure 4.11: Moisture retention curve measured at 0.15 m of depth. The whole dataset has been divided in 21 subsets which are characterised by different colours, according to the pluviometric events occured during the period August, 5, 2005 – February, 8, 2006.

loops defined by wetting and drying scanning curves. All the internal loops averagely last 7 to 10 days and are marked by a very narrow shape. Each set is characterized by a very fast imbibition which occured in about 10 hours, hence is very difficult to be recorded in detail, followed by a drainage phase showing a slower dynamic. This peculiar trend is reflected in the shape of internal scanning curves: the wetting branches have a pronounced slope whereas the drying paths are quite flat. All the meteoric events occured after August, 20, 2005 occured at a very high water content condition, and the pressure head values got close to zero, hence all the imbibition paths got close to the saturation limit.

Notice that for the same value of capillary pressure very different moisture content values have been experienced by the soil. Moreover, the same variation of capillary pressure $\Delta\psi$ correponds to very different ranges in terms of moisture content depending on the initial condition of the soil. For example, in the period August, 14–20, 2005 the soil experiences $\Delta\psi =$ 0.50 m as from December, 12 to 25, 2005 with a significant different moisture content condition (0.42 and 0.58, respectively).

4.5 Modeling capillary hysteresis in peat soils

Two different approaches have been considered to describe the capillary hysteresis in moisture retention curve outlined by the data collected at 0.15 m depth from August, 17, 2005 to February, 8, 2006 in the Zennare Basin.

4.5.1 Application of the Haverkamp *et al.* [2002] model to the Zennare Basin data

The model developed by Haverkamp *et al.* [2002] has been initially used to estimate the ibehavior of the volumetric water content corresponding to the measured capillary pressure data. The complete set main and scanning of curves requires the definition of three unknowns, namely mn, h_{gmd}, and θ_S, see equations (4.15) to (4.26). The main drying curve has been defined using the van Genuchten [1980] relationship (Figure 4.12b, yellow line). The experimental data shown in Figure 4.11 allow the estimate of the volumetric water content at the saturation limit corresponding to $\psi = 0$. The value of θ_S ranges from 0.65 at the ground surface to 0.90 at 0.60 m depth. This is consistent with the geotechnical classification of the Zennare organic soil [Gatti *et al.*, 2002] that is composed by a fibrous peat layer overlain by a shallow 0.5 m thick, partially decomposed peat unit.

Since the dataset recorded at 0.15 m depth shows a great variability of water content at the saturation limit, we elect to use θ_S value close to the maximum measured, i.e., 0.65, and a residual water content $\theta_r = 0.16$ in order to span all the θ range experienced by the soil.

The shape parameter n and α has been at first calibrated to reproduce the events occured at the beginning of the monitored period (Fit A). The values of the van Genuchten

Parameter	**Unit**	**Value**
θ_S	[-]	0.645
α^{-1}	[m^{-1}]	-0.1
n	[-]	1.700
θ_r	[-]	0.38

Table 4.2: Parameters of the van Genuchten retention curve calibrated on the dataset collected in the Zennare Basin field site (Fit A) and used as MDC for the application of the Haverkamp *et al.* [2002] hysteresis model.

[1980] parameters thus derived and used to identify the Main Drying Curve are reported in table 4.2. The curve is drawn by yellow dots in Figure 4.12(b) This parameter set allows a satisfactory reproduction of the volumetric water content dynamics only before September 2005 (Figure 4.12a). Conversely, θ is strongly underestimated thereafter, when the soil gets closer to the saturated condition (Figure 4.12a) due to an erroneous fit of the water content - pressure head subsets recorded after September 2005 (blue dots in Figure 4.12b). All the higher order scanning curves result very close to the main drying behavior.

Parameter	**Unit**	**Value**
θ_S	[-]	0.645
α^{-1}	[m^{-1}]	-0.5
n	[-]	1.700
θ_r	[-]	0.16

Table 4.3: Parameters of the van Genuchten retention curve calibrated the dataset collected at the Zennare Basin field site (fit B) and used as MDC for second aplpication of the‘Haverkamp *et al.* [2002] hysteresis model.

In order to obtain a more satisfactory reproduction of the data collected during fall and winter 2005–2006, a different set of parameters has been considered, trying to im-

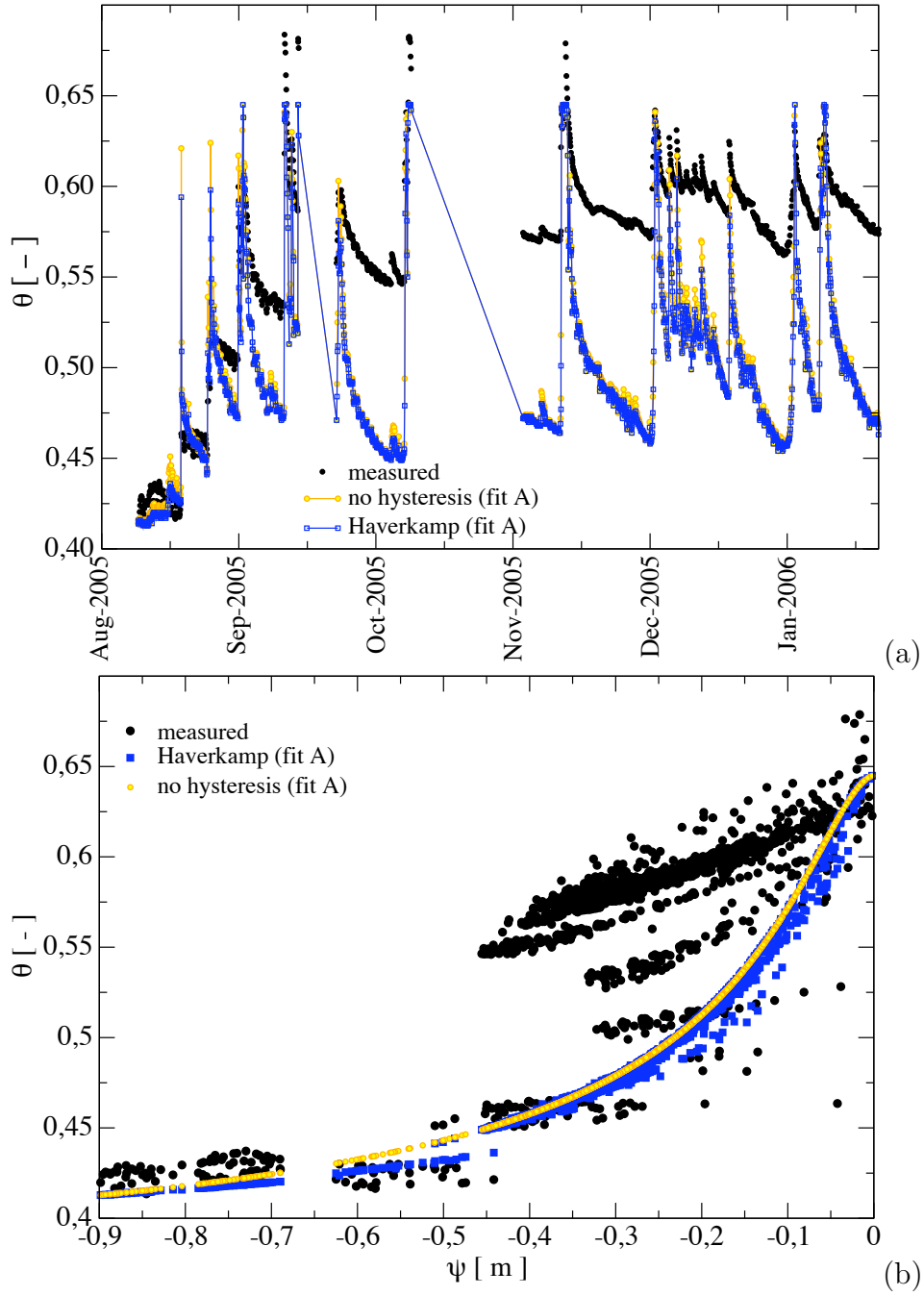

Figure 4.12: Haverkamp *et al.* [2002] model, fit A. Comparison between the measured and reconstructed i θ values (a) versus time and (b) versus ψ. the yellow behavior corresponds to the van Genuchten [1980] relationship used as MDC in Haverkamp *et al.* [2002] (see table 4.2

prove the description of the soil condition close to saturation (Fit B). The parameters thus obtained are summarized in table 4.3 and the θ versus ψ behavior is provided in Figure 4.13(b), yellow dots. The volumetric water content values resulting from the application of Haverkamp *et al.* [2002] model to the collected ψ data are shown in Figure 4.13(a). With this second setting the outcome largely overestimates the moisture content values until mid September, whereas the trend is better captured in the last part of the period of interest. The comparisons represented in Figures 4.12 and 4.13 clearly show that the hysteresis model developed according with Haverkamp *et al.* [2002] is not suitable for the description of the unsaturated hydrologic behavior of this peculiar type of soil (Figure 4.13b). The high variability of the volumetric water content at the saturation limit is not captured at all by this approach: the similarity hypothesis on which the Haverkamp *et al.* [2002] model is based on, associated with the impossibility of adopting a set of parameters specific for each curve family (i.e., one for wetting and a different one for drying) results in in a lack of capability to correctly describe the behavior of the collected dataset. In particular, all the inner scanning curves for values of θ close to θ_S collapse close to or on the main drying curve, and for values of pressure head ψ higher than -0.5 m the primary wetting and secondary drying curves describe an extremely narrow loop overestimating the measured data depending on the van Genuchten parameters. The lack of accuracy of the Haverkamp *et al.* [2002] approach in conditions close to saturation has been already observed by the authors themselves for clay soils. Haverkamp *et al.* [2002] suggested that this inaccuracy could be due to the alteration of the soil during the extraction process, observing that inexact reproduction occurs for very small values of pressure head. Therefore, from the capillarity point of view, the Zennare peats appear to have characteristics similar to fine grained soils (e.g., clay): for both soils the definition of all the scanning curves by scaling the MDC appears to be a strong limit in the Haverkamp *et al.* [2002] approach. The high range of water content conditions at ψ close to zero and the results obtained using the Haverkamp *et al.* [2002] model with the two different sets of parameters suggest that the use of distinct functional form for for wetting and drying curves is the first necessary step to obtain a more satisfactory description of the moisture retention curve in peat soils.

4.5.2 Application of the Parker and Lenhard [1987] model

As previously described, the approach proposed by Parker and Lenhard [1987] takes into account the hysteresis effect induced by (i) the entrapment of non-wetting fluid (i.e., air),

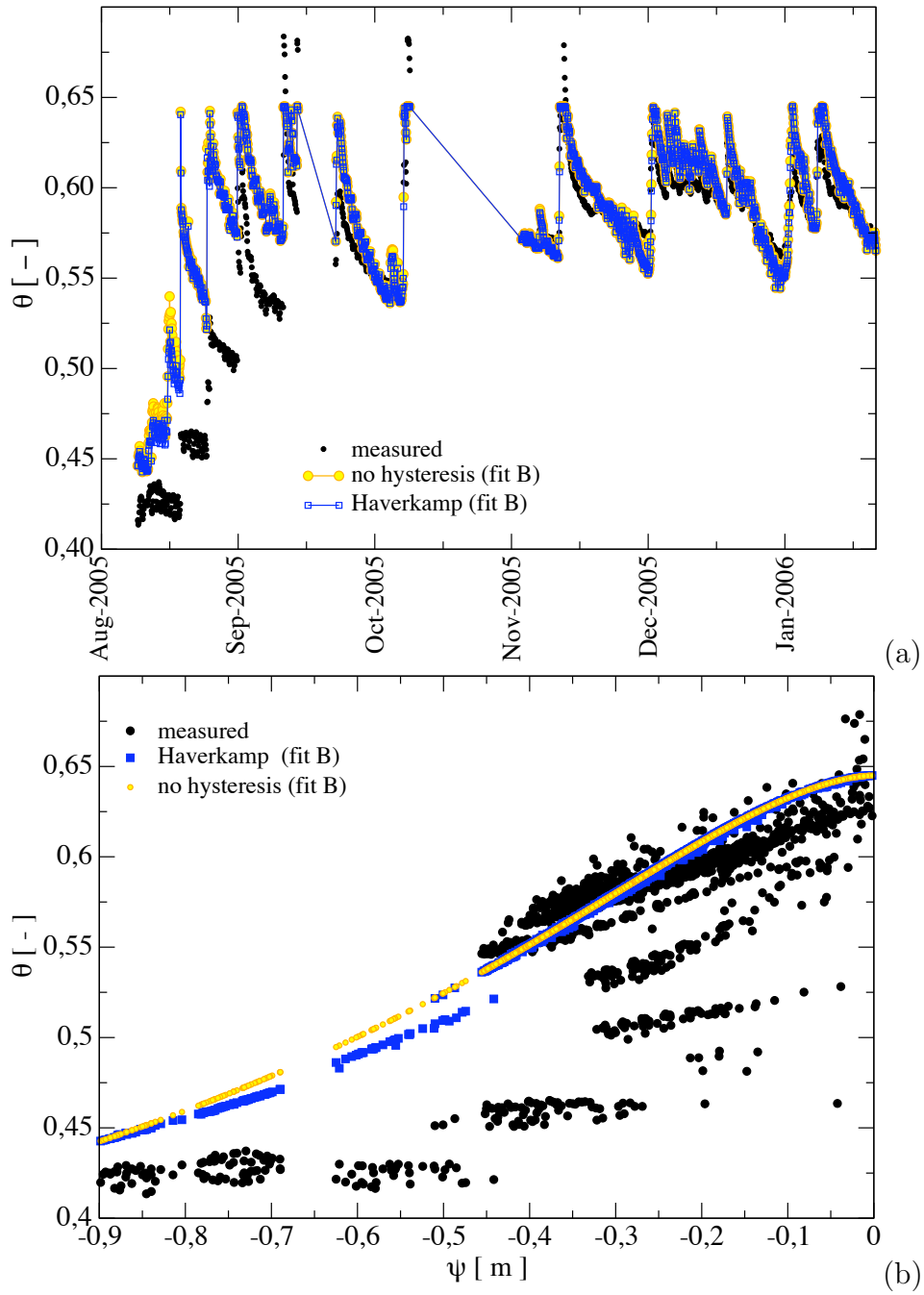

Figure 4.13: Haverkamp *et al.* [2002] model, fit B. Comparison between the measured and reconstructed θ values (a) versus time and (b) versus ψ. the yellow behavior corresponds to the van Genuchten [1980] relationship used as MDC in Haverkamp *et al.* [2002] (see Table 4.3).

(ii) the different contact angles associated with drainage and imbibition processes, and (iii) irregular pore geometry. The model has been here adapted in order to describe a single phase flow system, assuming the capillary pressure head $\psi = -P_w/\gamma_w$. The model allows the use of different parameters for the main wetting and the main drying curve, and derive the internal scanning curves by means of geometricaly scaling the main branches of the family they belong to. Therefore, this approach seems to be suited to describe the moisture retention curve in peat soils.

Parameter	**Unit**	**Value**
θ_S	[-]	0.645
$^{\mathrm{D}}\alpha^{-1}$	[m^{-1}]	-0.5
$^{\mathrm{I}}\alpha^{-1}$	[m^{-1}]	-0.1
n	[-]	1.700
θ_r	[-]	0.16
$S_m = \theta_S\theta_r$	[-]	0.2481
$^{MWC}\bar{S}_{ar}$	[-]	0.20

Table 4.4: Parameters of the van Genuchten retention curves used for the application of the Parker and Lenhard [1987] model to the dataset.

The set of parameters required for the application of the Parker and Lenhard [1987] hysteretical model is summarized in table 4.4. The values are those used in the two applications by the Haverkamp *et al.* [2002] approach. The irreducible water saturation S_{wm} has been calculated as θ_S by the θ_r value calibrated in Fit B. For the main wetting curve and all the scanning paths describing an imbibition process, we choose $^{\mathrm{D}}\alpha^{-1} = 0.1$ m^{-1} (as in Fit A for Haverkamp *et al.* [2002] model). $^{\mathrm{D}}\alpha^{-1} = 0.5$ m^{-1} (as in fit B) is chosen for the main drying curve and all the derived inner scanning. Figure 4.14(a) shows the measured θ values compared with the result obtained by the use of Parker and Lenhard [1987] approach, given the pressure head trend. Globally, the model is able to reproduce the θ evolution versus time more satisfactorily with respect to Haverkamp *et al.* [2002] approach. Almost all the range of variability of moisture content is covered and its dynamic close to saturation is much better captured. Also the slope of the drainage phases is generally well reproduced by Parker and Lenhard [1987] approach. The different inner scanning loops can be easily ditinguished from the main branches in the water content versus capillary pressure plot (Figure 4.14b) and are characterised by a narrow shape and by a trend that generally resembles that of the observed loops.

Nevertheless, during the first and the last parts of the series the measured moisture

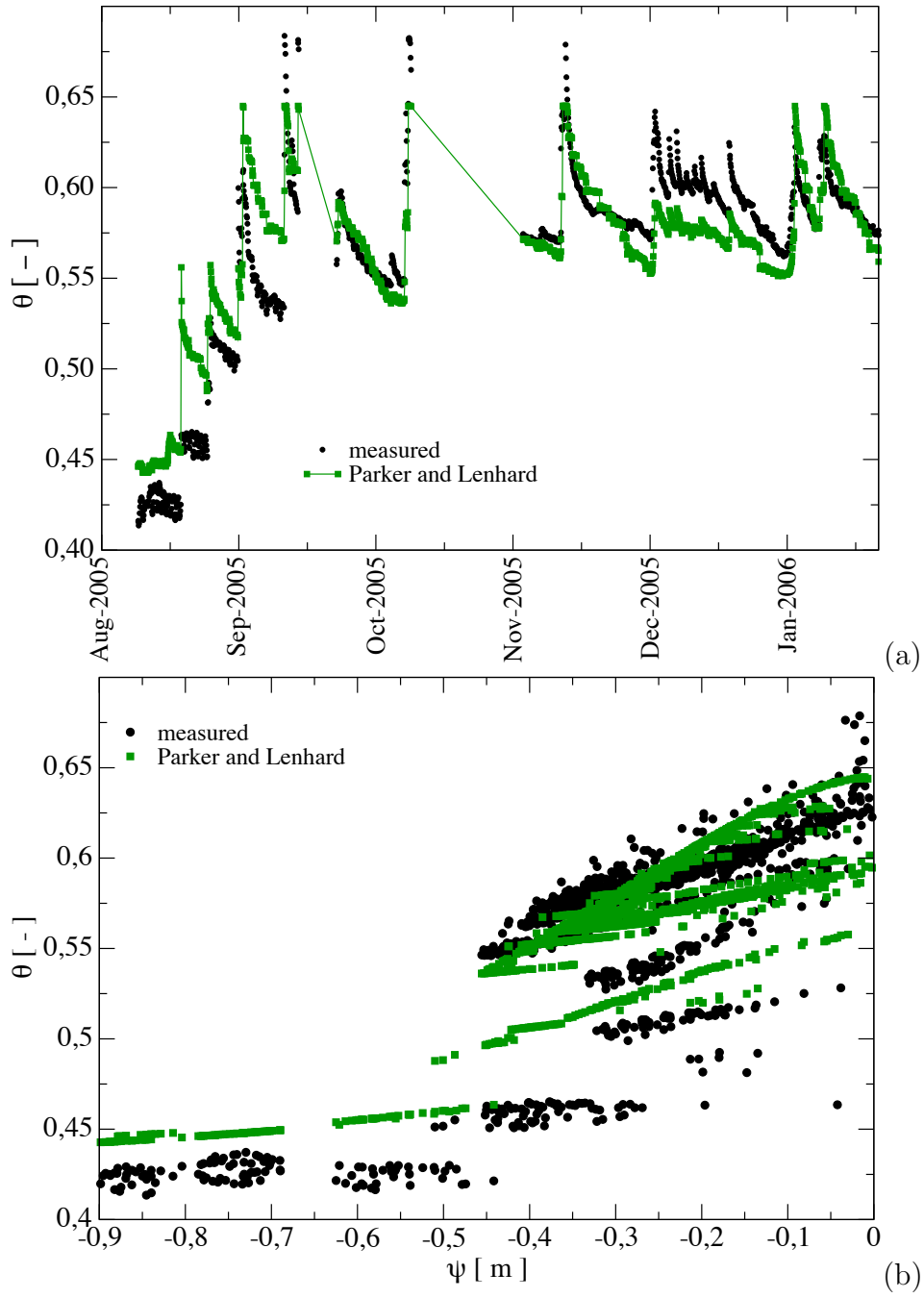

Figure 4.14: Parker and Lenhard [1987] model. comparison between the measured and reconstructed θ values (a) versus time and (b) versus ψ. the van Genuchten parameters used as to define the MDC and MWC are summarized in table 4.4.

content is still overestimated and underestimated respectively, although less than with the Haverkamp *et al.* [2002] model, fit B and A.

These discrepancies may be due to the assumption of a fixed matrix soil. In fact available data previously analyzed have shown that the peat matrix experiences a significant elastic deformation with water saturation. The porosity variations are likely to impact considerably on the moisture retention relationship.

4.5.3 Hysteresis and peat swelling/shrinkage effect on moisture retention curve

Peats respond to natural hydrologic cycles of precipitation and evapotranspiration with reversible deformations. This behavior induces changes of the porous matrix inducing an increase of the porosity in wetting phases (swelling), and a decrease (shrinking) when drying occurs. The wide variability range of the volumetric water content suggests the possibility of a combined effect between hydraulic retention and porosity variation. In order to explore this hypothesis, we developed an algorithm to include the porosity variation into the definition of moisture retention curves. We elect to use the model proposed by Camporese *et al.* [2006a] to describe the void index variation according with measured water content data $\theta^{measured}$. The equation that describes this dependency is:

$$e = \begin{cases} (\vartheta_0 + 1)^{1-\delta}(\vartheta + 1)^{\delta} - 1 & \text{if } \vartheta \leq \vartheta_0 \\ \vartheta & \text{if } \vartheta > \vartheta_0 \end{cases}, \tag{4.43}$$

and it is nonlinear because the moisture ratio $\vartheta = \theta^{measured}(1 + e)$ is a function of the void index. The values of the ϑ_0 and δ parameters have been chosen according to the calibration developed by Camporese *et al.* [2006a]. The linearization of equation (4.43) using the Newton-Raphson technique has allowed to calculate the time evolution of the void index according with water content, hence of the soil porosity, and the water content at saturation limit, as:

$$\phi = \theta_S = \frac{e}{1 + e} \tag{4.44}$$

Finally, the new estimate of water content, that includes both the effect of hysteresis, as evaluated through the Parker and Lenhard [1987] model, and the swelling/shrinkage behavior of peat soils, is calculated from equation (4.10) as:

$$\theta = (\theta_S - \theta_r)\,\theta^* + \theta_r \tag{4.45}$$

where $\theta^* = \bar{S}_w$ is the effective saturation calculated using Parker and Lenhard [1987] approach.

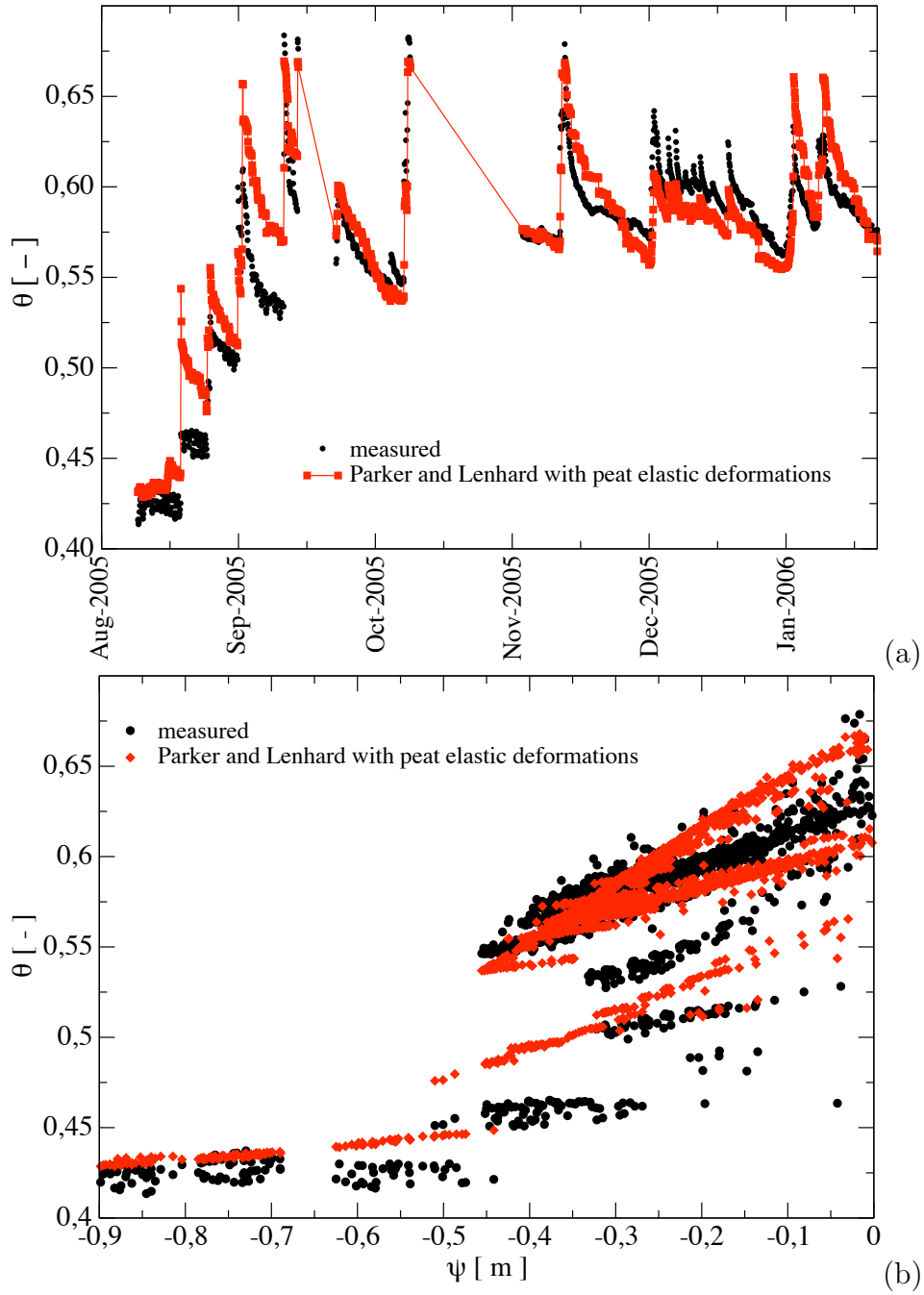

Figure 4.15: Parker and Lenhard [1987] model coupled with the porosity variation model for the peat soil. Comparison between the measured and reconstructed θ values (a) versus time and (b) versus ψ.

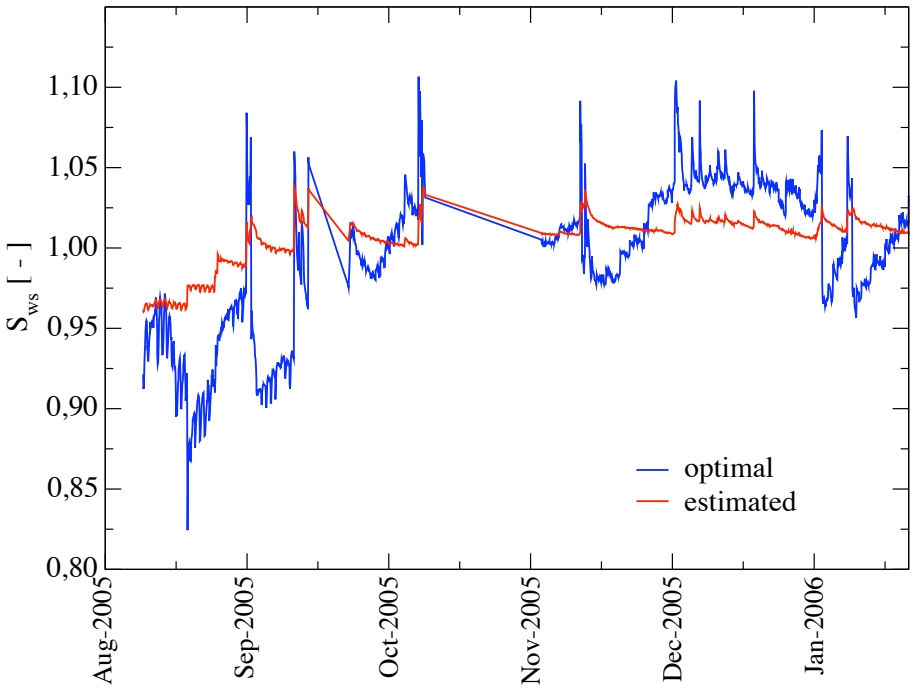

Figure 4.16: Optimal value of water saturation in completely saturated conditions compared with the estimate obtained by dividing θ_s, calculated with 4.43, by the reference porosity $\phi = 0.645$.

The results obtained by combining equation 4.45 with the Parker and Lenhard [1987] model are shown in Figure 4.15. A general improvement of the θ dynamics reproduction is observed in the whole period. In particular, the moisture content data collected over the first 15 days are only slightly overestimated , and the moisture content peaks are very well captured due to the consideration of the porosity increase. Also the data collected in December 2005, that are underestimated when only the hysteresis function has been addresse (Figure 4.14), are now better reproduced. In this way the retention function spans the whole observed range of moisture content (Figure 4.15b) and the result confirms the importance of including swelling/shrinkage of peats in the definition of retention properties.

Figure 4.16 shows the time behavior of the water saturation corresponding to the moisture content at the saturation limit. The blue line provides the values calculated as:

$$S_{wS}^{opt} = \frac{1}{\phi}\left[\frac{1}{\bar{S}_w}\left(\theta^{meas} - \theta_r + \theta_r \bar{S}_w\right)\right] \tag{4.46}$$

where S_{wS}^{opt} is the "optimal" value of water saturation at the saturation limit that allows the perfect match of the measured data, ϕ is the reference porosity and is assumed equal to 0.645 as in the Parker and Lenhard [1987] model application. S_{wS}^{opt} varies between 0.8

and 1.1, hence higher than 1, meaning that the peat soil accumulates part of the incoming water not only in the voids but also in the matrix (hygroscopic material). The red line represents the water saturation value corresponding to the water content at the saturation limit θ_S evaluated as

$$S_{ws} = \frac{\theta_S}{\phi} \tag{4.47}$$

where ϕ is the value of porosity used for the calibration of moisture retention curve including hysteresis effect only, i.e., 0.645. The trend does not show strong variations as S_{wS}^{opt}, but is characterised by peak values in correspondance to the maximum values of S_{wS}^{opt}. A further improvement of the retention dynamics could be finally obtained by a proper calibration of the parameters δ and ϑ_S. Finally the comparison of the retention functions estimated with all the different approaches is shown in Figure 4.17.

4.6 Conclusions

The ground water flow within a porous medium in variably saturated condition requires the specification of the moisture retention curve, i.e. a relationship between the pressure head and the volumetric water content. This relationship is highly non-linear and is marked by capillary hysteresis. For organic soils, this relation is also influenced by the variation of the porosity during wetting/drying cycles. A field site was instrumented in 2002 in the Zennare Basin, Italy, to study both the hydrological dynamics of cropped peat soils. An accurate analysis of the main recorded hydrological variables has been initially carried out. Then a study aimed at an accurate definition of the moisture retention curve in the unsaturated peat soils is developed. In particular, the capillary hysteresis model proposed by Parker and Lenhard [1987], results to be the more suited to describe the retention relation in organic soils. This model takes into account the effects of nonwetting fluid entrapment and computes the drying and wetting scanning curves by geometrically scaling the main drying and the main wetting curves, respectively. Afterwads, an algorithm that includes in the hysteretical retention curves the swelling/shrinkage dynamic described with the aid of the model proposed by Camporese *et al.* [2006a] has been developed, through a suitable adjustment of the moisture content parameter at saturated conditions.

The modelling approach has been finally applied to the moisture content - pressure head dataset collected at the Zennare Basin from August 2005 to February 2006 with a satisfactorily match of the collected data. The results confirm that the description of the

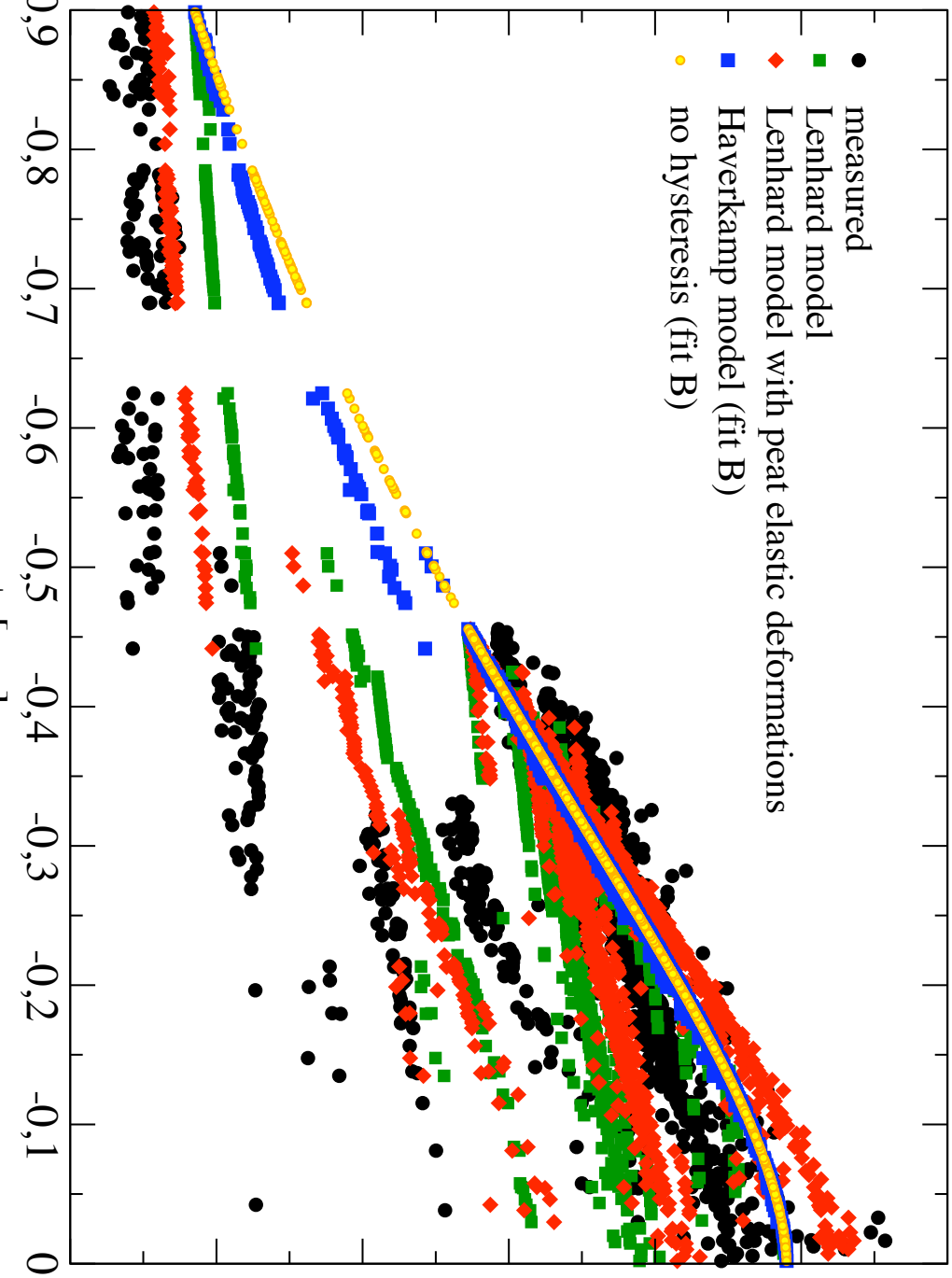

Figure 4.17: Comparison between the experimental θ–ψ values at 0.15 m depth and the retention curves estimated using a calibrated van Genuchten [1980] relationship (yellow dots), Haverkamp *et al.* [2002] (blue squares), Parker and Lenhard [1987] (green squares) models, and Parker and Lenhard [1987] model coupled with Camporese *et al.* [2006a] relation (red symbol).

hydraulic retention curve in deformable soils requires to include both the effect of capillary hysteresis and the variation of the void index, hence the soil porosity, with saturation. A possible future development will consist in the implementation of the algorithm that couples the Parker and Lenhard [1987] model with with the Camporese *et al.* [2006a] relation for porosity variation into a 3D variably saturated flow simulator in order to reproduce more accuratly the flow dynamics in peat soils. This will introduce another source of non-linearity with new numerical issues related to the convergence of the nonlinear solver that should be explored.

Chapter 5

Modeling of air and water flow in intertidal marshes

In the last decades a growing interest in the scientific comunity for the wetlands as areas marked by a strong connection between terrestrial environments and deep water aquatic systems connected by floods and tide has been recorded. These delicate intertidal zones are characterized by a high biodiversity and by a strong connection of the atmosphere and the subsurface in terms of air fluxes. A complete description of the hydrological dynamics that mark these peculiar ecosystems requires the determination of the oxygen budget as determined by its inflow from the atmosphere through the soil surface, by its diffusion through the root system, and by its consumption by plant roots. Richards equation, usually adopted for the simulation of water infiltration in soils in variably saturated conditions, assumes that air is readily displaced by water, hence is not able to account for the actual fluxes of air. Therefore in the simulation of flow in salt marshes one needs to take into account the entrapped air on the water infiltration in the soils and its movement. A two-phase flow model has been developed in order to investigate the effects of air flow in the wetlands dynamics. A pressure based formulation has been chosen to allow for natural treatment of the complex and nonlinear boundary conditions to be imposed at the soil-atmosphere interface to take into account the interplay between evapo-transpiration during emersion periods and tidal fluctuations during soil submersion.

A two-phase modeling approach is to be prefered in this situation. With this approach both air and water movements due to pressure variations are considered simultaneously, yielding a more correct mathematical representation of the physical phenomena in action in a wetland soil. Typically, two-phase flow simulators employ water pressure and saturation as principal unknowns. The main reason for this choice is the good numerical

properties, in terms of stability and mass conservation of this approach. However, the boundary conditions that need to be imposed at the surface to follow the natural dynamics of a tidal system (especially periodical soil emersion and submersion) are more naturally inposed on water and air phase pressures. Using these as principal variables, however, leads to numerical difficulties that manifest as non convergence of the nonlinear solver and mass conservation problems. Here we try to overcome these difficulties following the guidelines reported by Celia *et al.* [1990]; Celia and Binning [1992]; Rathfelder and Abriola [1994]; Forsyth *et al.* [1995].

Hence our formulation is developed with the fundamental purpose to ensure the preservation of the elemental expansion of saturation time derivative through a proper definition of the capacity coefficient.

First a review of the main contributes to the qualitative and quantitative description of the wetlands dynamics is reported, then the mathematical and numerical approach is discussed. Finally, some test cases are described and the future developments outlined.

5.1 Literature Review

Coastal tidal areas, namely marshes, lagoons, estuaries, are important dinamical systems that act as mediators between the terrestrial and the aquatic (marine) environments. Wetlands are among the world's most productive environments, cradles of biological diversity, providing the water and primary productivity upon which countless species of plants and animals depend for survival. The Ramsar Convention [Ramsar Convention Secretariat, 2006] stated the importance of these delicate areas, assuming as mission "*the conservation and wise use of all wetlands through local and national actions and international cooperation, as a contribution towards achieving sustainable development throughout the world*". In the last decade the scientific interest for the intertidal areas dynamics has been renewed [Fagherazzi *et al.*, 1999; Rinaldo *et al.*, 1999a,b; Friedrichs and Perry, 2001; Gardner, 2008; Tosatto *et al.*, 2009], and the importance of an interdisciplinary approach for a deep understanding of their morphogenesis and evolution has been established. A quantitative description and predictive explanation of their transformations requires the explicit incorporation of both the living and non-living components [Ursino *et al.*, 2004; Marani *et al.*, 2004, 2006a]. Particularly relevant in this ecogeomorphological context is halophytic vegetation, i.e. plants adapted to live in hypoxic and high salinity conditions, which crucially affect the overall geomorphological and ecological evolution of a wetland [Marani *et al.*, 2006b]. Up to now the mechanisms that favor the colonization

by this type of plants of wetlands with soils close to total saturation, i.e. when flooding occurs and vertical infiltration from the surface and through the uppermost unsaturated soil tends to completely saturate the upper soil layers, are still nebulous. Under these conditions, a buried aerated layer delimited by the infiltration front on the top and the water table on the bottom can exist only if the root water uptake balances the water infiltrating.

Chapman [1938] was the first to point out, through the use of buried gas traps, the presence of an aerated layer persistent even when the tide floods the salt-marsh surface. Chapman also observed a correlation between the typical depth of halophytic vegetation roots and the depth of such layer, but he was not able to establish if the presence of the aerated layer induced the colonization by the halophytic vegetation, or the presence of the roots induced the existence of the aerated stratum. In the following, several authors [e.g., Chapman, 1940; Stevenson and Emery, 1958; Clarke and Hannon, 1969] noticed a buried aerated layer in different areas. Dacey and Howes [1984], observing the results of some laboratory and in-field experiments, formulated the hypothesis that the water table movement in *Spartina alterniflora*-dominated marshes might be induced by root water uptake.

Most of the first theoretical and numerical studies of salt marshes subsurface phenomena considered only the dynamics of the saturated flow [e.g., Harvey *et al.*, 1987; Li *et al.*, 1997, 2000], and disregarded the processes in the unsaturated part, the more important in the eco-hydrological perspective. Hemond and Fifield [1982] pioneered the numerical studies of the influence of tidal fluctuations and evapotranspiration on subsurface flow in the inner portion of salt marshes characterised by organic soils. The authors emphasized the importance of using a two-dimensional model that includes the effects of swelling/shrinkage of the peat soils in the transition zone close to the channel bank where the horizontal flow is predominant, hence were the flow-dynamic is much more complex. Springer *et al.* [1999] developed a numerical groundwater flow model coupled with a conceptual riparian vegetation model to predict hydrologic conditions favorable to maintaining riparian vegetation downstream of a reservoir for non-intertidal areas.

The first quantitative modeling description of ecohydrological interactions in the unsaturated soil layer of salt marshes and of their giving rise to complex aeration patterns was provided by Ursino *et al.* [2004], who proposed a finite element model of saturated/unsaturated subsurface flow based on Richards' equation in a schematic salt marsh, driven by tidal fluctuations and evapotranspiration. The Ursino *et al.* [2004] model shows that salt marsh subsurface flow depends on the distance from the nearest creek or channel

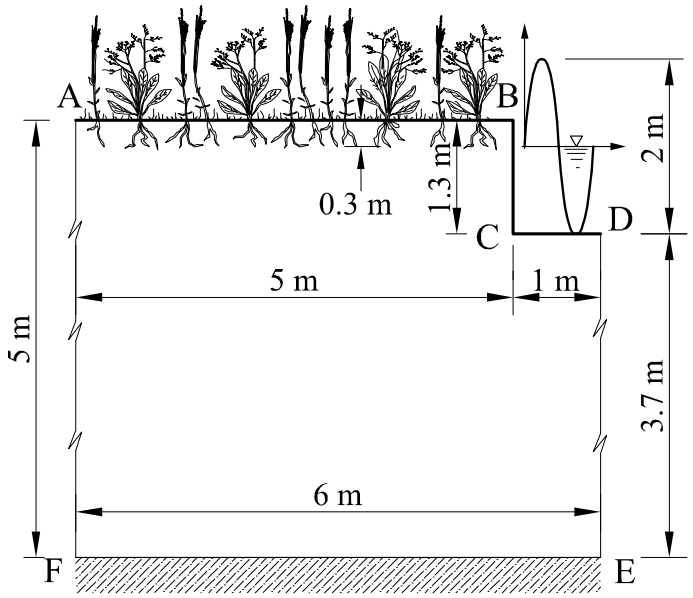

Figure 5.1: Schematic representation of the model domain. No-flux boundary conditions are imposed on boundaries AF and FE. A hydrostatic vertical pressure distribution is imposed on boundary DE. A pressure value corresponding to the instantaneous tidal level is specified on CD. Boundary conditions on BC implement the possible existence of a seepage face during ebb. Boundary conditions on AB impose flux or pressure head depending on the instantaneous marsh submersion/emersion condition. An outgoing water flux corresponding to root water uptake is specified in the soil layer within 0.30 m from the marsh surface [after Marani *et al.*, 2006a].

and that the subsurface water movement near tidal creeks is both vertical and horizontal, while farther from creeks, it is primarily vertical. Moreover, their study showed that if the soil saturated conductivity is relatively low (10^{-6} ms^{-1}) a persistently unsaturated zone is present below the soil surface even after the tide has flooded the marsh, providing evidence of the presence of a buried aerated layer allowing a prolonged presence of oxygen for aerobic root respiration. Furthermore, they showed that a strong positive feedback exists between the plants and the persistence of the aerated layer, since the vegetaion transpiration increases the extent and persistence of the aerated zone. Wilson and Gardner [2005] back the thesis of the existence of positive feedbacks between vegetation transpiration and saturated/unsaturated water flow with a numerical study that is based on the same system configuration as [Ursino *et al.*, 2004] but with different boundary conditions for the subsurface flow.

Marani *et al.* [2006b] improved the study proposed by Ursino *et al.* [2004] incorporating (i) more realistic soil characteristic representations, (ii) different possible boundary conditions, according with Wilson and Gardner [2005] and Marani *et al.* [2006b], including

Table 5.1: Parameters defining the soil types explored in the simulations [after Marani *et al.*, 2006b].

	Description	K_x [m/s]	K_z [m/s]	ψ_s [m]	S_{wr}	n	ϕ
SOIL1	high conductivity	10^{-5}	10^{-5}	-0.041	0.15	1.89	0.4
SOIL2	average conductivity	10^{-6}	10^{-6}	-0.130	0.15	1.89	0.4
SOIL3	average conductivity, anisotropic	10^{-7}	10^{-8}	-1.30	0.15	1.89	0.4
SOIL4	low conductivity	10^{-8}	10^{-8}	-1.30	0.15	1.89	0.4

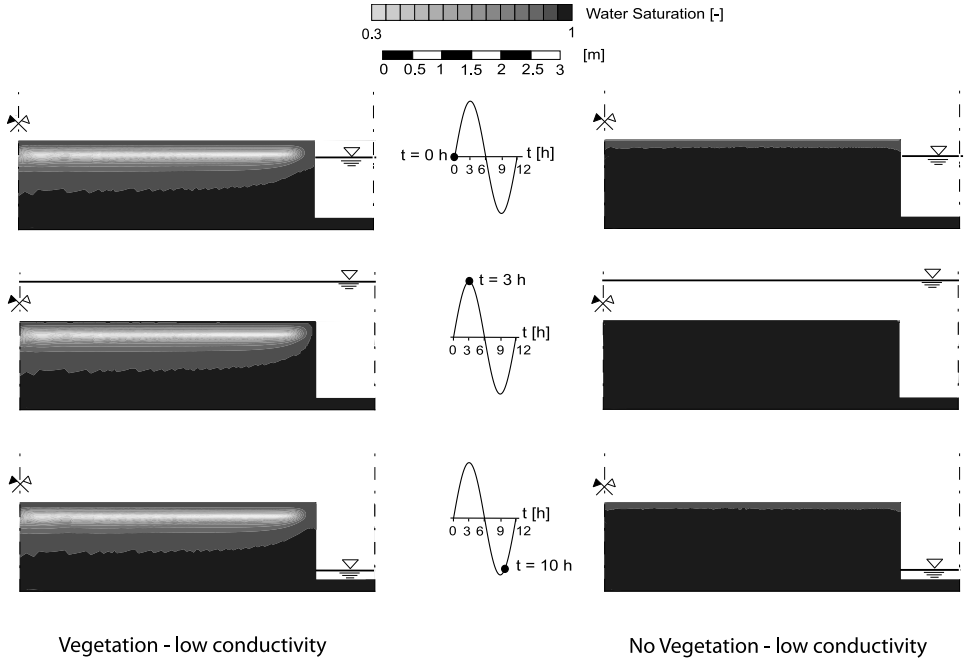

Figure 5.2: Time evolution of soil saturation (left) in a vegetated marsh and (right) in a nonvegetated tidal flat of equal elevation for the low conductivity soil type [after Marani *et al.*, 2006b]

seepage faces and atmospheric inputs (Figure 5.1); (iii) heterogeneous material properties and hydraulic characteristics (see Table 5.1); (iv) a simple vertical distribution of root water uptake within the upper 0.30 m of soil; (v) more realistical description of the different hydrologic regimes in non-vegetated tidal flats with respect to salt marshes.

The saturated/unsaturated water flow in salt marsh is studied by numerically solving the Richards' equation by means of a two dimensional triangle-based finite element simulator originally developed by Paniconi and Putti [1994]. The results obtained assuming an average evapotranspiration rate of 8 mm/d is assumed by the authors as representative of a realistic daily-averaged value. Figures 5.2 shows the results obtained by Marani *et al.* [2006b] for a soil characterised by a low isotropic hydraulic conductivity (SOIL4). A

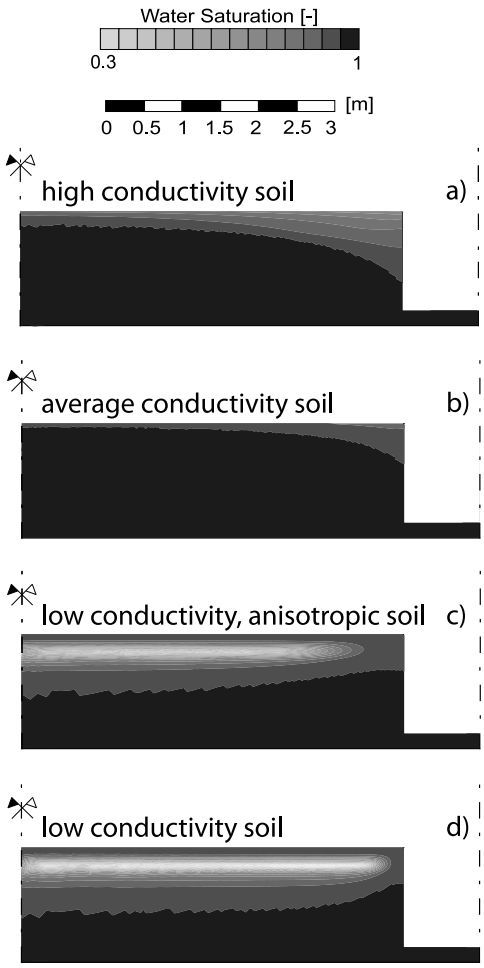

Figure 5.3: Soil water saturation averaged over a tidal cycle for marshes with the different soil types [after Marani *et al.*, 2006b]

permanently aerated layer exists in the vegetated case (thickness of about 0.30 m, roughly 0.10 m below the surface) as a result of root water uptake. Note that the soil is more aerated near the channel in the nonvegetated case, while the area of preferential aeration (with much lower water saturation values than in the previous case) is located in the inner portion of the vegetated marsh [Marani *et al.*, 2006b]. The application of the model to four different types of soil with increasing hydraulic conductivity, gives some interesting insights on the persistence of the aerated layer and the relation with soil permeability (Figure 5.3). Mean soil aeration over a tidal cycle decreases from a high-conductivity to an average-conductivity soil. On the contrary, it increases when passing from an average-conductivity to a low-conductivity soil. This transition is quite sharp and is due to the establishment of a balance between infiltration from the flooded marsh surface and root water uptake. The results confirm the classic field observations [Chapman, 1940] that the

aeratated layer might be absent close to ditches, because of horizontal water movement. The differences between isotropic and anisotropic soil cases show how the aeration regime is mainly governed by the vertical hydraulic conductivity, while horizontal redistribution is only effective within a short distance from the channel (about 1 m for the realistic horizontal hydraulic conductivity values assumed for SOIL3 and SOIL4) [Marani *et al.*, 2006b].

The role of air flow in the soil needs to be further addressed. Richards equation does not simulate movement of the gas phase and only applies when the gas phase is well connected to the atmosphere. In the tidal flow domain developed by Ursino *et al.* [2004] and adopted also by Marani *et al.* [2006b], the horizontal upper surface of the marsh is instantaneously inundated by the tide, isolating the gas phase from the atmosphere. This approximation is likely to lead to less aerated conditions in the model than in reality due to the fact that water fluxes are in reality partially opposed by the air presence.

Li and Lockington [2005] addressed the problem by using the two-phase flow simulator TOUGH2 [Pruess *et al.*, 1999] and including a depth-dependent sink function to represent evapotranspiration. The model is based on the mass balance equations of both phases [Bear, 1972] and the flow equation is described using the Darcy's law modified considering the permeability change owned to the presence of the other phase which occupies part of the void space. The mathematical formulation is completed by the specification of the constitutive equations relating phase saturations to capillary pressure and relative permeabilities to phase saturations [Brooks and Corey, 1964; van Genuchten, 1980] and by a function that describes the root water uptake dependent on the actual water saturation. The pressure and the saturation of air are assumed as primary variables, and in order to implement the boundary conditions assumes that the marsh surface and marsh-creek interfaces are covered by a thin layer of "imaginary material". This layer is such that its degree of saturation is equal to 0 if submerged in water and 1 if exposed in the air, and its absolute permeability is sufficiently large so that it can approximate with adequate accuracy the "free water" in the channel and "free air" in the atmosphere close to the soil surface [Li and Lockington, 2005]. Their results show that the effect of the airflow on water flow is not negligible when the marsh surface is submerged by tidal water, and different aeration patterns are obtained. Nevertheless, the positive feedback mechanism deduced from the simulations of the single-phase flow model of Ursino *et al.* [2004] is confirmed: pioneer plants increase evapotranspiration rates and absolute soil permeability and weaken the capillarity effects inducing the devolpment of other vegetation species in the salt-marsh [Li and Lockington, 2005].

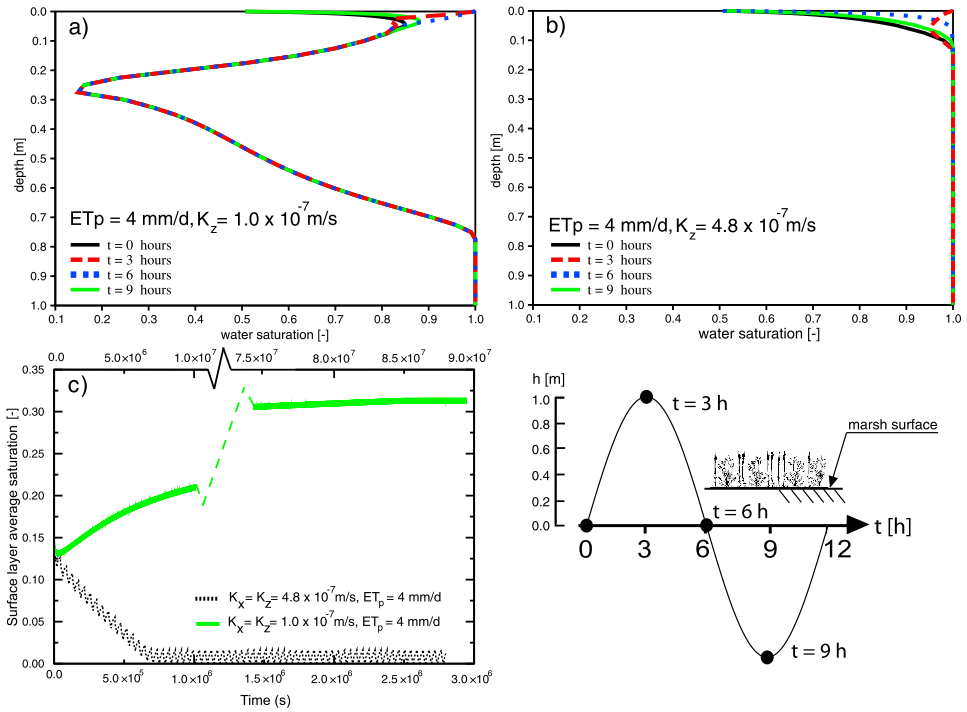

Figure 5.4: Dynamics of soil aeration for ETp = 4 mm/d and saturated hydraulic conductivity (a) below and (b) above the maximum conductivity threshold for the establishment of an aerated layer beneath the flooded surface. (c) The time required to bring the system to a periodic behavior, which is used as the reference condition in which to compute spatially averaged saturations [after Tosatto *et al.*, 2009].

Tosatto *et al.* [2009] proposed another two-phase flow model to simulate studied a 1-D system representing the marsh interior. Spatial boundary conditions are considered to improve the physical description of the atmosphere, vegetation, and soil interface proposed by [Li and Lockington, 2005]. On the bottom and of the sides of the 5 m high column [Marani *et al.*, 2006b] a no-flux boundary condition is imposed. On the top, if the marsh surface is flooded by the tidal water the wetting phase pressure is imposed according to the water level, whereas in the opposite case a fixed value of water saturation suitably calibrated on the topmost layer is imposed. The sensitivity of this value on the results was found to be low. Several numerical experiments were used to determine the minimum transpiration rate that allows the existence of a permanent buried aerated layer as a function of saturated conductivity. After running the simulations until it exhibited a periodic behavior and did not retain any memory of the arbitrary initial condition, Tosatto *et al.* [2009] took the minimum transpiration rate for permanent aeration to occur as the minimum value for which air saturation is greater than zero throughout a tidal cycle (Figure 5.5) Repetition of this analysis for different values of the saturated hydraulic

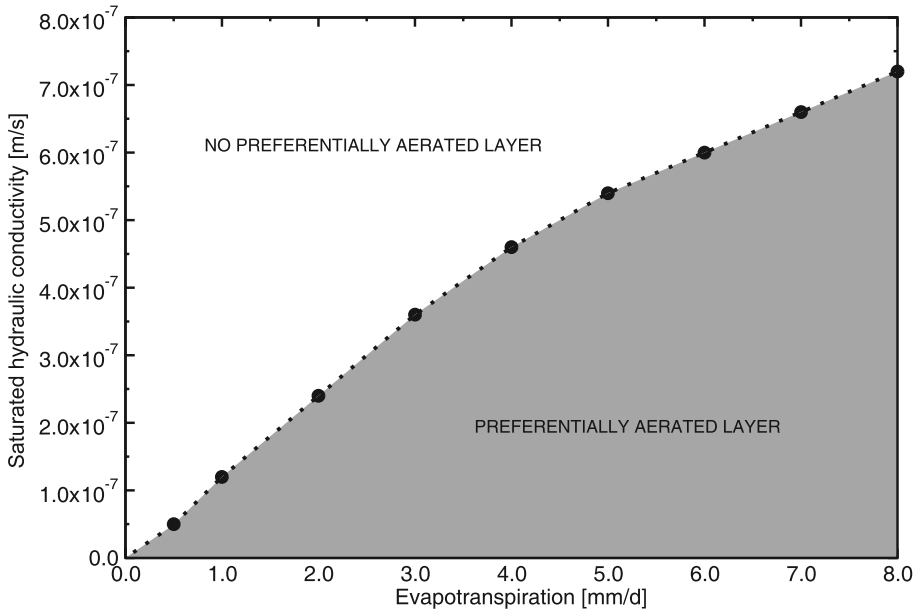

Figure 5.5: Saturated hydraulic conductivity and evapotranspiration rate values for which an aerated layer beneath the saturated surface starts to appear [after Tosatto *et al.*, 2009]

conductivity allows the determination of the relation between K_s and the minimum transpiration rate for which an aerated layer is sustained. A limit transpiration rate exists for a large range of realistic values of the saturated hydraulic conductivity (Figure 5.5). A comparison with the results provided by Marani *et al.* [2006b] shows that for a given value of the saturated hydraulic conductivity, the minimum value of the transpiration rate for which an aerated layer occurs is much smaller than the value obtained from the approach based on Richards equation, confirming the importance of considering the air flow dynamic. Both Li and Lockington [2005] and Tosatto *et al.* [2009] handle the boundary conditions at the interface soil - atmosphere using stratagems induced by the choice of primary variables in the respective models, and not representing the actual physical processes occurring in the field. A more natural approach requires th imposition of water pressure in the case the tidal level is higher than the marsh surface, and of the air pressure equal to the atmospheric value when the sea level is below the ground surface. With the aim of a more accurate description of the dynamics that characterize the salt-marshes, the following two-phase flow model using the pressures of the two phases as primary unknowns is developed and described in the following sections.

5.2 Mathematical Model of Air and Water Flow

5.2.1 General form for the mass balance equations

Continuity equation for a phase α compressible can be written as:

$$\frac{\partial}{\partial t}\left(\rho_\alpha \phi S_\alpha\right) = \nabla \cdot \left[\rho_\alpha \overrightarrow{q}_\alpha\right] + \rho_\alpha f_\alpha \tag{5.1}$$

where:

- t: time [s]
- ρ_α: density of the fluid α [$\mathrm{kg} \cdot \mathrm{m}^{-3}$]
- $\phi = V_v/V_T$: porosity of the medium [–]
- $S_\alpha = V_\alpha/V_v$: saturation of the fluid α [–]
- $\overrightarrow{q}_\alpha$: filtration velocity of the fluid α [$\mathrm{m} \cdot s^{-1}$]
- f_α: forcing term [s^{-1}]
- ∇: gradient operator [m^{-1}]

For isothermal flows in the vertical direction, the generalized Darcy's law for two immiscible fluids such as pure water and air, may be written as:

$$\overrightarrow{q}_\alpha = -K_S K_{r\alpha} \nabla \left(\frac{p_\alpha}{\rho_\alpha g} + z\right) \tag{5.2}$$

The saturated conductivity for the phase α is defined as:

$$K_S = \frac{k \rho_\alpha g}{\mu_\alpha} \tag{5.3}$$

hence:

$$\begin{aligned} \overrightarrow{q}_\alpha &= -\frac{k \rho_\alpha g}{\mu_\alpha} K_{r\alpha} \nabla \left(\frac{p_\alpha}{\rho_\alpha g} + z\right) \\ &= -k \frac{K_{r\alpha}}{\mu_\alpha} \left(\nabla p_\alpha + \rho_\alpha g \overrightarrow{\eta}_z\right) \\ &= -k \lambda_\alpha \left(\nabla p_\alpha + \rho_\alpha g \overrightarrow{\eta}_z\right) \end{aligned} \tag{5.4}$$

where:

- $K_{r\alpha}$: relative hydraulic conductivity [–]

- μ_α: viscosity of the fluid α [Pa·s]
- p_α: pressure of the fluid α [Pa]
- k: intrinsic permeability [m^2]
- g: gravity acceleration [$m \cdot s^{-2}$]
- $\overrightarrow{\eta}_z = [0, 0, 1]^T$: unit vertical vector [–]
- λ_α: phase α mobility [$(Pa \cdot s)^{-1}$]

Substituing the Darcy's law given by (5.4) in (5.1) and considering the specific case of water and air, the mass conservation equations will be, respectively:

Mass conservation of water

$$\frac{\partial}{\partial t}\left(\phi \rho_w S_w\right) = \nabla \cdot \left[\rho_w \frac{\mathrm{k} K_{rw}\left(S_w\right)}{\mu_w}\left(\nabla p_w + \rho_w g \overrightarrow{\eta}_z\right)\right] + \rho_w f_w \tag{5.5}$$

Mass conservation of air

$$\frac{\partial}{\partial t}\left(\phi \rho_a S_a\right) = \nabla \cdot \left[\rho_a \frac{\mathrm{k} K_{ra}\left(S_a\right)}{\mu_a}\left(\nabla p_a + \rho_a g \overrightarrow{\eta}_z\right)\right] + \rho_a f_a \tag{5.6}$$

5.2.2 Auxiliary equations and constitutive models

In order to determine a solution to this system, in addition to the two PDEs shown above, nine auxiliary relationships are needed and described in the following. Among the saturations of the two phases the ensuing relation is valid:

$$S_w + S_a = 1 \tag{5.7}$$

whereas, since air and water are two immiscible fluids (air diffusion into water is neglected), there exist a pressure difference (*capillary pressure*) between the two fluids:

$$p_c = p_g - p_w \tag{5.8}$$

In a general context of isothermal two phase flow, the densities of both fluids depend on the respective pressures:

Water density

$$\rho_w = \rho_w\left(p_w\right) \tag{5.9}$$

Air density

$$\rho_a = \rho_a\left(p_a\right) \tag{5.10}$$

Water viscosity

$$\mu_w = \mu_w\left(p_w\right) \tag{5.11}$$

Air viscosity

$$\mu_a = \mu_a\left(p_a\right) \tag{5.12}$$

The PDEs system is strongly nonlinear because relative permeabilities depend on water saturation, the last one depends in turn on capillary pressure, wheras phase densities and viscosities depend on the corresponding phase pressure. Capillary properties for a two phase system may be described using several different constitutive laws, in particular the relationship between water saturation and capillary pressure

$$S_w = S_w\left(p_c\right) \tag{5.13}$$

may be described by the one presented by van Genuchten (1980):

$$S_e = \frac{S_w - S_{wr}}{1 - S_{wr}} = \left[1 + \left(\alpha_{vg}\frac{p_c}{\rho_w g}\right)^n\right]^{1/n-1} \tag{5.14}$$

where:

- S_e: effective water saturation
- S_{wr}: residual water saturation
- $\alpha_{vg} = 1/p_s$: inverse of the air entry pressure p_s
- n_{vg}: fitting parameter, with values usaully ranging between $1.25 < n < 6$

Dependence of water residual conductivity on water saturation [Mualem, 1976]:

$$K_{rw} = \sqrt{S_e}\left[1 - \left(1 - S_e^{1/m}\right)^m\right]^2 \tag{5.15}$$

Dependence of air residual conductivity on water saturation [Mualem, 1976]:

$$K_{ra} = \left(1 - S_e\right)^2\left(1 - S_e^{1/m}\right)^{2m} \tag{5.16}$$

We have 11 unknowns, 5 of which are related to water (p_w,S_w,ρ_w,μ_w,K_{rw}), 5 to air (p_a,S_a,ρ_a,μ_a,K_{ra}) and the capillary pressure p_c. The generic boundary conditions are:

$$\begin{aligned} p_w &= p_1 \text{ on } \Gamma_{Dw} \\ p_a &= p_2 \text{ on } \Gamma_{Da} \\ -\left[\frac{\mathrm{k}K_{rw}(S_w)}{\mu_w}(\nabla p_w + \rho_w g \overrightarrow{\eta}_z)\right] \cdot \overrightarrow{n} &= q_{nw} \text{ on } \Gamma_{Nw} \\ -\left[\frac{\mathrm{k}K_{ra}(S_a)}{\mu_a}(\nabla p_a + \rho_a g \overrightarrow{\eta}_z)\right] \cdot \overrightarrow{n} &= q_{na} \text{ on } \Gamma_{Na} \end{aligned} \tag{5.17}$$

where $\Gamma = \Gamma_{Dw} + \Gamma_{Da} + \Gamma_{Nw} + \Gamma_{Na}$ is the border of the domain. Dimensionally, p_1 e p_2 are expressed in [Pa], wheras q_{nw} and q_{na} are expressed as $[m \cdot s^{-1}]$. The following relationships also stand:

$$\begin{aligned} S_s &= \rho_w g \left(\frac{\partial \phi}{\partial p_w} + \phi \cdot \frac{\partial \rho_w}{\partial p_w}\right) \\ &= \rho_w g (c_b + \phi\beta) \end{aligned} \tag{5.18}$$

where S_s is the *elastic storage coefficient*.

Hypothesis 1:

Let us assume that the water is incompressible whereas the air is a perfect gas, the state equation for both fluids may be written as:

$$\rho_\alpha = \rho_{0\alpha}\left(\frac{p_\alpha}{p_0}\right)^m \tag{5.19}$$

where $\rho_{0\alpha}$ is the specific mass of the fluid α at the atmospheric pressure p_0, namely

$$\rho_{0\alpha} = \begin{cases} 1000.0 \text{ kg} \cdot \text{m}^{-3} & \text{for water } (\alpha = w) \\ 1.161 \text{ kg} \cdot \text{m}^{-3} & \text{for air } (\alpha = a) \end{cases} \tag{5.20}$$

and

$$m = \begin{cases} 0 & \text{for water } (\alpha = w) \\ 1 & \text{for air } (\alpha = a) \end{cases} \tag{5.21}$$

Using the chain-rule the temporal derivatives in (5.5) and (5.6) become:

$$\frac{\partial}{\partial t}(\phi \rho_w S_w) = \rho_w S_w \frac{\partial \phi}{\partial t} + \phi \frac{\partial (\rho_w S_w)}{\partial t} \tag{5.22}$$

since $\rho_w = cost$, $\frac{\partial \rho_w}{\partial p_w} = 0$, it yields:

$$\frac{\partial \phi}{\partial p_w} = \frac{S_s}{\rho_w g} \frac{\partial p_w}{\partial t} \tag{5.23}$$

$$\begin{aligned} \frac{\partial (\rho_w S_w)}{\partial t} &= S_w \frac{\partial \rho_w}{\partial t} + \rho_w \frac{\partial S_w}{\partial t} \\ &= \rho_w \frac{\partial S_w}{\partial t} \end{aligned} \tag{5.24}$$

It follows that:

$$\frac{\partial}{\partial t} (\phi \rho_w S_w) = \rho_w \left[S_w \frac{S_s}{\rho_w g} \frac{\partial p_w}{\partial t} + \phi \frac{\partial S_w}{\partial t} \right] \tag{5.25}$$

Recalling the relationship (5.7) we can express the temporal derivative in (5.6) as follows:

$$\begin{aligned} \frac{\partial}{\partial t} (\phi \rho_a S_a) &= \frac{\partial}{\partial t} [\phi \rho_a (1 - S_w)] \\ &= \frac{\partial}{\partial t} (\phi \rho_a) - \frac{\partial (\phi \rho_a S_w)}{\partial t} \\ &= \rho_a \frac{\partial \phi}{\partial t} + \phi \frac{\partial \rho_a}{\partial t} - \left[\rho_a S_w \frac{\partial \phi}{\partial t} + \phi \frac{\partial (\rho_a S_w)}{\partial t} \right] \\ &= \rho_a \left[\frac{S_s}{\rho_w g} - S_w \frac{S_s}{\rho_w g} \right] \frac{\partial p_w}{\partial t} + \phi \left[\frac{\partial \rho_a}{\partial t} - \frac{\partial (\rho_a S_w)}{\partial t} \right] \\ &= \rho_a \left[(1 - S_w) \frac{S_s}{\rho_w g} \right] \frac{\partial p_w}{\partial t} + \phi \left[\frac{\partial \rho_a}{\partial t} - \frac{\partial (\rho_a S_w)}{\partial t} \right] \end{aligned} \tag{5.26}$$

If the porous medium is saturated in water, then $S_w = 1$ so the first part of the expression cancels, i.e.

$$\frac{\partial}{\partial t} (\phi \rho_a S_a) = \phi \left[\frac{\partial \rho_a}{\partial t} - \frac{\partial (\rho_a S_w)}{\partial t} \right] \tag{5.27}$$

Hypothesis 2:

In unsaturated conditions we assume:

$$\rho_a \left[\frac{S_s}{\rho_w g} - S_w \frac{S_s}{\rho_w g} \right] \frac{\partial p_w}{\partial t} \ll \phi \left[\frac{\partial \rho_a}{\partial t} - \frac{\partial (\rho_a S_w)}{\partial t} \right] \tag{5.28}$$

Hypothesis 3:

we assume that we can always neglect the first part of the temporal derivative, i.e.: $\rho_a [(S_s / (\rho_w g)) - S_w (S_s / (\rho_w g))] \partial p_w / \partial t$. The mass balance equations for water and air become respectively:

$$\rho_w \left[S_w \frac{S_s}{\rho_w g} \frac{\partial p_w}{\partial t} + \phi \frac{\partial (S_w)}{\partial t} \right] = \nabla \cdot [\rho_w k \lambda_w (S_w) (\nabla p_w + \rho_w g \overrightarrow{\eta}_z)] + \rho_w f_w \tag{5.29}$$

$$\phi\left[\frac{\partial \rho_a}{\partial t} - \frac{\partial}{\partial t}\left(\rho_a S_w\right)\right] = \nabla \cdot \left[\rho_a k \lambda_a\left(S_a\right)\left(\nabla p_a + \rho_a g \overrightarrow{\eta}_z\right)\right] + \rho_a f_a \tag{5.30}$$

in which:

$$\lambda_w = \frac{K_{rw}\left(S_w\right)}{\mu_w} \tag{5.31}$$

$$\lambda_a = \frac{K_{ra}\left(S_a\right)}{\mu_a} \tag{5.32}$$

are the mobilities of water and air. Neumann boundary conditions can be rewritten according to the definitions (5.31) and (5.32) as:

$$\begin{aligned} -\left[k\lambda_w\left(\nabla p_w + \rho_w g \overrightarrow{\eta}_z\right)\right] \cdot \overrightarrow{n} &= q_{nw} \text{ on } \Gamma_{Nw} \\ -\left[k\lambda_a\left(\nabla p_a + \rho_a g \overrightarrow{\eta}_z\right)\right] \cdot \overrightarrow{n} &= q_{na} \text{ on } \Gamma_{Na} \end{aligned} \tag{5.33}$$

5.3 Numerical Model

5.3.1 Numerical discretization

We use the *Method Of Lines* approach (MOL) [Sarmin and Chudov, 1963; Schiesser, 1991], by which the system of PDE is first discretized in space obtaining a system of ordinary differential equations in time coupled with the algebraic equations of state. An ODE solver (ideally a DAE solver) is then used to integrate in time.

Spatial discretization

The spatial discretization is performed using linear finite elements in conjunction with the Galerkin formulation. The finite element solution of the coupled system approximates the exact solution (p_w, p_a) by $(\hat{p}_w, \hat{p}_a)$ using linear basis functions $N\left(\mathbf{x}\right)$ defined over a domain Ω discretized by NE triangular finite elements and N nodes:

$$p_w \simeq \hat{p}_w = \sum_{j=1}^{N} p_{wj}\left(t\right) N_j\left(x, z\right) \tag{5.34}$$

$$p_a \simeq \hat{p}_a = \sum_{j=1}^{N} p_{aj}\left(t\right) N_j\left(x, z\right) \tag{5.35}$$

where p_{wj} and p_{aj} are the components of the nodal solution $\mathbf{p}_w$ and $\mathbf{p}_a$, respectively. The water saturation S_w, the air density ρ_a, and the product of air density ρ_a by water saturation S_w are approximated as:

$$S_w \simeq \hat{S}_w = \sum_{j=1}^{N} S_{wj}\left(t\right) N_j\left(x, z\right) \tag{5.36}$$

$$\rho_a \simeq \hat{\rho}_a = \sum_{j=1}^{N} \rho_{aj}(t) N_j(x,z) \tag{5.37}$$

$$S_w \rho_a = \xi \simeq \hat{\xi} = \sum_{j=1}^{N} \rho_{aj}(t) S_{wj}(t) N_j(x,z) \tag{5.38}$$

Mass balance equation for the water phase

Substituing the approximate solution and the capillary pressure expression into the mass balance equation of the water phase 5.29 the following residual is obtained:

$$L_1(\hat{p}_w, \hat{p}_a) = \nabla \cdot [\rho_w k \lambda_w (\nabla p_w + \rho_w g \overrightarrow{\eta}_z)] - \rho_w S_w \frac{S_s}{\rho_w g} \frac{\partial p_w}{\partial t} - \rho_w \phi \frac{\partial S_w}{\partial t} + \rho_w f_w \tag{5.39}$$

This residual is minimized by imposing an orthogonality constraint between the residual and the basis functions, which yields the Galerkin integral:

$$\int_\Omega L_1(\hat{p}_w, \hat{p}_a) N_i(x,z) = 0 \quad i = 1, \ldots, N \tag{5.40}$$

We assume that the coordinate directions are parallel to the principal directions of hydraulic anisotropy, so that the off-diagonal components of the permeability tensor k are zero:

$$k = \begin{bmatrix} k_x & 0 \\ 0 & k_z \end{bmatrix} \tag{5.41}$$

We make the following hypotheses:

Hypothesis 4:

S_s is "active" only when the medium is saturated in water ($S_w = 1$)

Hypothesis 5:

we assume $S_s \ll S_w$ and $S_s \ll \partial S_w / \partial p_w$.

From Hyp. 5 we obtain:

$$\int_\Omega \rho_w \hat{S}_w \frac{S_s}{\rho_w g} \frac{\partial \hat{p}_w}{\partial t} d\Omega \ll \int_\Omega \rho_w \phi \frac{\partial \hat{S}_w}{\partial \hat{p}_w} \frac{\partial \hat{p}_w}{\partial t} d\Omega = \int_\Omega \rho_w \phi \frac{\partial \hat{S}_w}{\partial t} \tag{5.42}$$

Expanding equation (5.40) we have:

$$\begin{aligned}
&\int_{\Omega} \left\{\nabla \cdot \left[\rho_w k \lambda_w \left(\nabla \hat{p}_w + \rho_w g \overrightarrow{\eta}_z\right)\right]\right\} N_i d\Omega \\
&- \int_{\Omega} \left[\rho_w S_w \frac{S_s}{\rho_w g} \frac{\partial \hat{p}_w}{\partial t}\right] N_i d\Omega \\
&- \int_{\Omega} \left[\rho_w \phi \frac{\partial \hat{S}_w}{\partial t}\right] N_i d\Omega \\
&+ \int_{\Omega} \rho_w f_w N_i d\Omega = 0 \qquad i = 1, \ldots, N
\end{aligned} \tag{5.43}$$

Using Green's Lemma for the spatial derivatives of the first integral we obtain:

$$\begin{aligned}
&\int_{\Omega} \left\{\nabla \cdot \left[\rho_w k \lambda_w \left(\nabla \hat{p}_w + \rho_w g \overrightarrow{\eta}_z\right)\right]\right\} N_i d\Omega = \\
&\qquad - \int_{\Omega} \rho_w k \lambda_w \left(\nabla \hat{p}_w + \rho_w g \overrightarrow{\eta}_z\right) \cdot \nabla N_i d\Omega \\
&+ \int_{\Gamma} \rho_w k \lambda_w \left[\left(\nabla \hat{p}_w + \rho_w g \overrightarrow{\eta}_z\right) \cdot \overrightarrow{n}\right] N_i d\Gamma \qquad i = 1, \ldots, N
\end{aligned} \tag{5.44}$$

Imposing Neumann boundary conditions on Γ_{Nw} we have

$$\begin{aligned}
&\int_{\Omega} \left\{\nabla \cdot \left[\rho_w k \lambda_w \left(\nabla \hat{p}_w + \rho_w g \overrightarrow{\eta}_z\right)\right]\right\} N_i d\Omega = \\
&\qquad - \int_{\Omega} \left[\rho_w k_z \lambda_w \left(\nabla \hat{p}_w + \rho_w g \overrightarrow{\eta}_z\right) \cdot \nabla N_i d\Omega\right. \\
&\qquad\qquad - \int_{\Gamma_{Nw}} \rho_w q_{nw} N_i d\Gamma \qquad i = 1, \ldots, N
\end{aligned} \tag{5.45}$$

If we substitute (5.45) into (5.43) and changing sign we obtain

$$\begin{aligned}
&\int_{\Omega} \rho_w k \lambda_w \left(\nabla \hat{p}_w \cdot \nabla N_i\right) d\Omega \\
&+ \int_{\Omega} \rho_w^2 k_z \lambda_w g \left(\overrightarrow{\eta}_z \cdot \nabla N_i\right) d\Omega \\
&+ \int_{\Omega} \rho_w S_w \frac{S_s}{\rho_w g} \frac{\partial \hat{p}_w}{\partial t} N_i d\Omega \\
&+ \int_{\Omega} \rho_w \phi \frac{\partial \hat{S}_w}{\partial t} N_i d\Omega \\
&- \int_{\Omega} \rho_w f_w N_i d\Omega \\
&+ \int_{\Gamma_{Nw}} \rho_w q_{nw} N_i d\Gamma = 0 \qquad i = 1, \ldots, N
\end{aligned} \tag{5.46}$$

Introducing (5.34) and (5.36), we obtain the following system of differential algebraic equations:

$$\begin{aligned}
&\sum_{j=1}^{N} \hat{p}_{wj} \int_{\Omega} \rho_w k \lambda_w \left(\nabla N_j \cdot \nabla N_i\right) d\Omega \\
&+ \sum_{j=1}^{N} \frac{\partial \hat{p}_{wj}}{\partial t} \int_{\Omega} \rho_w S_w \frac{S_s}{\rho_w g} N_j N_i d\Omega \\
&+ \sum_{j=1}^{N} \frac{\partial \hat{S}_{wj}}{\partial t} \int_{\Omega} \rho_w \phi N_j N_i d\Omega \\
&+ \int_{\Omega} \rho_w^2 k_z \lambda_w g \left(\overrightarrow{\eta}_z \cdot \nabla N_i\right) d\Omega \\
&- \int_{\Omega} \rho_w f_w N_i d\Omega \\
&+ \int_{\Gamma_{Nw}} \rho_w q_{nw} N_i d\Gamma = 0 \qquad i = 1, \ldots, N
\end{aligned} \tag{5.47}$$

Water stiffness and mass matrices coefficients

The system of Differential Algebraic Equations (DAEs) (5.47) can be rewritten in matricial form as:

$$H_w P_w + C_{w1} \frac{dP_w}{dt} + C_{w2} \frac{dS_w}{dt} + b_{w1} + b_{w2} = 0 \tag{5.48}$$

where

$$h_{wij} = \sum_{e=1}^{NE} h_{wij}^e = \sum_{e=1}^{NE} \int_{\Omega^e} \rho_w k \lambda_w^e \left(\nabla N_j^e \cdot \nabla N_i^e\right) d\Omega \tag{5.49}$$

$$c_{w1ij} = \sum_{e=1}^{NE} c_{w1ij}^e = \sum_{e=1}^{NE} \int_{\Omega^e} \rho_w S_w \frac{S_s}{\rho_w g} N_j^e N_i^e d\Omega \tag{5.50}$$

$$c_{w2ij} = \sum_{e=1}^{NE} c_{w2ij}^e = \sum_{e=1}^{NE} \int_{\Omega^e} \phi \rho_w N_j^e N_i^e d\Omega \tag{5.51}$$

$$b_{w1i} = \sum_{e=1}^{NE} b_{w1i}^e = \sum_{e=1}^{NE} \int_{\Omega^e} \rho_w^2 k_z \lambda_w^e g \left(\overrightarrow{\eta}_z \cdot \nabla N_i^e\right) d\Omega \tag{5.52}$$

$$b_{w2i} = \sum_{e=1}^{NE} b_{w2i}^e = -\sum_{e=1}^{NE} \int_{\Omega^e} \rho_w f_w N_i^e d\Omega + \sum_{e=1}^{NE} \int_{\Gamma_{Nw}^e} \rho_w q_{nw} N_i^e d\Gamma \tag{5.53}$$

In the above equations $H_w = \{h_{wij}\}$ is the water flow stiffness matrix, whereas $C_{w1} = \{c_{w1ij}\}$ and $C_{w2} = \{c_{w2ij}\}$ are the the mass (or capacity) matrices, $b_{w1} = \{b_{w1i}\}$ accounts for the gravitational gradient term, $b_{w2} = \{b_{w2i}\}$ incorporates the withdrawal or injection

rate and the prescribed boundary flux. k_z is the vertical component of the permeability tensor. Vector P_w contains the unknown nodal water pressure values, whereas vectors $\frac{dP_w}{dt}$ and $\frac{dS_w}{dt}$ contain the unknown nodal time derivatives values of water pressure and saturation. The linear basis function N_i^e for the generic triangle e with vertices i, j, k is $N_i^e = (a_i + b_i x + c_i z)/2A^e$ where the area A^e of the element can be calculated as

$$A_e = \frac{1}{2}\begin{vmatrix} 1 & x_i & z_i \\ 1 & x_j & z_j \\ 1 & x_k & z_k \end{vmatrix} \tag{5.54}$$

and

$$a_i = \begin{vmatrix} x_j & z_j \\ x_k & z_k \end{vmatrix} \tag{5.55}$$

$$b_i = -\begin{vmatrix} 1 & z_j \\ 1 & z_k \end{vmatrix} \tag{5.56}$$

$$c_i = \begin{vmatrix} 1 & x_j \\ 1 & x_k \end{vmatrix} \tag{5.57}$$

The ijth coefficent of matrices H_w, C_{w1}, and C_{w2} are given respectively by:

$$\begin{aligned} h_{wij} &= \sum_{e=1}^{NE} h_{wij}^e \\ c_{w1ij} &= \sum_{e=1}^{NE} c_{w1ij}^e \\ c_{w2ij} &= \sum_{e=1}^{NE} c_{w2ij}^e \end{aligned} \tag{5.58}$$

where:

$$\begin{aligned} h_{wij}^e &= \int_{\Omega^e} \rho_w k_x \lambda_w^e \frac{\partial N_j^e}{\partial x}\frac{\partial N_i^e}{\partial x} d\Omega^e + \int_{\Omega^e} \rho_w k_z \lambda_w^e \frac{\partial N_j^e}{\partial z}\frac{\partial N_i^e}{\partial z} d\Omega^e \\ &= \rho_w \frac{\lambda_w^e}{4A^e}\left(k_x b_i b_j + k_z c_i c_j\right) \end{aligned} \tag{5.59}$$

$$\begin{aligned} c_{w1ij}^e &= \int_{\Omega^e} \rho_w S_w \frac{S_s}{\rho_w g} N_j^e N_i^e d\Omega^e \\ &= \frac{S_s}{g} \cdot \begin{cases} \frac{1}{6} A^e & i = j \\ \frac{1}{12} A^e & i \neq j \end{cases} \end{aligned} \tag{5.60}$$

$$
\begin{aligned}
c^e_{w2ij} &= \int_{\Omega^e} \rho_w \phi N^e_j N^e_i d\Omega^e \\
&= \rho_w \phi \begin{cases} \dfrac{1}{6} A^e i = j \\ \dfrac{1}{12} A^e i \neq j \end{cases}
\end{aligned} \tag{5.61}
$$

Similarly, the ith coefficent of the vectors b_{w1} and b_{w2} can be defined as

$$
\begin{aligned}
b_{w1i} &= \int_{\Omega^e} \rho_w^2 k_z \lambda^e_w g \left(\overrightarrow{\eta}_z \cdot \nabla N^e_i \right) d\Omega^e \\
&= \rho_w^2 k_z \lambda^e_w g \int_{\Omega^e} \frac{\partial N^e_i}{\partial z} d\Omega^e \\
&= \rho_w^2 k_z \lambda^e_w g c_i \frac{A^e}{|A^e|}
\end{aligned} \tag{5.62}
$$

$$
\begin{aligned}
b_{w2i} &= -\int_{\Omega^e} \rho_w f_w N^e_i d\Omega^e + \int_{\Gamma^e_{Nw}} \rho_w q_{nw} N^e_i d\Gamma \\
&= -\rho_w f_w \frac{A^e}{3} + \rho_w q_{nw} \frac{l^e}{2}
\end{aligned} \tag{5.63}
$$

Mass matrices C_{w1} and C_{w2} are lumped for stability reasons, hence they are diagonal, whereas stiffness matrix H_w is symmetric positive definite.

Mass balance equation for the air phase

Following a similar procedure for the air mass balance equation (5.30) yields the expression:

$$
\begin{aligned}
&\int_\Omega \rho_a k \lambda_a \left(\nabla \hat{p}_a \cdot \nabla N_i \right) d\Omega \\
&+ \int_\Omega \rho_a^2 k_z \lambda_a g \left(\overrightarrow{\eta}_z \cdot \nabla N_i \right) d\Omega \\
&+ \int_\Omega \phi \frac{\partial \hat{\rho}_a}{\partial t} N_i d\Omega \\
&- \int_\Omega \phi \frac{\partial \hat{\xi}}{\partial t} N_i d\Omega \\
&- \int_\Omega \hat{\rho}_a f_a N_i d\Omega \\
&+ \int_{\Gamma_{Na}} \rho_a q_{na} N_i d\Gamma = 0 \quad i = 1, \ldots, N
\end{aligned} \tag{5.64}
$$

Introducing (5.35), (5.37), and (5.38) we obtain the following system of ordinary differential equations:

$$\begin{aligned}
&\sum_{j=1}^{N} \hat{p}_{aj} \int_{\Omega} \rho_a k \lambda_a \left(\nabla N_j \cdot \nabla N_i\right) d\Omega \\
&+ \sum_{j=1}^{N} \frac{\partial \hat{\rho}_{aj}}{\partial t} \int_{\Omega} \phi N_j N_i d\Omega \\
&- \sum_{j=1}^{N} \frac{\partial \hat{\xi}_{aj}}{\partial t} \int_{\Omega} \phi N_j N_i d\Omega \\
&+ \int_{\Omega} \hat{\rho}_a^2 k_z \lambda_a g \left(\overrightarrow{\eta}_z \cdot \nabla N_i\right) d\Omega \\
&- \int_{\Omega} \hat{\rho}_a f_a N_i d\Omega \\
&+ \int_{\Gamma_{Na}} \hat{\rho}_a q_{na} N_i d\Gamma = 0 \qquad i = 1, \ldots, N
\end{aligned} \tag{5.65}$$

Air stiffness and mass matrices coefficients

The system of differential equations (5.65) can be rewritten in matricial form as:

$$H_a P_a + C_a \left[\frac{d\rho_a}{dt} - \frac{d\xi}{dt}\right] + b_{g1} + b_{g2} = 0 \tag{5.66}$$

where

$$h_{aij} = \sum_{e=1}^{NE} h_{aij}^e = \sum_{e=1}^{NE} \int_{\Omega^e} \rho_a k \lambda_a^e \left(\nabla N_j^e \cdot \nabla N_i^e\right) d\Omega \tag{5.67}$$

$$c_{aij} = \sum_{e=1}^{NE} c_{aij}^e = \sum_{e=1}^{NE} \int_{\Omega^e} \phi N_j^e N_i^e d\Omega \tag{5.68}$$

$$b_{a1i} = \sum_{e=1}^{NE} b_{a1i}^e = \sum_{e=1}^{NE} \int_{\Omega^e} \rho_a^2 k_z \lambda_a^e g \left(\overrightarrow{\eta}_z \cdot \nabla N_i\right)^e d\Omega \tag{5.69}$$

$$b_{a2i} = \sum_{e=1}^{NE} b_{a2i}^e = -\sum_{e=1}^{NE} \int_{\Omega^e} \rho_a f_a N_i^e d\Omega + \sum_{e=1}^{NE} \int_{\Gamma_{Na}^e} \rho_a q_{na} N_i^e d\Gamma \tag{5.70}$$

In the above equations $H_a = \{h_{aij}\}$ is the air flow stiffness matrix, whereas $C_a = \{c_{aij}\}$ is the mass (or capacity) matrix, $b_{a1} = \{b_{a1i}\}$ accounts for the gravitational gradient term, $b_{a2} = \{b_{a2i}\}$ incorporates the withdrawal or injection rate and the prescribed boundary flux. Vector P_a contains the unknown nodal air pressure values, whereas vectors $d\rho_a/dt$ and $d\xi/dt$ contain the unknown nodal time derivatives values of air density and of the product of air density by water saturation.

The coefficient of the local stiffness and capacity matrices can be defined as follows:

$$\begin{aligned} h^e_{aij} &= \int_{\Omega^e} \rho_a k_x \lambda^e_w \frac{\partial N^e_j}{\partial x}\frac{\partial N^e_i}{\partial x} d\Omega^e + \int_{\Omega^e} \rho_a k_z \lambda^e_w \frac{\partial N^e_j}{\partial z}\frac{\partial N^e_i}{\partial z} d\Omega^e \\ &= \rho_a \frac{\lambda^e_a}{4A^e}\left(k_x b_i b_j + k_z c_i c_j\right) \end{aligned} \tag{5.71}$$

$$\begin{aligned} c^e_{aij} &= \int_{\Omega^e} \phi N^e_j N^e_i d\Omega^e \\ &= \phi \begin{cases} \dfrac{1}{6}A^e & i = j \\ \dfrac{1}{12}A^e & i \neq j \end{cases} \end{aligned} \tag{5.72}$$

In the same way we can define the ith component of the vectors b_{a1} and b_{a2}:

$$\begin{aligned} b_{a1i} &= \int_{\Omega^e} \rho_a^2 k_z \lambda^e_a g\left(\overrightarrow{\eta}_z \cdot \nabla N^e_i\right) d\Omega^e \\ &= \rho_a^2 k_z \lambda^e_a g \int_{\Omega^e} \frac{\partial N^e_i}{\partial z} d\Omega^e \\ &= \rho_a^2 k_z \lambda^e_a g c_i \frac{A^e}{|A^e|} \end{aligned} \tag{5.73}$$

$$\begin{aligned} b_{a2i} &= -\int_{\Omega^e} \rho_a f_a N^e_i d\Omega^e + \int_{\Gamma^e_{Na}} \rho_a q_{na} N^e_i d\Gamma \\ &= -\rho_a f_a \frac{A^e}{3} + \rho_a q_{na}\frac{l^e}{2} \end{aligned} \tag{5.74}$$

Also in this case the mass matrix C_a is lumped for stability reasons, hence it is diagonal, whereas stiffness matrix H_a is symmetric positive definite.

Time discretization

The temporal discretization of equations (5.48) and (5.66) is obtained by Euler backward finite difference, giving rise to the following nonlinear system of albebraic equations to be solved at each time step:

$$H_w P^{n+1}_w + \frac{C_{w1}}{\Delta t^{(n)}}\left[P^{n+1}_w - P^n_w\right] + \frac{C_{w2}}{\Delta t^{(n)}}\left[S^{n+1}_w - S^n_w\right] + b_{w1}\left(S^n_w\right) + b_{w2} = 0 \tag{5.75}$$

$$H_a P^{n+1}_a + \frac{C_a}{\Delta t^{(n)}}\left[\rho^{n+1}_a - \rho^n_a\right] - \frac{C_a}{\Delta t^{(n)}}\left[\xi^{n+1} - \xi^n\right] + b_{g1}\left(\rho_a S^n_w\right) + b_{g2}\left(\rho^n_a\right) = 0 \tag{5.76}$$

where Δt^n is the time step size; $n+1$ and n are the current and the previous time step, respectively.

5.3.2 Nonlinear scheme

At each time step the nonlinear system resulting from (5.75) and (5.76) is solved by means of Picard iterative method. To this aim the equations (5.75) and (5.76) are rewritten as:

$$f\left(u^{n+1}\right) = A\left(u^{n+1}\right)u^{n+1} - b^{*}u^{n+1} = 0 \tag{5.77}$$

Expanding $f\left(u^{n+1}\right)$ and denoting with r the nonlinear iteration counter, we obtain:

$$f\left(u^{n+1,r+1}\right) = f\left(u^{n+1,r}\right) + f'\left(u^{n+1i,r}\right)s^{r+1} + \ldots = 0 \tag{5.78}$$

where $s^{r+1} = \left(u^{n+1,r+1} - u^{n+1,r}\right)$ is the current search direction vector. The Newton's iteration reads:

$$J\left(u^{n+1,r}\right)s^{r+1} = -f\left(u^{n+1,r}\right) \quad u^{n+1,r+1} = u^{n+1,r} + s^{r+1} \tag{5.79}$$

where the Jacobian matrix is given by $J = A + A'u - b'$, the superscript indicates vector differentiation. In the case of the model we developed, the full Jacobian is approximated by neglecting A' and b', i.e. the Picard scheme is used.Nonlinear convergence is achieved when the search direction norm fullfills one of the following tests:

$$\|s^{r+1}\| \leq \epsilon_{nl} \quad \text{and} \quad \max_i|s_i^{r+1}| \leq \epsilon_{nl} \tag{5.80}$$

where $\|\cdot\|$ is the Euclidean norm. Another possibility is to consider a test based on the relative nonlinear residual:

$$\|f\left(u^{n+1,r+1}\right)\| \leq \epsilon_{nl}\|f\left(u^{n+1,0}\right)\| \tag{5.81}$$

If we expand $S_w^{n+1,r+1}$, $\rho_a^{n+1,r+1}$ and $\xi^{n+1,r+1}$ according with (5.78) the following expansions hold:

$$S_w^{n+1,r+1} = S_w^{n+1,r} + \frac{\partial S_w}{\partial p_c}^{n+1,r}\left(p_c^{n+1,r+1} - p_c^{n+1,r}\right) + \ldots \tag{5.82}$$

Recalling (5.8)

$$\begin{aligned} S_w^{n+1,r+1} &= S_w^{n+1,r} + \frac{\partial S_w}{\partial p_c}^{n+1,r}\left[\left(p_a^{n+1,r+1} - p_w^{n+1,r+1}\right) - \left(p_a^{n+1,r} - p_w^{n+1,r}\right)\right] \\ &= S_w^{n+1,r} + \frac{\partial S_w}{\partial p_c}^{n+1,r}\left[\left(p_a^{n+1,r+1} - p_a^{n+1,r}\right) - \left(p_w^{n+1,r+1} - p_w^{n+1,r}\right)\right] \end{aligned} \tag{5.83}$$

$$\rho_a^{n+1,r+1} = \rho_a^{n+1,r} + \frac{\partial \rho_a}{\partial p_a}^{n+1,r}\left(p_a^{n+1,r+1} - p_a^{n+1,r}\right) + \ldots \tag{5.84}$$

$$\begin{aligned}\xi^{n+1,r+1} = S_w \rho_a^{n+1,r+1} = \xi^{n+1,r} + \frac{\partial \xi}{\partial p_a}^{n+1,r} \left(p_a^{n+1,r+1} - p_a^{n+1,r}\right) + \\ + \frac{\partial \xi}{\partial p_w}^{n+1,r} \left(p_w^{n+1,r+1} - p_w^{n+1,r}\right)\end{aligned} \tag{5.85}$$

Applying the chain-rule we obtain:

$$\begin{aligned}\frac{\partial \xi}{\partial p_a}^{n+1,r} &= \rho_a \frac{\partial S_w}{\partial p_a} + S_w \frac{\partial \rho_a}{\partial p_a} \\ &= \rho_a \frac{\partial S_w}{\partial p_c}\frac{\partial p_c}{\partial p_a} + S_w \frac{\partial \rho_a}{\partial p_a} \\ &= \rho_a \frac{\partial S_w}{\partial p_c} + S_w \frac{\partial \rho_a}{\partial p_a}\end{aligned} \tag{5.86}$$

$$\begin{aligned}\frac{\partial \xi}{\partial p_w}^{n+1,r} &= \rho_a \frac{\partial S_w}{\partial p_w} + S_w \frac{\partial \rho_a}{\partial p_w} \\ &= \rho_a \frac{\partial S_w}{\partial p_c}\frac{\partial p_c}{\partial p_w} \\ &= -\rho_a \frac{\partial S_w}{\partial p_c}\end{aligned} \tag{5.87}$$

If we introduce expressions (5.86) and (5.87) in (5.85)

$$\begin{aligned}\xi^{n+1,r+1} = \xi^{n+1,r} + \left[\rho_a \frac{\partial S_w}{\partial p_c} + S_w \frac{\partial \rho_a}{\partial p_a}\right]^{n+1,r} \left(p_a^{n+1,r+1} - p_a^{n+1,r}\right) \\ - \rho_a \frac{\partial S_w}{\partial p_c}^{n+1,r} \left(p_w^{n+1,r+1} - p_w^{n+1,r}\right)\end{aligned} \tag{5.88}$$

We define:

$$R = \text{diag}\left\{\rho_{ai}\right\} \tag{5.89}$$

$$S = \text{diag}\left\{S_{wi}\right\} \tag{5.90}$$

$$U = \text{diag}\left\{\frac{\partial \rho_a}{\partial p_{ai}}\right\} \tag{5.91}$$

$$W = \text{diag}\left\{\frac{\partial S_w}{\partial p_{ci}}\right\} \tag{5.92}$$

$$\delta_w = p_w^{n+1,r+1} - p_w^{n+1,r} \tag{5.93}$$

$$\delta_a = p_a^{n+1,r+1} - p_a^{n+1,r} \tag{5.94}$$

Introducing the previous expressions in (5.83), (5.84), and (5.88) leads to the following approximations:

$$S_w^{n+1,r+1} = S_w^{n+1,r} + W^{n+1,r}\delta_a^{n+1} - W^{n+1,r}\delta_w^{n+1} \tag{5.95}$$

$$\rho_a^{n+1,r+1} = \rho_a^{n+1,r} + U^{n+1,r}\delta_a^{n+1} \tag{5.96}$$

$$\begin{aligned}\xi^{n+1,r+1} &= \xi^{n+1,r} + R^{n+1,r}W^{n+1,r}\left(\delta_a^{n+1} - \delta_w^{n+1}\right) \\ &+ SU^{n+1,r}\delta_a^{n+1} \\ &= \xi^{n+1,r} + R^{n+1,r}W^{n+1,r}\delta_a^{n+1} \\ &- R^{n+1,r}W^{n+1,r}\delta_w^{n+1} \\ &+ S^{n+1,r}U^{n+1,r}\delta_a^{n+1}\end{aligned} \tag{5.97}$$

Water

If we rearrange the terms of (5.75) in such a way that all terms evaluated at time step n are moved to the right hand side as well as the vectors b_{w1} and b_{w2}, it yields

$$H_w P_w^{n+1,r+1} + \frac{C_{w1}}{\Delta t^{(n)}} P_w^{n+1,r+1} + \frac{C_{w2}}{\Delta t^{(n)}} S_w^{n+1,r+1} = \frac{C_{w1}}{\Delta t^{(n)}} P_w^n + \frac{C_{w2}}{\Delta t^{(n)}} S_w^n - \left\{b_{w1}\left(S_w^n\right) + b_{w2}\right\} \tag{5.98}$$

If we apply the Picard linearization scheme to (5.98):

$$\begin{aligned}H_w\left(P_w^{n+1,r} + \delta_w^{n+1}\right) + \frac{C_{w1}}{\Delta t^{(n)}}\left(P_w^{n+1,r} + \delta_w^{n+1}\right) + \frac{C_{w2}}{\Delta t^{(n)}}\left[S_w^{n+1,r} + W^{n+1,r}\delta_a^{n+1} - W^{n+1,r}\delta_w^{n+1}\right] = \\ = \frac{C_{w1}}{\Delta t^{(n)}} P_w^n + \frac{C_{w2}}{\Delta t^{(n)}} S_w^n - \left\{b_{w1}\left(S_w^n\right) + b_{w2}\right\}\end{aligned} \tag{5.99}$$

$$\begin{aligned}\left[H_w + \frac{C_{w1}}{\Delta t^{(n)}} - \frac{C_{w2}}{\Delta t^{(n)}}W\right]^{n+1,r}\delta_w^{n+1} + \left[\frac{C_{w2}}{\Delta t^{(n)}}W\right]^{n+1,r}\delta_a^{n+1} = \\ = -\left\{\frac{C_{w1}}{\Delta t^{(n)}}\left(P_w^{n+1,r} - P_w^n\right) + \frac{C_{w2}}{\Delta t^{(n)}}\left(S_w^{n+1,r} - S_w^n\right) + H_w P_w^{n+1,r} + b_{w1}\left(S_w^n\right) + b_{w2}\right\}\end{aligned} \tag{5.100}$$

We define the following matrices

$$A_w^{n+1,r} = \left[H_w + \frac{C_{w1}}{\Delta t^{(n)}} - \frac{C_{w2}}{\Delta t^{(n)}}W\right]^{n+1,r} \tag{5.101}$$

$$B_w^{n+1,r} = \frac{C_{w2}}{\Delta t^{(n)}}W^{n+1,r} \tag{5.102}$$

and the right hand side as the vector

$$d_w^{n+1,r} = -\left\{\frac{C_{w1}}{\Delta t^{(n)}}\left(P_w^{n+1,r} - P_w^n\right) + \frac{C_{w2}}{\Delta t^{(n)}}\left(S_w^{n+1,r} - S_w^n\right) + H_w P_w^{n+1,r} + b_{w1}\left(S_w^n\right) + b_{w2}\right\} \tag{5.103}$$

we can rewrite the system as:

$$A_w^{n+1,r}\delta_w^{n+1} + B_w^{n+1,r}\delta_a^{n+1} = d_w^{n+1,r} \tag{5.104}$$

Air

We proceed in a similar way for the air phase: first we rewrite (5.76) in such a way that only the terms multiplied by the unknown vectors evaluated at the current time step $n+1$ are on the left hand side:

$$H_a P_a^{n+1,r+1} + \frac{C_a}{\Delta t^{(n)}} \left[\rho_a^{n+1,r+1} - \xi^{n+1,r+1}\right] = \frac{C_a}{\Delta t^{(n)}} \left[\rho_a^n - \xi^n\right] - b_{g1}\left(\rho_a^n S_w^n\right) - b_{g2}\left(\rho_a^n\right) \quad (5.105)$$

Introducing the relationships (5.96) and (5.97) it yields:

$$\begin{aligned} &H_a\left(P_a^{n+1,r} + \delta_a^{n+1}\right) + \frac{C_a}{\Delta t^{(n)}}\left(\rho_a^{n+1,r} + U^{n+1,r}\delta_a^{n+1}\right) + \\ &-\frac{C_a}{\Delta t^{(n)}}\left(\xi^{n+1,r} + R^{n+1,r}W^{n+1,r}\delta_a^{n+1} - R^{n+1,r}W^{n+1,r}\delta_w^{n+1} + S^{n+1,r}U^{n+1,r}\delta_a^{n+1}\right) \\ &= \frac{C_a}{\Delta t^{(n)}}\left[\rho_a^n - \xi^n\right] - b_{g1}\left(\rho_a^n S_w^n\right) - b_{g2}\left(\rho_a^n\right) \end{aligned} \quad (5.106)$$

$$\begin{aligned} &l\left[H_a + \frac{C_a}{\Delta t^{(n)}}U^{n+1,r} - \frac{C_a}{\Delta t^{(n)}}\left(R^{n+1,r}W^{n+1,r} + S^{n+1,r}U^{n+1,r}\right)\right]\delta_a^{n+1} + \frac{C_a}{\Delta t^{(n)}}R^{n+1,r}W^{n+1,r}\delta_w^{n+1} \\ &= -\left\{H_a P_a^{n+1,r} + \frac{C_a}{\Delta t^{(n)}}\left[\left(\rho_a^{n+1,r} - \rho_a^n\right) - \left(\xi^{n+1,r} - \xi^n\right)\right] + b_{g1}\left(\rho_a^n S_w^n\right) + b_{g2}\left(\rho_a^n\right)\right\} \end{aligned} \quad (5.107)$$

We define two matrices $A_a^{n+1,r}$ and $B_a^{n+1,r}$

$$A_a^{n+1,r} = \left[H_a + \frac{C_a}{\Delta t^{(n)}}\left(U - RW - SU\right)\right]^{n+1,r} \quad (5.108)$$

$$B_w^{n+1,r} = \left[\frac{C_a}{\Delta t^{(n)}}RW\right]^{n+1,r} \quad (5.109)$$

and the right hand side as the vector

$$d_a^{n+1,r} = -\left\{H_a P_a^{n+1,r} + \frac{C_a}{\Delta t^{(n)}}\left[\left(\rho_a^{n+1,r} - \rho_a^n\right) - \left(\xi^{n+1,r} - \xi^n\right)\right] + b_{g1}\left(\rho_a^n S_w^n\right) + b_{g2}\left(\rho_a^n\right)\right\} \quad (5.110)$$

we can rewrite the system as:

$$A_a^{n+1,r}\delta_a^{n+1} + B_a^{n+1,r}\delta_w^{n+1} = d_a^{n+1,r} \quad (5.111)$$

Global linear system

The final linear system that will be solved at each Picard iteration will be:

$$K\delta = d \quad (5.112)$$

The system matrix K is non-symmetric in general case and explicitely it is:

$$K = \begin{bmatrix} A_w^{n+1,r} & B_w^{n+1,r} \\ B_a^{n+1,r} & A_a^{n+1,r} \end{bmatrix} \tag{5.113}$$

The vector of the unknowns is:

$$\delta = \begin{bmatrix} \delta_w^{n+1} \\ \delta_a^{n+1} \end{bmatrix} \tag{5.114}$$

and the right hand side is:

$$d = \begin{bmatrix} d_w \\ d_g \end{bmatrix} \tag{5.115}$$

The linear system is solved using either GMRES or BiCGStab. Dirichlet boundary conditions are imposed after the discretized system has been completely assembled imposing the value of the boundary condition on the right hand side and substituing the diagonal entry of the system matrix K with one and all the extra-diagonal entries with zero.

The solution of the system (5.112) leads to the determination of the nodal values of both the main unknowns of the problem, namely:

$$p_w^{n+1,r+1} = p_w^{n+1,r} + \delta_w^{n+1} \tag{5.116}$$

$$p_a^{n+1,r+1} = p_a^{n+1,r} + \delta_a^{n+1} \tag{5.117}$$

The capillarity relationships lead to the determination of $S_w^{n+1,r+1}$ and through proper laws also the calculus of $\rho_a^{n+1,r+1}$ is allowed.

5.3.3 Time stepping

The accuracy of the initial guess is of primary importance in order to obtain a fast nonlinear convergence, but it is influenced by the time step size. For this reason the value of Δt is adapted during the simulation according with the so-called *Heuristic Time Stepping* (HTS) procedure according with the algorithm proposed by Paniconi and Putti [1994] and D'Haese *et al.* [2006] The current Δt value is increased by a factor Δt_{mag} (up to a maximum Δt_{max}) if convergence at the previous iteration is achieved in fewer than $itmax_1$ iteration, it is left unchanged if convergence required between $itmax_1$ and $itmax_2$ iterations, and it is decreased by a factor Δt_{red} (down to a minimum Δt_{min}) if convergence required more than $itmax_2$ iterations. If convergence is not achieved (i.e. the maximum number of iterations $itmax$ is exceeded), the iterative process is repeated

(*back stepping*) using a reduced time step size (by a factor Δt_{red}, down to Δt_{min}). The values of the magnification and reduction factors Δt_{mag}, Δt_{red}, the maximum number of nonlinear iterations $itmax$,$itmax_1$, and $itmax_2$ are set empirically.

5.4 Mass Balance Calculation

The validity of the model is verified checking that the Mass Balance is respected:

$$M_{in} + M_{out} - \Delta M_{stor} = 0 \tag{5.118}$$

where

- M_{in}: total inflow mass between current and previous time level (> 0 by definition)
- M_{out}: total outflow mass between current and previous time level (< 0 by definition)
- ΔM_{stor}: total mass storage change between current and previous time level (> 0 for net increase in storage)

Since the solution is not exact, the mass balance is considered satisfied numerically if δ_M defined as:

$$\delta_M = M_{in} + M_{out} - \Delta M_{stor} \tag{5.119}$$

is such that it is less than 5% of $M_{in} + M_{out}$

To calculate the total inflow mass of water, the fluxes that enter through the Dirichlet nodes have to be computed as the components of the vector q computed as:

$$q = K^* \delta - d^* \tag{5.120}$$

relative to the nodes on which boundary conditions are imposed. K^* is the global matrix of the linear system before imposition of the Dirichlet boundary conditions and similarly, d^* is the right hand side of the global linear system before the imposition of Dirichlet boundary conditions.

If a Dirichlet boundary condition relative to water phase is imposed on node i, the expression of the i-th component of vector q is:

$$q_{i,w}^{n+1} = q_{dir,iw}^{n+1} = \sum_{j=1}^{n} \left[A_{w,ij}^{n+1,r} \delta_{w,j}^{n+1} \right] + \sum_{j=1}^{n} \left[B_{w,ij}^{n+1,r} \delta_{a,j}^{n+1} \right] - d_{w,i} \tag{5.121}$$

where all block matrices A_w and B_w as well as the right hand side d_w are evaluated before imposing boundary conditions. Introducing equations (5.101), (5.102), and (5.103)

$$\begin{aligned} q_{dir,iw}^{n+1} = & \sum_{j=1}^{n} \left(H_{w,ij} + \frac{C_{w1,ij}}{\Delta t} - \frac{C_{w2,ij}}{\Delta t} W_{w,ij} \right)^{n+1,r} \left(P_{w,j}^{n+1,r+1} - P_{w,j}^{n+1,r} \right) \\ & + \left[\left(\frac{C_{w2,ij}}{\Delta t} W_{w,ij} \right)^{n+1,r} \left(P_{a,j}^{n+1,r+1} - P_{a,j}^{n+1,r} \right) \right] \\ & + H_{w,ij}^{n+1,r} P_{w,j}^{n+1,r} + \left(\frac{C_{w1,ij}}{\Delta t} \right)^{n+1,r} \left(P_{w,j}^{n+1,r} - P_{w,j}^{n} \right) + \left(\frac{C_{w2,ij}}{\Delta t} \right)^{n+1,r} \left(S_{w,j}^{n+1,r} - S_{w,j}^{n} \right) \\ & + b_{w1,i} \left(S_{w,i}^{n} \right) + b_{w2,i} \end{aligned} \tag{5.122}$$

The definition of the inflow and outflow fluxes and masses of air is basically the same. If a Dirichlet boundary condition relative to the air phase is imposed on node i, the expression of the i-th component of vector q is:

$$q_{i,a}^{n+1} = q_{dir,ia}^{n+1} = \sum_{j=1}^{n} \left[A_{a,ij}^{n+1,r} \delta_{a,j}^{n+1} \right] + \sum_{j=1}^{n} \left[B_{a,ij}^{n+1,r} \delta_{w,j}^{n+1} \right] - d_{a,i} \tag{5.123}$$

Introducing equations (5.108), (5.109), and (5.110) (recalling that $A_{a,ij}^{n+1,r}$, $B_{a,ij}^{n+1,r}$, and $d_{a,i}$ are all considered before the imposition of the boundary conditions) and re-arranging terms the air flux through the i-th Dirichlet boundary node looks like:

$$\begin{aligned} q_{dir,ia}^{n+1} = & \sum_{j=1}^{n} H_{a,ij} P_{a,j}^{n+1,r+1} \\ & + C_{a,ij} \left[U \left(P_a^{n+1,r+1} - P_a^{n+1,r} \right) - \left(R_{ij} W_{ij} + S_{ij} U_{ij} \right) \left(P_a^{n+1,r+1} - P_a^{n+1,r} \right) \right] \\ & + C_{a,ij} \left[\left(\rho_a^{n+1,r+1} - \rho_a^{n} \right) - \left(\xi^{n+1,r+1} - \xi^{n} \right) + R_{ij} W_{ij} \left(P_a^{n+1,r+1} - P_a^{n+1,r} \right) \right] \\ & + b_{a1} + b_{a2} \end{aligned} \tag{5.124}$$

The total mass inflow N_{Din} coming from the Dirichlet boundary nodes at the current time level is calculated as:

$$N_{Din} = \sum_{i=1}^{N_{Pin}} q_{Din} \tag{5.125}$$

where:

- N_{Pin}: total number of Dirichlet nodes from which enters a mass flux
- $q_{Din}(i)$: mass flux entering from the i-th Dirichlet node

The total mass outflow N_{Dout} going out from the Dirichlet boundary nodes at the current time level is calculated as:

$$N_{Dout} = \sum_{i=1}^{N_{Pout}} q_{Dout} \tag{5.126}$$

where:

- N_{Pout}: total number of Dirichlet nodes from which a mass flux goes out of the domain
- $q_{Dout}(i)$: mass flux going out from the i-th Dirichlet node

The total mass inflow N_{Nin} coming from the Neumann boundary nodes at the current time level is calculated as:

$$N_{Nin} = \sum_{i=1}^{N_{Qin}} \rho_w q_{Nin} \tag{5.127}$$

where:

- N_{Qin}: total number of Neumann nodes from which enters a mass flux
- $q_{Nin}(i)$: mass flux entering from the i-th Neumann node

The total mass outflow N_{Nout} going out from the Neumann boundary nodes at the current time level is calculated as:

$$N_{Nout} = \sum_{i=1}^{N_{Qout}} \rho_w q_{Nout} \tag{5.128}$$

where:

- N_{Qout}: total number of Neumann nodes from which a mass flux goes out of the domain
- $q_{Nout}(i)$: mass flux going out from the i-th Neumann node

where q_{Nin} and q_{Nin} are prescribed by file by the user and dimensionally are $[m^2 s^{-1}]$, hence N_{Nout} are $[Kgm^{-1}s^{-1}]$.

Similarly we can define N_{Dinp},N_{Doutp},N_{Ninp}, and N_{Noutp} that are the values of total mass inflow from the Dirichlet boundary nodes, the total mass outflow from the Dirichlet boundary nodes, total mass inflow from the Neumann boundary nodes, and total mass outflow from the Neumann boundary nodes respectively at the *previous* time level.

The total inflow from the Dirichlet nodes at the current time step is defined as:

$$M_{Din} = \frac{N_{Din} + N_{Dinp}}{\Delta t} \tag{5.129}$$

while the the total outflow from the Dirichlet nodes at the current time step is defined as:

$$M_{Dout} = \frac{N_{Dout} + N_{Doutp}}{\Delta t} \tag{5.130}$$

Similarly, we define the total inflow from the Neumann nodes at the current time step:

$$M_{Nin} = \frac{N_{Nin} + N_{Ninp}}{\Delta t} \tag{5.131}$$

and the total outflow from the Neumann nodes at the current time step as:

$$M_{Nout} = \frac{N_{Nout} + N_{Noutp}}{\Delta t} \tag{5.132}$$

Dimensionally M_{Din}, M_{Dout}, M_{Nin}, and M_{Nout} are $[kg\, m^{-1}]$. It is worth noting that we are considering 2D case: in 3D case I would have actually [kg]. We can also think at this 2D model as the model of a vertical section of thickness 1 m: in that case also the dimension will be physically significant.

The total inflow and outflow mass between the current and the previous time level are defined respectively as:

$$M_{in} = M_{Din} + M_{Nin} \tag{5.133}$$

and

$$M_{out} = M_{Dout} + M_{Nout} \tag{5.134}$$

that dimensionally are obviously $[kg\, m^{-1}]$.

The mass of water initially present in the subsurface is calculated as:

$$M^0_{stor,\alpha} = \begin{cases} \displaystyle\sum_{i=1}^{N} \rho_w A_{nod_i} S_{w_i} \phi & \text{for } \alpha = w \\ \displaystyle\sum_{i=1}^{N} \rho_w A_{nod_i} \left(1 - S_{w_i}\right) \phi & \text{for } \alpha = a \end{cases} \tag{5.135}$$

where A_{nod_i} is the area relative to the node i. The mass of water in the domain at time t is evaluated both with relations (5.135), and as

$$M^t_{stor,\alpha} = M^0_{stor,\alpha} + \sum_{\tau=\Delta t}^{t} \Delta M_{stor,\alpha_\tau} \tag{5.136}$$

where $\Delta M_{stor,\alpha_\tau}$ is the variation in the storage for each time step τ for the phase α that is calculated as:

$$\Delta M_{stor,\alpha} = \begin{cases} \sum_{i=1}^{N} A_{nod_i} \left\{ \rho_w \left[\hat{S}_{w_i} \frac{S_s}{\rho_w g} \left(P_{w_i}^{k+1,r+1} - P_{w_i}^{k} \right) + \phi \left(S_{w_i}^{k+1} - S_{w_i}^{k} \right) \right] \right\} \text{for } \alpha = w \\ \sum_{i=1}^{N} A_{nod_i} \phi \left\{ \left(\rho_a^{k+1} - \rho_a^{k} \right) - \left[\left(\rho_{a_i} S_{w_i} \right)^{k+1} - \left(\rho_{a_i} S_{w_i} \right)^{k} \right] \right\} \text{for } \alpha = a \end{cases} \tag{5.137}$$

where:

$$\hat{S}_{w_i} = \frac{1}{2} \left(S_{w_i}^{k+1} + S_{w_i}^{k} \right) \tag{5.138}$$

The relative mass balance error is evaluated in the code both with respect to the sum $M_{in} + M_{out}$, namely:

$$e_{rel1} = 100 \frac{\delta_M}{M_{in} + M_{out}} = 100 \frac{M_{in} + M_{out} - M_{stor}}{M_{in} + M_{out}} \tag{5.139}$$

as well as with respect to the in-coming mass only, i.e.:

$$e_{rel2} = 100 \frac{\delta_M}{M_{in}} = 100 \frac{M_{in} + M_{out} - M_{stor}}{M_{in}} \tag{5.140}$$

5.5 Test cases

The correct functioning of the model has been tested using some test cases taken in the literature. In the following three tests will be presented, all based on the example originally appeared in Miller *et al.* [1998], where it was used to test a Richards' based simulator in case of water infiltration in a soil initially characterized by very dry conditions.

5.5.1 Test1: simple sandbox initially completely dry

The first problem consist in the study of the infiltration of water induced by the presence of a pond 0.10 m deep over part of the surface of a sandy soil completely drained. The test is a re-adaptation of the example originally presented by Miller *et al.* [1998] to study the thougher conditions, from the numerical point of view, of infiltration and consideres a domain that consists in a sandy box 3 m wide by 3 m initially drained to equilibrium. The capillary retention curve, i.e. the relation between the water saturation and the capillary pressure is determined using the empirical relationship proposed by van Genuchten [1980], whereas the dependence of relative conductivities of the two phases on water saturation are described through Mualem [1976] formulas. Figures 5.6(a) and (b) represent the moisture

retention curve and the conductivity relations adopted, respectively. The parameters used are sumed up in Table 5.2 as well as the soil and fluids properties. The water table is assumed to be at the bottom of the column, hence the whole domain is in unsaturated conditions. The domain has been discretized using a structured mesh of 1426 nodes and

Property	**Unit**	**Sand**	
θ_r	[-]	0.093	
θ_s	[-]	0.301	
α_{vg}	$[m^{-1}]$	5.470	
n_{vg}	[-]	4.264	
K_s	$[m \cdot s^{-1}]$	$5.83 \cdot 10^{-5}$	
S_s	$[m^{-1}]$	$1.0 \cdot 10^{-6}$	
Fluid properties	**Unit**	**water**	**air**
density ρ	$[\mathrm{kg} \cdot \mathrm{m}^{-3}]$	1000	$\rho_a\,(p_a)$
viscosity μ	$[\mathrm{Pa} \cdot \mathrm{s}]$	$0.1 \cdot 10^{-2}$	$1.77 \cdot 10^{-05}$

Table 5.2: van Genuchten [1980] capillary retention curve parameters, soil, and fluids parameters.

z_1 [m]	z_2 [m]	Δz [m]
3.0	2.9	0.0125
2.9	2.7	0.0250
2.7	2.5	0.0500
2.5	0.0	0.1000

Table 5.3: Test 1. Vertical discretization of the domain

2700 triangles with an horizontal discretization $\Delta x = 0.1$ m and a vertical discretization Δz varing with the depth according with Table 5.3. A constant water pressure head of 0.10 m is applied over the region defined by $z = Z = 3$ m and 1 m $\leq x \leq$ 2 m. The remaining part of the upper boundary, the bottom one, and along the lateral sides hydrostatic water pressure is assumed. A no-flux boundary condition for the air is imposed on the part of the top where the water ponding condition is considered. The remaining boundaries, i.e. the two sides and the bottom of the domain as well as the part of the upper boundary, are open to air with a constant pressure equal to the atmospheric $p_{atm} = 101325$ Pa (Table 5.4). The initial conditions of water, air, and capillary pressure as well as water saturation are summarized in Table 5.5 and are shown in Figure 5.7.

The initial conditions of water, air, and capillary pressure of water pressure head for

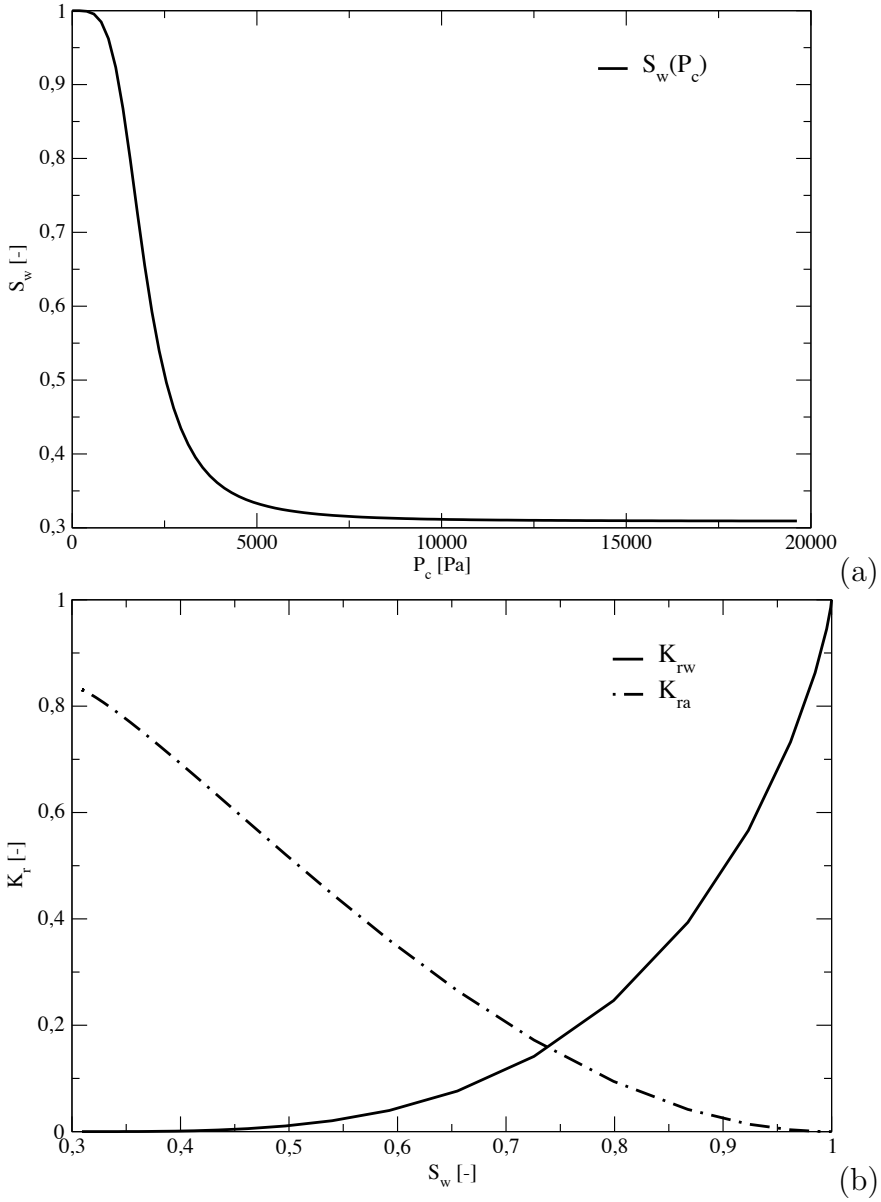

Figure 5.6: (a) Capillary retention curve. (b) Water and air relative conductivity K_{rw} and K_{ra} relationship with water saturation.

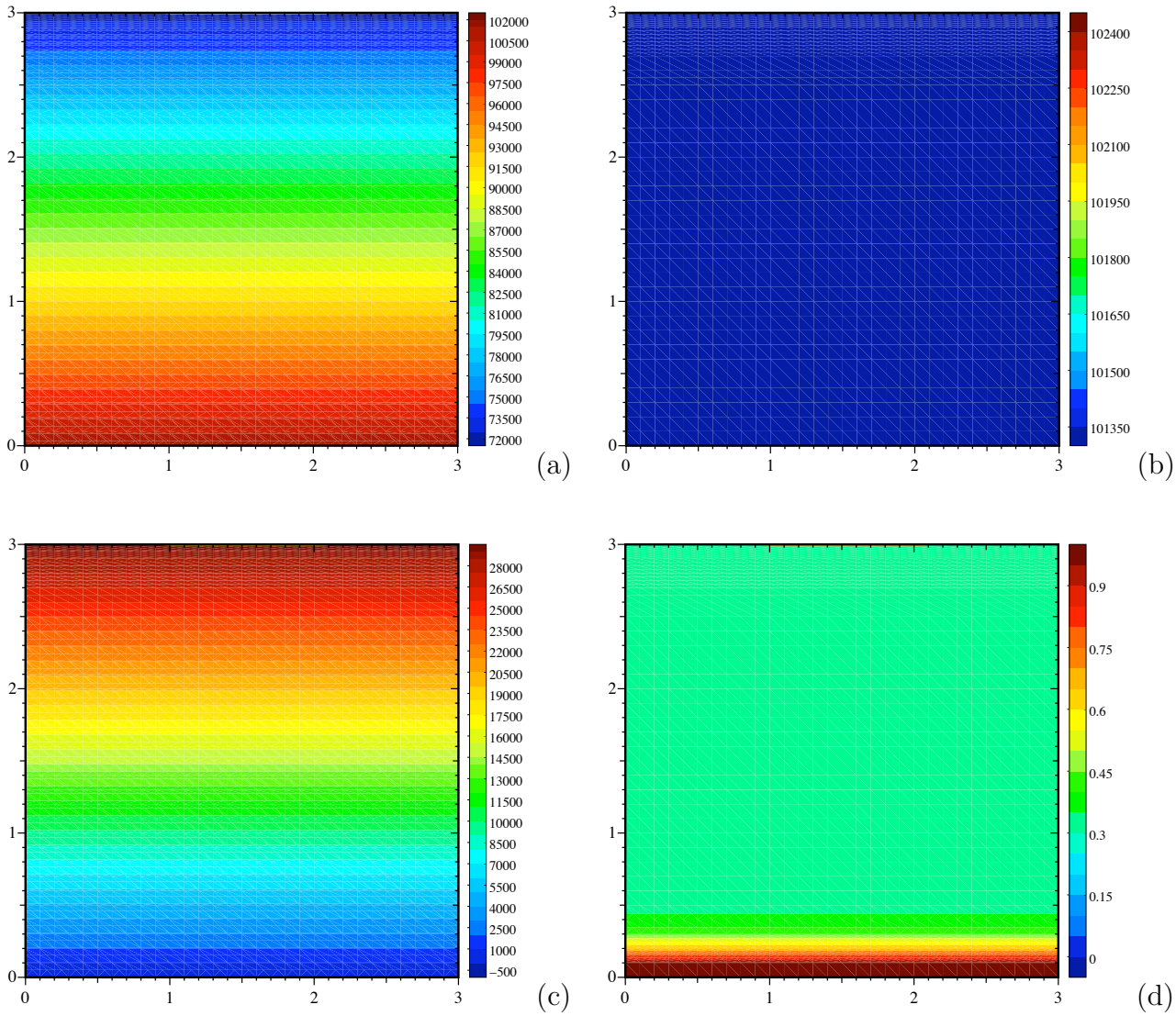

Figure 5.7: Test 1. Initial condition of (a) water, (b) air, (c) capillary pressure, and (d) water saturation.

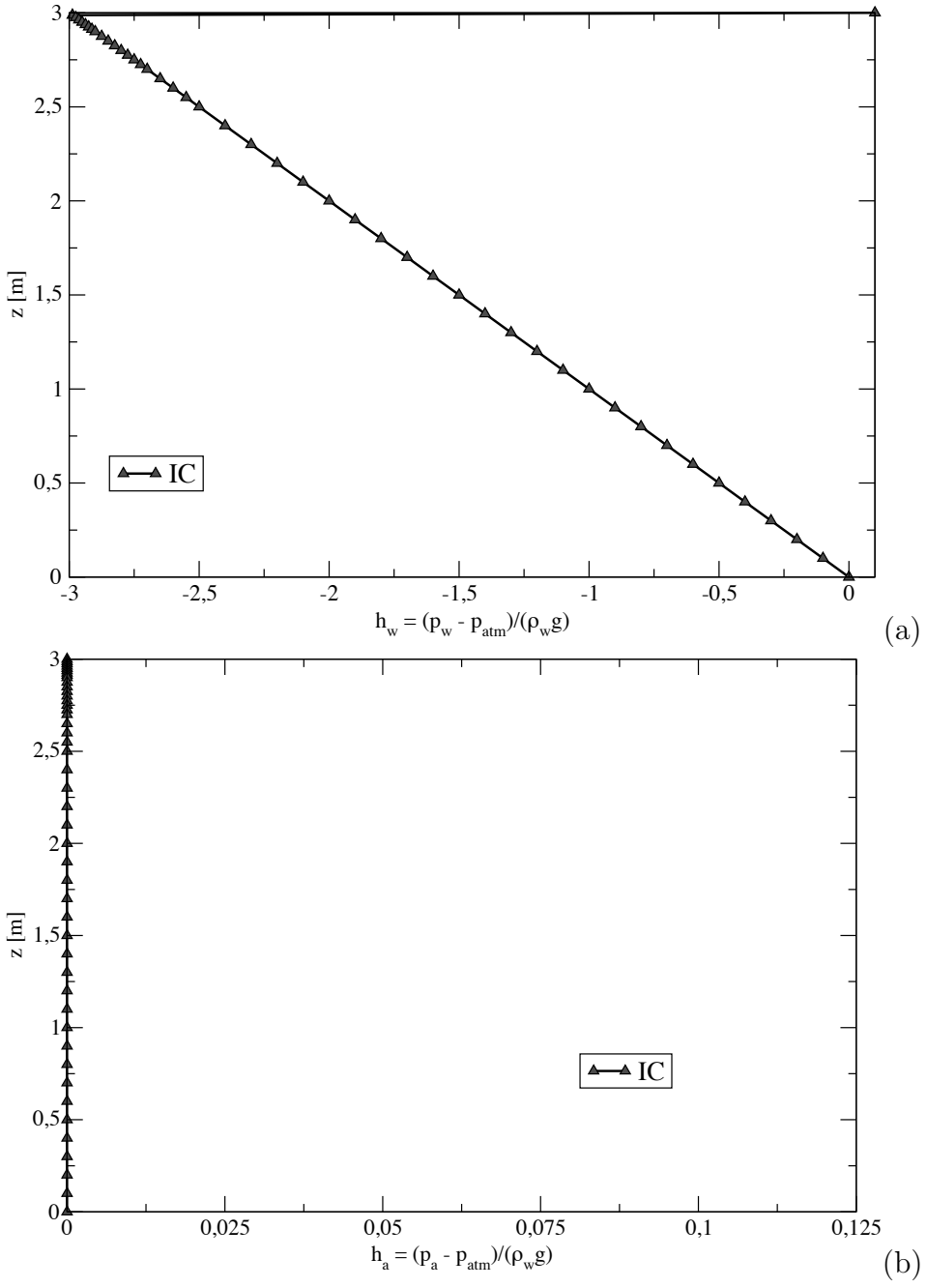

Figure 5.8: Test 1. Initial condition of (a) water and (b) air pressure in terms of water pressure head for the vertical symmetry axis.

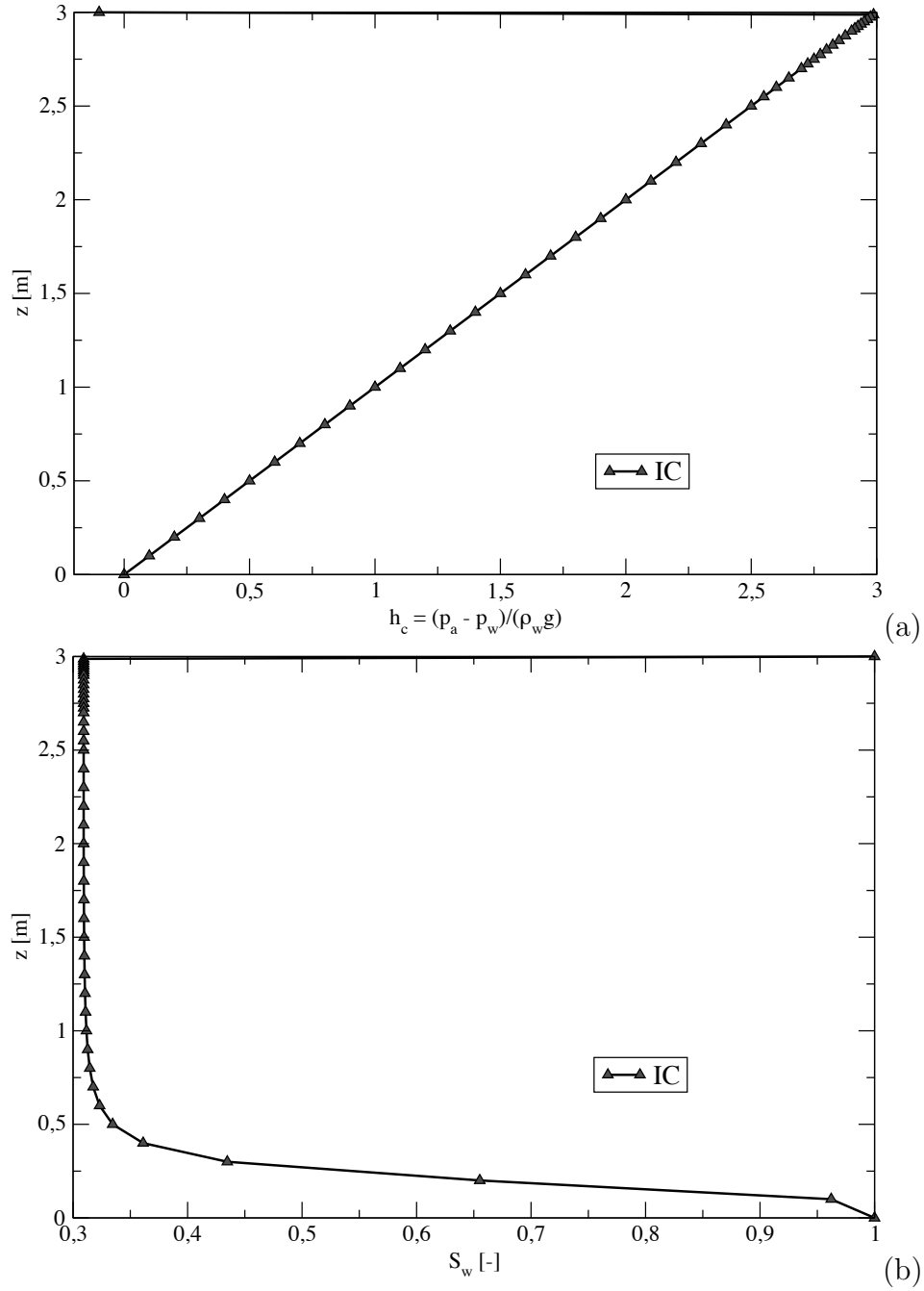

Figure 5.9: Test 1. (a) Initial condition of capillary pressure in terms of water head for the vertical symmetry axis. (b) Initial condition of water saturation for the vertical symmetry axis.

x	**z**	**Phase**	B.C.
$0 \leq x < 1$, $2 < x \leq 3$	$z = 3$	water	$p_w = p_{atm} - z \cdot \rho_w \cdot g$
		air	$p_a = p_{atm}$
$1 \leq x \leq 2$	$z = 3$	water	$p_w = p_{atm} + h_{pond} \cdot \rho_w \cdot g$
		air	$-\left[\frac{\mathrm{k}K_{ra}}{\mu_a}(S_a) \cdot (\nabla p_a + \rho_a g \eta_z)\right] \cdot n = 0$
$x = 0$, $x = 3$	$0 \leq z < 3$	water	$p_w = p_{atm} - z \cdot \rho_w \cdot g$
		air	$p_a = p_{atm}$
$0 \leq x \leq 3$	$z = 0$	water	$p_w = p_{atm}$
		air	$p_a = p_{atm}$

Table 5.4: Test 1. Boundary conditions imposed on the primary unknowns.

Variable	**IC**
water pressure	$p_w = p_{atm} - z \cdot \rho_w \cdot g$
air pressure	$p_a = p_{atm}$
capillary pressure	$p_c = p_a - p_w = -z \cdot \rho_w \cdot g$
water saturation	$S_w = S_w(p_c)$

Table 5.5: Test 1. Initial conditions of water, air and capillary pressure. Water saturation is calculated as a function of capillary pressure with the van Genuchten [1980] relation.

the vertical symmetry axis of the square domain are shown in Figures 5.8(a), 5.8(b), and 5.9(a), respectively. In order to be able to compare the trends, all the pressures are expressed in terms of meters of water head in excess to the atmospheric pressure. The initial conditions of water saturation and air density are also shown in Figures 5.9(b), and 5.10. The infiltration period has been carried out for the entire simulation.

The parameters adopted for the nonlinear scheme and the Heuristic Time Stepping (HTS) are sumed up in Table 5.6.

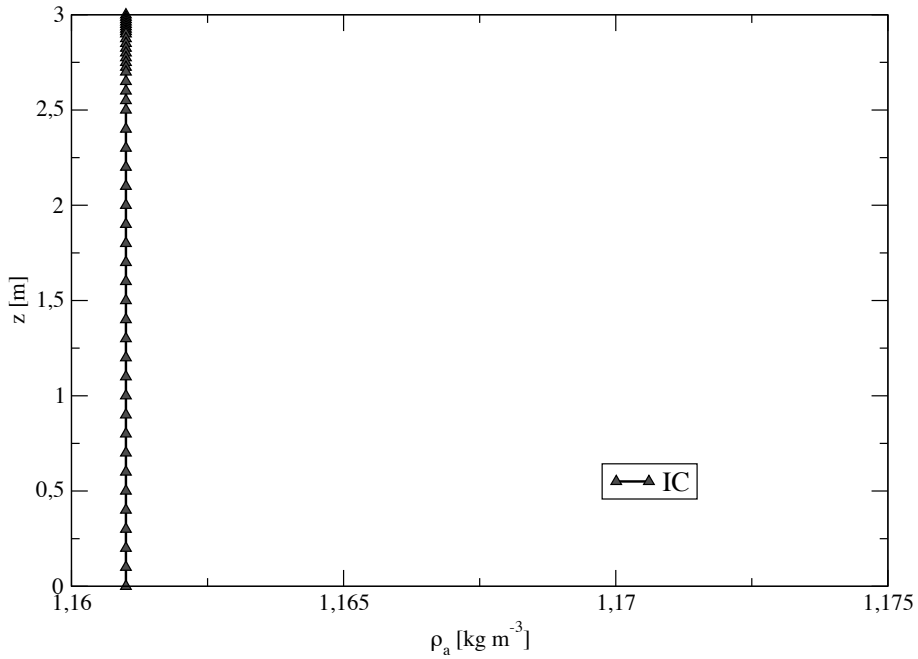

Figure 5.10: Test 1. Initial condition of air density for the vertical symmetry axis.

Parameter	Unit	Value
Maximum # of nonlinear iterations $itmax$	[-]	50
Maximum # of nonlinear iterations $itmax_1$	[-]	30
Minimum # of nonlinear iterations $itmax_2$	[-]	20
Magnification factor Δt_{mag}	[-]	1.05
Reduction factor Δt_{red}	[-]	0.5
Maximum allowed time step Δt_{max}	[s]	6480
Minimum allowed time step Δt_{min}	[s]	10^{-07}
Initial time step Δt_{ic}	[s]	10^{-07}
Simulated time t_{max}	[s]	6480.0
Linear tollerance ϵ_l	[-]	10^{-05}
Non-linear tollerance ϵ_l	[-]	1

Table 5.6: Test 1. Nonlinear and HTS paramenters.

Results

Parameter	Unit	Value
Total linear system solution time	[s]	41.46
Total simulation time	[s]	160.63
Total # of time steps	[-]	451
Total # of backstepping	[-]	0
Total # of linear iterations	[-]	46427
Total # of nonlinear iterations	[-]	2463
Avg. nonlinear iterations per time step	[-]	5.46
Avg. linear iterations per time step	[-]	102.94
Avg. linear iterations per nonlinear iteration	[-]	18.85
Rel. water mass balance error based on caeras	[%]	1.88810E-01
Rel. water mass balance error based on cerras	[%]	1.70172E-01
Rel. air mass balance error based on caeras	[%]	-1.92272E-01
Rel. air mass balance error based on cerras	[%]	1.68006E-01

Table 5.7: Test 1. Timing results after 6480 s of water infiltration.

The timing results after 6480 s of water infiltration are reported in Table 5.7. The evolution of the number of nonlinear iteration during the entire simulation and of the average number of linear iterations for each time step are shown in Figure 5.11(a) and (b), respectively. The evolution of the time step size during the whole simulation is shown in Figure 5.11(c): no backstepping occured during the whole simulation. The distribution of water pressure, air pressure and capillary pressure at the end of the simulation are shown in Figure 5.12(a), (b), and (c), respectively. Figure 5.12(d) shows the water saturation distribution. Figures (5.13a), (5.13b), (5.14a) show the evolution of the water, the air, and the capillary pressure all in terms of water pressure head. Figures (5.14b), and (5.15) show the water saturation and the air density along the vertical simmetry axis. The arrows show the change of the portraied variable profile with simulation time increase. The water infiltrates for the entire simulation period, reaching a depth of almost 2 m from the top of the domain. The water flux flowing through the central part of the top boundary into the domain is shown in Figure 5.16(a). No water flows out of the domain through the remaining sides (Figure 5.16b). The entering water compresses the air present in the domain, that experiences a pressure increase of the order of 1000 Pa in the central part of the topmost layers, i.e. close to the water ponding, whereas close to the open boundaries air flows out of the domain. The air density increases accordingly (Figures 5.17a and b). The evolution of the masse of both water and air flowing into and out of the domain as

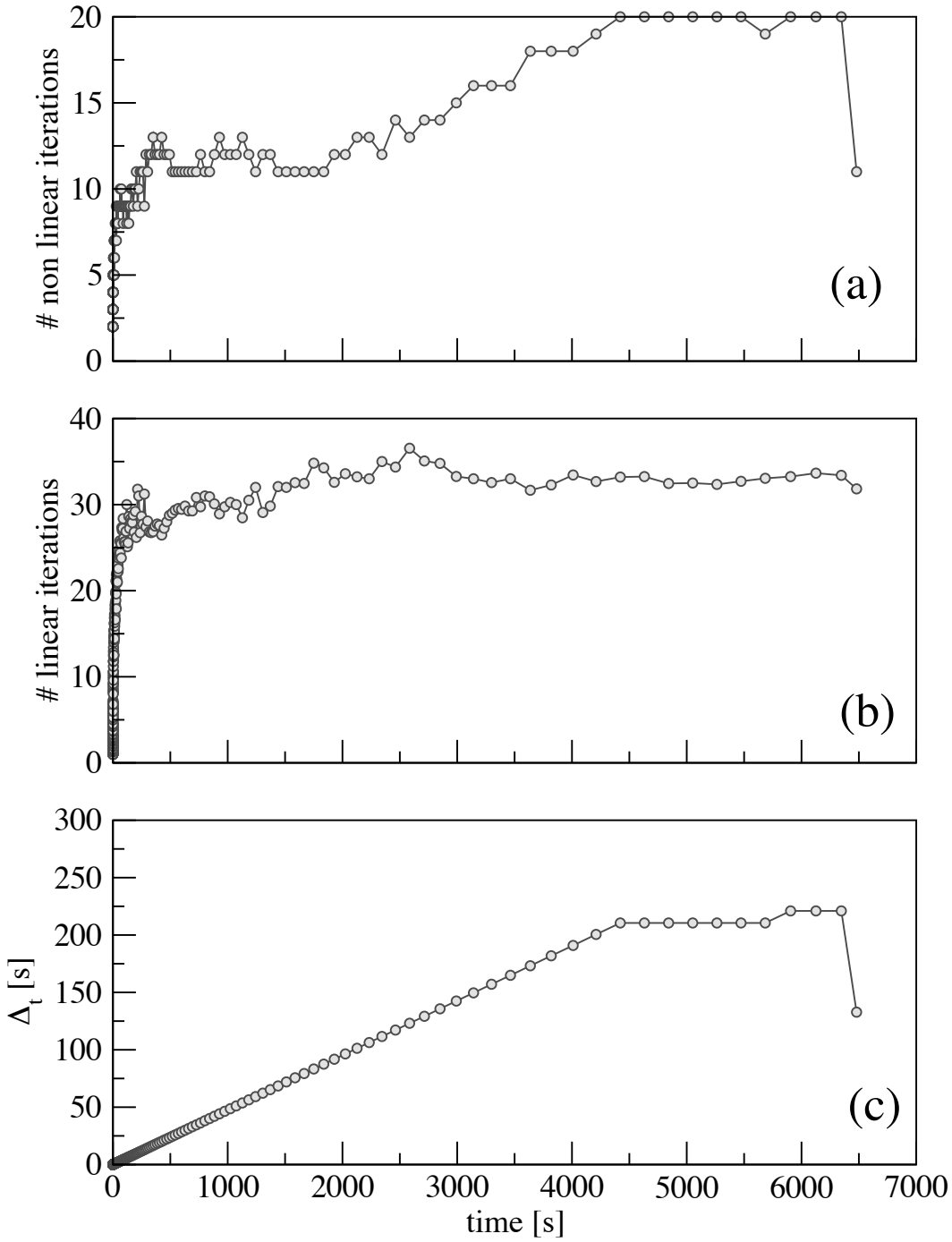

Figure 5.11: Test 1. (a) Nonlinear iterations per time step, (b) average linear iterations per time step, and (c) time step Δt variation for the entire simulation.

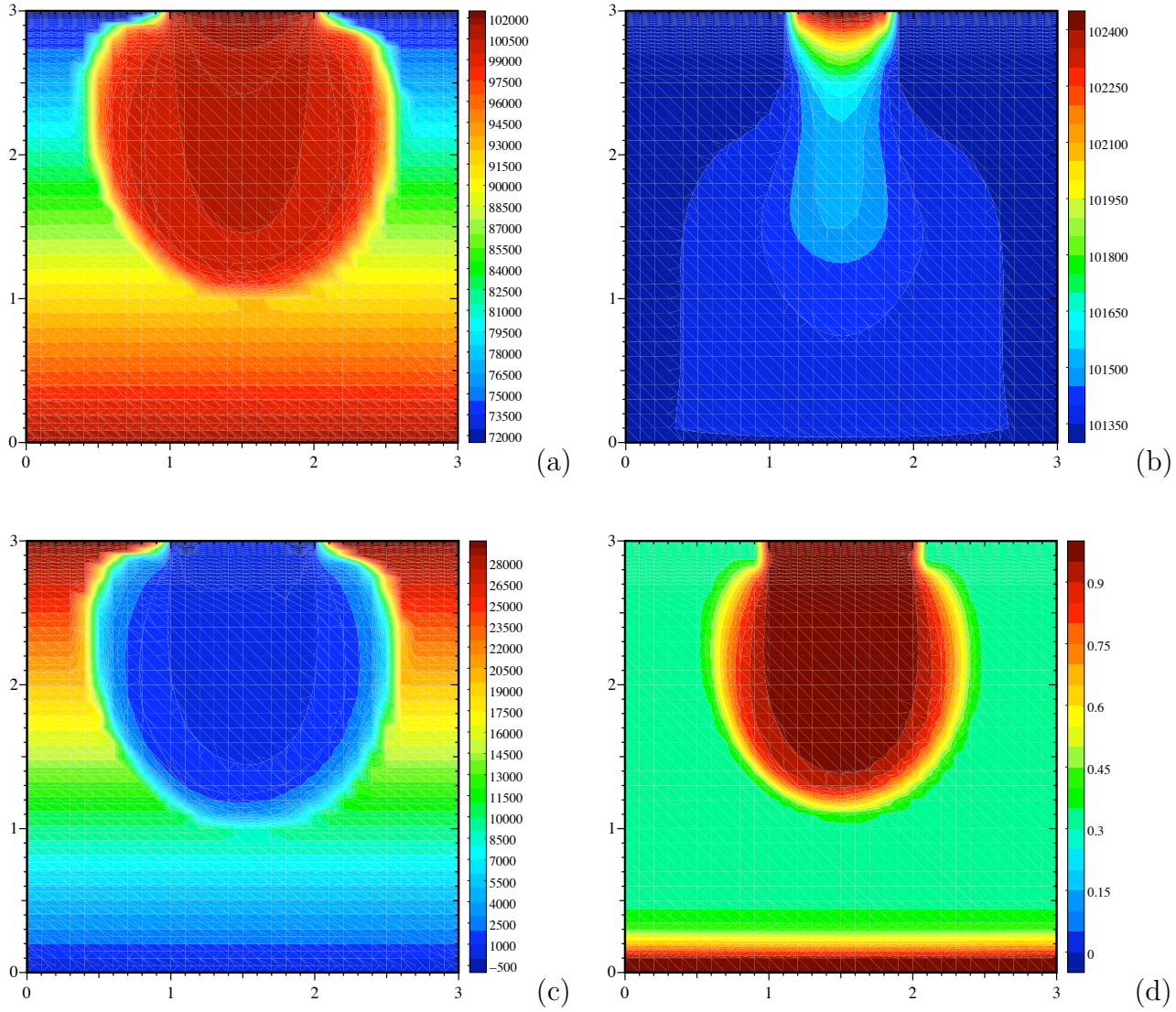

Figure 5.12: Test 1. (a) Water, (b) air, (c) capillary pressure, and (d) water saturation condition at the end of the simulation in the entire domain.

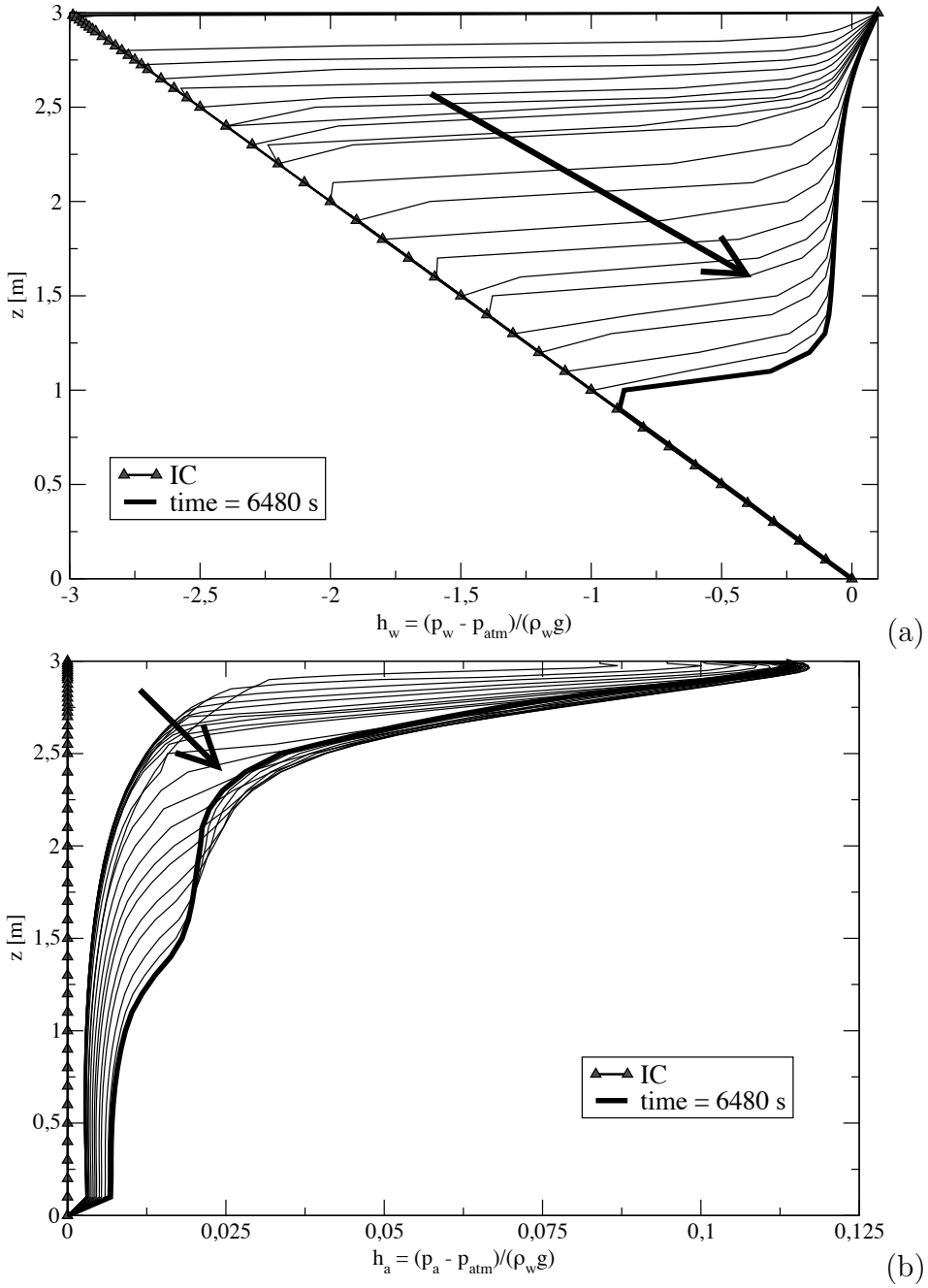

Figure 5.13: Test 1. Evolution of (a) water and (b) air pressure in terms of water pressure head for the vertical symmetry axis.

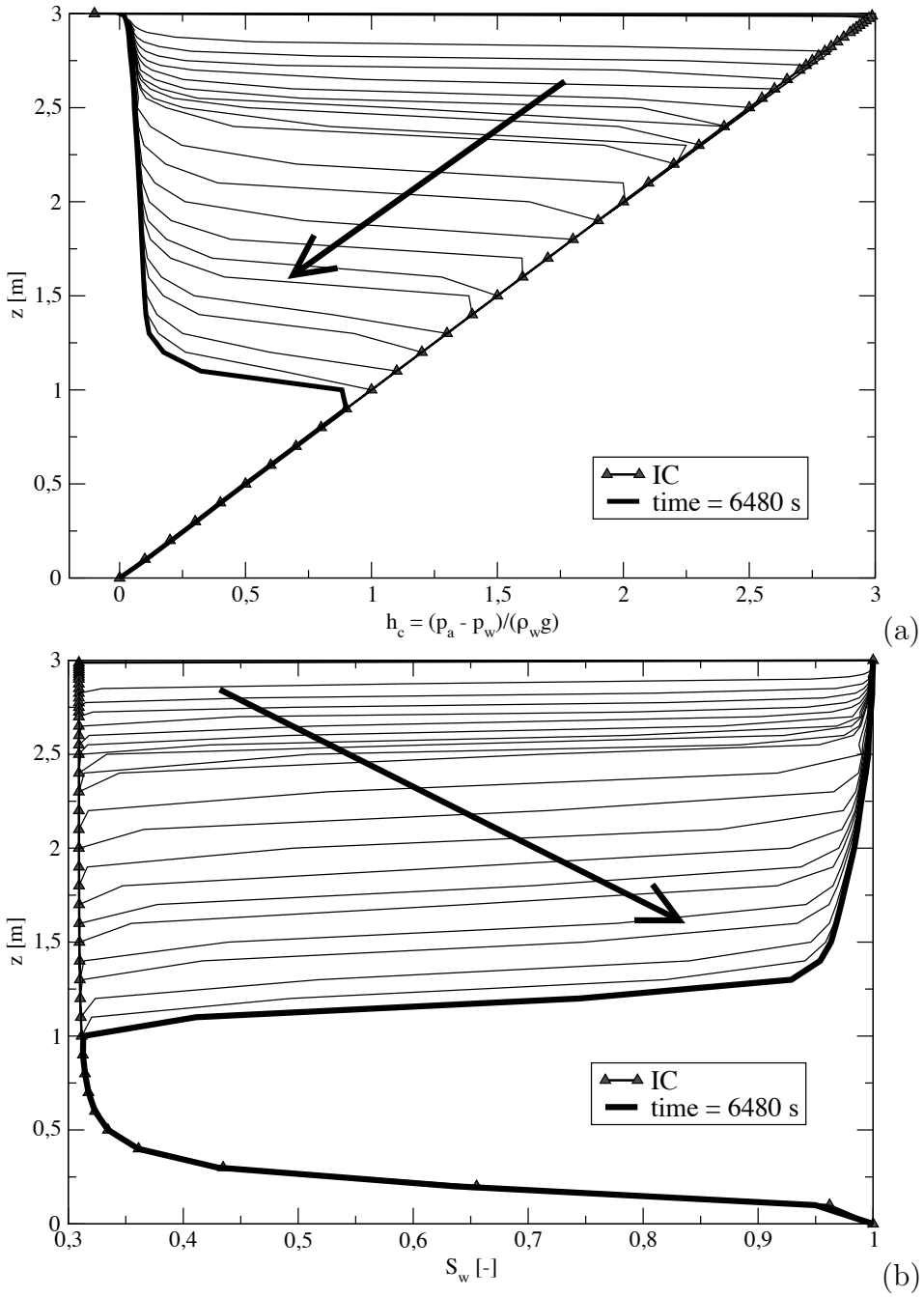

Figure 5.14: Test 1. Evolution of the (a) capillary pressure in terms of water pressure head and (b) of the water saturation for the vertical symmetry axis.

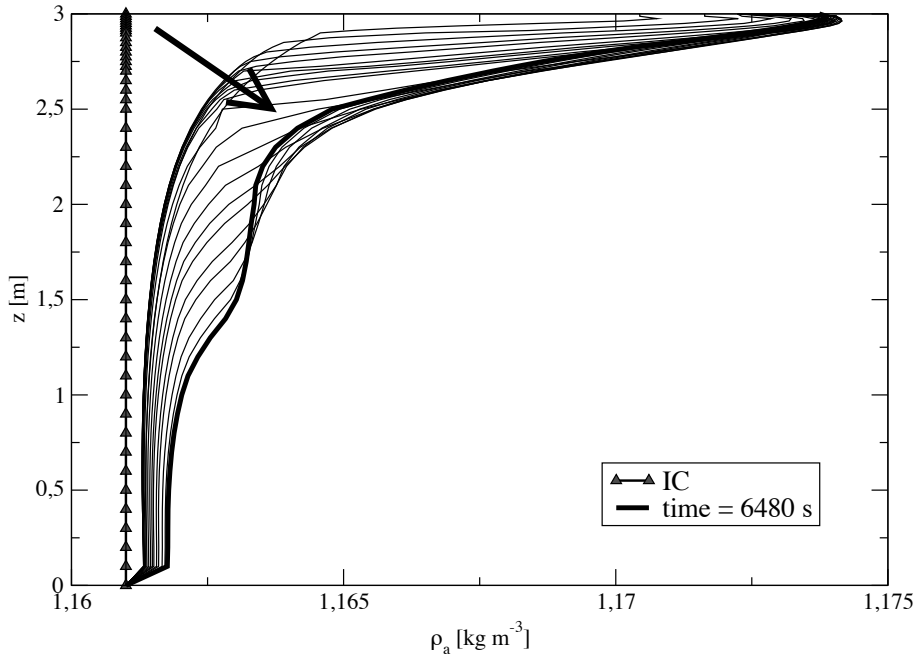

Figure 5.15: Test 1. Evolution of air density ρ_a for the vertical section of the square domain such at $x = 1.5m$.

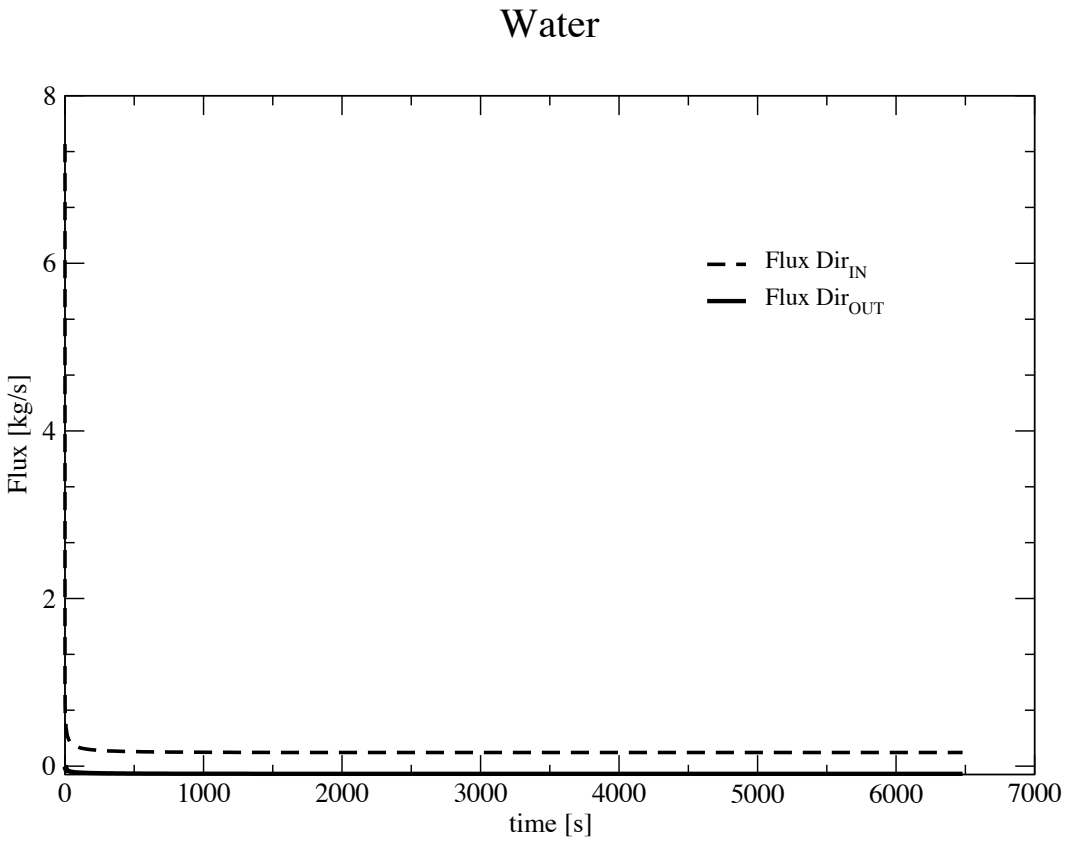

Figure 5.16: Test 1. (a) Water in- and (b) out-fluxes from the Dirichlet nodes

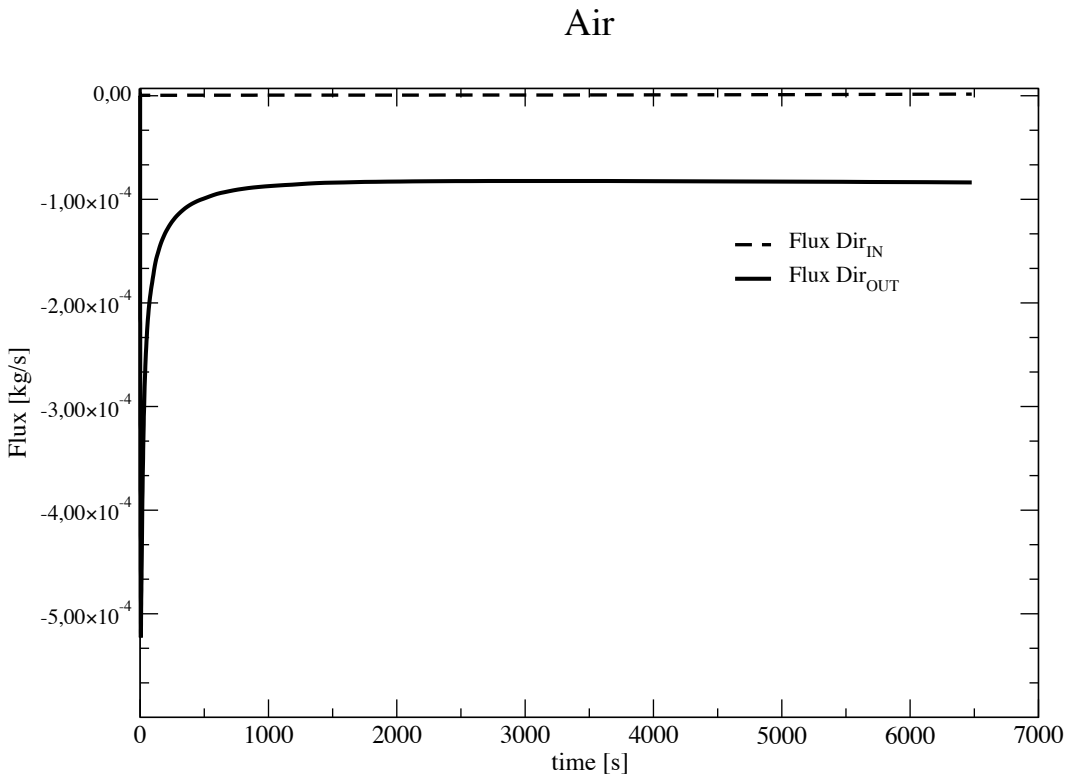

Figure 5.17: Test 1. (a) Air in- and (b) out-fluxes from the Dirichlet nodes

well as the complete mass balance for both phases, i.e. the sum of the in and out masses minus the storage ΔM_{stor}, are portraied in Figures 5.18 and 5.19, respectively.

Figure 5.20(a) shows the evolution of the relative mass balance error evaluated according with equation 5.139. Similarly, the air relative mass balance error is shown in Figure 5.20(b). In both cases after the first time steps, the relative mass balance error is less than ± 2 %. In order to evaluate the mass conservativity of the numerical dicretization developed, the same test has been run several times using different values for the maximum time step allowed, namely Δt_{max} (Table 5.8). The relative mass balance error evolution during the simulation for water and air is shown in Figures 5.21(a) and (b), respectively. The evolution of the relative mass balance error for both phases is almost equivalent for all Δt_{max} choices. A small increase of the cumulative mass balance error can be detected with the maximum time step Δt_{max} rise until Δt_{max} is less than 200 s (Figure 5.22). For a value of time step greater or equal to 200 s the cumulative mass balance error tends to a constant value.

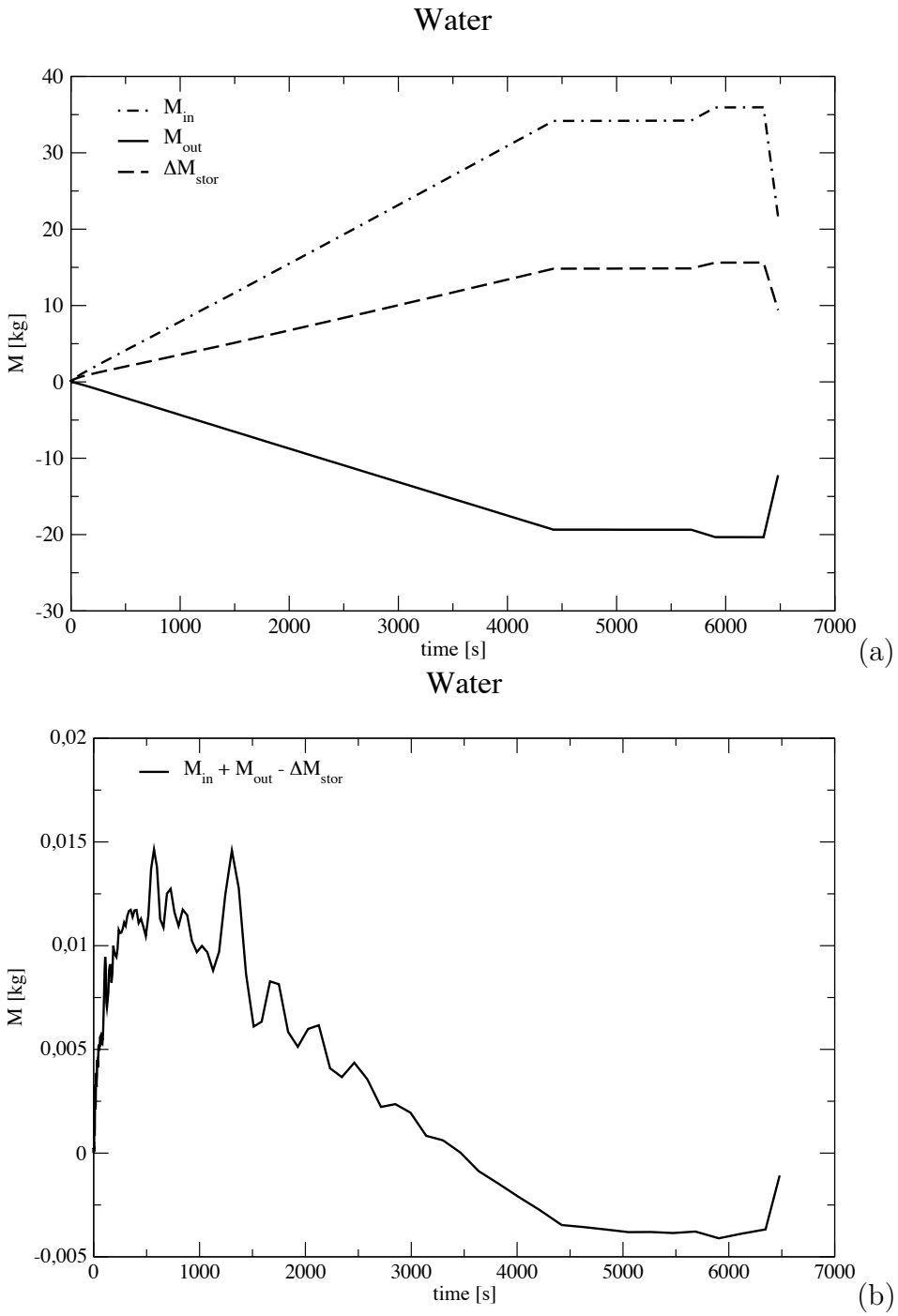

Figure 5.18: Test 1. (a) Input, output, and stored mass of water during the simulation. (b) The water mass balance $M_{in} + M_{out} - \Delta M_{stor}$ with respect to time is shown.

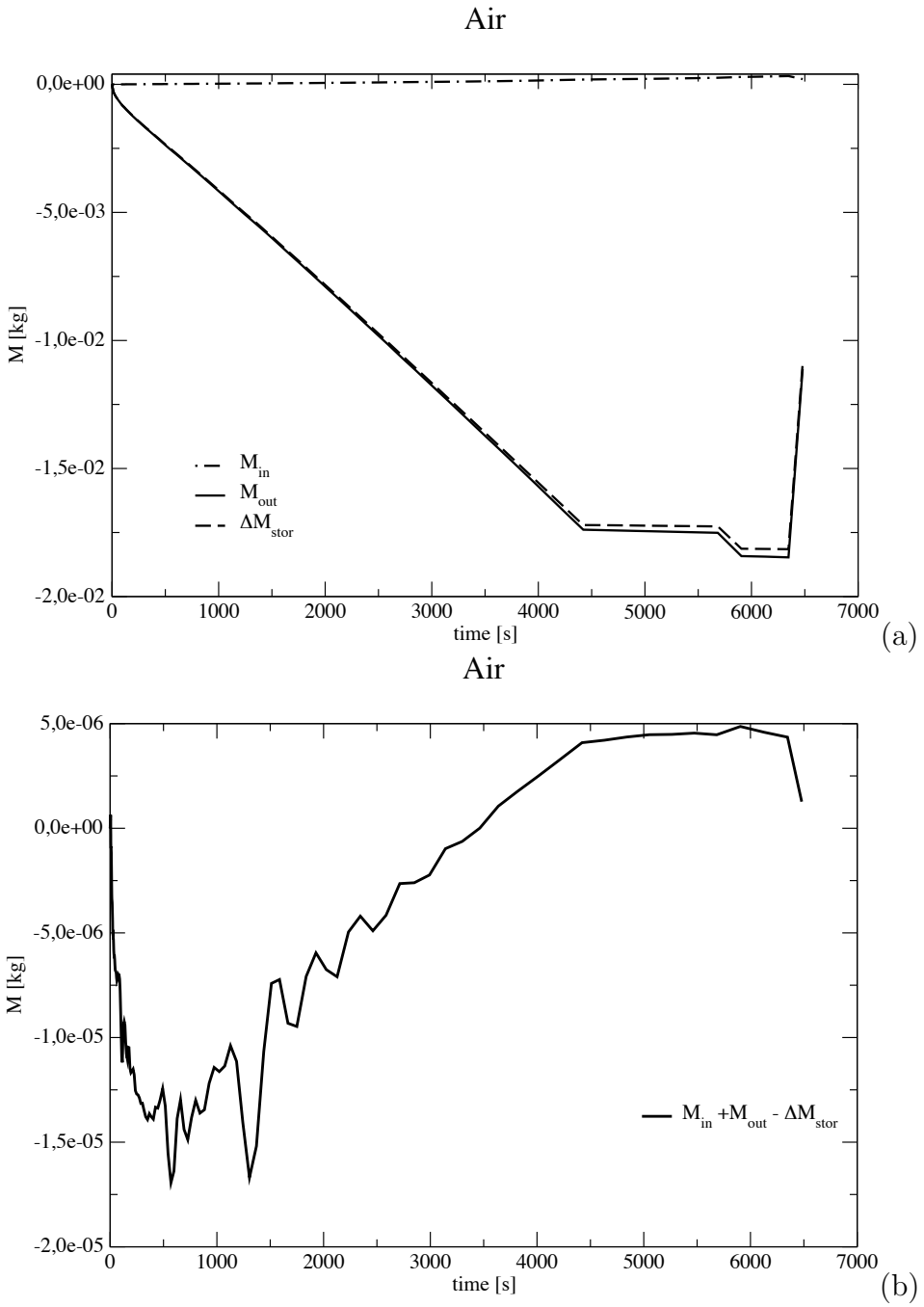

Figure 5.19: Test 1. (a) Input, output and out masses of air during the simulation. (b) The air mass balance $\mathrm{M}_{in} + \mathrm{M}_{out} - \Delta\mathrm{M}_{stor}$ with respect to time is shown.

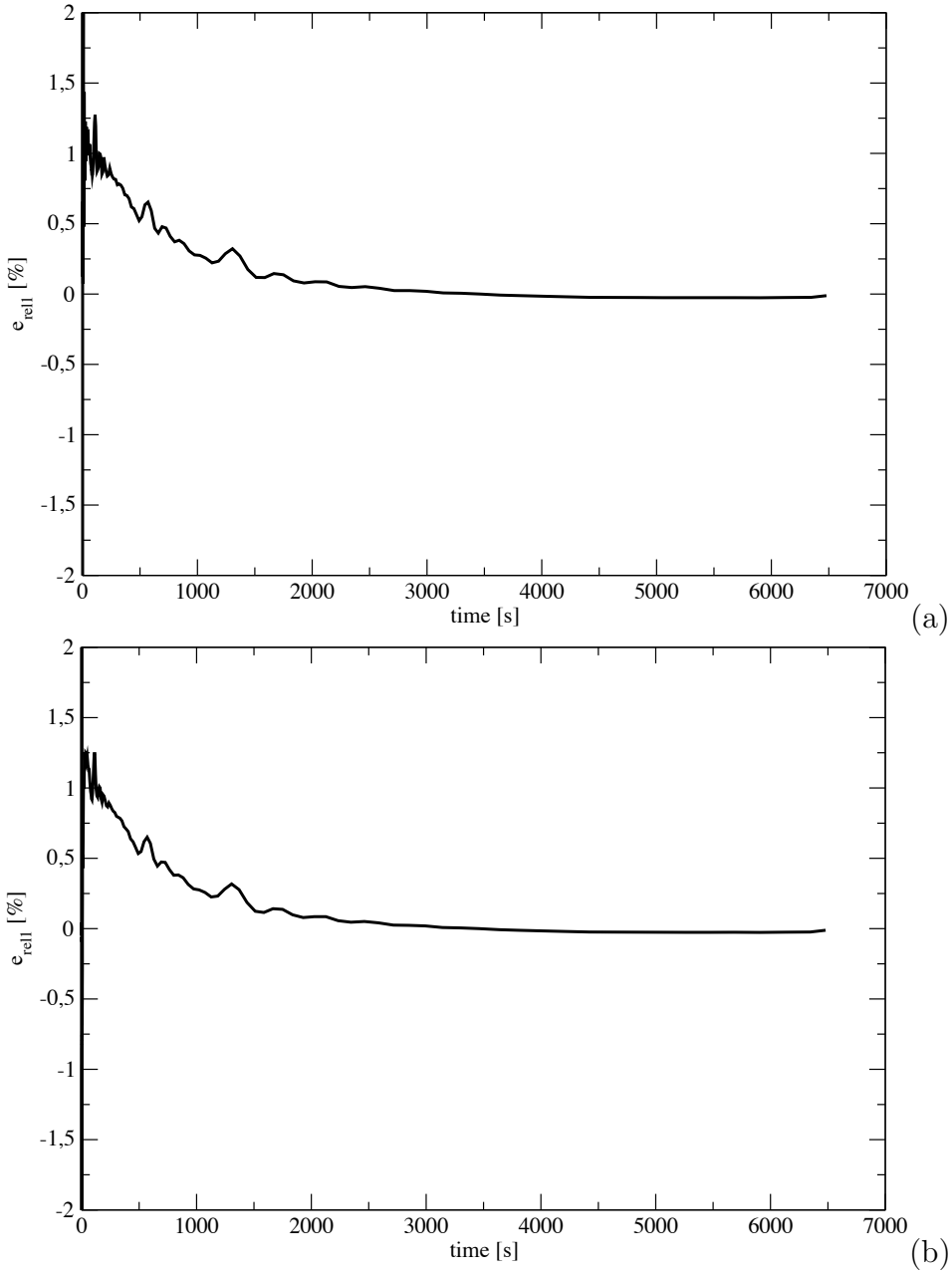

Figure 5.20: Test 1. Relative mass balance error of (a) water and (b) air.

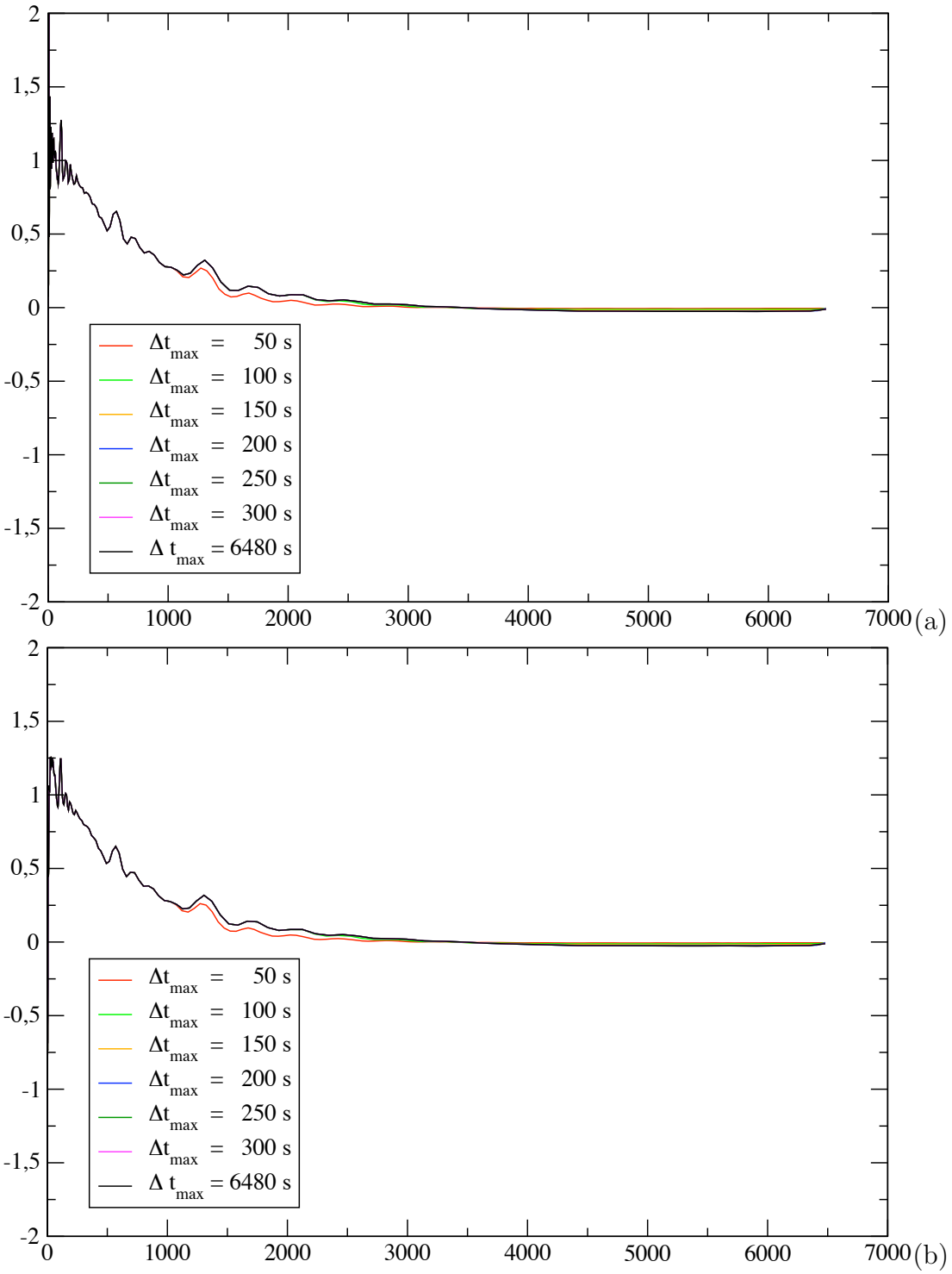

Figure 5.21: Test 1. Evolution of the relative mass balance error e_{rel1} for the (a) water and (b) air phases during the whole simulation.

Test case	Δt_{max} [s]	e_{rel1} water	e_{rel1} air
Test1a	50	1.71977E-01	-1.75306E-01
Test1b	100	1.83209E-01	-1.86611E-01
Test1c	150	1.86428E-01	-1.89858E-01
Test1d	200	1.88368E-01	-1.91825E-01
Test1e	250	1.88810E-01	-1.92272E-01
Test1f	300	1.88810E-01	-1.92272E-01
Test1g	6480	1.88810E-01	-1.92272E-01

Table 5.8: Test 1. Mass balance error for both water and air changing the maximum time step allowed Δt_{max}

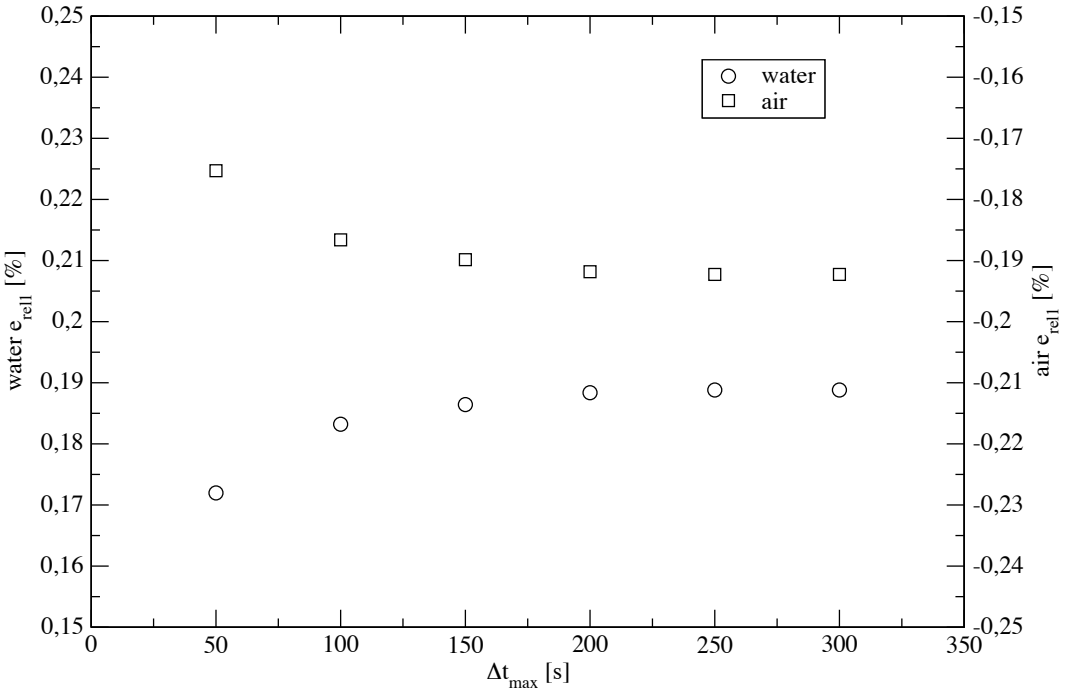

Figure 5.22: Test 1. Cumulative mass balance error variation according with Δt_{max} changes.

5.5.2 Test2: simple sandbox with water table at $z = 2\ m$ and $p_a = p_w$ under it

This test is based on the previous one and it is developed in order to understand the consequences of having a domain such that part is unsaturated and part is completely saturated. The idea is to get closer to the situation that occurs in the wetlands where the water table is usually pretty close to the soil surface. The domain is still the sandy box 3 m wide by 3 m high considered before. The same soil and fluids parameters given in Table 5.2 are used. The domain has been discretized using a structured mesh of 2108

z_1 [m]	z_2 [m]	Δz [m]
3.0	2.7	0.0125
2.7	2.5	0.0250
2.5	1.5	0.0500
1.5	0.0	0.1000

Table 5.9: Test 2. Vertical discretization of the domain

nodes and 4020 triangles with an horizontal discretization $\Delta x = 0.1$ m and a vertical discretization Δz varing with the depth according with Table 5.9. The mesh is more refined close to the surface and to the water table, in order to ensure a more accurate transition from the unsaturated to the saturated zone.

Variable	IC	
water pressure	$p_w = p_{atm} + (z_{wt} - z) \cdot \rho_w \cdot g$	
air pressure	$p_a = p_{atm}$	if $z > z_{wt}$
	$p_a = p_w$	if $z \leq z_{wt}$
capillary pressure	$p_c = p_a - p_w = -z \cdot \rho_w \cdot g$	if $z > z_{wt}$
	$p_c = p_a - p_w = 0.0$	if $z \leq z_{wt}$
water saturation	$S_w = S_w(p_c)$	

Table 5.10: Test 2. Initial conditions of water, air and capillary pressure. Water saturation is calculated as a function of capillary pressure with van Genuchten relation.

A constant water pressure head of 0.10 m has been applied over the region defined by $z = Z = 3$ m and 1 m $\leq x \leq 2$ m. Hydrostatic water pressure was assumed on the remaining part of the upper boundary, the bottom one and along the lateral sides according with the water table height that is initially supposed to be at $z = z_{wt} = 2$ m.

x	**z**	**Phase**	B.C.
$0 \leq x < 1$, $2 < x \leq 3$	$z = 3$	water	$p_{atm} + (z_{wt} - z) \cdot \rho_w \cdot g$
		air	$p_a = p_{atm}$
$1 \leq x \leq 2$	$z = 3$	water	$p_w = p_{atm} + h_{pond} \cdot \rho_w \cdot g$
		air	$-\left[\frac{\mathrm{k}K_{ra}}{\mu_a}(S_a) \cdot (\nabla p_a + \rho_a g \eta_z)\right] \cdot n = 0$
$x = 0$, $x = 3$	$0 \leq z < 3$	water	$p_{atm} + (z_{wt} - z) \cdot \rho_w \cdot g$
	$z > z_{wt}$	air	$p_a = p_{atm}$
	$z \leq z_{wt}$		$p_a = p_w$
$0 \leq x \leq 3$	$z = 0$	water	$p_w = p_{atm}$
		air	$p_a = p_w$

Table 5.11: Test 2. Boundary conditions imposed on the primary unknowns.

The part of the upper boundary where there was no ponding water was open to air with a constant pressure equal to the atmospheric pressure, i.e. 101325 Pa, as well as the upper part of the sides such that $z > z_{wt}$. A Dirichlet boundary condition on air such that the capillary pressure was equal to zero was imposed on the part of the sides with a height lower than z_{wt} and on the bottom. Corresponding to the region of the upper boundary on which water ponding condition was imposed a no-flux Neumann boundary condition for the air was imposed (Table 5.11). The initial conditions of water, air, and capillary pressure as well as water saturation are summarized in Table 5.10 and are shown in Figure 5.23. It is to note that the air pressure under the water table is assumed to be such that the capillary pressure is equal to zero, hence the water saturation is equal to 1. The initial conditions of water, air, and capillary pressure of water pressure head for the vertical symmetry axis of the square domain are shown in Figures 5.24(a), 5.24(b), and 5.25(a), respectively. The water saturation and air density initial condition are also shown in Figures 5.25(b), and 5.26. The infiltration period has been carried out for the entire simulation. Non-linear and heuristic time stepping (HTS) parameters are reported in Table (5.12).

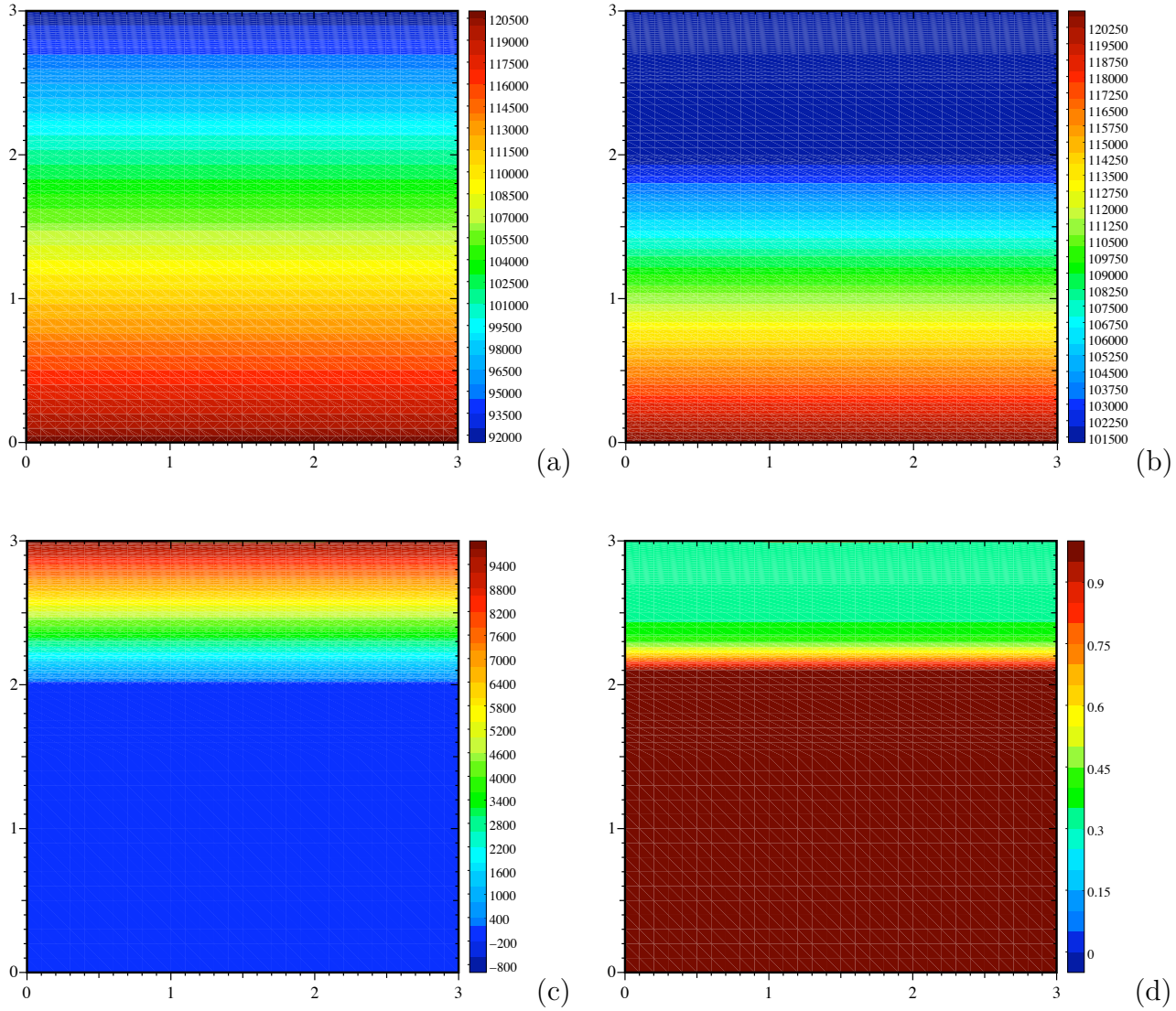

Figure 5.23: Test 2. Initial condition of (a) water pressure, (b) air pressure, (c) capillary pressure, and (d) water saturation.

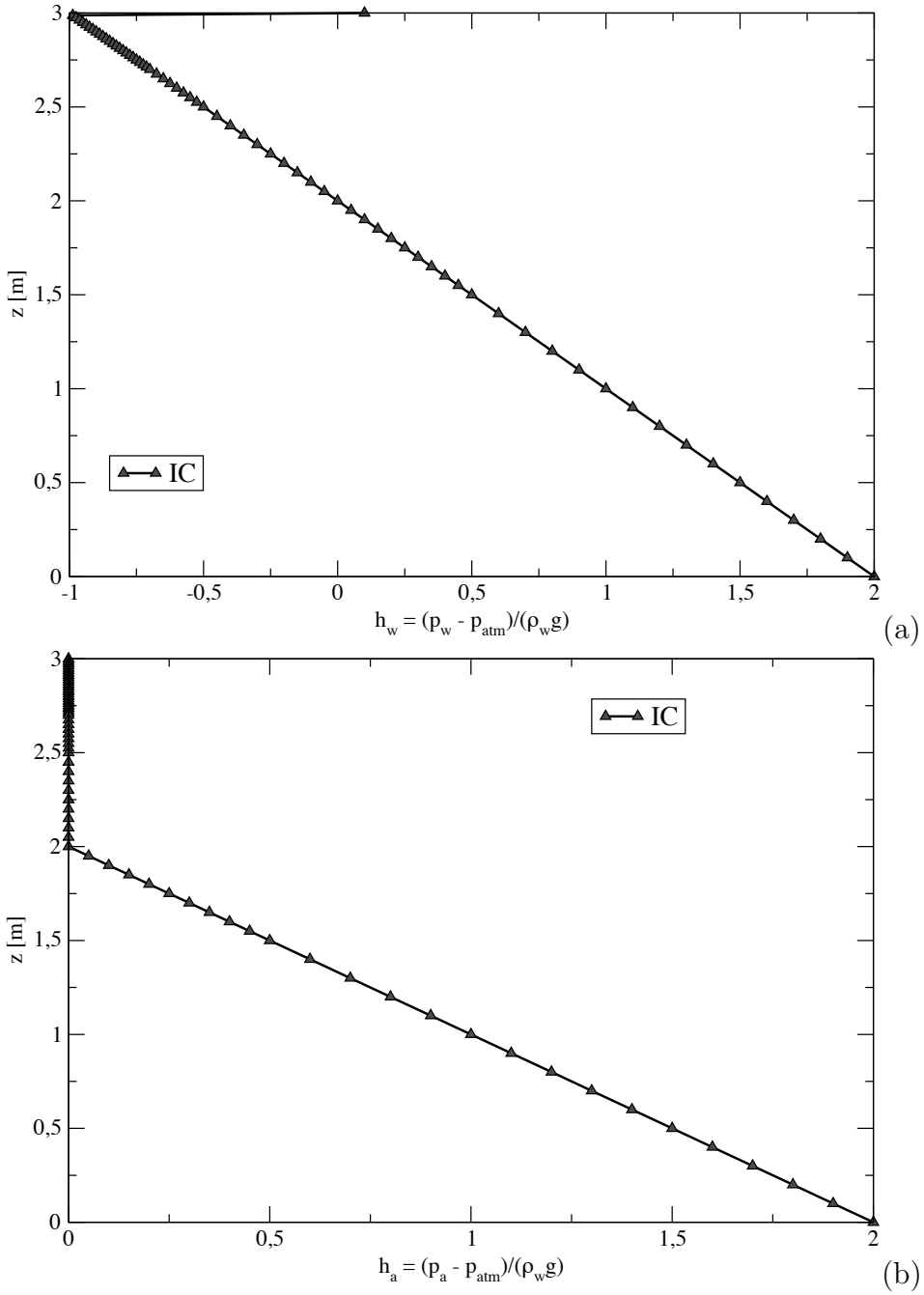

Figure 5.24: Test 2. Initial condition of water pressure (a) and air pressure (b) in terms of water pressure head for the vertical symmetry axis.

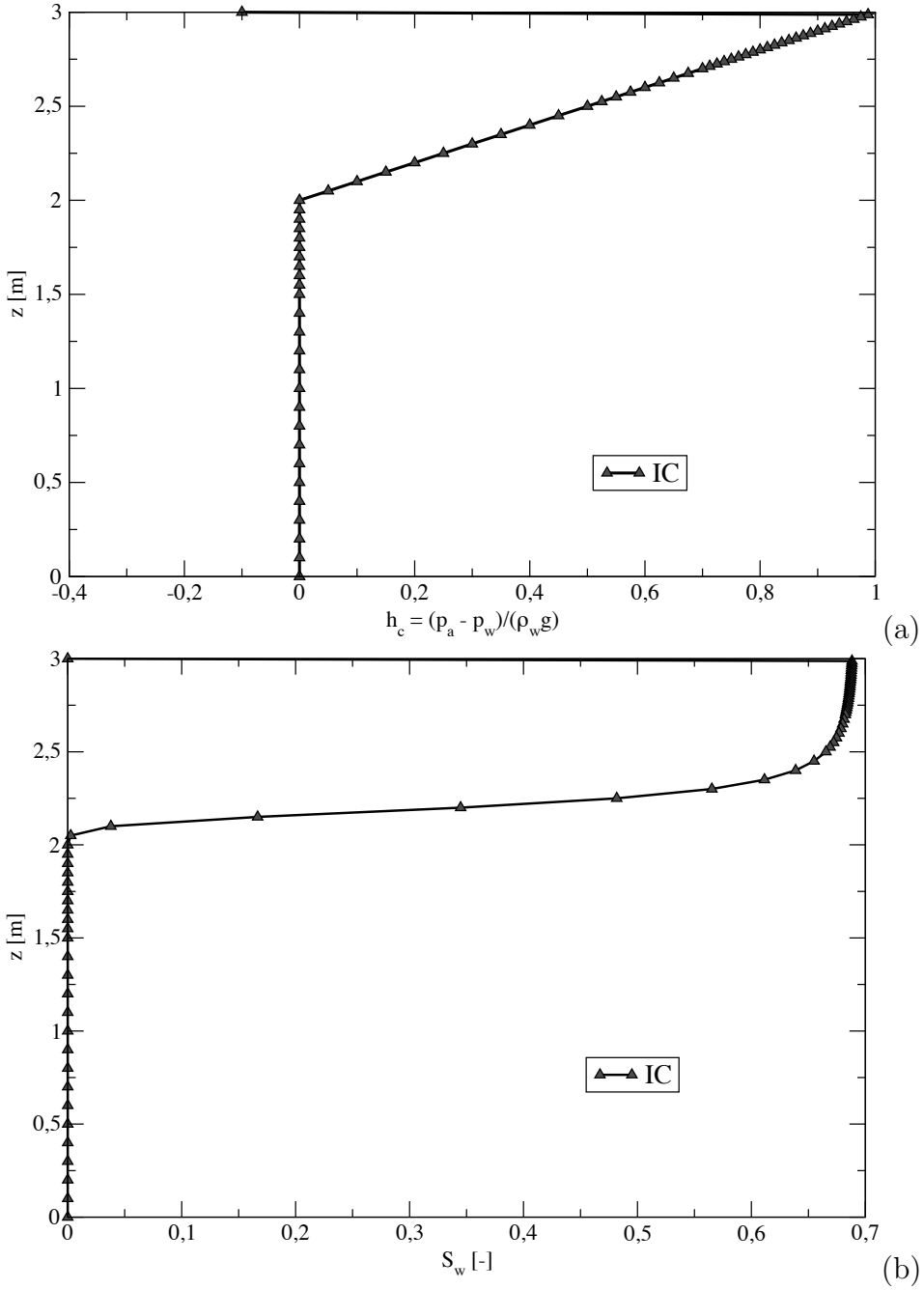

Figure 5.25: Test 2. (a) Initial condition of capillary pressure in terms of water pressure in terms of water pressure head for the vertical symmetry axis. (b) Initial condition of water saturation for the vertical symmetry axis.

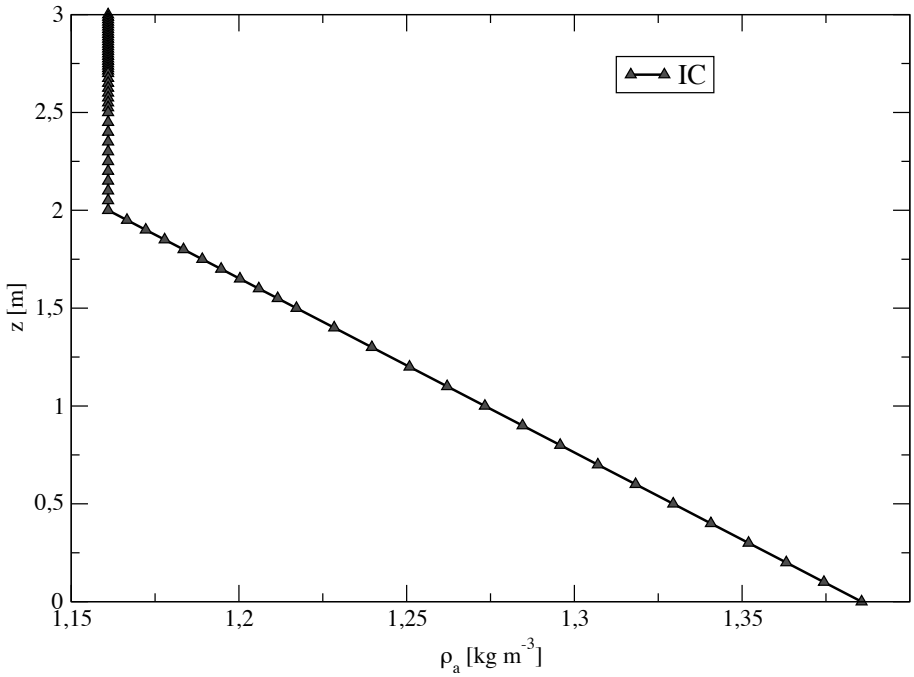

Figure 5.26: Test 2. Initial condition of air density for the vertical symmetry axis.

Parameter	Unit	Value
Maximum # of nonlinear iterations *itmax*	[-]	50
Maximum # of nonlinear iterations *itmax1*	[-]	30
Minimum # of nonlinear iterations *itmax2*	[-]	20
Magnification factor Δt_{mag}	[-]	1.05
Reduction factor Δt_{red}	[-]	0.5
Maximum allowed time step Δt_{max}	[s]	10^{+03}
Minimum allowed time step Δt_{min}	[s]	10^{-08}
Initial time step Δt_{ic}	[s]	10^{-07}
Simulated time t_{max}	[s]	$1.0e^{+04}$
Linear tollerance ϵ_l	[-]	10^{-05}
Non-linear tollerance ϵ_l	[-]	1

Table 5.12: Test 2. Nonlinear and HTS paramenters.

Results

Parameter	Unit	Value
Total linear system solution time	[s]	85.85
Total simulation time	[s]	359.86
Total # of time steps	[-]	482
Total # of backstepping	[-]	2
Total # of linear iterations	[-]	70291
Total # of nonlinear iterations	[-]	2370
Avg. nonlinear iterations per time step	[-]	4.92
Avg. linear iterations per time step	[-]	145.83
Avg. linear iterations per nonlinear iteration	[-]	29.66
Rel. water mass balance error based on caeras	[%]	1.53677E+00
Rel. water mass balance error based on cerras	[%]	1.53677E+00
Rel. air mass balance error based on caeras	[%]	-1.54405E+00
Rel. air mass balance error based on cerras	[%]	1.53508E+00

Table 5.13: Test 2. Timing results after 10000 s of water infiltration.

The timing results after 10000 s of water infiltration are shown in Table (5.13). The evolution of the number of nonlinear iteration during the entire simulation, of the average number of linear iterations for each time step are shown in Figure 5.27(a) and (b), respectively. Figure 5.27 shows the evolution of time step size during the whole simulation: 2 backstepping occured namely at $t = 2515$ s and at $t = 3339$ s (Figure 5.27c).

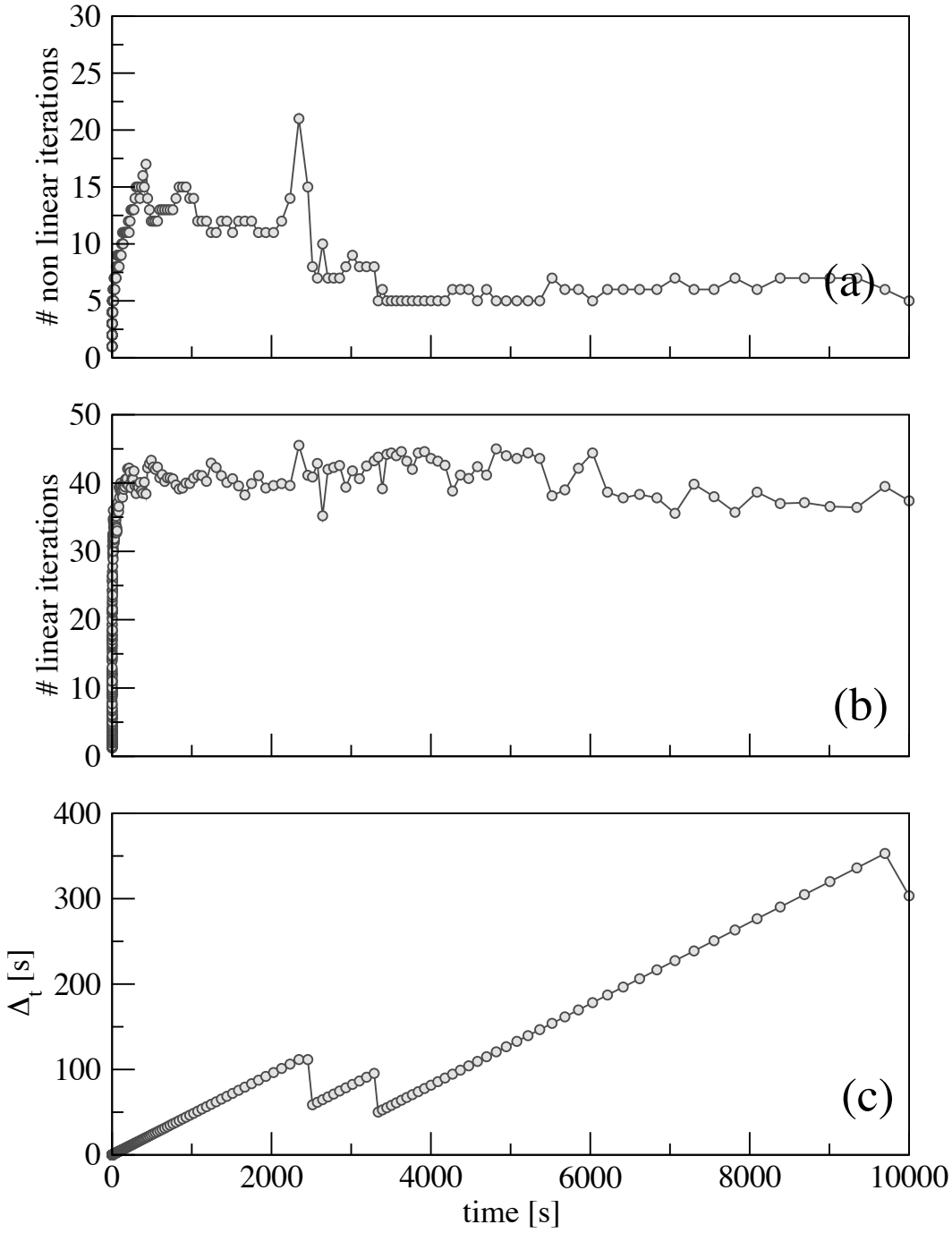

Figure 5.27: Test 2. (a) Nonlinear iterations per time step, (b) average linear iterations per time step, and (c) time step Δt variation for the entire simulation.

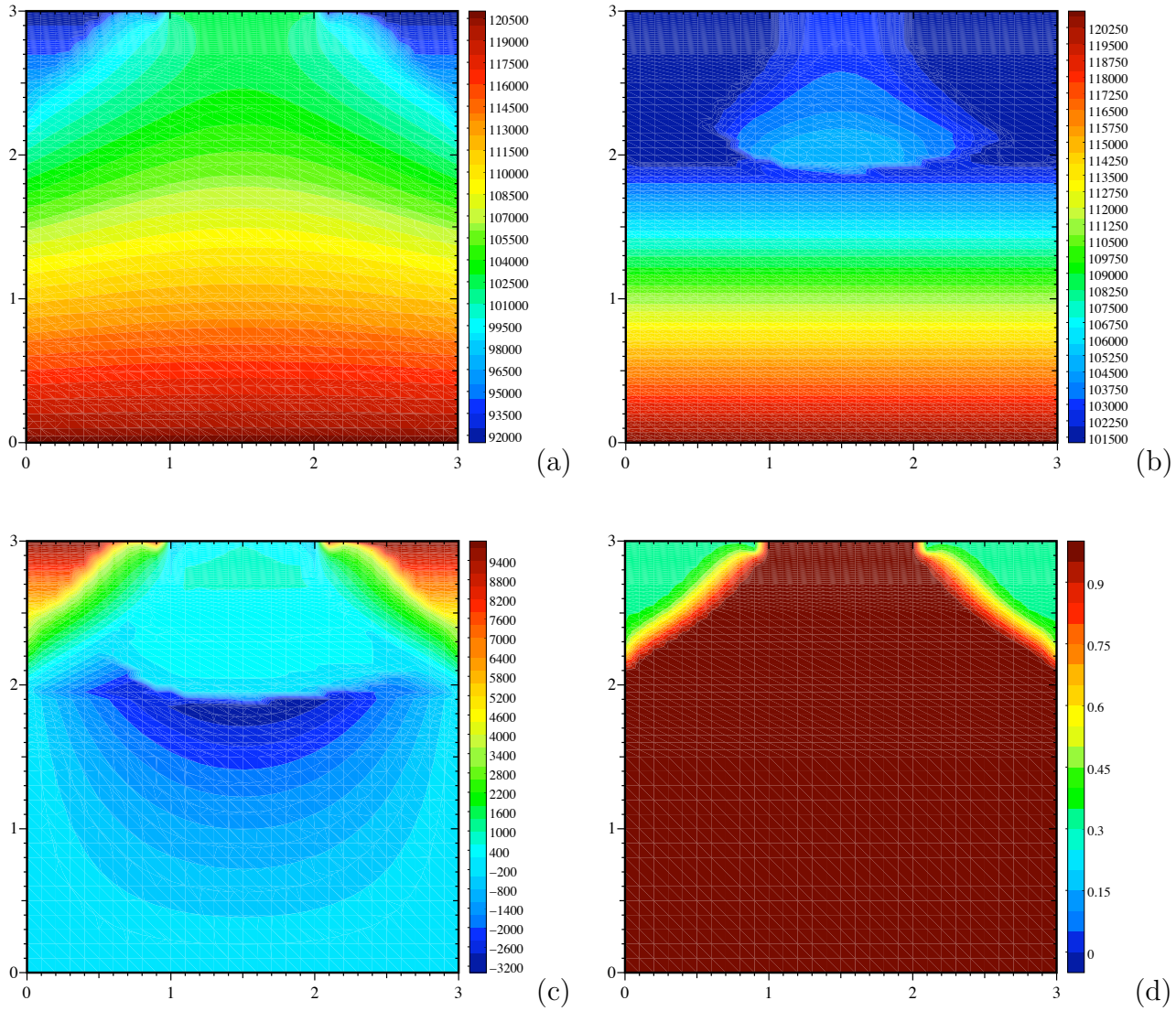

Figure 5.28: Test 2. (a) Water pressure, (b) air pressure, (c) capillary pressure, and (d) water saturation condition at the end of the simulation in the entire domain.

The distribution of water pressure, air pressure and capillary pressure at the end of the simulation are shown in Figures 5.28(a), (b), and (c), respectively. Figure 5.28(d) shows the water saturation distribution. Figures 5.29(a), 5.29(b), 5.30(a), 5.30(b), and 5.31 show the evolution of the water, the air, and the capillary pressure all in terms of water pressure head, and of the water saturation and air density along the vertical simmetry axis. The evolution of the fluxes through Dirichlet boundary nodes of water and air during the simulation are shown in Figures 5.32(a) and (b), respectively.

The water infiltrates for the entire simulation period, reaching the original water table level, i.e. $z = 2$ m. The air originally present in the upper part of the domain is

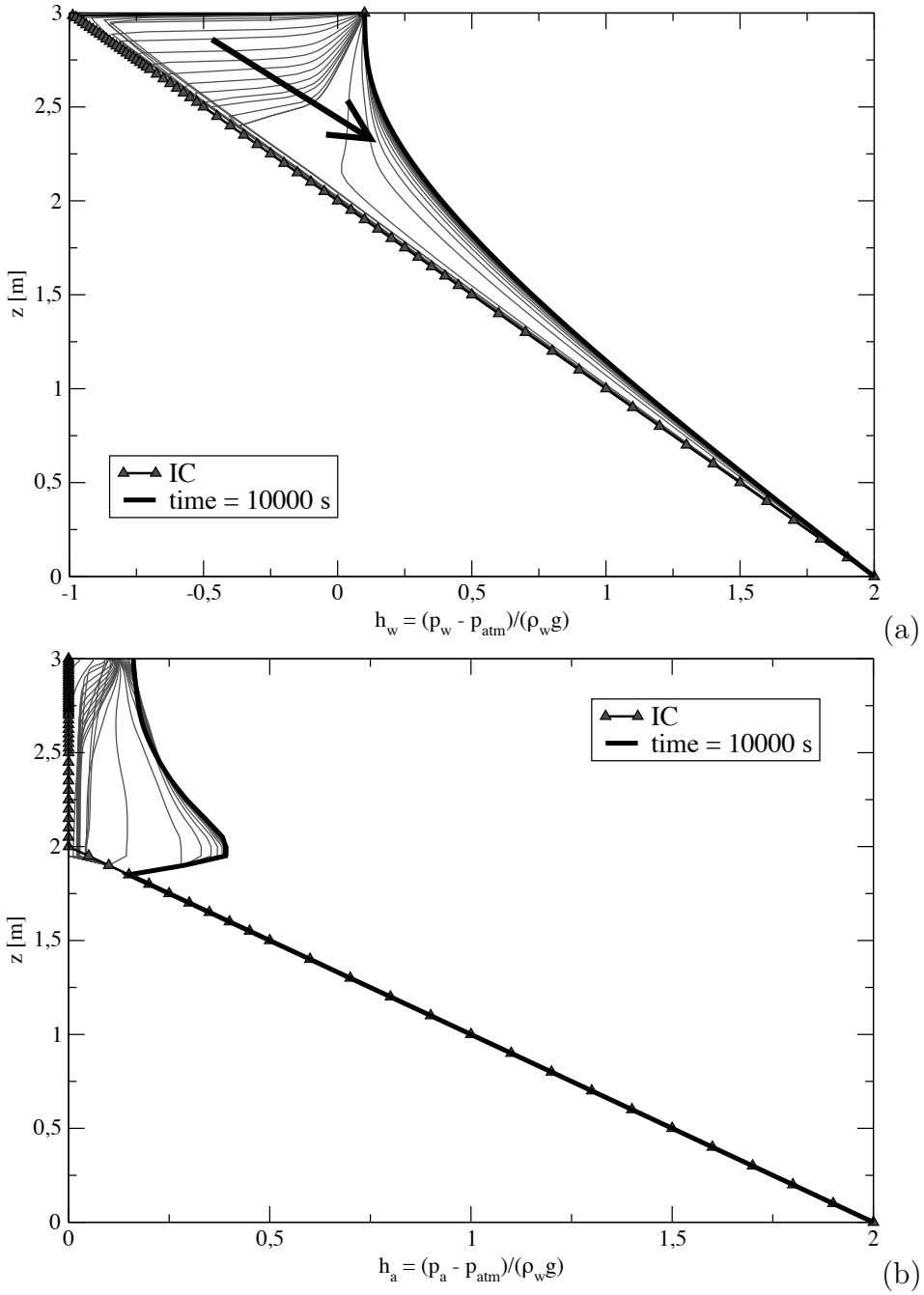

Figure 5.29: Test 2. Evolution of water (a) and (b) air pressure in terms of water pressure head for the vertical symmetry axis.

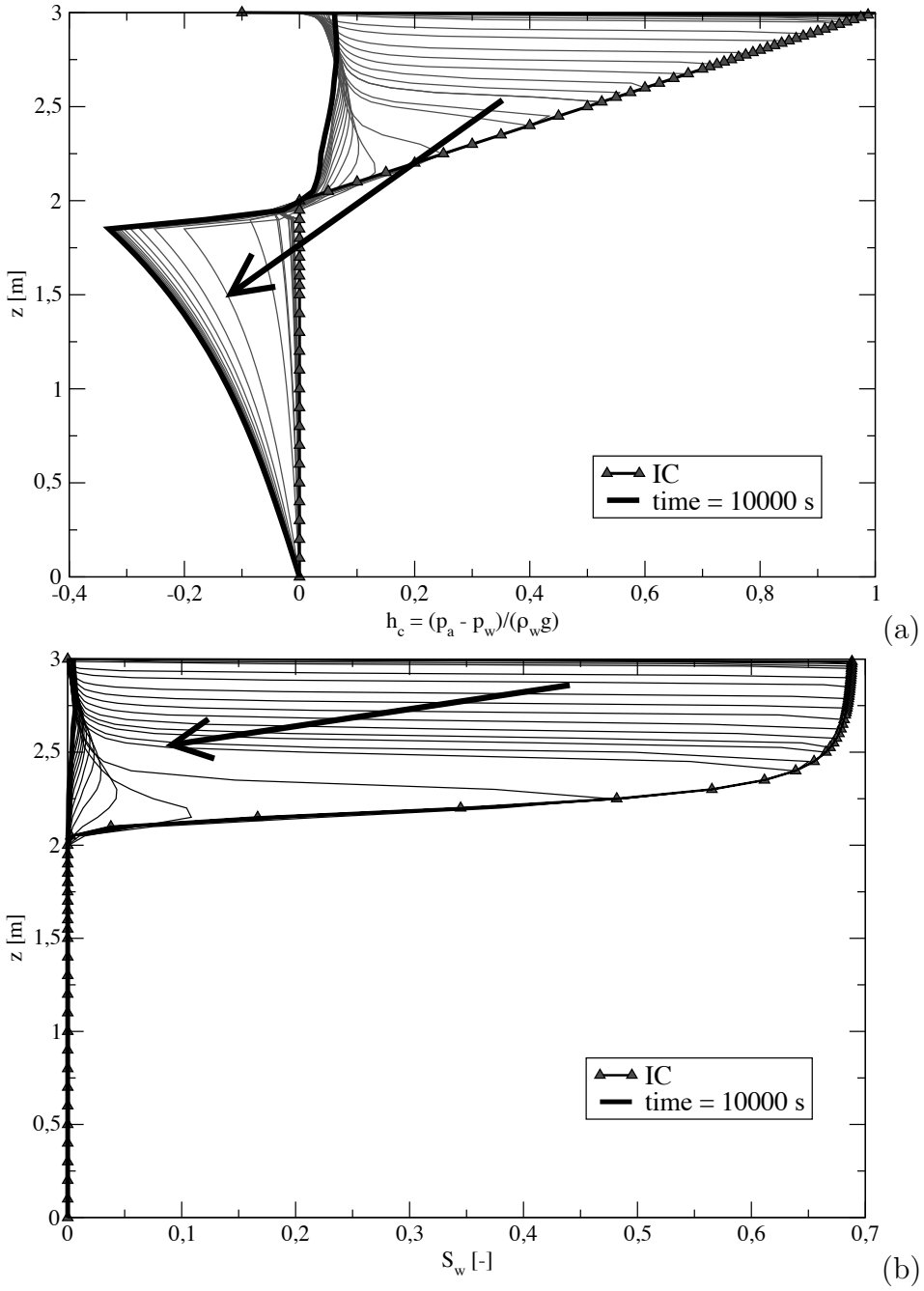

Figure 5.30: Test 2. (a) Evolution of the capillary pressure in terms of water pressure head and (b) of the water saturation for the vertical symmetry axis.

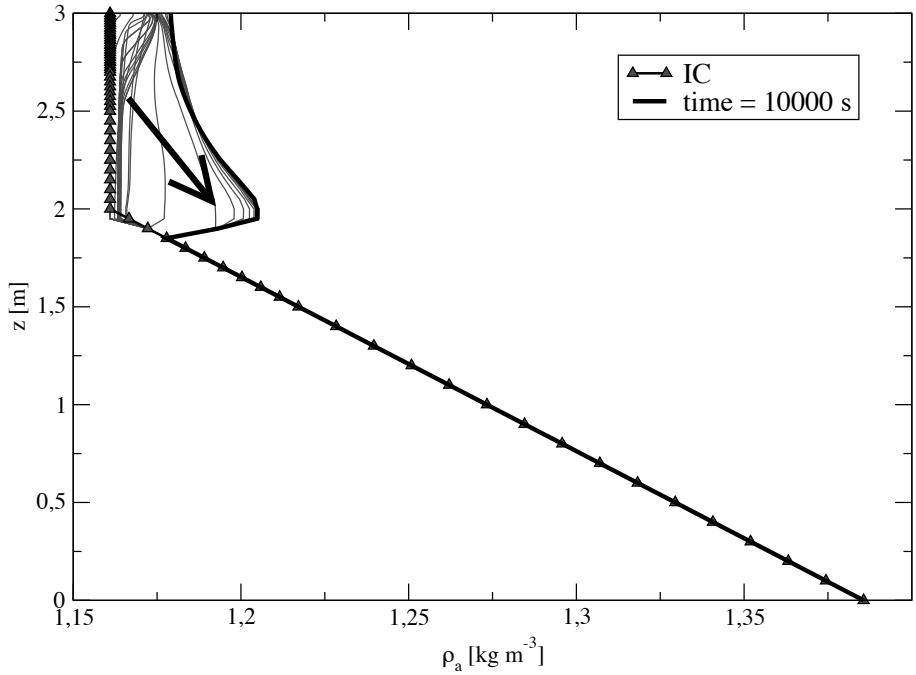

Figure 5.31: Test 2. Evolution of air density ρ_a for the vertical section of the square domain such at $x = 1.5m$.

compressed between the infiltrating water fron and the freeboard. An evident increase of the air pressure, hence of ots density, can be detected close to the upper part of the domain and in the central part, close to the water table. The evolution of the in- and out-masses as well as the absolute error in the mass balance evaluation of both water and air, namely

$$M_{in} + M_{out} - \Delta M_{stor} \tag{5.141}$$

are portraied in Figures 5.33 and 5.34, respectively.

Figure 5.35(a) shows the evolution of mass balance error evaluated respect to the complete balance. Similarly, the air relative mass balance error (calculated according with 5.139) is shown in Figure 5.35(b): it has to be noticed that close to the end of the simulation it is higher than 5%.

5.5.3 Test3: simple sandbox with water table at $z = 2\ m$ and $p_g = p_{atm}$ under it

This test is based on the previous one and it differs from it because under the water table the air pressure is chosen equal to the atmospheric pressure, as in the Richards' assumption ([Philip, 1969]). The domain is still the sandy box 3 m wide by 3 m high

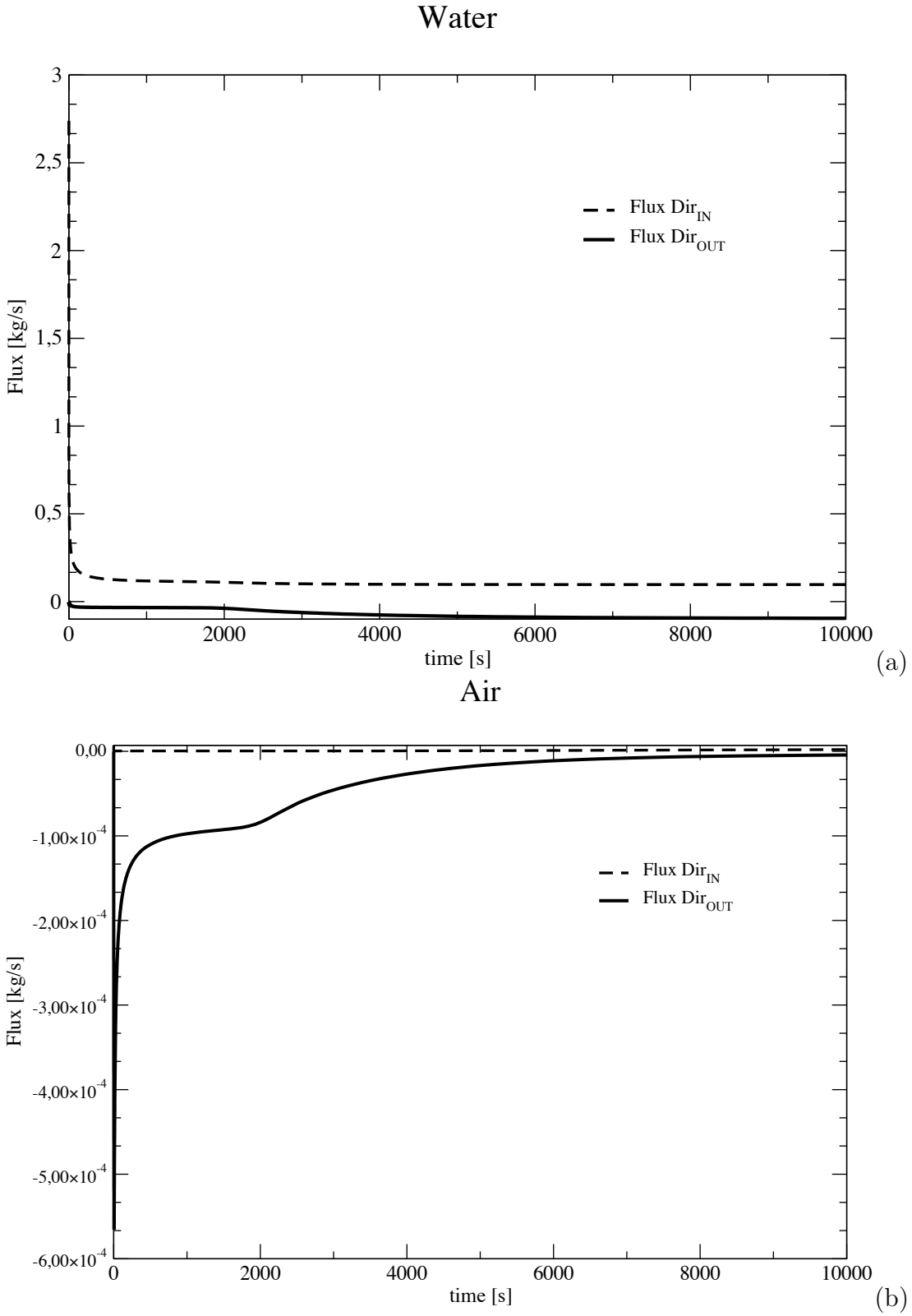

Figure 5.32: Test 2. (a) Water and (b) air in- and out-fluxes from Dirichlet boundary nodes

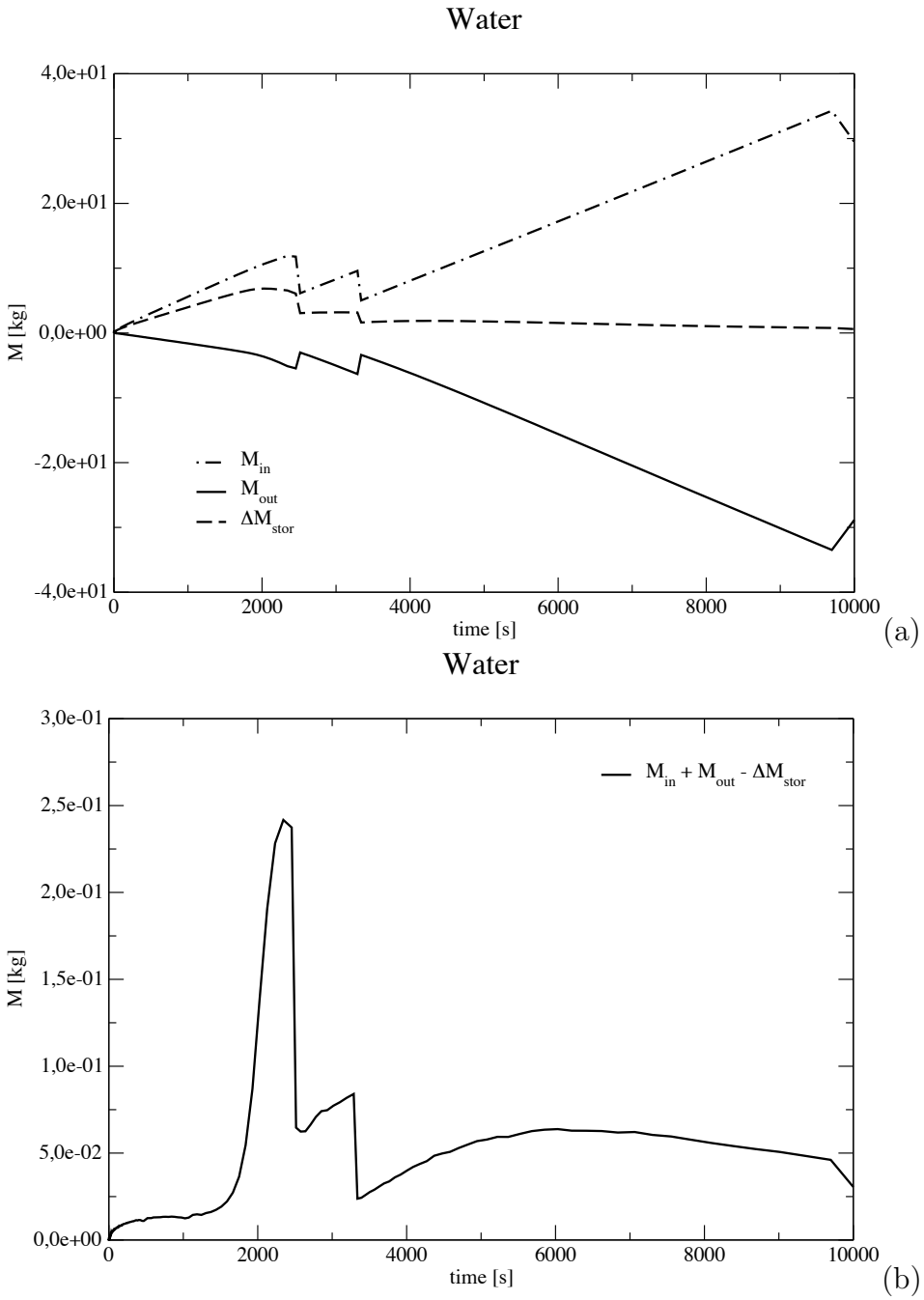

Figure 5.33: Test 2. (a) Input, output and stored masses of water during the simulation. (b) Water mass balance absolute error evolution in time.

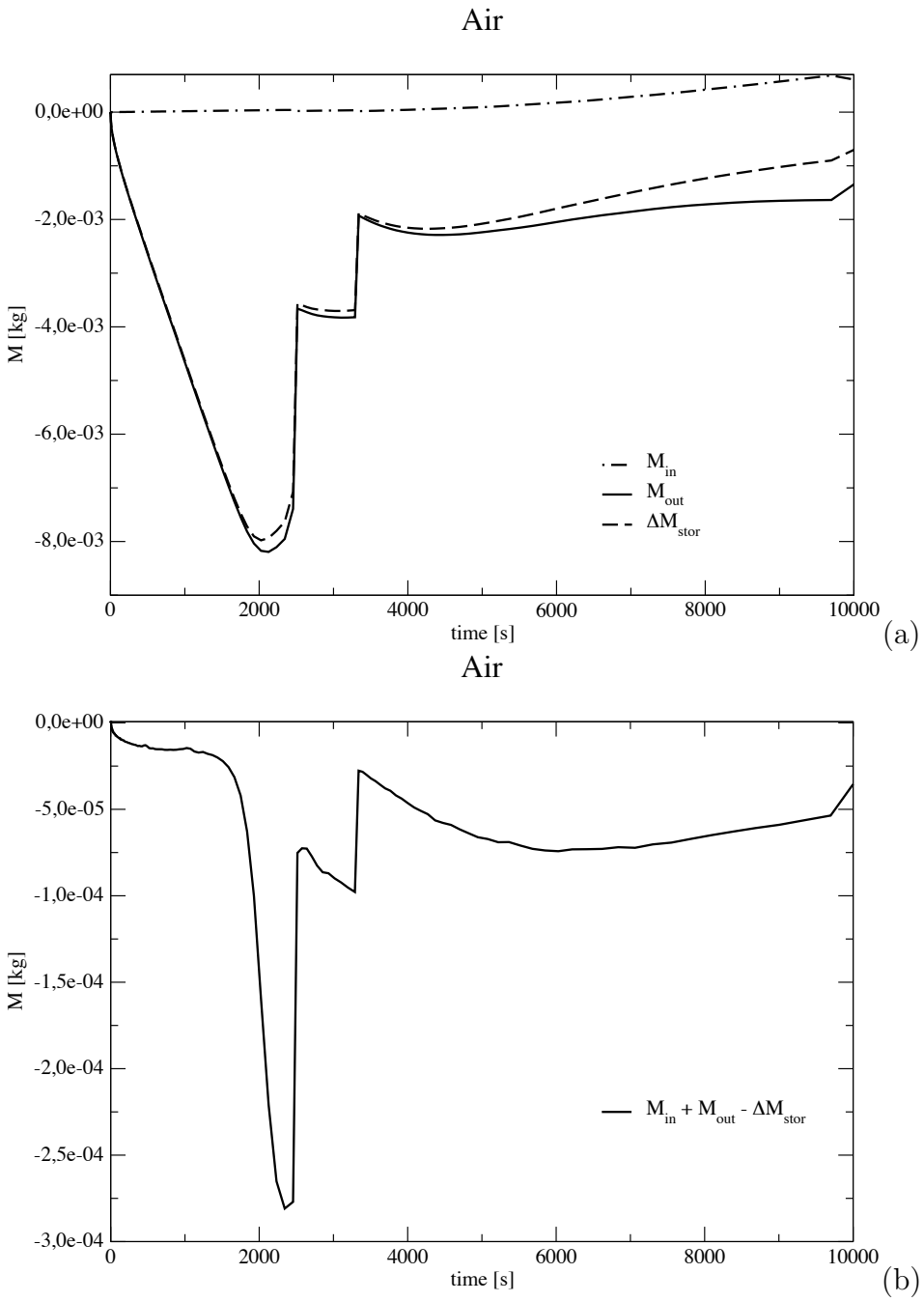

Figure 5.34: Test 2. (a) Input, output and stored masses of air during the simulation. (b) Air mass balance absolute error evolution in time.

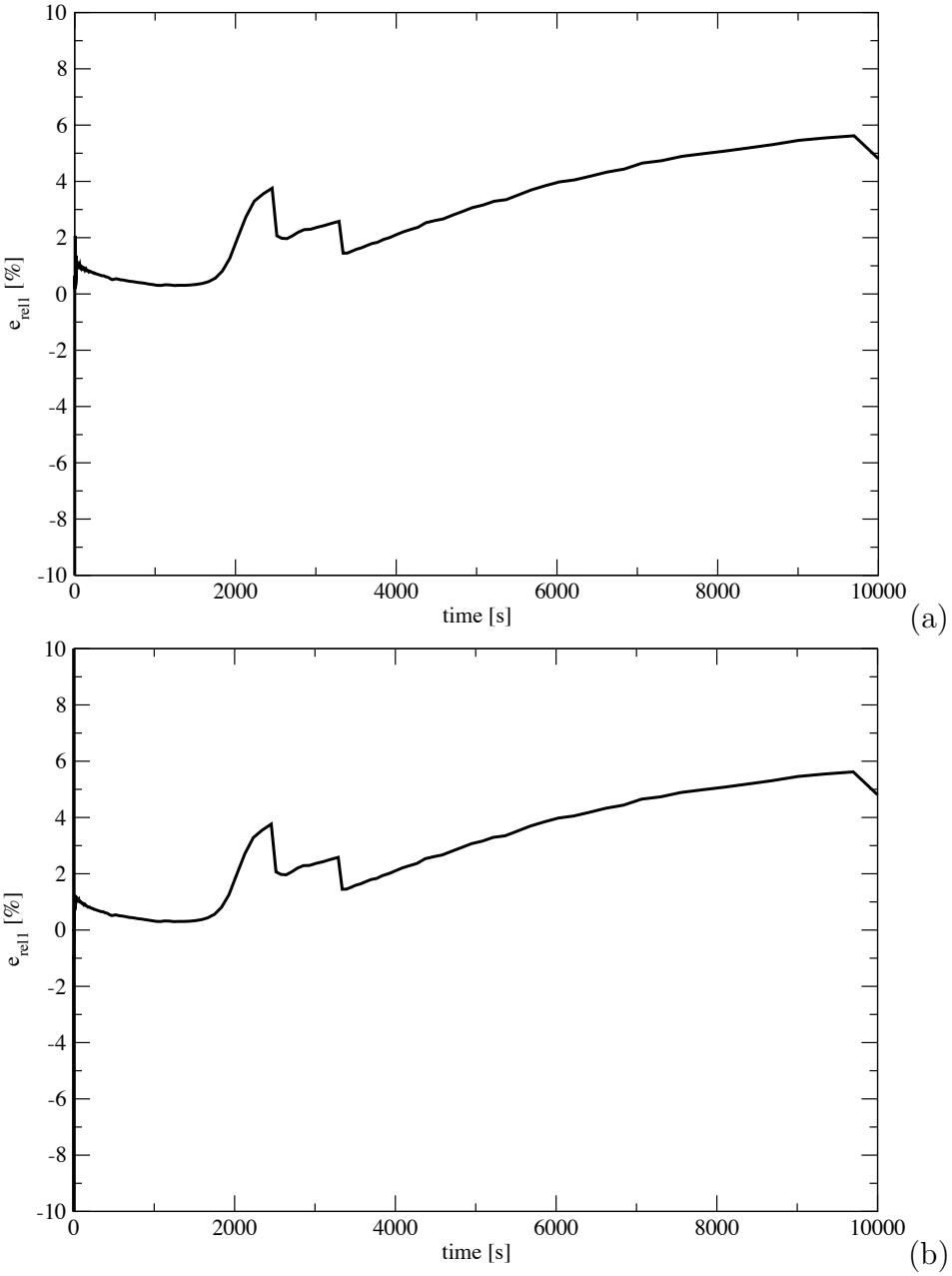

Figure 5.35: Test 2. Relative mass balance error of (a) water and (b) air.

considered before. The same soil and fluids parameters given in Table 5.2 are used. The

z_1 [m]	z_2 [m]	Δz [m]
3.0	2.7	0.0125
2.7	2.5	0.0250
2.5	1.5	0.0500
1.5	0.0	0.1000

Table 5.14: Test 3. Vertical discretization of the domain

domain has been discretized using a structured mesh of 2108 nodes and 4020 triangles with an horizontal discretization $\Delta x = 0.1$ m and a vertical discretization Δz varing with the depth according with Table 5.14. The vertical discretization is more refined close to the surface and to the water table, in order to ensure a more accurate transition from the unsaturated to the saturated zone.

Variable	IC
water pressure	$p_w = p_{atm} + (z_{wt} - z) \cdot \rho_w \cdot g$
air pressure	$p_a = p_{atm}$
capillary pressure	$p_c = p_a - p_w = -z \cdot \rho_w \cdot g$
water saturation	$S_w = S_w(p_c)$

Table 5.15: Test 3. Initial conditions of water, air and capillary pressure. Water saturation is calculated as a function of capillary pressure with van Genuchten relation.

x	**z**	**Phase**	B.C.
$0 \leq x < 1$, $2 < x \leq 3$	$z = 3$	water	$p_{atm} + (z_{wt} - z) \cdot \rho_w \cdot g$
		air	$p_a = p_{atm}$
$1 \leq x \leq 2$	$z = 3$	water	$p_w = p_{atm} + h_{pond} \cdot \rho_w \cdot g$
		air	$-\left[\frac{\mathrm{k} K_{ra}}{\mu_a}(S_a) \cdot (\nabla p_a + \rho_a g \eta_z)\right] \cdot n = 0$
$x = 0$, $x = 3$	$0 \leq z < 3$	water	$p_{atm} + (z_{wt} - z) \cdot \rho_w \cdot g$
		air	$p_a = p_{atm}$
$0 \leq x \leq 3$	$z = 0$	water	$p_w = p_{atm}$
		air	$p_a = p_{atm}$

Table 5.16: Test 3. Boundary conditions imposed on the primary unknowns.

A constant water pressure head of 0.10 m has been applied over the region defined by $z = Z = 3$ m and 1 m $\leq x \leq$ 2 m. Hydrostatic water pressure was assumed on

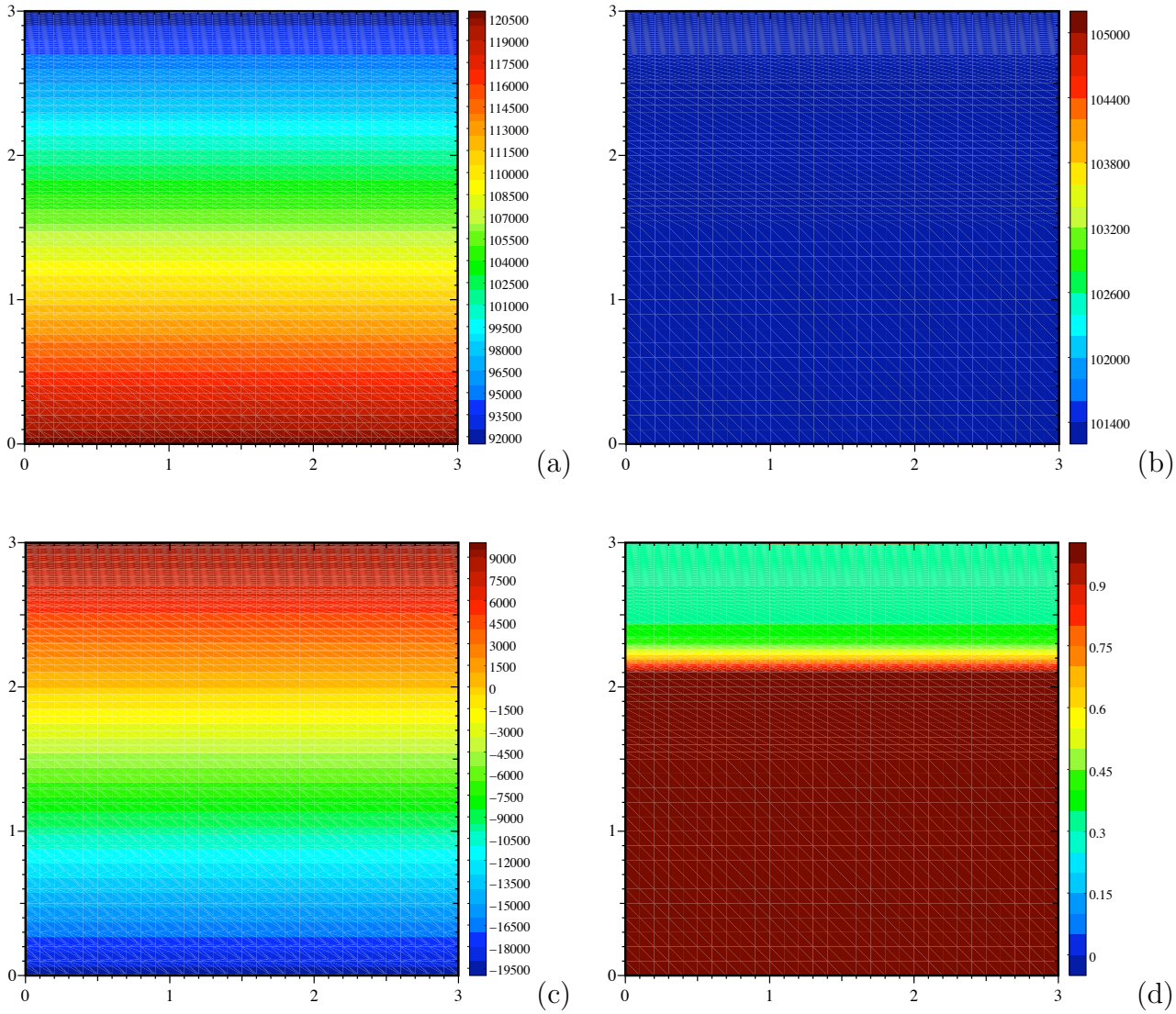

Figure 5.36: Test 3. Initial condition of (a) water, (b) air, (c) capillary pressure, and (d) water saturation.

the remaining part of the upper boundary, the bottom one and along the lateral sides according with the water table height that is initially supposed to be at $z = z_{wt} = 2$ m.

The part of the upper boundary where there was no ponding water was open to air with a constant pressure equal to the atmospheric pressure, i.e. 101325 Pa, as well as on the sides and on the bottom. Corresponding to the region of the upper boundary on which water ponding condition was imposed a no-flux Neumann boundary condition for the air was imposed (Table 5.16). The initial conditions of water, air, and capillary pressure as well as water saturation are summarized in Table 5.15 and are shown in Figure 5.36.

The initial conditions of water, air, and capillary pressure of water pressure head for

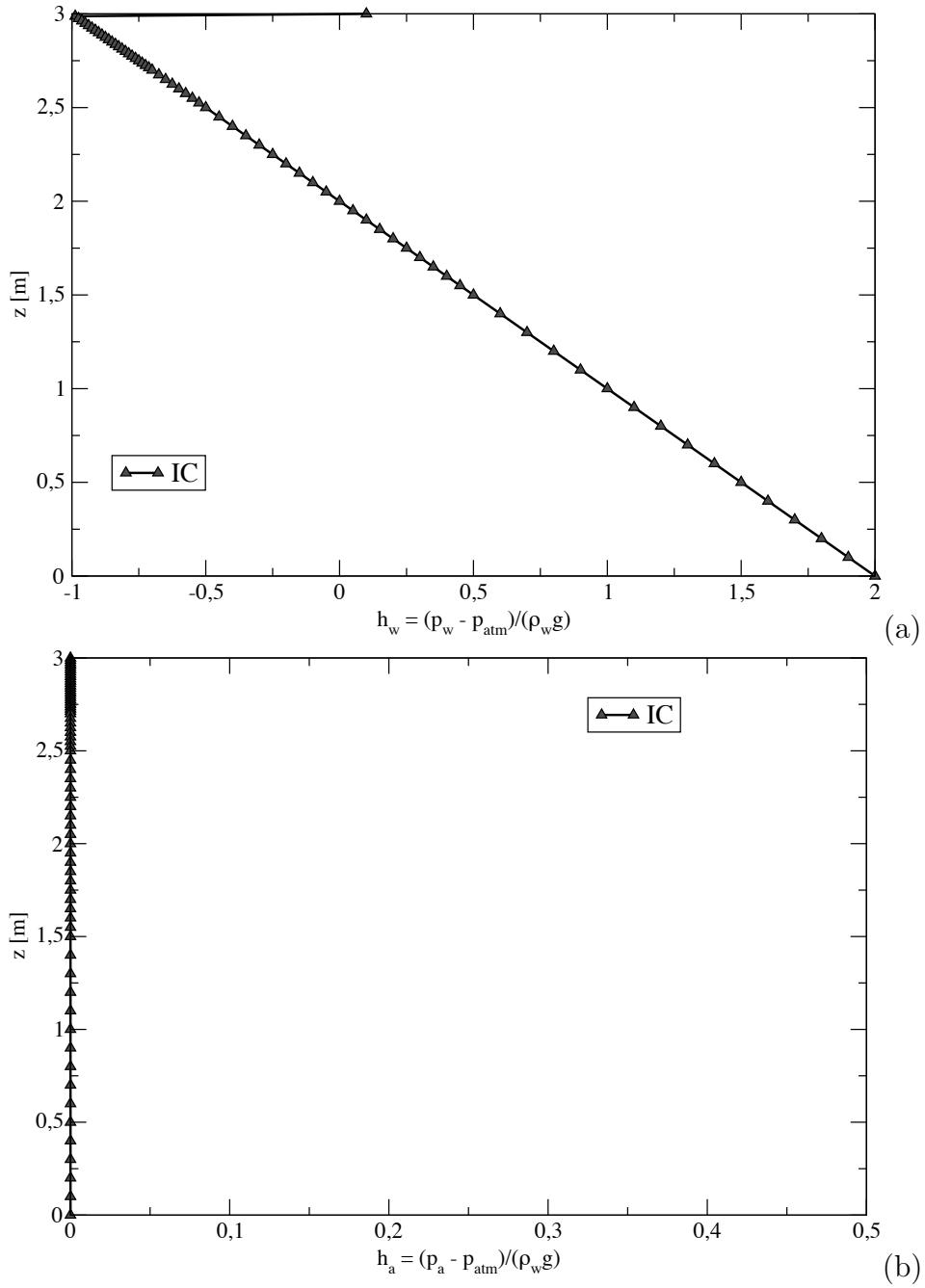

Figure 5.37: Test 3. Initial condition of water pressure (a) and air pressure (b) in terms of water pressure head for the vertical symmetry axis.

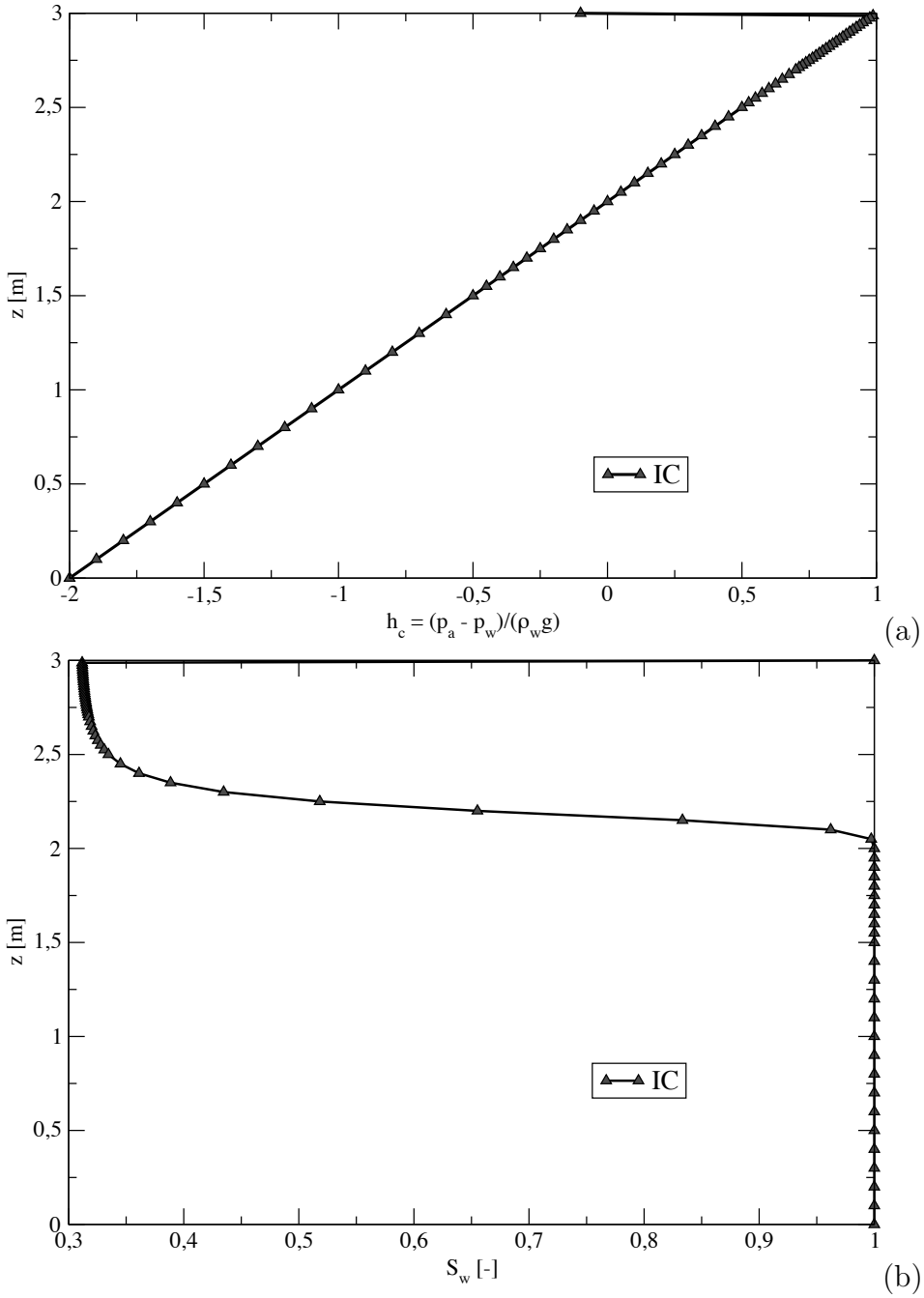

Figure 5.38: Test 3. (a) Initial condition of capillary pressure in terms of water pressure in terms of water pressure head for the vertical symmetry axis. (b) Initial condition of water saturation for the vertical symmetry axis.

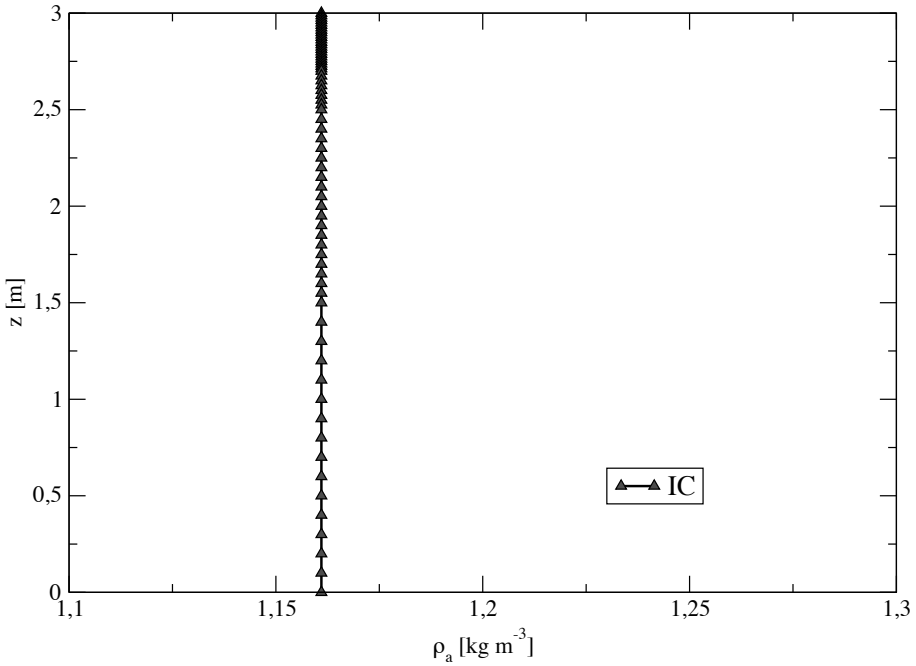

Figure 5.39: Test 3. Initial condition of air density for the vertical symmetry axis.

the vertical symmetry axis of the square domain are shown in Figures 5.37(a), 5.37(b), and 5.38(a), respectively. The water saturation and air density initial condition are also shown in Figures 5.38(b), and 5.39. The infiltration period has been carried out for the entire simulation. Non-linear and heuristic time stepping (HTS) parameters are reported in Table (5.17).

Parameter	Unit	Value
Maximum # of nonlinear iterations *itmax*	[-]	50
Maximum # of nonlinear iterations *itmax1*	[-]	30
Minimum # of nonlinear iterations *itmax2*	[-]	20
Magnification factor Δt_{mag}	[-]	1.05
Reduction factor Δt_{red}	[-]	0.5
Maximum allowed time step Δt_{max}	[s]	10^{+03}
Minimum allowed time step Δt_{min}	[s]	10^{-08}
Initial time step Δt_{ic}	[s]	10^{-07}
Simulated time t_{max}	[s]	$1.0e^{+04}$
Linear tollerance ϵ_l	[-]	10^{-05}
Non-linear tollerance ϵ_l	[-]	1

Table 5.17: Test 3. Nonlinear and HTS paramenters.

Results

Parameter	Unit	Value
Total linear system solution time	[s]	85.96
Total simulation time	[s]	271.16
Total # of time steps	[-]	482
Total # of backstepping	[-]	2
Total # of linear iterations	[-]	70283
Total # of nonlinear iterations	[-]	2360
Avg. nonlinear iterations per time step	[-]	4.90
Avg. linear iterations per time step	[-]	145.82
Avg. linear iterations per nonlinear iteration	[-]	29.78
Rel. water mass balance error based on caeras	[%]	1.53677E+00
Rel. water mass balance error based on cerras	[%]	1.53677E+00
Rel. air mass balance error based on caeras	[%]	-1.54405E+00
Rel. air mass balance error based on cerras	[%]	1.53508E+00

Table 5.18: Test 3. Timing results after 10000 s of water infiltration.

The timing results after 10000 s of water infiltration are shown in Table (5.18). The evolution of the number of nonlinear iteration during the entire simulation, of the average number of linear iterations for each time step are shown in Figure 5.40(a) and (b), respectively. Figure 5.40 shows the evolution of time step size during the whole simulation: 2 backstepping occured namely at $t = 2515$ s and at $t = 3339$ s (Figure 5.27c).

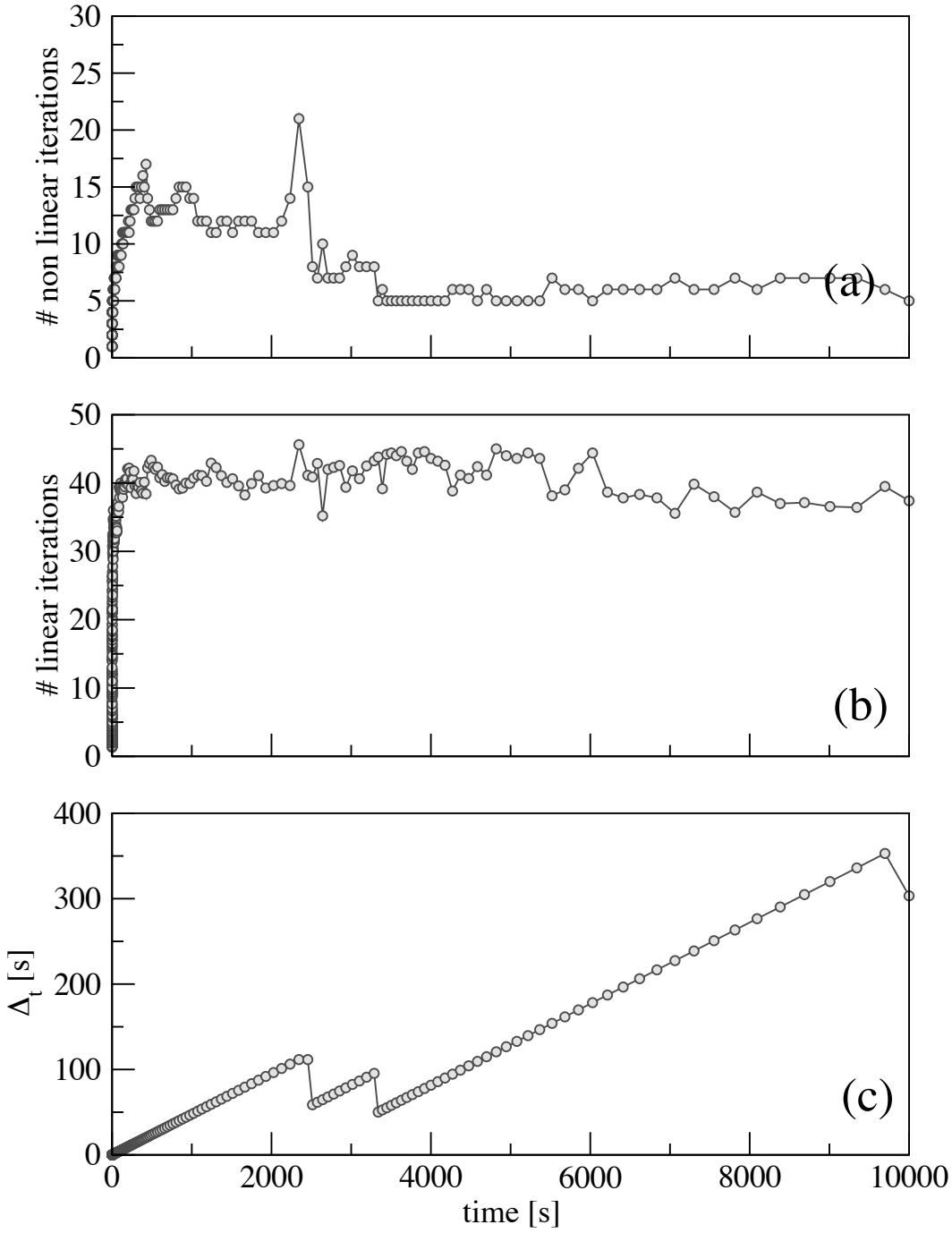

Figure 5.40: Test 3. (a) Nonlinear iterations per time step, (b) average number of linear iterations per time step, and (c) time step Δt variation for the entire simulation.

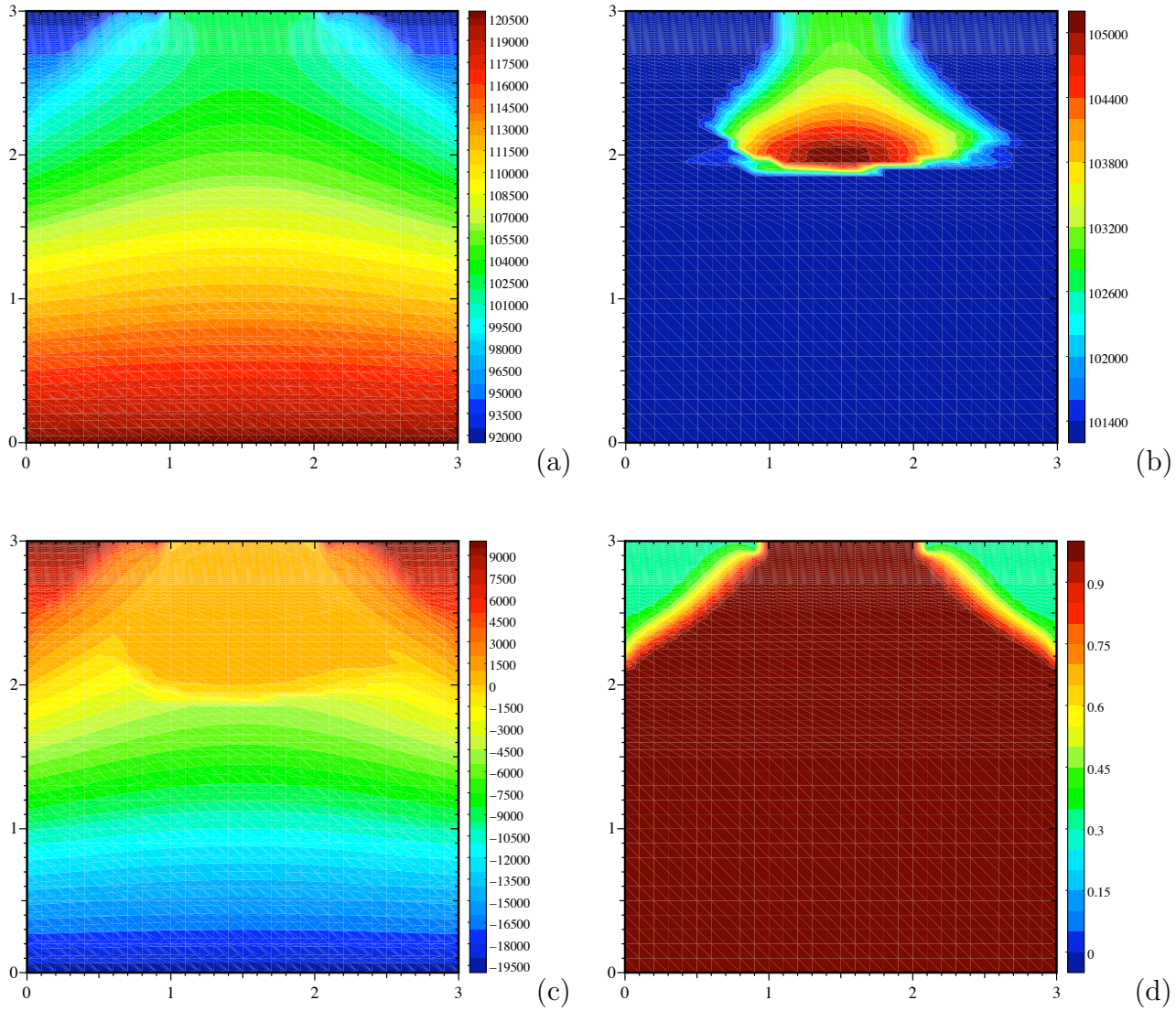

Figure 5.41: Test 3. (a) water, (b) air, (c) capillary pressure, and (d) water saturation condition at the end of the simulation in the entire domain.

The distribution of water, air, and capillary pressure at the end of the simulation are shown in Figures 5.41(a), (b), and (c), respectively. Figure 5.41(d) shows the water saturation distribution. Figures 5.42(a), 5.42(b), 5.43(a), 5.43(b), and 5.44 show the evolution of the water, the air, and the capillary pressure all in terms of water pressure head, and of the water saturation and air density along the vertical simmetry axis. The evolution of the fluxes through Dirichlet boundary nodes of water and air during the simulation are shown in Figures 5.45(a) and (b), respectively. The choice of an initial value of air pressure equal to the atmospheric one doesn't affect the results that look identical to those obtained in Test 2. The evolution of the masses of the two phases going

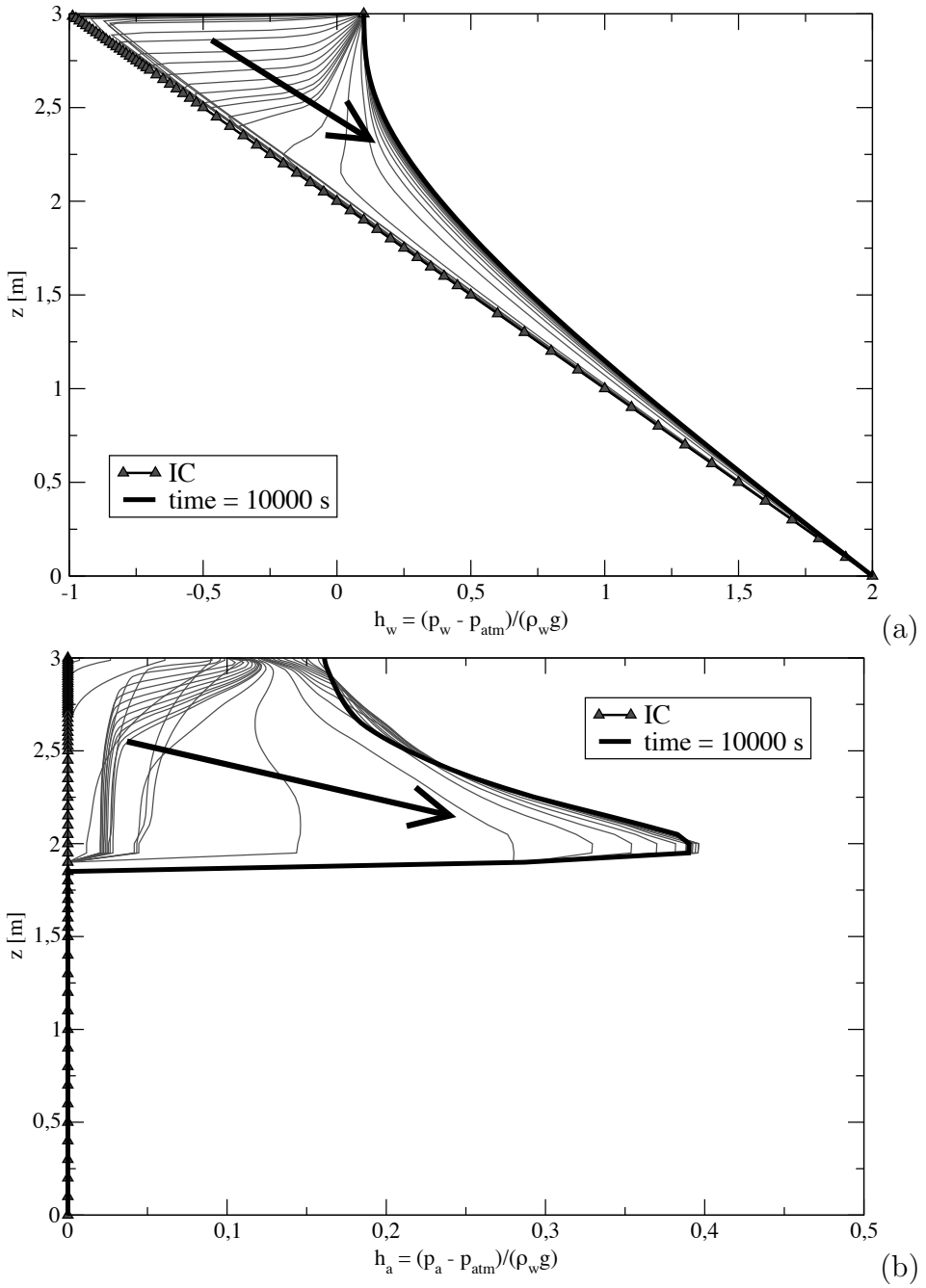

Figure 5.42: Test 3. Evolution of water (a) and (b) air pressure in terms of water pressure head for the vertical symmetry axis.

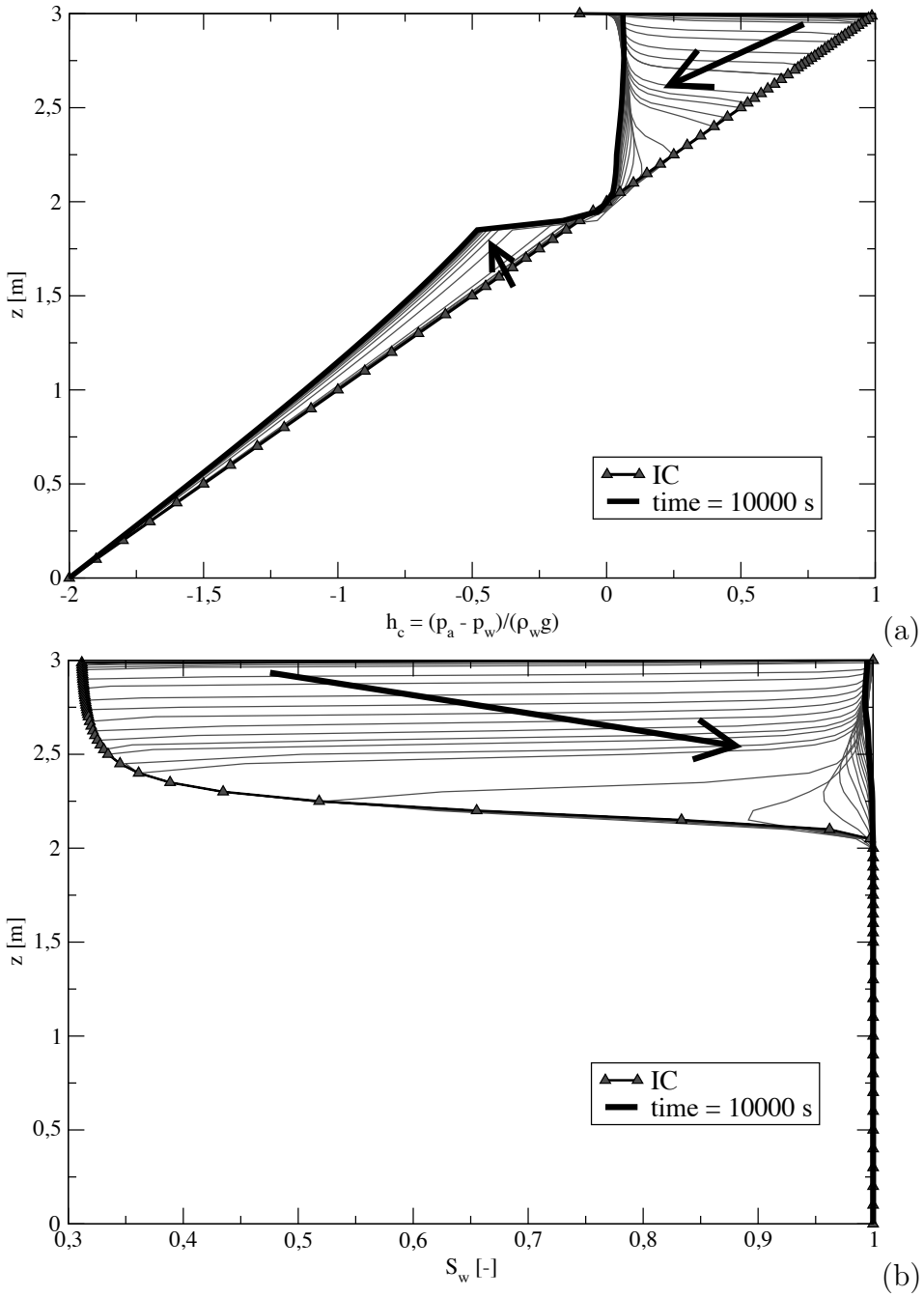

Figure 5.43: Test 3. (a) Evolution of the capillary pressure in terms of water pressure head and (b) of the water saturation for the vertical symmetry axis.

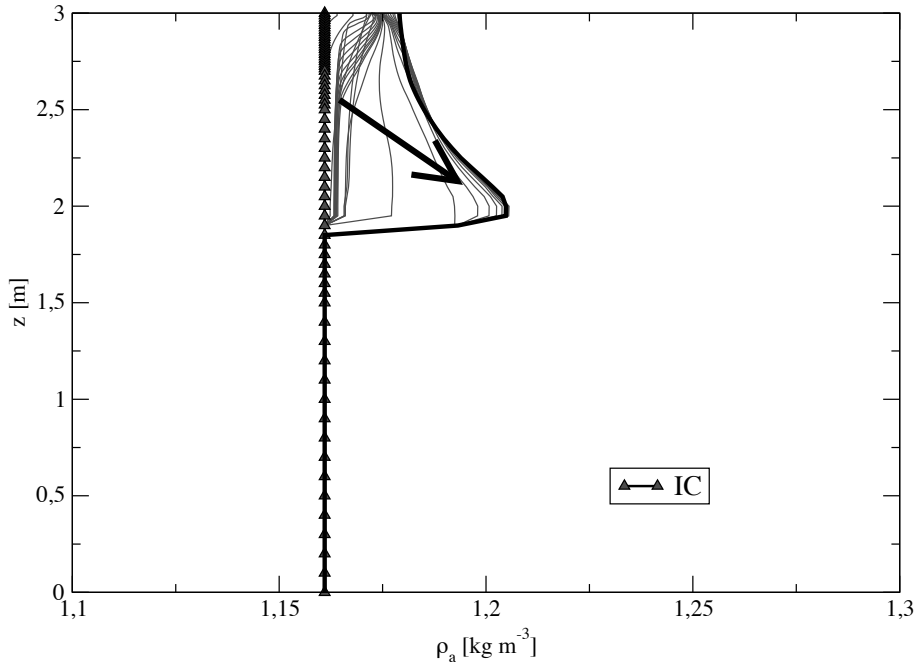

Figure 5.44: Test 3. Evolution of air density ρ_a for the vertical section of the square domain such at $x = 1.5m$.

in and out of the domain through the boundaries as well as the complete mass balance of water and air are portraied in Figures 5.46 and 5.47, respectively.

Figure 5.48(a) shows the evolution of mass balance error evaluated respect to the complete balance. Similarly, the air relative mass balance error (calculated according with 5.139) is shown in Figure 5.48(b): it has to be noticed that close to the end of the simulation it is higher than 5%.

5.6 Conclusions

The wetlands are delicate environments that are suffering in recent times because of the increasing human pressure and the effects of climate change. Understanding the dynamics that relate atmosphere, vegetation, and subsurface flow in these peculiar ecosystems requires a detail description of the phenomena that take place in the vadose zone. Richards equation based approaches are not able to account for the consequences of the entrapped air on the water infiltration in the sal marsh soils. In order to include the air dynamic, a two-phase flow model has been developed. The peculiarity of the approach presented is related to the choice of the water and air phase pressures as primary variables in order to treat the nonlinear boundary conditions that arise at the marsh surface in a natural

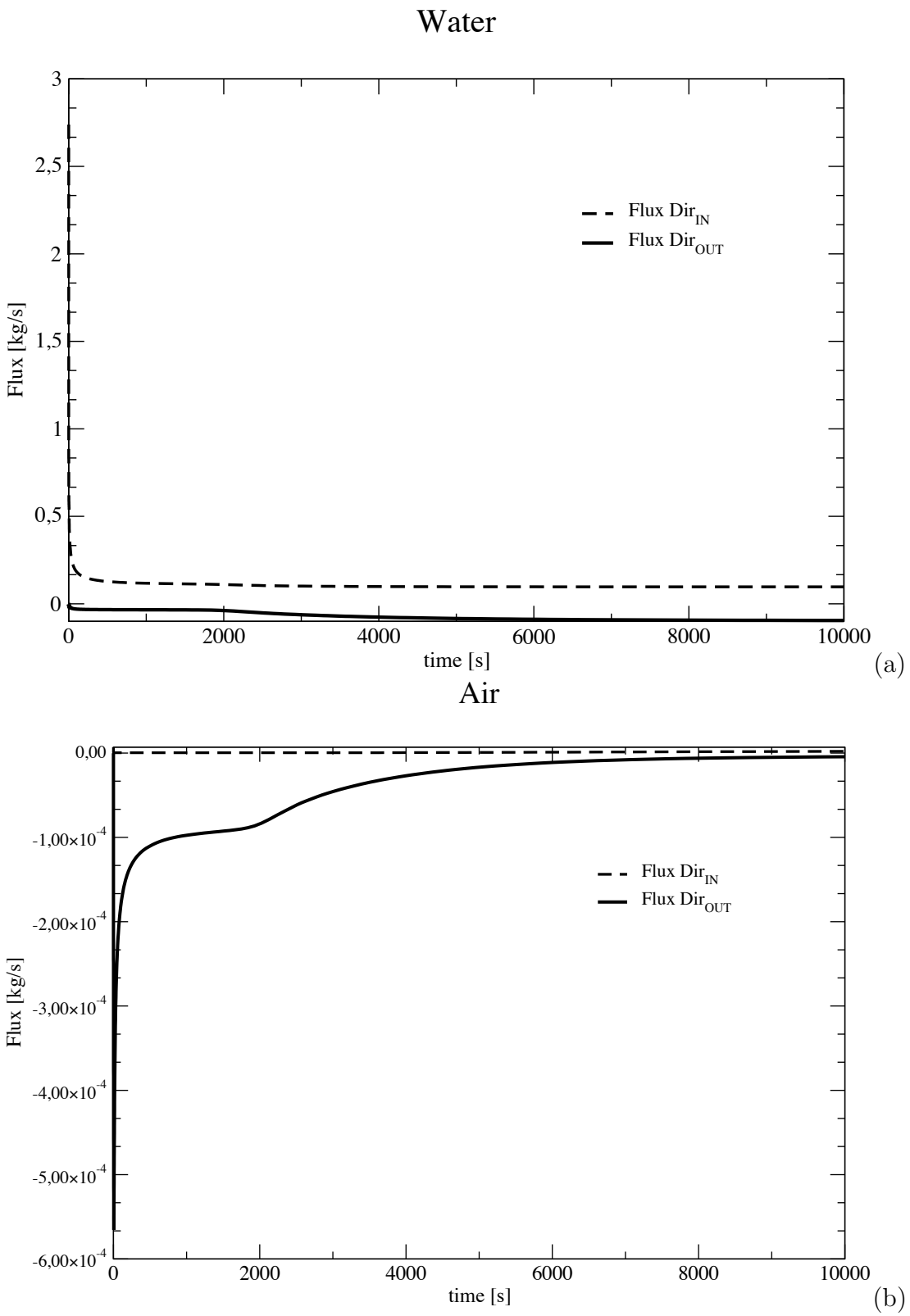

Figure 5.45: Test 3. (a) Water and (b) air in- and out-fluxes from Dirichlet boundary nodes

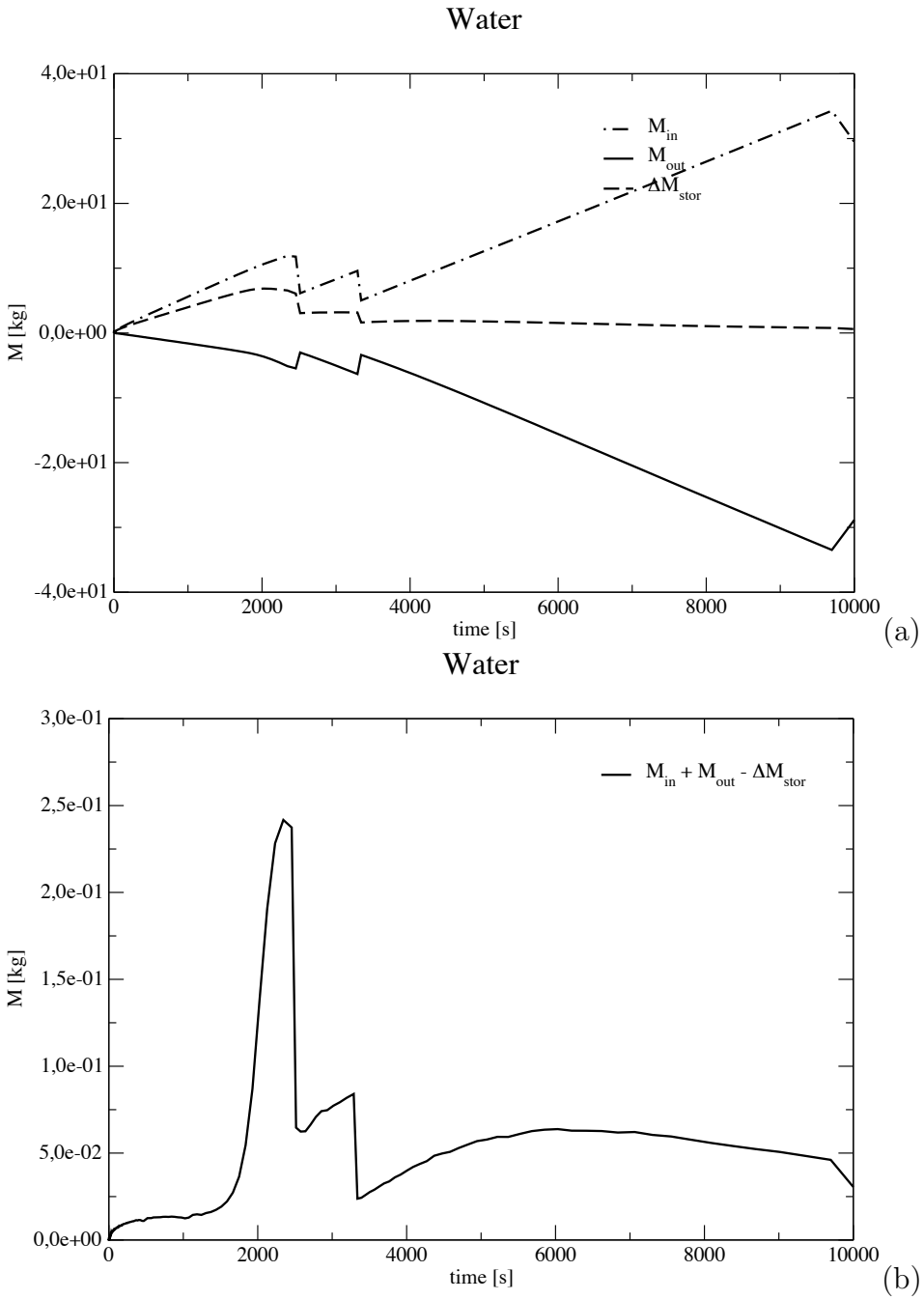

Figure 5.46: Test 3. (a) Input, output, and stored mass of water during the simulation. (b) Evolution of the absolute error in the water mass balance in time.

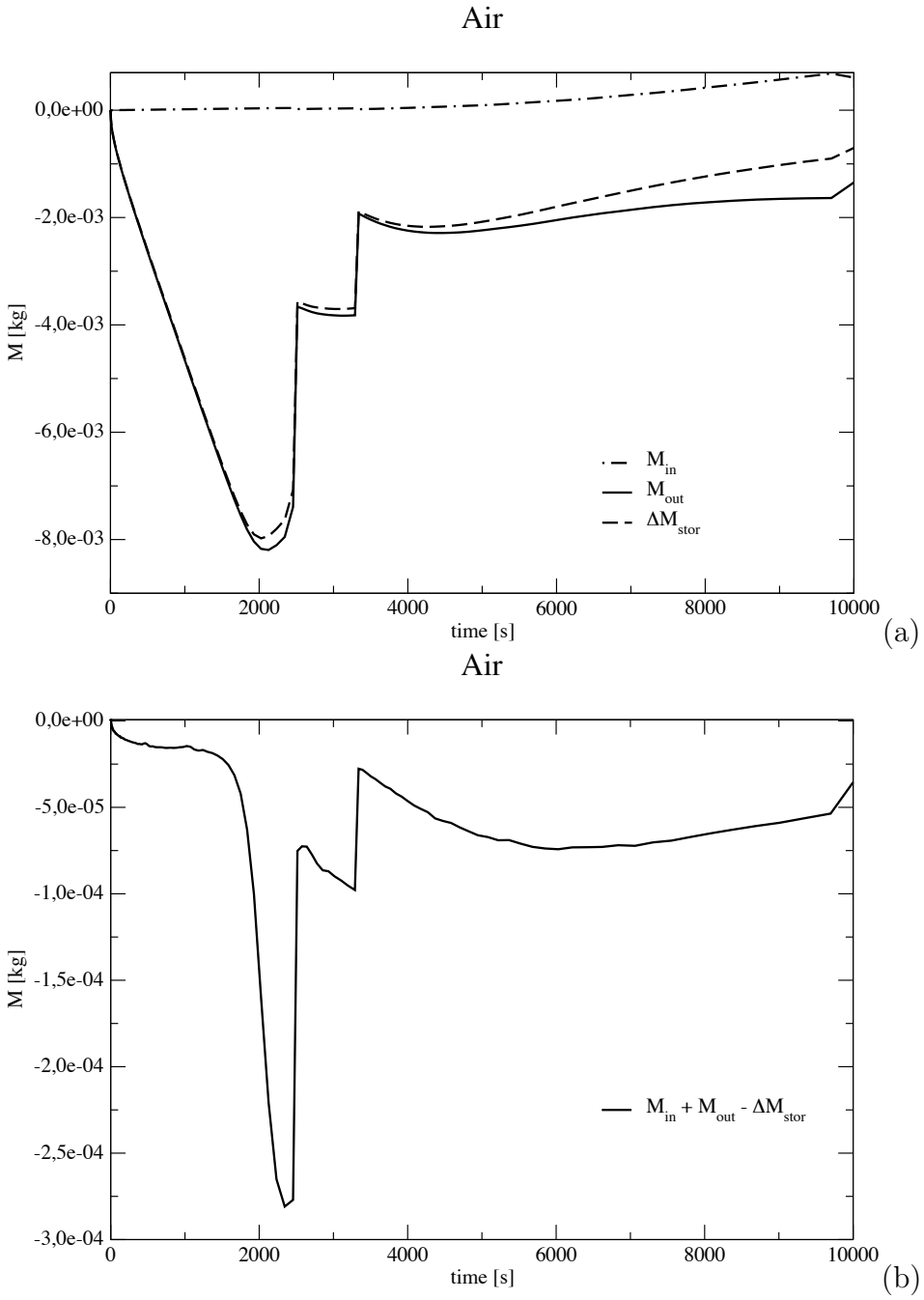

Figure 5.47: Test 3. Input, output, and stored mass of air during the simulation. (b) Air mass balance absolute error evolution in time.

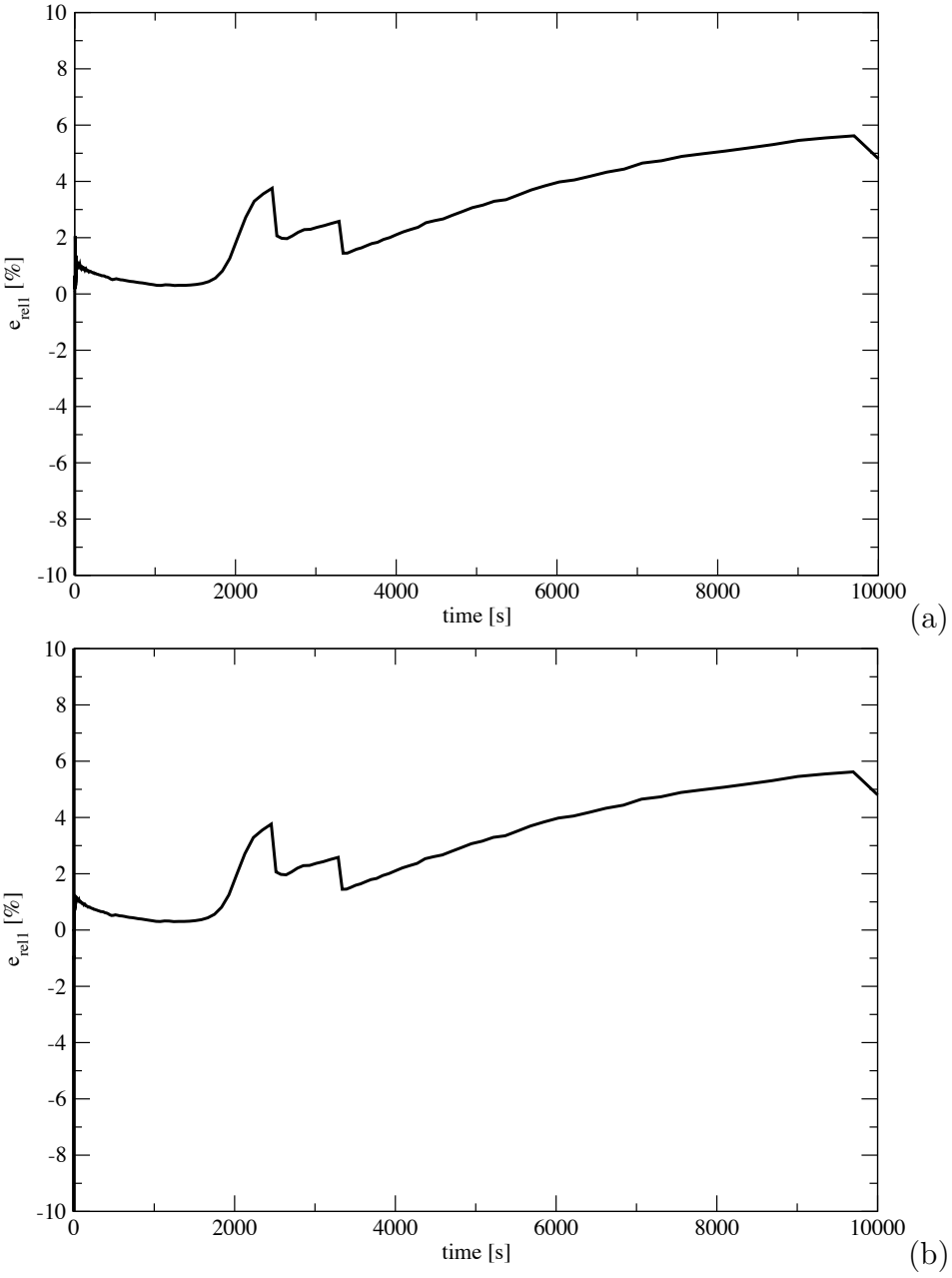

Figure 5.48: Test 3. Relative mass balance error of (a) water and (b) air.

way. The results of the application of the model to some test cases aimed at verifying the effect of the inclusion of the air dynamics in the simulation of the water flow in the vadose zone are presented. In the following, we intend to span more complicated examples, that will include the vegetation transpiration and the tidal forcing in order to reproduce and analyse the phenomena that occur in the intertidal areas.

Bibliography

Adam, P. (1990). *Saltmarsh Ecology*. Cambridge Univ. Press, New York.

Andriesse, J. P. (1988). Nature and management of tropical peat veils. Soils Bullettin 59, FAO.

Armentano, T. V. and Menges, E. S. (1986). Patterns of change in the carbon balance of organic soil-wetlands of the temperate zone. *J. Ecol.*, **74**(3), 755–774.

Armstrong, W. (1982). Waterlogged soils. In J. R. Etherington, editor, *Environment and Plant Ecology*, pages 290–330. John Wiley and Son.

Arrhenius, S. (1889). Über die Reaktionsgeschwindigkeit bei der Inversion von Rohrzucker durch Säuren. *Z. Phys. Chem.*, **4**(26), 226–248.

Bagagiolo, F. and A.Visintin (2000). Hysteresis in filtration through porous media. *Z. Anal. Anwedungen*, **19**, 977–997.

Baird, A. J. (1997). Field estimation of macropore functioning and surface hydraulic conductivity in a fen peat. *Hydrological Processes*, **11**(3), 287–295.

Bear, J. (1972). *Dynamics of Fluids in Porous Media*. Elsevier, New York.

Bixio, A. C., Orlandini, S., Paniconi, C., and Putti, M. (2000). Physically-based distributed model for coupled surface runoff and subsurface flow simulation at the catchment scale. In L. Bentley, editor, *Computational Methods in Water Resources*, volume 2, pages 1093–1099. Balkema.

Boon, J. D. (1975). Tidal discharge asymmetry in a salt marsh drainage system. *Limnol. Oceanogr*, **20**, 71–80.

Boon, J. D. and Byrne, R. J. (1981). On basin hypsometry and the morphodynamic response of coastal inlets. *Marine Geology*, **40**, 27–48.

Bozkurt, S., Lucisano, M., Moreno, L., and Neretnieks, I. (2001). Peats as a potential analogue for the long-term evolution in landfills. *Earth Sci. Rev.*, **53**, 95–147.

Brambati, A., Carbognin, L., Quaia, T., Teatini, P., and Tosi, L. (2003). The Lagoon of Venice: geological setting, evolution and land subsidence. *Episodes*, **26**(3), 264–268.

Bronswijk, J. J. B. (1990). Shrinkage geometry of a heavy clay soil at various stresses. *Soil Sci. Soc. Am. J.*, **54**, 1500–1502.

Brooks, R. H. and Corey, A. T. (1964). Hydraulic properties of porous media. Hydrology Paper 3, Colorado State University, Fort Collins, CO.

Camporese, M., Putti, M., Salandin, P., and Teatini, P. (2004). Modeling peatland hydrology and related elastic deformation. In C. T. Miller, M. W. Farthing, W. G. Gray, and G. F. Pinder, editors, *Computational Methods in Water Resources*, volume 2, pages 1453–1465, Amsterdam. Elsevier.

Camporese, M., Gambolati, G., Putti, M., Teatini, P., Bonardi, M., Rizzetto, F., Tosi, L., Ferraris, S., Gasparetto Stori, G., Nicoletti, V., Silvestri, S., and Salandin, P. (2005). Monitoring and modeling peat soil subsidence in the Venice Lagoon. In A. Zhang *et al.*, editor, *Land Subsidence (Proc. 7th Int. Symp. on Land Subsidence)*, volume II, pages 543–551. Shangai Scientific & Technical Publ.

Camporese, M., Ferraris, S., Putti, M., Salandin, P., and Teatini, P. (2006a). Hydrological modeling in swelling/shrinkage peat soils. *Water Resour. Res.*, **42**, W06420, doi:10.1029/2005WR004495.

Camporese, M., Gambolati, G., Putti, M., and Teatini, P. (2006b). Peatland subsidence in the Venice watershed. In *Developments in Earth surface processes. Peatland: basin evolution and depository of records on global environmental and climate changes*, volume 9, pages 529–559. I. P. Martini *et al.*, Amsterdam, The Netherlands.

Camporese, M., Putti, M., Salandin, P., and Teatini, P. (2008). Spatial variability of CO_2 efflux in a drained cropped peatland south of Venice, Italy. *J. Geophys. Res.*, **113**, G04018, doi:10.1029/2008JG000786.

Camporese, M., Paniconi, C., Putti, M., and Orlandini, S. (2010). Surface-subsurface flow modeling with path-based runoff routing, boundary condition-based coupling, and assimilation of multisource observation data. *Water Resour. Res.*, **46**, W02512, doi:10.1029/2008WR007536.

Carbognin, L., Gambolati, G., Putti, M., Rizzetto, F., Teatini, P., and Tosi, L. (2006). Soil contamination and land subsidence raise concern in the Venice watershed, Italy. In C. A. Brebbia *et al.*, editor, *Management of Natural Resources, Sustainable Development and Ecological Hazards*, pages 691–700. WIT Press.

Celia, M. A. and Binning, P. (1992). A mass conservative numerical solution for twophase flow in porous media with application to unsaturated flow. *Water Resour. Res.*, **28**(10), 2819–2828.

Celia, M. A., Bouloutas, E. T., and Zarba, R. L. (1990). General massconservative numerical solution for the unsaturated flow equation. *Water Resour. Res.*, **26**(7), 1483–1496.

Chapman, V. J. (1938). Studies in salt-marsh ecology III. the water table, soil aeration and drainage. *J. Ecol.*, **26**, 157–178.

Chapman, V. J. (1940). Studies in salt-marsh ecology: Sections VI and VII. comparison with marshes on the east coast of north america. *J. Ecol.*, **28**, 118–152.

Childs, E. C. and Collis-George, N. (1950). The permeability of porous materials. *Proc.Roy.Soc.*, **201**, 392–405.

Clarke, L. D. and Hannon, N. J. (1969). The mangrove swamp and salt marsh communities of the sydney district: II. the holocoenotic comples with particular reference to physiography. *J. Ecol.*, **57**, 213–234.

Colonna, J., Brissaud, F., and Millet, J. L. (1972). Evolution of capillary and relative permeability hysteresis. *Soc. Pet. Eng. J.*, **12**, 28–38.

Dacey, J. W. H. and Howes, B. L. (1984). Water uptake by roots controls water table movement and sediment oxidation in short spartina marsh. *Science*, **224**, 487–489.

Dagan, G. (1989). *Flow and Transport in Porous Formations*. Springer, Berlin.

Dane, J. H. and Wierenga, P. J. (1975). Effect of hysteresis on the prediction of infiltration, redistribution and drainage of water in a layered soil. *J. Hydrol.*, **25**, 229–242.

Darby, H. C. (1956). *The draining of the fens*. Cambridge University Press, Oxford.

Dasberg, S. and Neuman, S. P. (1977). Peat hydrology in the Hula Basin, Israel: I. properties of peat. *J. Hydrol.*, **32**, 219–239.

Davidson, E. A. and Janssens, I. A. (2006). Temperature sensitivity of soil carbon decomposition and feedback to climate change. *Nature*, **440**, 165–173.

Davis, J. F. and Engeberg, C. A. (1955). A report on investigation of subsidence of organic soils. *Michigan Agricultural Experiment Station Quarterly Bullettin*, **37**.

De Marsily, G. (1986). *Quantitative hydrogeology : groundwater hydrology for engineers*. Academic Press, San Diego.

Deverel, S. J. and Rojstaczer, S. (1996). Subsidence of agricultural lands in the Sacramento-San Joaquin Delta, California: Role of aqueous and gaseous carbon fluxes. *Water Resour. Res.*, **32**(8), 2359–2367.

D'Haese, C. M., Putti, M., Paniconi, C., and Verhoest, N. E. (2006). Assessment of adaptive and heuristic time stepping for variably saturated flow. *Int. J. Numer. Meth. Fluids*, **53**(7), 1173–1193.

Enderby, J. A. (1955). The domain of hysteresis. Part I, independent domains. *Fraday Soc. Trans.*, **51**, 835–848.

Evans, M. G., Burt, T. P., Holden, J., and Adamson, J. K. (1999). Runoff generation and water table fluctuations in blanket peat: evidence from UK data spanning the dry summer of 1995. *J. Hydrol.*, **221**, 141–160.

Everett, D. H. and Smith, F. (1954). A general approach to hysteresis - Part 2: Development of the domain theory. *Fraday Soc. Trans.*, **50**, 187–197.

Everett, D. H. and Whitton, W. I. (1952). A general approach to hysteresis. *Fraday Soc. Trans.*, **48**, 749–757.

Fagherazzi, S., Bertoluzzi, A., Dietrich, W., Adami, A., Lanzoni, S., Marani, M., and Rinaldo, A. (1999). Tidal networks: 1. Automatic network extraction and preliminary scaling features from digital terrain maps. *Water Resour. Res.*, **35**, 3891–3904.

Fornasiero, A., Gambolati, G., Putti, M., Teatini, P., Ferraris, S., Pitacco, A., Rizzetto, F., Tosi, L., Bonardi, M., and Gatti, P. (2002). Subsidence due to peat soil loss in the Zenare Basin (Italy): design and set-up pf the fiel experiment. In P. Campostrini, editor, *Scientific Research and Safeguarding of Venice (CORILA Research Program 2001 Results)*, pages 201–215. La Garangola, Venezia, Italy.

Fornasiero, A., Putti, M., Teatini, P., Ferraris, S., Rizzetto, F., and Tosi, L. (2003). Monitoring of hydrological parameters related to peat oxidation in a subsiding coastal basin south of Venice, Italy. In E. Servat, W. Najem, C. Leduc, and A. Shakeel, editors, *Hydrology of the Mediterranean and Semiarid Regions*, volume 278, pages 458–462. IAHS.

Forsyth, P. A., Wu, Y. S., and Pruess, K. (1995). Robust numerical methods for saturated-unsaturated flow with dry initial conditions in heterogeneous media. *Adv. Water Resources*, **18**(1), 25–38.

Francese, R., Galgaro, A., Farinatti, A., Putti, M., Teatini, P., Rizzetto, F., and Tosi, L. (2002). Geophysical investigation within the Zennare Basin (Venice). In P. Campostrini, editor, *Scientific Research and Safeguarding of Venice (CORILA Research Program 2001 Results)*, pages 229–239. La Garangola, Padova, Italy.

Freibauer, A., Rounsevell, M. D. A., Smith, P., and Verhagen, J. (2004). Carbon sequestration in the agricultural soils of europe. *Geoderma*, **122**, 1–23.

Frich, P., Alexander, L. V., Della-Marta, P., Gleason, B., Haylock, M., G, A. M., Tank, K., and Peterson, T. (2002). Observed coherent changes in climate extremes during the second half of the twentieth century. *Clim. Res.*, **19**, 193–212.

Friedrichs, C. T. and Perry, J. E. (2001). Tidal salt marsh morphodynamics: A synthesis. *J. Coastal Res.*, pages 6–36.

Fuller, A. G. T. R. M. and Eastwood, J. A. (1998). Supervised versus unsupervised methods for classification of coasts and river corridors from airborne remote sensing. *Int. J. Remote Sens.*, **19**, 3423–3431.

Galloway, D., Jones, D. R., and Ingebritsen, S. E. (1999). Land subsidence in the United States. Circular 1182, U.S. Geological Survey.

Gambolati, G. (1973). Equation of One-Dimensional Vertical Flow of Groundwater 1. The Rigorous Theory. *Water Resour. Res.*, **9**(4), 1022–1028.

Gambolati, G., Putti, M., Teatini, P., Camporese, M., Ferraris, G., Gasparetto Stori, G., Nicoletti, V., Rizzetto, F., Silvestri, S., and Tosi, L. (2005). Peatland oxidation enhances subsidence in the venice watershed. *EOS Trans. AGU*, **86**(23), 217–224.

Gambolati, G., Putti, M., Teatini, P., and Gasparetto Stori, G. (2006). Subsidence due to peat oxidation and impact on drainage infrastructures in a farmland catchment south of the Venice Lagoon. *Environ. Geol.*, **49**, 814–820.

Gardner, L. R. (2008). Comment on "Spatial organization and ecohydrological interactions in oxygen-limited vegetation ecosystems" by Marco Marani *et al. Water Resour. Res.*, **35**, 3891–3904.

Gatti, P., Bonardi, M., Tosi, L., Rizzetto, F., Fornasiero, A., Gambolati, G., Putti, M., and Teatini, P. (2002). The peat deposit of the subsiding Zennare Basin, south of the Venice Lagoon, Italy: Geotechnical classification and preliminary mineralogical characterization. In P. Campostrini, editor, *Scientific Research and Safeguarding of Venice (CORILA Research Program 2001-2003)*, pages 241–257. La Garangola, Venezia, Italy.

Gatto, P. and Carbognin, L. (1981). The Lagoon of Venice: Natural environmental trend and man-induced modification. *Hydrol. Sci. B.*, **26**, 379–391.

Gilham, R. W., Klute, A., and Heermann, D. F. (1976). Hydraulic properties of a porous medium; measurements and empirical representation. *Soil Sci. Soc. Am. J.*, **40**, 203–207.

Glaser, P. H., Chanton, J. P., Morin, P., Rosenberry, D. O., Siegel, D. I., Ruud, O., Chasar, L. I., and Reeve, A. S. (2004). Surface deformations as indicators of deep ebullition fluxes in a large northern peatland. *Global Biogeochem. Cycles*, **18**, GB1003, doi:10.1029/2003GB002069.

Gray, W. G. and Hassanizadeh, S. M. (1991). Unsaturated flow theory including interfacial phenomena. *Water Resour. Res.*, **27**, 1855–1863.

Gronlund, A., Hauge, A., Hovde, A., and Rasse, D. P. (2008). Carbon loss estimate from cultivated peat soils in Norway: a comparison of three methods. *Nutr. Cycl. Agroecosyst.*, pages doi:10.1007/s10705–008–9171–5.

Haines, W. B. (1930). Studies in the physical properties of soils. the hysteresis effect in capillary properties, and the modes of moisture distribution associated therewith. *Journal of Agricoltural Science*, **20**, 97–116.

Hanks, R. J., Klute, A., and Bresler, E. (1969). A numerical method for estimating infiltration, redistribution, drainage and evaporation of water from of water from soil. *Water Resour. Res.*, **5**(5), 1064–1069.

Harvey, J. W., German, P. A., and Odum, W. E. (1987). Geomorphological controls of subsurface hydrology in the creekbank zone of regularly flooded tidal marsh. *Estuarine Coastal Mar. Sci.*, **25**, 677–691.

Hassanizadeh, S. W. and Gray, W. G. (1990). Mechanics and thermodynamics of multiphase flow in porous media including interphase boundaries. *Adv. Water Resour.*, **13**, 169–186.

Haverkamp, R., Reggiani, P., Ross, P. J., and Parlange, J. Y. (2002). Soil-water hysteresis predistion model based on theory and geometric scaling. *Environmental Mechanics: Water,Mass and Energy transfer in the Biosphere, Geophys. Monograph. Ser.*, **129**, 213–246.

Heinen, M. and Raats, P. A. C. (1997). Hysteretic hydraulic properties of a coarse sand horticultural substrate. In M. T. van Genuchten *et al.*, editor, *Characterization and Measurements of the Hydraulic properties of unsaturated porous media I*, pages 467–476. Dept. of Environmental Sciences, University of California, Riverside, California.

Hemond, H. F. and Fifield, J. L. (1982). Flow in salt marsh peat: A model and field study. *Limnol. Oceanogr.*, **27**(1), 126–136.

Hendriks, R. F. A. (2004). An analytical equation for describing the shrinkage characteristic of peat soils. In J. Päivänen, editor, *Wise Use of Peatlands, Proceedings of the 12th International Peat Congress*, pages 1343–1348, Jyväskylä, Finland. Int. Peat Society.

Hillel, D. (1980). *Fundamentals of soil physics.* Accademic Press Inc., New York.

Hoa, N. T., Gaudu, R., and Thirriot, C. (1977). Influence of hysteresis effects on transient flowsin saturated-unsaturated porous media. *Water Resour. Res.*, **13**, 992–996.

Hobbs, N. B. (1986). Mire morphology and the properties and behaviour of some British and foreign peats. *Q. J. Eng. Geol.*, **19**, 7–80.

Holden, J. (2005). *Peatland hydrology and carbon release: why small-scale process matters*, volume 363. Philos. T. Roy. Soc. A.

Holden, J. and Burt, T. P. (2003). Hydrological studies on blanket peat: the significance of the acrotelm-catotelm model. *J. Ecol.*, **91**, 86–102.

Hopmans, J. W. and Dane, J. H. (1986). Temperature dependence of soil water retention curves. *Soil Sci. Soc. Am. J.*, **50**, 562–567.

Hutchinson, J. N. (1980). The record of peat wastage in the East Anglian fenlands at Holme Post, 1848-1978 a.d. *J. Ecol.*, **68**(1), 229–249.

IPCC (2007). Climate change 2007: Synthesis report. Technical report, Intergovernamental Panel on Climate Change.

Jaynes, D. B. (1984). Comparison of soil-water hysteresis model. *J. Hydrol.*, **75**, 287–299.

Jongedyk, H. A. *et al.* (1950). Subsidence of muck soils in northern Indiana. Circular 366, Purdue University Agricultural Experiment Station.

Jungkunst, H. F. and Fiedler, S. (2007). Latitudinal differentiated water table control of carbon dioxide, methane and nitrous oxide fluxes from hydromorphic soils: feedbacks to climate change. *Glob. Change Biol.*, **13**, 1–16.

Kaluarachchi, J. J. and Parker, J. C. (1987). Effects of hysteresis with air entrapment on water flow in the unsaturated. *Water Resour. Res.*, **23**, 1967–1976.

Kellner, E. and Lundin, L.-C. (2001). Calibration of Time Domain Reflectometry for water content in peat soil. *Nordic Hydrology*, **32**(4/5), 315–332.

Kellner, E., Waddington, J. M., and Price, J. S. (2005). Dynamics of biogenic gas bubbles in peat: Potential effects on water storage and peat deformation. *Water Resour. Res.*, **41**, W08417, doi:10.1029/2004WR003732.

Kennedy, G. W. and Price, J. S. (2004). Simulating soil water dynamics in a cutover bog. *Water Resour. Res.*, **40**, W12410, doi:10.1029/2004WR003099.

Kennedy, G. W. and Price, J. S. (2005). A conceptual model of volume-change controls on the hydrology of cutover peats. *J. Hydrol.*, **302**(1–4), 13–27.

Kool, J. B. and Parker, J. C. (1987). Development and evaluation of closed-form expressions for hysteretic soil hydraulic properties. *Water Resour. Res.*, **23**, 105–114.

Land, C. S. (1968). Calculation of imbibition relative permeability for two and three phase flow from rock properties. *Trans. Am. Inst. Min. Metall. Pet. Eng.*, **243**, 149–156.

Lenhard, R. and Parker, J. (1987a). Measurements and prediction of saturation-pressure relationshiops in three phase porous media sustems. *Journal of Contaminant Hydrology*, **1**, 407–424.

Lenhard, R. and Parker, J. (1987b). A model for hysteretic constitutive relations governing multiphase flow 2. permeability-saturation relations. *Water Resour. Res.*, **23**(12), 2197–2206.

Lenhard, R., Parker, J., and Kaluarachchi, J. (1989). A model for hysteretic constitutive relations governing multiphase flow 3. refinements and numerical simulations. *Water Resour. Res.*, **25**(7), 1727–1736.

Lenhard, R., Parker, J., and Kaluarachchi, J. (1991). Comparing simulated and experimental hysteretic twophase transient fluid flow phenomena. *Water Resour. Res.*, **27**(8), 2113–2124.

Leonard, L. A. and Luther, M. E. (1995). Flow hydrodynamics in tidal marsh canopies. *Limnol. Oceanogr.*, **40**, 1474–1484.

Letts, M. G., Roulet, N. T., Comer, N. T., Skarupa, M. R., and Verseghy, D. L. (2000). Parametrization of peatland hydraulic properties for the Canadian Land Surface Scheme. *Atmosphere Ocean*, **38**(1), 141–160.

Li, H. and Lockington, D. (2005). Aeration for plant root respiration inatidal marsh. *Water Resour. Res.*, **41**.

Li, L., Barry, D. A., and Pattiaratchi, C. B. (1997). Numerical modelling of tide-induced beach water table fluctuations. *Coastal Eng.*, **30**, 105–123.

Li, L., Barry, D. A., Cunningham, C., Stagnitti, F., and Parlange, J. Y. (2000). A two-dimensional analytical solution of groundwater response to tidal loading in an estuary and ocean. *Adv. Water Resources*, **23**, 825–833.

Løddesøl, A. (1949). Soil conservation problems in Norway. Experience paper prepared for Section Meetings, Land Resources 1(b) on Methods of Soil Conservation for the United Nations' Economic and Social Council, E 1 Consf. 2/Sec/W.87, 23 March, 1949.

Marani, M., Lanzoni, S., Silvestri, S., and Rinaldo, A. (2004). Tidal landforms, patterns of halophytic vegetation and the fate of the Lagoon of Venice. *J. Mar Syst.*, **51**, 191–210.

Marani, M., Bellucco, E., Ferrari, S., Silvestri, S., D'Alpaos, A., Lanzoni, S., Feola, A., and Rinaldo, A. (2006a). Analysis, synthesis and modelling of high-resolution observations of saltmarsh ecogeomorphological patterns in the Venice Lagoon. *Estuar. Coast. Shelf S.*, **69**(3–4), 414–426.

Marani, M., Silvestri, S., Bellucco, E., Ursino, N., Comerlati, A., Tosatto, O., and Putti, M. (2006b). Spatial organization and ecohydrological interactions in oxygenlimited vegetation ecosystems. *Water Resour. Res.*, **42**, W06D06, doi:10.1029/2005WR004582.

Melling, L., Hatano, R., and Goh, K. J. (2005). Soil CO_2 flux from three ecosystems in tropical peatland of Sarawak, Malaysia. *Tellus*, **57B**, 1–11.

Miller, C. T., Williams, G. A., Kelley, C. T., and Tocci, M. D. (1998). Robust solution of richards equation for nonunifom porous media. *Water Resour. Res.*, **34**, 2599–2610.

Morari, F., Lugato, E., Berti, A., and Giardini, L. (2006). Long-term effects of recommended management practices on soil carbon changes and sequestration in northeastern Italy. *Soil Use Manage.*, **22**, 71–81.

Morrow, N. R. (1965). Capillary equilibrium in porous materials. *Soc. Pet. Eng. J.*, **5**, 15–24.

Mount, J. and Twiss, R. (2005). Subsidence, sea level rise, and seismicity in the Sacramento-San Joaquin Delta, San Francisco. *San Francisco Estuary and Watershed Sci.*, **3**(1).

Mualem, Y. (1973). Modified approach to capillary hysteresis based on a similarity hypothesis. *Water Resour. Res.*, **9**, 1324–1331.

Mualem, Y. (1974). A conceptual model of hysteresis. *Water Resour. Res.*, **10**, 514–520.

Mualem, Y. (1976). A new model predicting the hydraulic conductivity. *Water Resour. Res.*, **13**(3), 3033–3040.

Mualem, Y. (1977). Extension of the similarity hypothesis used for modeling the soil water characteristics. *Water Resour. Res.*, **13**(4), 773–780.

Mualem, Y. (1984). A modified dependent-domain theory of hysteresis. *Soil Sci.*, pages 283–291.

Mualem, Y. and Dagan, G. (1975). A dependence domain model of capillary hysteresis. *Water Resour. Res.*, **11**, 452–460.

Myllys, M. and Simojoki, A. (1996). Calibration of time domain reflectometry (tdr) for soil moisture measurements in cultivated peat soils. *Suo*, **47**, 1–6.

Nash, J. E. and Sutcliffe, J. V. (1970). River flow forecasting through conceptual models. Part I - A discussion of principles. *J. Hydrol.*, **10**, 282–290.

Néel, L. (1942). Théories des lois d'aimantation de lord raileigh. *Cah. Phys.*, **12**, 1–20.

Néel, L. (1943). Théories des lois d'aimantation de lord raileigh. *Cah. Phys.*, **13**, 19–30.

Nicoletti, V., Silvestri, S., Rizzetto, F., Tosi, L., Putti, M., and Teatini, P. (2003). Use of remote sensing for the delineation of surface peat deposits south of the Venice Lagoon (Italy). In *IGARSS 2003, International Geoscience and Remote Sensing Symposium*, volume IV, pages 2881–2883. Institute of Electrical and Electronics Engineers, Inc.

Nieuwenhuis, H. S. and Schokking, F. (1997). Land subsidence in drained peat areas of the Province of Friesland, The Netherlands. *Q. J. Eng. Geol.*, **30**, 37–48.

Nieveen, J. P., Campbell, D. I., Schipper, L. A., and Blair, I. J. (2005). Carbon exchange of grazed pasture on a drained peat soil. *Glob. Change Biol.*, **11**, 607–618.

O'Kane, J., Pokrovskii, A., and Flynn, D. (2004). The fest model for testing the importance of hysteresis in hydrology. In *Proceedings of EGU conference, Vol. 6, 07303.*

Oleszczuk, R., Bohne, K., Szatylowicz, J., Brandyk, T., and Gnatowski, T. (2003). Influence of load on shrinkage behavior of peat soils. *J. Plant Nutr. Soil Sci.*, **166**, 220–224.

Otten, W., Raats, P. A. C., and Kabat, P. (1997). Hydraulic properties of root zone substrates in greenhouse horticulture. In M. T. van Genuchten *et al.*, editor, *Characterization and Measurements of the Hydraulic properties of unsaturated porous media I*, pages 477–488. Dept. of Environmental Sciences, University of California, Riverside, California.

Paniconi, C. and Putti, M. (1994). A comparison of Picard and Newton iteration in the numerical solution of multidimensional variably saturated flow problems. *Water Resour. Res.*, **30**(12), 3357–3374.

Parker, J. and Lenhard, R. (1987). A model for hysteretic constitutive relations governing multiphase flow 1. saturation-pressure relations. *Water Resour. Res.*, **23**(12), 2187–2196.

Parker, J. C., Lenhard, R. J., and Kuppusamy, T. (1987). A parametric model for constitutive properties relations in multiphase porous media systems. *Water Resour. Res.*, **23**, 618–624.

Parlange, J. Y. (1976). Capillary hysteresis and relationship between drying and wetting curves. *Water Resour. Res.*, **12**, 224–228.

Pestrong, R. (1965). The development of drainage patterns on tidal marshes. Publ. Geol. Sci. Tech. Rep. 10, Stanford Univ., Stanford, California.

Pethick, J. (1984). *An Introduction to Coastal Geomorphology*. Edward Arnold, England.

Philip, J. R. (1969). Hydrostatics and hydrodynamics in swelling soils. *Water Resour. Res.*, **5**(5), 1070–1077.

Pickens, J. F. and Gilham, R. W. (1980). Finite element analysis of solute transport under hysteretic unsaturated flow conditions. *Water Resour. Res.*, **16**, 1071–1078.

Poulovassilis, A. (1962). Hysteresis of pore water: An application on the concept of independent domains. *Soil Sci.*, **93**, 405–412.

Poulovassilis, A. and Childs, E. C. (1971). The hysteresis of pore water : the non-independence of domains. *Soil Sci.*, **112**, 301–312.

Preisach, F. (1935). Über die magnetische nachwirkung. *Z Physik*, **94**, 277–302.

Price, J. S. (2003). Role and character of seasonal peat soil deformation on the hydrology of undisturbed and cutover peatlands. *Water Resour. Res.*, **39**(9), 1241, doi:10.1029/2002WR001302.

Price, J. S. and Schlotzhauer, S. M. (1999). Importance of shrinkage and compression in determining water storage changes in peat: the case of a mined peatland. *Hydrol. Process.*, **13**, 2591–2601.

Pruess, K., Oldenburg, C., and Moridis, G. (1999). TOUGH2 Users Guide, Version 2.0. Report, Lawrence Berkeley Laboratory, Berkeley, California.

Pyatt, D. G. and John, A. L. (1989). Modelling volume changes in peat under conifer plantations. *J. Soil Sci.*, **40**, 695–706.

Quinton, W. L., Gray, D. M., and Marsh, P. (2000). Subsurface drainage from hummock-covered hillslopes in the Arctic tundra. *J. Hydrol.*, **237**, 113–125.

Ramsar Convention Secretariat (2006). *The Ramsar Convention Manual: a guide to the Convention on Wetlands (Ramsar, Iran 1971).* Secretariat, Gland, Switzerland, 4^{th} edition.

Rathfelder, K. and Abriola, L. (1994). Mass conservative numerical solutions of the head-based richards equation. *Water Resour. Res.*, **30**(9), 2579–2586.

Rinaldo, A., Fagherazzi, S., Lanzoni, S., Marani, M., and Dietrich, W. (1999a). Tidal networks: 2. Watershed delineation and comparative net- work morphology. *Water Resour. Res.*, **35**, 3905–3917.

Rinaldo, A., Fagherazzi, S., Lanzoni, S., Marani, M., and Dietrich, W. (1999b). Tidal networks: 3. Landscape-forming discharges and studies in empirical geomorphic relationships. *Water Resour. Res.*, **35**, 3919–3929.

Rizzetto, F., Tosi, L., Carbognin, L., Bonardi, M., and P.Teatini (2003). Geomorphological setting and related hydrogeological implications of the coastal plain south of the Venice Lagoon (Italy). In E. Servat *et al.*, editor, *Hydrology of the Mediterranean and Semiarid Regions*, volume 278, pages 463–470. Int. Assoc. of Hydrol. Sci., Gentbrugge, Belgium.

Roe, H. B. (1936). A study of depth of ground-water level on yields of crops grown on peat lands. Bulletin 330, University of Minnesota Agricultural Experiment Station.

Rojstaczer, S. and Deverel, S. J. (1993). Time dependence in atmospheric carbon inputs from drainage of organic soils. *Geophys. Res. Lett.*, **20**, 1383–1386.

Rojstaczer, S. and Deverel, S. J. (1995). Land subsidence in drained histosols and highly organic mineral soils of California. *Soil Sci. Soc. Am. J.*, **59**(4), 1162–1167.

Russo, D., Jury, W. A., and Butters, G. L. (1989). Numerical analysis of solute transport during transient irrigation: 1. the effect of hysteresis and profile eterogeneity. *Water Resour. Res.*, **25**, 2109–2118.

Sarmin, E. N. and Chudov, L. A. (1963). On the stability of the numerical integration of systems of ordinary differential equations arising in the use of the straight line method. *USSR Computational Mathematics and Mathematical Physics*, **3**(6), 1537–1543.

Schär, C., Vidale, P. L., Lüthi, D., Frei, C., Häberli, C., Liniger, M. A., and Appenzeller, C. (2004). The role of increasing temperature variability in european summer heat waves. *Nature*, **427**, 332–335.

Schiesser, W. E. (1991). *The Numerical Method of Lines: Integration of Partial Differential Equations*. Academic Press, San Diego, California.

Schipper, L. A. and McLeod, M. (2002). Subsidence rates and carbon loss in peat soils following conversion to pasture in the Waikato Region, New Zealand. *Soil Use Manage.*, **18**, 91–93.

Schlotzhauer, S. M. and Price, J. S. (1999). Soil water flow dynamics in a managed cutover peat field, Quebec: Field and laboratory investigations. *Water Resour. Res.*, **35**(12), 3675–3683.

Schothorst, C. J. (1977). Subsidence of low moor peat soils in the western Netherlands. *Geoderma*.

Schwärzel, K., Renger, M., Sauerbrey, R., and Wessolek, G. (2002). Soil physical characterics of peat soils. *J. Plant Nutr. Soil Sci.*, **165**, 479–486.

Scott, P. S., Farquar, G. J., and Kouwen, N. (1983). Hysteretic effects on net infiltration. Technical report, Am.Soc.Agric.Eng., Chicago, Illinois, USA.

Si, B. C. and Kachanoski, R. G. (2000). Unified solution for infiltration and drainage with hysteresis: Theory and field test. *Soil Sci. Soc. Am. J.*, **64**, 30–36.

Silvestri, S. and Marani, M. (2004). Salt marsh vegetation and morphology, modelling and remote sensing observations. In S. Fagherazzi *et al.*, editor, *Ecogeomorphology of Tidal Marshes, Coastal Estuarine Stud.*, volume 59, pages 5–25, Washington D. C. AGU.

Silvestri, S., Marani, M., Rinaldo, A., and Marani, A. (2000). Vegetazione alola e morfologia lagunare. Technical report, Atti dellIstituto Veneto di Scienze, Lettere ed Arti, 68, Classe di scienze siche, matematiche e naturali.

Silvestri, S., Marani, M., and Marani, A. (2003). Hyperspectral remote sensing of salt marsh vegetation, morphology and soil topography. *Phys. Chem. Earth*, **28**, 15–25.

Silvestri, S., Defina, A., and Marani, M. (2005). Tidal regime, salinity and salt-marsh plant zonation. *Estuar. Coast. Shelf S.*, **62**, 119–130.

Silvola, J., Alm, J., Ahlholm, U., Nykänen, H., and Martikainen, P. J. (1996). CO_2 fluxes from peat in boreal mires under varying temperature and moisture conditions. *J. Ecol.*, **84**, 219–228.

Skoropanov, S. G. (1962). Drainage norms for peat bog soils. *Gidrotehnika i Melioratsiya*, **1**, 3440. Translated from Russian for USDA and NSF in Jerusalem, Israel, 1968. Available from U.S. Department of Commerce Clearing House for Federal Scientific and Technical Information; Springfield, VA 22151.

Smiles, D. E. (2000). Hydrology of swelling soils: a review. *Aust. J. Soil Res.*, **38**, 501–521.

Springer, A. E., Wright, J. M., Shafrothand, P. B., Stromberg, J. C., and Patten, D. T. (1999). Coupling groundwater and riparian vegetation models to assess effects of reservoir releases. *Water Resour. Res.*, **35**(12), 3621–3630.

Steel, T. J. and Pye, K. (1997). The development of salt marsh tidal creek networks: Evidence from the uk. In C. C. Sci. and E. Assoc., editors, *Canadian Coastal Conference*, Guelph. Ontario.

Stephens, J. C. (1969). Peat and muck drainage problems. *Journal of the irrigation and drainage division*, **95**, 285–305.

Stephens, J. C., Allen Jr, L. H., and Chen, E. (1984). Organic soil subsidence. In T. L. Holzer, editor, *Man-induced land subsidence*, volume VI of *Reviews in Engineering Geology*, pages 107–122. The Geological Society of America, Boulder, Colorado 80301.

Stevenson, R. E. and Emery, K. O. (1958). *Marshlands at Newport Bay, California*. Allan Hancock Found. Publ. Occas. Pap., Univ. of Southern Calif. Press, Los Angeles.

Suddeth, R. J., Mount, J., and Lund, J. R. (2010). Levee Decisions and Sustainability for the Sacramento San Joachim Delta. *San Francisco Estuary and Watershed Sci.*, **8**(2), 1–23.

Teatini, P., Putti, M., Gambolati, G., Ferraris, S., and Camporese, M. (2004). Reversible/irreversible peat surface displacements and hydrological regime in the Zennare Basin, Venice. In P. Campostrini, editor, *Scientific Research and Safeguarding of Venice*

(CORILA Research Program 2001-2003, 2002 Results), volume II, pages 93–106. La Garangola, Venezia,Italy.

Terzaghi, K. (1943). *Theoretical Soil Mechanics*. John Wiley, Hoboken, N.J.

Topp, G. C. (1969). Soil-water hysteresis measured in a sandy loam and compared with the hysteretic domain model. *Soil Sci. Soc. Am. Proc.*, **33**, 643–651.

Topp, G. C. (1971). Soil-water hysteresis: the domain theory extended to pore interaction conditions. *Soil Sci. Soc. Am. J.*, **35**, 219–225.

Topp, G. C. and Miller, E. E. (1966). Hysteresis moisture characteristics and hydraulic conductivities for glassbead media. In *Soil. Sci. Amer. Proc.*, volume 30, pages 156–162.

Topp, G. C., Davis, J. L., and Annan, A. P. (1980). Electromagnetic determination of soil water content: Measurements in coaxial transmission lines. *Water Resour. Res.*, **16**(3), 574–582.

Tosatto, O., Belluco, E., Silvestri, S., Ursino, N., Comerlati, A., Putti, M., and Marani, M. (2009). Reply to comment by L. R. Gardner on "Spatial organization and ecohydrological interactions in oxygenlimited vegetation ecosystems". *Water Resour. Res.*, **45**, W05604, doi:10.1029/2007WR006345.

Ungar, I. A. (1991). *Ecophysiology of Vascular Halophytes*. CRC Press, Boston, Mass.

Ursino, N., Silvestri, S., and Marani, M. (2004). Subsurface flow and vegetation patterns in tidal environments. *Water Resour. Res.*, **40**, W05115, doi:10.1029/2003WR002702.

Van den Akker, J. J. H. and Hendriks, R. F. A. (1997). Shrinkage characteristics of Dutch peat soils. In *Proc. Int. Congr. "Peat in horticulture - its use and sustainability*, pages 156–182, Amsterdam, The Netherlands.

van Genuchten, D. R. N. M. T. and Biggar, J. W. (1986). Water flow and solute transport processes in the unsaturated zone. *Water Resour. Res.*, **22**, 89–108.

van Genuchten, M. T. (1980). A closed-form equation for predicting the hydraulic conductivity of unsaturated soils. *Soil Sci. Soc. Am. J.*, **44**, 892–898.

Visintin, A. (1993). *Differential models of hysteresis*. Springer.

Vries, F. T. D. (2003). Practical use of a hydrological model for peatlands in borneo; modeling the sungai sebangau catchment in central kalimantan, indonesia. Technical report, Alterra, Wageningen, The Netherlands.

Waddington, J. M. and Roulet, N. T. (1997). Groundwater flow and dissolved carbon movement in a boreal peatland. *J. Hydrol.*, **191**, 122–138.

Waddington, J. M., Warner, K. D., and Kennedy, G. W. (2002). Cutover peatlands: a persistent source of atmospheric CO_2. *Global Biogeochem. Cy.*, **16**(1), 1–7.

Wei, C. and Dewoolkar, M. M. (2006). Formulation of capillary hysteresis with internal state variables. *Water Resour. Res.*, **42**, 1855–1863.

Weiss, R., Alm, J., Laiho, R., and Laine, J. (1998). Modeling moisture retention in peat soils. *Soil Sci. Soc. Am. J.*, **62**(2), 305–313.

Willmott, C. (1948). On the evaluation of model performance in physical geography. In G. Gaille and C. Willmott, editors, *Spatial Statistics and Models*, pages 443–460. Reidel Publishing Co.

Wilson, A. M. and Gardner, L. R. (2005). Comment on "subsurface flow and vegetation patterns in tidal environments" by nadia ursino, sonia silvestri, and marco marani. *Water Resour. Res.*, **41**, W07021, doi:10.1029/2004WR003554.

Wösten, J. H. M., Ismail, A. B., and van Wijk, A. L. M. (1997). Peat subsidence and its practical implications: a case study in Malaysia. *Geoderma*, **78**, 25–36.

Wösten, J. H. M., Clymans, E., Page, S. E., Rieley, J. O., and Limin, S. H. (2008). Peat-water interrelationships in a tropical peatland ecosystem in Southeast Asia. *Catena*, **73**, 212–224.